Università degli Studi di trieste

Dipartimento di Fisica

Divisione di Astrofisica

Dust Evolution in Galaxy Cluster Simulations

PhD Candidate:
Eda Gjergo

Supervisor:
Dr. Gian Luigi Granato

School Coordinator:
Livio Lanceri

Co-Supervisor:
Dr. Giuseppe Murante

Academic Advisor:
Prof. Stefano Borgani

January 30, 2019

Doctoral Thesis
Academic Year 2017:2018
Cycle XXXI

Dust Evolution in Galaxy Cluster Simulations

EDA GJERGO

Department of Physics
Division Astrophysics
University of Trieste
Trieste, Italy 2018

Dust Evolution in Galaxy Cluster Simulations

EDA GJERGO
Department of Physics, Astrophysics Division
University of Trieste

PhD Candidate:	Eda Gjergo
Supervisor:	Dr. Gian Luigi Granato,
	INAF Astronomical Observatory of Trieste
Referee:	Prof. Alessandro Bressan,
	SISSA International School for Advanced Studies
Referee:	Prof. Manolis Plionis,
	Aristotle University of Thessaloniki

Doctoral Thesis 2018:2019
Department of Physics
Astrophysics Division
University of Trieste
Via Bazzoni 2, Trieste, 34143
Telephone +39 040 3199 133
Email gjergo@oats.inaf.it

A thesis submitted in fulfillment of the requirements for the degre of Doctor Philosophiae in Physics

Typeset in LaTeX
Trieste, Italy 2018

Abstract

Gaseous astrophysical media are splattered with solid agglomerates of molecules we call cosmic dust. Dust ranges in size between a few Angstroms and a few microns. While dust accounts only for one percent of the mass in the interstellar medium (ISM) of a Milky Way-like galaxy, it reprocesses about a third of its starlight, mostly in the UV and optical bands, and reemits it in the infrared. It is almost impossible to interpret correctly the spectral energy distribution (SED) of a galaxy without accounting for dust in some way. Dust affects not only the observation but also the evolution of galaxies. In fact, its surface is a catalyst for the formation of molecules, most important of which is H_2. These molecules are efficient gas coolants and accelerate the gravitational collapse of molecular clouds, the cradles for star formation.

Observations, in particular, are quite sensitive to dust properties such as composition and grain size. A need emerges to include dust within theoretical models of galaxy and galaxy cluster evolution. The INAF Astronomical Observatory of Trieste, among other things, has developed a custom state-of-the-art cosmological N-body simulation of galaxy clusters based on the GADGET-3 code. The code calculates dynamics with a tree-Particle-Mesh method, where the simulated 'particles' actually represent massive ensembles of substances of different types, specifically dark matter, gas, stars, and black holes. The interactions between gas particles are treated with Smoothed-Particle Hydrodynamics, there is also star formation, radiative cooling, stellar and active galactic nuclei (AGN) feedback, and chemical evolution by stellar nucleosynthesis.

Adding dust to this framework however has not been feasible until now. Tracing the continuous grain size (or its discrete approximation) would burden with additional dimensions the already heavy particle structure and calculations, slowing down the runs to impractical rates. Dust was instead treated in post processing

(Granato et al., 2015), and its properties were assumed a priori. Then Hirashita (2015) proposed an approximation. Instead of computing the grain size continuum, he postulated that dust grains are divided between large (nominally 0.1μm) and small (nominally 0.01μm). He therefore adapted a comprehensive one-zone dust evolution model (Asano et al., 2013) to this approximation. The binary grain size distribution was selected for both observational and modeling reasons. When dust grains are produced in the envelopes of evolved stars or in supernova remnants, the dominant size is around 0.1μm. In the ISM however, smaller dust is often just as prevalent or at times even dominant. This suggests that ISM evolution alters the grain size distribution. The phenomenon is captured in the modeling. Some processes are most efficient on one grain size over the other, or at times they have opposite effects on each size domain.

We successfully adapted the Hirashita (2015) model to our custom GADGET-3 cosmological zoom-in simulation code, specifically we embedded the model so that each simulated gas particle will trace, on top of the usual gas elements obtained from stellar and supernovae yields, also small and large dust grains. We tested our method on four massive (two $M_{200} \geq 3 \times 10^{14} M_{\odot}$ and two $M_{200} \geq \times 10^{15} M_{\odot}$) galaxy clusters. We also improved on previous dust production routines, which assumed a fixed dust condensation efficiency for each element. Instead, we form the two most representative dust species observed in nature: carbonaceous dust and astrophysical silicates, based on the element abundance produced by stellar or supernovae yields.

At the peak of star formation activity at $z \gtrsim 3$ when proto-clusters start to assemble, we find that the gas particles in our simulations are rich in dust, as expected. In order to test the impact of dust processes on dust growth other than stellar production, we ran simulations with dust production and destruction alone, without any grain-gas or grain-grain interactions. Dust is enhanced by a factor of two to three due to the processes occurring in the ISM. We investigated variations of the model through different runs to understand the interdependence of all the processes.

We were able to reproduce the dust abundance to metallicity relations observed in local galaxies, however we under-produced the dust content of galaxy clusters around $z \lesssim 0.5$ observed by IRAS, Planck, and Herschel observations. This discrepancy can be mended only by assuming a lower sputtering efficiency, which erodes dust grains in the hot Intracluster Medium (ICM). The abundance of the two dust species, silicates and carbonaceous dust, is also slightly different from the Milky Way average, and from the common values adopted in calculations of dust reprocessing. These differences may have a strong impact on the predicted SED. This method lays the

groundwork for further developments, such as cosmological simulations of single galaxies, , or the refinement of radiative cooling routines with H_2 catalysis on grain surfaces.

Dedication

I am indebted to a long list of mentors and friends which have inspired me and will continue to do so for many years to come. First of all, I would like to thank my primary supervisor Gian Luigi Granato for disciplining my enthusiasm into a more attentive, careful, and critical approach to scientific research. I am grateful for his painstaking guidance over these years, and for the constructive discussions. I appreciate Giuseppe Murante's generosity in sharing his knowledge and for always finding the time to help everyone. I owe him a great deal of my improvements in computing. I am lucky to have been inspired by Stefano Borgani's humble excellence and passion for cosmological research. I benefited from fruitful conversations with PierLuigi Monaco who impressed me with a sharp and clear mind. Special thanks to Francesca Matteucci who, while not an official supervisor, has been a pillar of strength to me with her warmth, passionate character, and dynamic scientific intuition. I value the support and optimism I received from her through thick and thin.

Thanks to Steve Kuhlmann, for being beyond a supervisor, a dear friend, for introducing me to the world of research with countless opportunities. Thank you for believing in my potential and for encouraging me to pursue a career in Astrophysics. Thanks to Arthur Lubin for inspiring me with his resilience, charisma, love of mathematics, and ability to always let me see and seek the big picture. Thanks to Yurii Shylnov for being one of the most honest, humble, yet excellent professors I have ever had. Thanks to Salman Habib, Katrin Heitmann, Sergei Shandarin, for the scientific perspicacity and thought-provoking conversations. Thanks to Fabio Pasian for encouraging me to apply to the PhD program in the first place.

Thanks to Cinthia Ragone-Fuguera, Gabriella de Lucia, Gabriele Cescutti, Andrea Biviano, Emiliano Sefusatti, Emiliano Munari, Elena Rasia, Barbara Sartoris, Fabio Fontanot, Veronica Biffi, Umberto Maio, David Goz, Alex Saro, and Marta Spinelli for galvanizing my scientific curiosity with the arrays of research fields and personalities they havex exposed me to. Thanks to my fellow PhD students who showed me excellence does not come at the cost of a balanced life, but because of it. Thanks

to my friends Emanuele Spitoni, Fiorenzo Vincenzo, Lorenzo Gioannini, Carlo De Masi, Valeria Grisoni, Anna Zoldan, Chiara Moretti, Luigi Bassini, Federico Rizzo, Paolo Simonetti, Dan Eckhart, and Angela Faust, whom between jokes, intellectual curiosity, authenticity, and originality, brought fun into my days, softened my quarter-life crisis, and affected my outlook on important issues.

Thanks to my dearest friends Carlo e Zina Magnelli, Linda Corsi, and Maria Luisa Princivalli, whose wisdom, optimism, affection, knowledge, and spiritual generosity brightened my life when I needed it most. You are like family. Margherita Hack, your memory lives within me every day. You showed me a way of being I aspire to master, with your relentless dedication, pure heart, minimalist lifestyle, scientific enterprise, devotion to humanity, to nature, to fairness. Thank you for having opened your heart to me and for believing in me from the very start. Dear Aldo de Rosa, I treasure you more than you could remember in your last years. I will never forget how nurturing, affectionate, and encouraging you've been to me, and how you helped me grow in between jokes and tease.

I owe any and all of my achievements to my mother, who raised me to value integrity, kindness, justice, and excellence, and who devoted every ounce of herself to help me grow every day. Thank you for your unconditional love and positivity, for your trust and encouragement. Thank you for being there for me always.

I hope to somehow repay and thank all of you for the way you enriched and shaped my life.

Acknowledgements

Eda Gjergo was supported by the INAF 2015 PhD grant "Galaxy clusters in their infancy: confronting simulated and observed IR/sub-mm properties". This project has received funding from the European Union's Horizon 2020 Research and Innovation Programme under the Marie Sklodowska-Curie grant agreement No 73437. The simulations were carried out at the following facilities (i) Mendieta Cluster from CCAD-UNC, which is part of SNCAD-MinCyT, Argentina; (ii) European Exascale System Interconnect and Storage (iii) CINECA (Italy), with CPU time assigned through ISCRA proposals and an agreement with the University of Trieste. The post-processing and analysis has been performed using the PICO HPC cluster at CINECA through our expression of interest. This publication has received funding from the European Union's Horizon 2020 research and innovation program under grant agreement No 730562 [RadioNet]. We thank Volker Springel for providing the non-public version of the GADGET3 code, and Peter Camps for prompt assistance and advice in using the radiative transfer code SKIRT. The analysis was conducted using IPython2 (Pérez and Granger, 2007), SciPy3 (Jones et al., 2001), NumPy4 (Van Der Walt et al., 2011), and MatPlotLib5 (Hunter, 2007).

I am grateful for the insightful comments and suggestions provided by the referee Alessandro Bressan which helped me to improve this manuscript.

Eda Gjergo, Trieste, November 2018

to my mother

Contents

List of Figures

List of Tables

List of Acronyms and Symbols

AGB Asymptotic Giant Branch
AGN Active Galactic Nuclei
AMR Adaptive Mesh Refinement
BCG Brightest Cluster Galaxy
CGM Circumgalactic Medium
CNM Cold Neutral Medium
DtG Dust-to Gas Ratio
FIR Far-Infrared
GRB Gamma Ray Bursts
HIM Hot Ionized Medium
ICM Intracluster Medium
IGM Intergalactic Medium
IR Infrared
ISM Interstellar Medium
LMC Large Magellanic Cloud
LTE Local Thermal Equilibrium
MC Molecular Clouds
MIR Mid-Infrared
MW Milky Way
NIR Near-Infrared
PAH Polycyclic Aromatic Hydrocarbons
SF Star Formation
SFR Star Formation Rate
SMC Small Magellanic Cloud
SN Supernova
SED Spectral Energy Distribution
WIM Warm Ionized Medium
WNM Warm Neutral Medium

z Cosmological Redshift

Z Metallicity

1

Introduction

1.1 The role of dust in the cosmic evolution

Dust is a mixture of smoke-sized (10 Å to a few μm) solid, sometimes icy, agglomerates of mostly carbon or silicon-based minerals. Dust constitutes about 1% of the Interstellar Medium (ISM). However, on average it reprocesses 30% (Bernstein et al., 2002) of starlight in local galaxies. The percentage can grow to up to 99% (Clements et al., 1996) for ultra-luminous infrared high-redshift galaxies. It is estimated that about 50% of all the starlight emitted across the history of the Universe has been reprocessed by dust (Hauser and Dwek, 2001). In the past decades, there has been a growing appreciation from both observational and theoretical studies for the important role that dust plays in cosmic evolution as well as observations. Its complex interplay with cosmic evolution, and more specifically with galaxy evolution, has to do with dust depletion but also production of important gas coolants. On one hand, dust depletes the interstellar gas of about half of its metals such as Carbon, Oxygen, and Iron. On the other hand, grain surfaces act as catalysts for the formation of molecules such as H_2, also important gas coolants. Observationally, the spectral energy distribution (SED) of various objects, especially galaxies, could not be understood without accounting for dust. Dust is efficient at absorbing and scattering UV and optical light, therefore obscuring the appearance of astrophysical objects in the visible bands. Toward longer wavelengths into the infrared (IR), its attenuation efficiency decreases gradually (See Figure 1.1). Instead, dust re-emits the absorbed energy as thermal radiation from the IR all the way to the sub-mm.

Little explored is however the distribution of dust in the hot diffuse medium of galaxy clusters. Estimates based on IR emission, extinctions or modeling of Intracluster Medium (ICM) gas suggest dust should be capped at an abundance with upper limit 2 to 3 dex lower than within a Milky-Way-like ISM.

The present work aims at investigating the abundance evolution of dust in the gas

of galaxy cluster simulations.

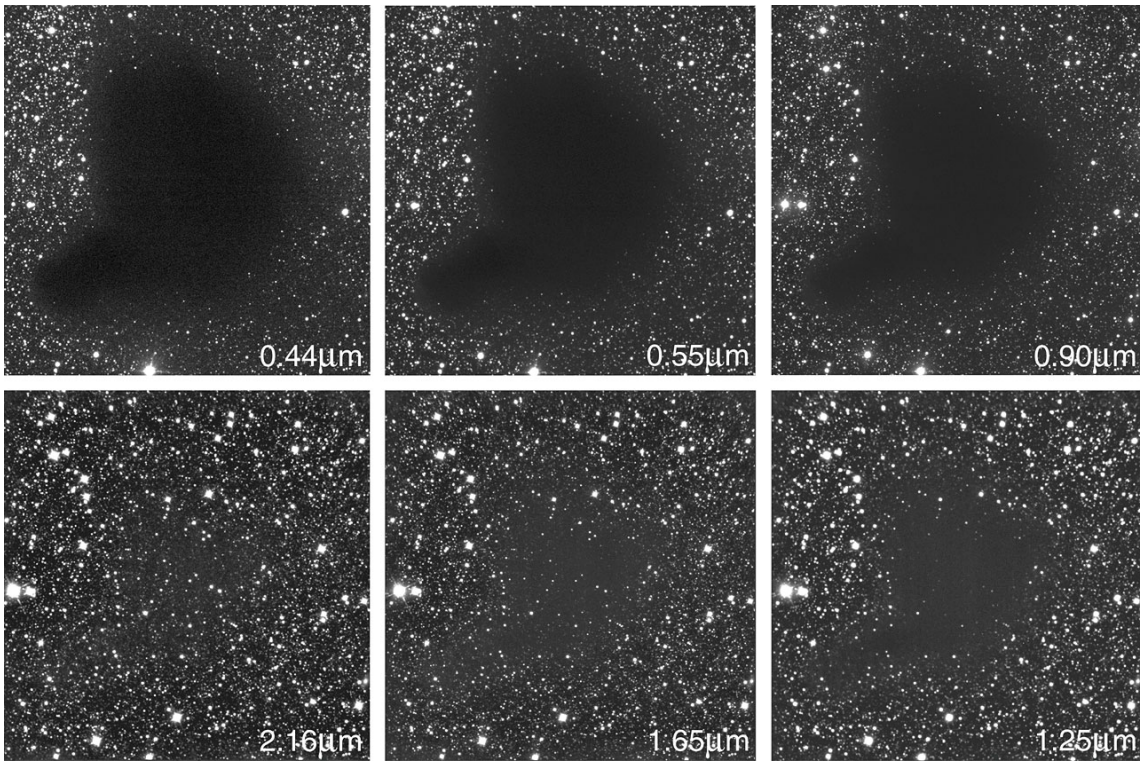

Figure 1.1: The dark cloud B68 photographed at different wavelengths from blue (0.44μm) to NIR (2.16μm) the top 3 from right to left are observed in the BVI filters from the FORS1 instrument at Very Large Telescope UT1, the bottom 3, from left to right are observed in the JHK filters from the SofI instrument at the New Technology Telescope. The dust-rich cloud is located at a distance of 160 pc toward the Ophiucus constellation. As the wavelength increases, the dust obscuration diminishes until it nearly disappears in the NIR. [©European Southern Observatory (1999)]

1.1.1 ISM Properties

The ISM is the inhomogeneous medium onto which stars are embedded and from which they originate. Stars in turn feed energy and metal-enriched mass back to the ISM, affecting its physical and chemical makeup and contributing to the ISM complex evolution. A wide range of densities and temperatures characterize the ISM. Eventually, the ISM will reach thermal pressure equilibrium in multiple phases as listed in Table 1.1. A distinction was initially identified between two of these phases: the Cold Neutral Medium (CNM) averaging at a temperature of 100 K, and the Warm Neutral Medium (WNM), much warmer at $T \sim 10^4$K. Field (1969) predicted that gas at the intermediate temperatures 10^2 – 10^4K is not thermally

stable and, depending on its density and the magnetic fields present, will either condense in the CNM or it will diffuse in the WNM. In the density/temperature range of the WNM it is possible to find not only neutral but also ionized gas, the Warm Ionized Medium (WIM), visible in the Galactic synchrotron background, around radio signals from pulsars, and in the faint optical emissions of singly ionized Oxygen and Nitrongen (OII and NII Mierkiewicz et al., 2006; Reynolds et al., 1973). McKee and Ostriker (1977) noted that supernova explosions (SNe) would produce bubbles of hot ($T \sim 10^6$K) ionized gas much hotter than WNM/WIM. However, cooling times at 10^6K are considerably longer than for lower, non fully ionized regimes. Therefore, the temperature distribution in the range $10^4 < T < 10^6$K should not be evenly distributed, rather it should be skewed to 10^6K. This class of ISM is called Hot Ionized Medium (HIM).

Component	Temp. (K)	n (cm^{-3})
Molecular clouds (MC)	10-20	10^2 – 10^6
Cold Neutral Mdm (CNM)	50-100	20 – 50
Warm Neutral Mdm (WNM)	6000-10000	0.2 – 0.5
Warm Ionized Mdm (WIM)	$\sim$ 8000	0.2 – 0.5
Hot Ionized Mdm (HIM)	$\sim 10^6$	$\sim 6.5 \sim 10^{-3}$

Table 1.1: Temperature (K) and number density (cm^{-3}) for different components of the ISM. [From Ferrière (2001)].

An example of the cooling rate efficiency, calculated assuming solar metallicity, is reported in Figure 1.2 from Gnat and Ferland (2012) as a function of temperature from the WNM all the way to the HIM. The first peak in cooling efficiency around $2 \sim 10^4$K occurs due to hydrogen Lyα cooling. With increasing temperatures the hydrogen neutral fraction decreases and with it its cooling efficiency. Thermal bremsstrahlung by ions dominates cooling at higher temperatures. The thick grey curve represents the total contribution from all the elements broken down with the thinner lines at the bottom. The fine dashed line represents a computation with slightly different prescriptions.

There is one last important phase of the ISM, the molecular cloud (MC), which constitutes about 50% of the mass and 1–2% of the volume of the gas in the MW (e.g. Blitz et al., 2007). MCs are hence a cold and dense phase of the ISM, rich in molecules such as H_2 and CO, mixed in varying relative ratios (e.g. Pineda et al.,

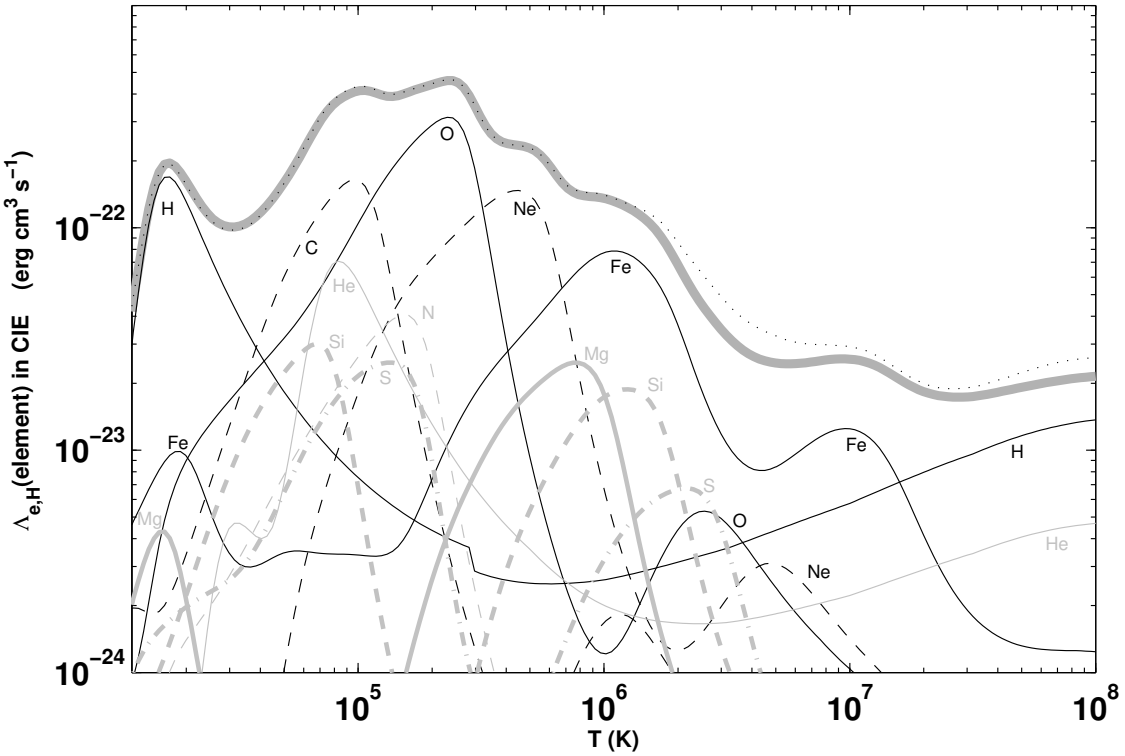

Figure 1.2: An example of calculations for element-by-element cooling efficiencies over temperature assuming solar elemental abundance. The cooling efficiencies are computed with CLOUDY (Ferland et al., 2017). [From Gnat and Ferland (2012)].

2013). MCs are the only regions suited to undergo the gravitational collapse necessary for star formation. Observationally, the rate at which the stars will form is governed by the Schmidt-Kennicut relation (Schmidt, 1959) which states that the star formation rate (SFR) is proportional to the total surface density of molecular and atomic gas, or $\Sigma_{SFR} \propto \Sigma_{gas}^{n}$. A value of $n = 1.4 \pm 0.15$ best fits spiral and starburst galaxies, this is the n value commonly taken as representative for the relation (Kennicutt, 1998), but the fit parameters may vary depending on the SFR tracer (possible tracers are H_α, H_I and CO, Kennicutt et al., 2007).

In reality, the distinction between all these pressure equilibrium phases of the ISM is an idealized picture. Many observed ISM regions exhibit in fact intermediate temperatures (e.g. Heiles and Troland, 2003), or a mix of ionization states. The observed ISM is often unstable and undergoing turbulent dynamics owing to feedback mechanisms or inflow of gas (For an overview, see Klessen and Glover, 2016).

ISM physical and chemical states are the factors which ultimately dictate ISM properties and behaviour. However, it is useful to classify the medium also depending on its location relative to other astrophysical structures. The ISM of a galaxy will

be surrounded by a hot ($T \sim 10^6$K) diffuse ionized corona. While it is difficult to identify or even define precise galaxy borders (Fukugita and Peebles, 2006), the gas outside galaxies but within the galaxy's Virial radius is called the Circumgalactic Medium (CGM) (e.g., Tumlinson et al., 2017). The gas in between galaxies is called IGM and in between clusters is the ICM, acronyms which stand respectively for Intergalactic and Intracluster Medium. Each of these media plays a different role as a probe for structure evolution. The CGM is an active component of galaxy formation as it regulates gas inflow, galactic feedback and recycling. The IGM allows to study the gas metallicity across cosmic times in the Lyman-alpha forest (Lyα) absorption lines, and it is especially important at high ($3 < z < 20$) redshift to study structure formation in the smallest comoving scales (Viel et al., 2005). Finally the ICM, the tenuous hot reservoir of at least 80% of the baryonic mass of the cluster (e.g., Finoguenov et al., 2003), emits in the X-ray, feature that has been used to detect clusters out to $z > 1$ (Rosati et al., 2002). It is possible through X-ray observations of the ICM by *Suzaku* and *XMM-Newton* to the study of temperature and metallicity gradients of nearby clusters (e.g. the Fornax cluster, Murakami et al., 2011).

1.1.1.1 Gas Metallicity

Only 2% of the cosmic gas today is composed of elements heavier than Carbon (included). Hydrogen contributes to the large bulk of the gas mass today at 70%, followed by Helium at 28% (For a review, consult Matteucci, 2001). We call metallicity the mass of all the elements heavier than H and He divided by the total gas. Elements from Carbon to Uranium are produced by stellar nucleosynthesis, elements with atomic number between 5 and 8 are produced via the process of cosmic ray spallation. The abundance of elements is highest in galactic centers, and decreases with radius.

In Table 1.2 we report from Bocchio and Jones (2013) the element abundances of Carbon, Nitrogen, Oxygen, Magnesium, Silicon, and Iron as observed in the line of sight toward ζ Ophiuchi. With the exception of Nitrogen, these are the most common components of dust. ζ Ophiuchi is a bright O9.5V star that has been heavily studied over the decades. It is surrounded by a thick medium, and some refractory elements are heavily depleted up to 2 dex. ζ Oph is commonly studied in absorption-line spectroscopy studies. As observational evidence suggests that, on average, the ISM abundances are similar to the solar abundances (Asplund et al.,

Table 1.2: Elemental abundances towards ζ Oph. From Bocchio and Jones (2013)

X	$(N_X/N_H)^{a}_{\odot}$ (ppm)	$(N_{X,\mathrm{gas}}/N_H)^{b}_{\odot}$ (ppm)	$(N_{X,\mathrm{dust}}/N_H)_{\odot}$ (ppm)	$10^3(M_{X,\mathrm{gas}}/M_H)_{\odot}$
C	295 ± 36	$135 \pm 33^{d,e}$	160 ± 49	1.92 ± 0.59^{e}
		$85 \pm 20^{d,f}$	210 ± 41	2.52 ± 0.49^{f}
N	74.1 ± 9.0	78 ± 13^{g}	-14 ± 16	0
O	537 ± 62	295 ± 36^{d}	242 ± 72	3.87 ± 1.15
		383^{c}	154 ± 8	2.46 ± 0.13
Mg	43.7 ± 4.2	4.5 ± 0.5^{g}	39 ± 4	0.94 ± 0.10
Si	35.5 ± 3.0	1.7 ± 0.5^{h}	34 ± 3	0.95 ± 0.08
Fe	34.7 ± 3.3	0.13 ± 0.01^{g}	35 ± 3	1.96 ± 0.17

[a] Asplund et al. (2009)
[b] Assuming $N(H) + 2N(H_2) = 10^{21.13\pm0.03}\mathrm{cm}^{-2}$
[c] Assuming $N_{O,\mathrm{dust}}/N_H = 154$ ppm (parts per million)
[d] Cardelli et al. (1993),
[e] If $f(C_{\mathrm{II}}]2325\text{Å}) = 4.78 \times 10^{-8}$ (Morton, 2003).
[f] If $f(C_{\mathrm{II}}]2325\text{Å}) = 1 \times 10^{-7}$ (Sofia et al., 2011)
[g] Savage et al. (1992).
[h] Cardelli et al. (1994)

2009), by subtracting from the observed element abundance on the solar surface the observed ISM abundance in the line of sight, we may obtain an estimate on how many metals are locked into dust. Depletion is commonly expressed for an element X with (for an overview, e.g., Jenkins, 2009):

$$[X_{gas}/H] = \log\left(\frac{N(X)}{N(H)}\right) - \log\left(\frac{X}{H}\right)_{\odot} \tag{1.1}$$

Where $(X/H)_{\odot}$ is the solar abundance, and $N(X)$ is the number density of the element (or hydrogen for $N(H)$).
For the Carbon abundance, two different values of oscillator strength[1] f are tested. The latest come from COPERNICUS measurements (Sofia et al., 2011) and predict less carbon than previous studies.

[1] the dimensionless probability for an atom or molecule to absorb or emit radiation in transitions between energy levels.

1.1.2 Dust Observables and Properties

Dust models are inextricable from observational constraints. It is possible to model various properties such as the chemical composition of dust, its total mass, the size distribution of dust grains, and the evolution of all these quantities with time. The bulk of our knowledge on dust comes from the analysis of electromagnetic radiation. There are other techniques which provide valuable clues on dust modeling, such as laboratory experiments which reproduce astrophysical ambient conditions, as well as meteorite or solar grain direct capture. In this section we give an overview of the essential dust features as interpreted by the leading dust models.

1.1.2.1 Extinction curves and UV/optical Absorptions

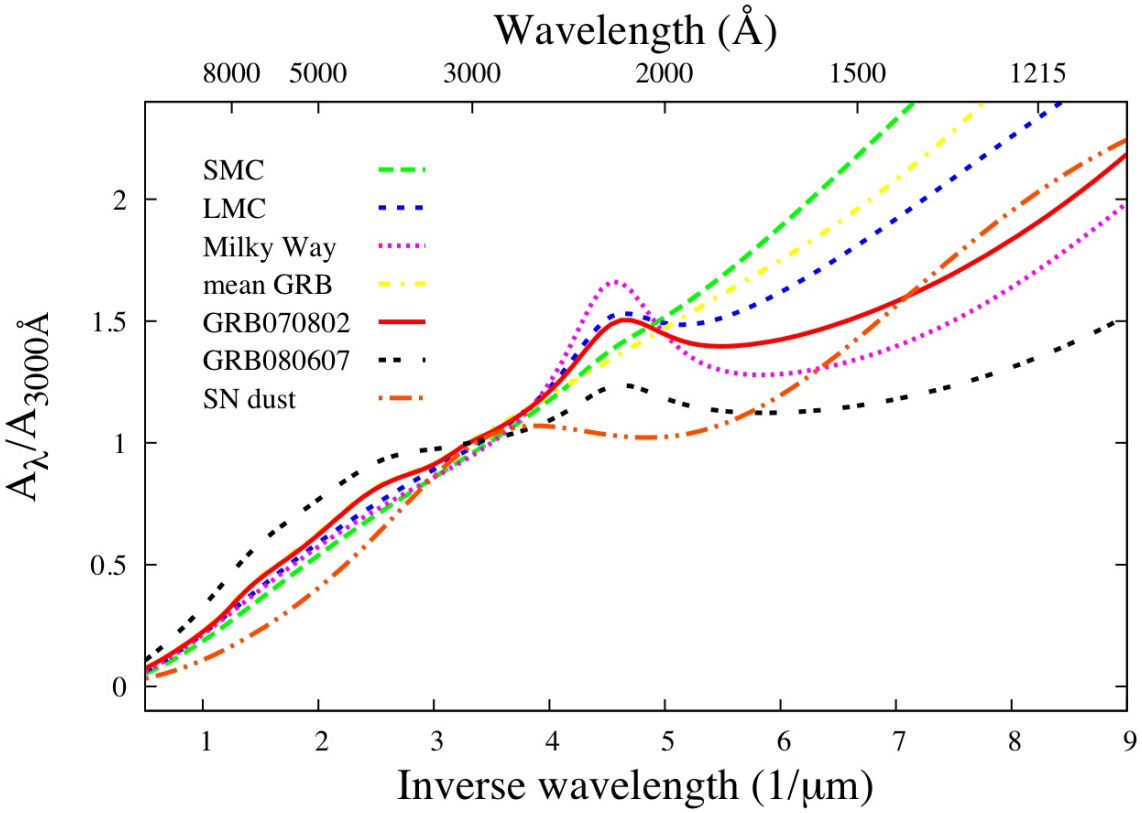

Figure 1.3: Average extinction curves from numerous lines of sight to the Small Magellanic Cloud (SMC; large-dash, green), the Large Magellanic Clouds (LMC; small-dash, blue), to the Milky Way (dots, pink), and to a sample of GRBs (dot-dash, yellow Schady et al., 2011). The figure also shows the extinction curves best-fit to the SED of GRB070802 (solid red Elíasdóttir et al., 2009), GRB080607 (blank-dash black Perley et al., 2011) and the theoretical extinction law from SN produced dust (dot-dot-dash orange Todini and Ferrara, 2001). [©Patricia Schady]

Extinction curves such as the one in Figure 1.3 along with SEDs offer among the most powerful observational constraints on dust. Also extinction curves depend strongly on dust composition and grain size distribution. The extinction as a function of wavelength λ is defined as :

$$A_\lambda = 2.5 \log_{10} \left(\frac{F_\lambda^0}{F_\lambda} \right) \tag{1.2}$$

where F_λ is the observed flux and F_λ^0 is the flux of the same object if it were not dust-obscured (Draine, 2003). The value of F_λ^0 is generally obtained via the identification and observation of a similar object with little to no dust contamination. Extinction is more efficient on bluer wavelengths, with the net total effect of making the optical appearance of the dust-obscured object redder. The phenomenon is in fact named reddening.

From Figure 1.3 we are able to appreciate dust extinction on a variety of objects. In particular, our barred-spiral Milky Way (MW) has a prominent bump around 2175 Å which is absent in the small irregular Small Magellanic Cloud. The source of the bump is not yet completely clear, but models (Weingartner and Draine, 2001) point to either small graphene grains (this has been the leading hypothesis for decades, and it still is favored) or large agglomerates of Polycyclic Aromatic Hydrocarbons (PAHs), a family of carbonaceous grains arranged in ring-like structures (explained more in detail in Section 4.1.1.3). Either way, the signal has been attributed since its discovery to the π^* excitations of sp^2-bonded carbon sheets (Draine, 2011). The smooth extinction trend that goes as λ^{-1} of the SMC can be obtained with models excluding PAHs. The theoretical extinction law of supernovae (SNe) differs considerably from the MW profile, which is a clear example of how much dust properties vary over time and depending on the environment that hosts dust. Extinction curves of GRBs offer the possibility to investigate far away young galaxies, widening the otherwise small sample available in our Local Group.

1.1.2.2 IR Emission spectrum

The energy dust absorbs at UV/optical wavelengths is re-radiated thermally at longer IR wavelengths. In the IR, dust opacity falls steeply. Observing an astronomical object simultaneously in the UV/optical and in IR wavebands may help constrain more tightly the "dustiness" of its medium than with extinction in UV/optical alone (See Section 3.1). A dusty object which is otherwise dim in the optical, will lighten up due to dust reprocessing in the IR.

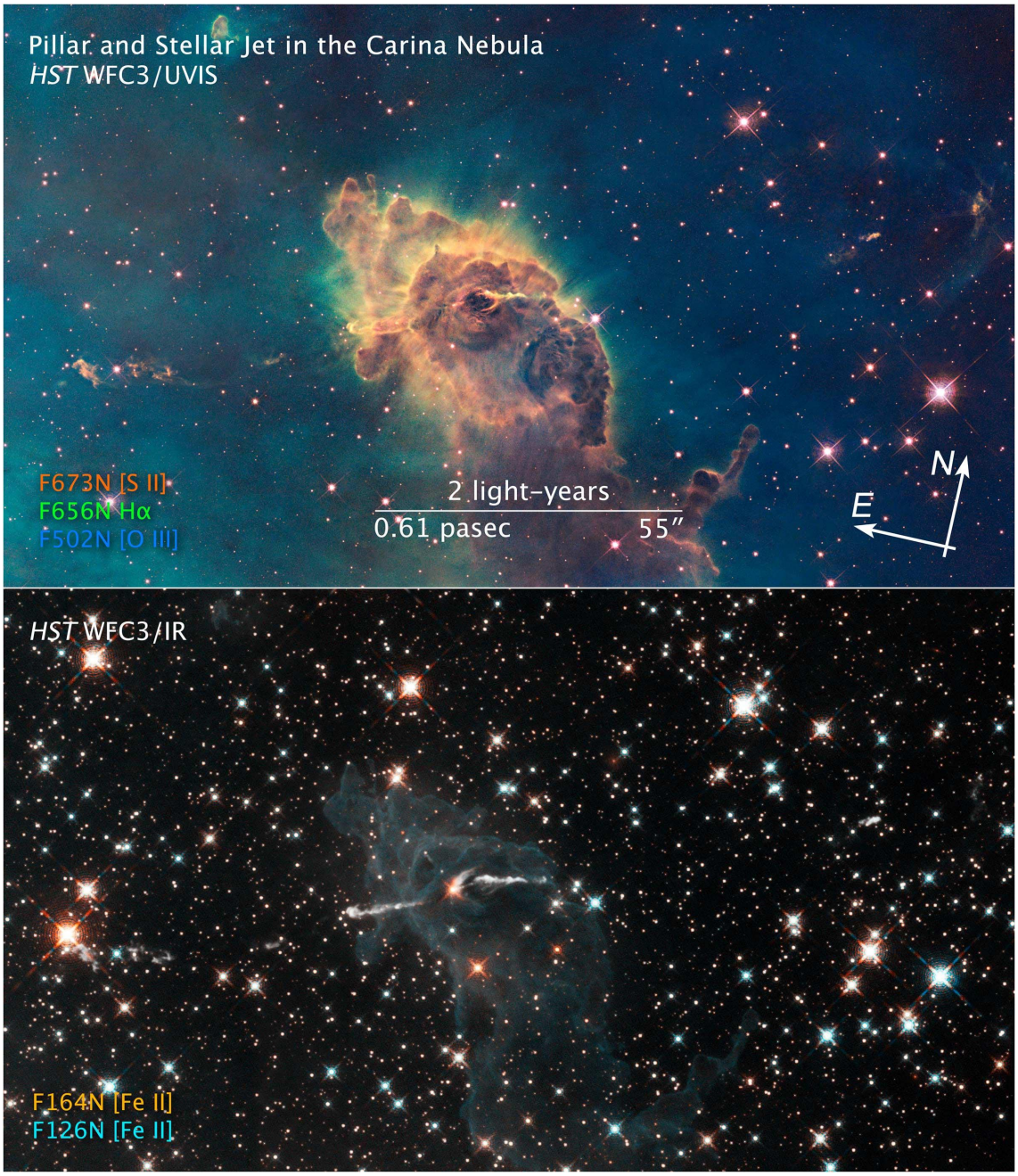

Figure 1.4: Hubble's Wide Field Camera 3 observed the Carina Nebula July 24 through July 30, 2009 in UV/optical (top) and IR (bottom) wavebands. The composite image was made from filters that isolate emission from iron, magnesium, oxygen, hydrogen, and sulfur. [©NASA, ESA, and the Hubble SM4 ERO Team]

Figure 1.4 is the HST observation with the Wide Field Camera (WFC3) of a pillar in the Carina Nebula, located 7500 light years away in the Southern Hemisphere, taken with UV/optical (top) and IR (bottom) filters. The nebula is a star formation (SF)

site. The gas, rich in dust, obscures the radiation from the nearly formed stars as well as the background. Colors represent different WFC3 filters fine-tuned to detect the emission of various ionized gas-phase elements as indicated by the legend.

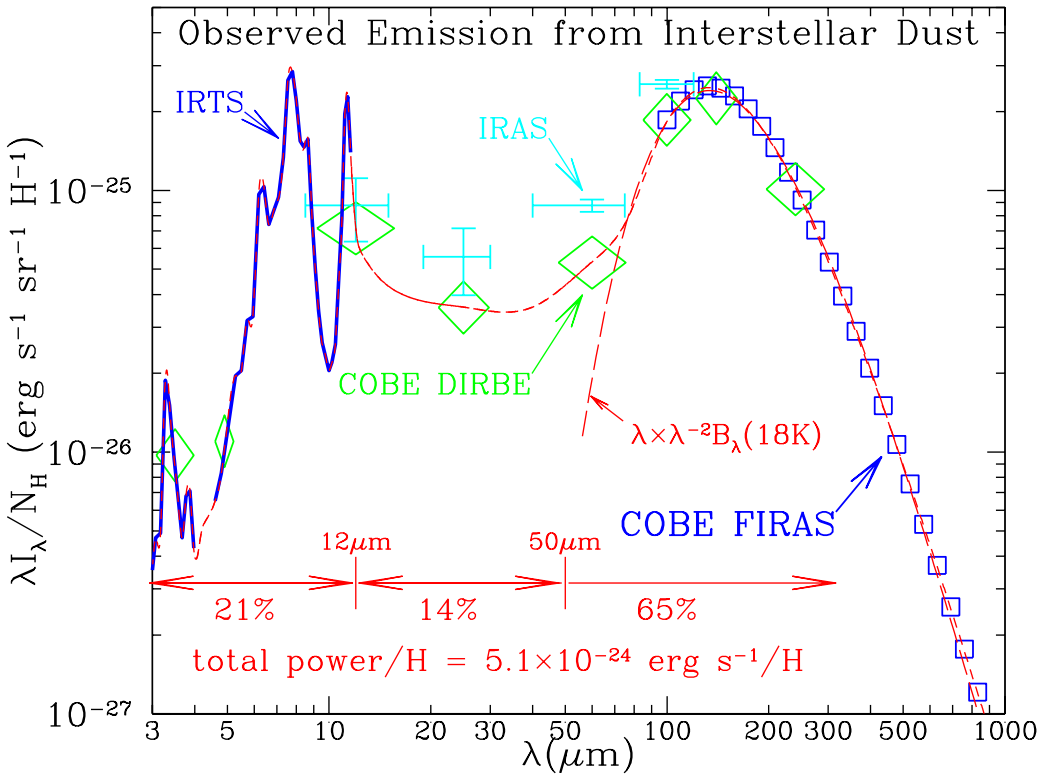

Figure 1.5: Observed emission spectrum of diffuse interstellar dust in the Milky Way. Crosses: IRAS (Boulanger and Perault, 1988); squares: COBE-FIRAS Finkbeiner et al. (1999); diamonds: COBE-DIRBE (Arendt et al., 1998); heavy curve for 3 – 4.5 μm and 5 – 11.5μm: IRTS (Onaka et al., 1996; Tanaka et al., 1996). The total power $\sim 5.1 \times 10^{-24}$ ergs s^{-1}/H is estimated from the interpolated broken line. [From Draine (2004)]

It is possible to isolate the composite dust emission in the IR as shown in Figure 1.5 (Draine, 2004). The two spectroscopic portions are taken at mid-infrared (MIR) wavelengths with the spectroscope IRTS (Onaka et al., 1996; Tanaka et al., 1996) and they are based on observations of the galactic plane. The far-infrared (FIR) measurements are taken at higher galactic latitudes with the all-sky IRAS (Boulanger and Perault, 1988) and COBE (Arendt et al., 1998; Finkbeiner et al., 1999) surveys.

The MIR spectroscopic signatures are common in other environments of the Milky Way (MW) such as planetary nebulae, reflection nebulae (e.g. Cesarsky et al., 1996),

molecular clouds, all of which are sites rich in freshly-produced new dust. Each of these peaks is consistent and now generally attributed to bending and stretching modes of PAH molecules in both neutral and ionized states. The PAH origin of the MIR spectral profile is confirmed with the high sensitivity *Spitzer Space Telescope* observations of the MW (Draine and Li, 2007), but had also been detected with the *Infrared Space Observatory* (ISO) around evolved C-rich stars (Beintema et al., 1996).

The MIR spectrum consists of only 21% of the total radiated power. 15% is the power radiated between 12 and 50 μm. Radiation in this range is associated with particles of grain size $a < 100$Å. The remaining 65% is radiated in the FIR, which is instead associated with larger grains $a \gtrsim 100$Å. Grain sizes fall within a wide range of 50Å to $\sim 2\mu$m.

We have already mentioned *Spitzer* and *ISO* telescopes. Other breakthroughs were possible thanks to the *Herschel Space Observatory*, operative between 2009 and 2013 (Pilbratt et al., 2010). It observed FIR ($50\mu\text{m} \gtrsim \lambda \gtrsim 200\mu\text{m}$) and sub-millimeter wavelengths ($200\mu\text{m} \gtrsim \lambda \gtrsim 1000\mu\text{m}$). The *Atacama Large Millimeter/sub-millimeter Array* (ALMA) is a ground-based telescope with 66 antennas fully operational since 2013 which managed to detect dust in high redshift galaxies up to $z \sim 6$ (Spilker et al., 2016; Scoville et al., 2016). They also unveiled the complex molecular chemistry of the ISM in the MW (e.g. Lindberg et al., 2014; Zanardo et al., 2014) as well as in nearby galaxies (e.g. Costagliola et al., 2015; Garrod et al., 2017). The *Stratospheric Observatory for Infrared Astronomy* (SOFIA Young et al., 2012) is a NASA airplane that provides higher angular resolutions with dust emission imaging between 5 – 240μm.

1.1.2.2.1 Galaxy SED and absorption/emission fitting Models of the SED continuum from UV to sub-mm offer useful constraints on various dust properties, especially dust mass, grain size, and also chemical composition. Particularly interesting is the SED of galaxies. The SED profiles will in fact change dramatically depending on the morphology. Starburst galaxies, rich in young, dusty stars, have most of their emitted starlight reprocessed in the IR. On the other hand, homogeneous elliptical galaxies display UV/optical SED profiles comparatively close to their equivalent dust-unobscured starlights. Ellipticals are in fact characterized by old stellar populations, therefore most of their dust should have eroded away by destruction processes over long galactic histories. Models such as Silva et al. (1998) have managed to fit the SED continuum of various galactic morphologies with high

accuracy (Refer to Section 3.1 for an in-depth discussion).

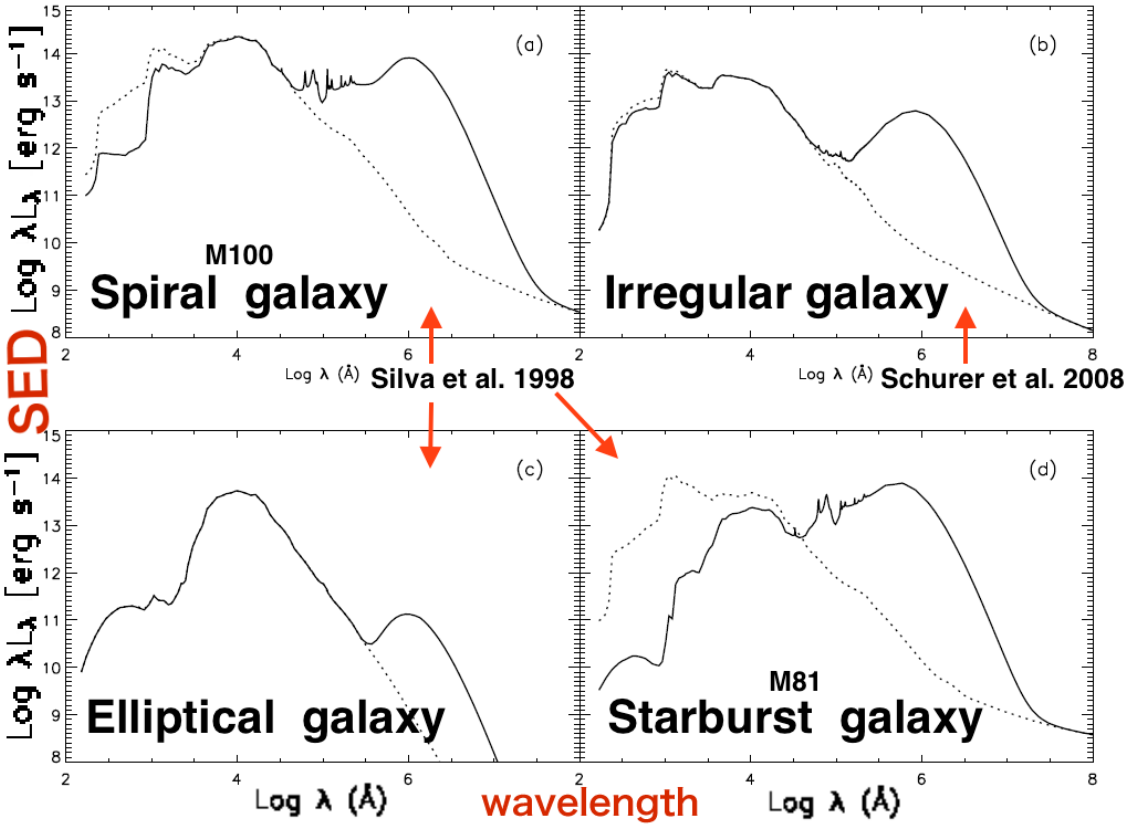

Figure 1.6: Intrinsic SED (dashed lines) and dust reprocessed SED (solid lines) over wavelength for four different galaxy morphologies. The spiral galaxy (M100), the starburst galaxy (M81), and the elliptical galaxy were computed in Silva et al. (1998). The standard elliptical galaxy was extrapolated from the Arimoto (1996) template combined with observations of ellipticals from the UV-to-FIR (Mazzei et al., 1994; Impey et al., 1986). The standard irregular galaxy curves are computed in Schurer et al. (2008), and are based on obervations of Spitzer Infrared Nearby Galaxies Survey (SINGS Dale et al., 2007) of magellanic-type irregular galaxies.

With the large plethora of newly available data on dust, the DUSTPEDIA group (Davies et al., 2017) undertook the task of employing *Herschel*, *Planck*, as well as data from the *Wide-field Infrared Survey Explorer* (WISE Wright et al., 2010) and the *Galaxy Evolution Explorer* (GALEX Bianchi, 2014) to evaluate the SED of over a thousand galaxies.

1.1.2.3 Dust in the X-ray

Dust absorbs and scatters X-rays, making a point source appear to be surrounded by a diffuse halo (Overbeck, 1965). Dust-scatted X-ray halos were observed for the first

time by Rolf (1983) using the data of GX 339 + 4 with the IPC on Einstein. The satellite ROSAT provided better resolutions, allowing Predehl and Schmitt (1995) to examine 25 point sources and four supernova remnants. They found that the majority of dust causing the halo formation should not reside in highly clumped clouds, and that dust and gas must be largely cospatial. In the past two decades, the two observatories Chandra and XMM-Newton, satellites developed respectively by NASA and ESA, provided sufficient resolution to extract detailed information on the chemistry of dust, ISM depletion (e.g. Costantini et al., 2005; Ueda et al., 2005) as well as dust distributions (e.g. Yao et al., 2003) around X-ray sources. Future missions like Athena will improve the hard ray ($E > 1$ keV) sensitivity, and it will be possible to penetrate the dense environment of the Galactic center. Laboratory measurements of synchrotron emissions have also been employed to constrain dust abundances in astrophysical objects. For example, Zeegers et al. (2017) used the Si innermost shell emission lines to obtain the silicate abundance around the low mass X-ray binary GX 5-1.

1.1.2.4 Dust Composition

While our understanding of dust composition is far from complete and is due for refinement (Jones, 2013), it is safe to affirm that the majority of dust is composed of two species: silicates and carbonaceous dust. There are several tools that permit a composition investigation. Spectral features can point to the presence of dust, and the fitting of extinction curves and SEDs require assumptions on compositions, constraining in turn dust properties. There are also direct methods such as the analysis of meteorites (Clayton et al., 1997) or the collection stratospheric smoke with airplanes (Sandford, 1987). However, direct methods are hampered by necessary selection effects due to the harsh environmental phenomena which might have altered the samples either upon Earth contact or during the formation of our solar system. These samples cannot be considered representative of the ISM dust (Draine, 2004). Another indicator to the presence and composition of dust is metal depletion (Jenkins, 2009). Metal depletion cannot provide information on the mineralogy of dust (Jones, 2014), but it can help constrain dust stoichiometry, or the relative abundance of the condensed elements. From nucleosynthesis studies, certain environments like SN remnants or stellar atmospheres are expected to exhibit a given chemical composition. Instead, some elements are underabundant, and their depletion rates are consistent with the element's condensation temperature T_c (Field, 1974; Savage and

Sembach, 1996). The condensation temperature is the temperature below which at least 50% of a certain gas-phase compound condenses into a solid-phase (Lodders, 2003). Elements with a high T_c will condense sooner as a gas cools. Such elements are called "refractory". Silicon, magnesium, and iron are considered refractory elements. Those elements which condense at lower condensation temperatures are called volatile. Examples are Zinc, Sulfur, and Phosphorous. The depletion of Si and Mg, two major silicate constituents, aid into estimating the abundance of silicates (Kemper et al., 2004; Ueda et al., 2005; Costantini et al., 2005; Zhukovska et al., 2018, e.g.). Fe is another silicate constituent, but as its depletion ratio is higher than Si or Mg, depletion suggests Fe is incorporated in dust species other than silicates, such as oxides (e.g. Wickramasinghe and Wickramasinghe, 1993; Voshchinnikov and Henning, 2010; Dwek, 2016).

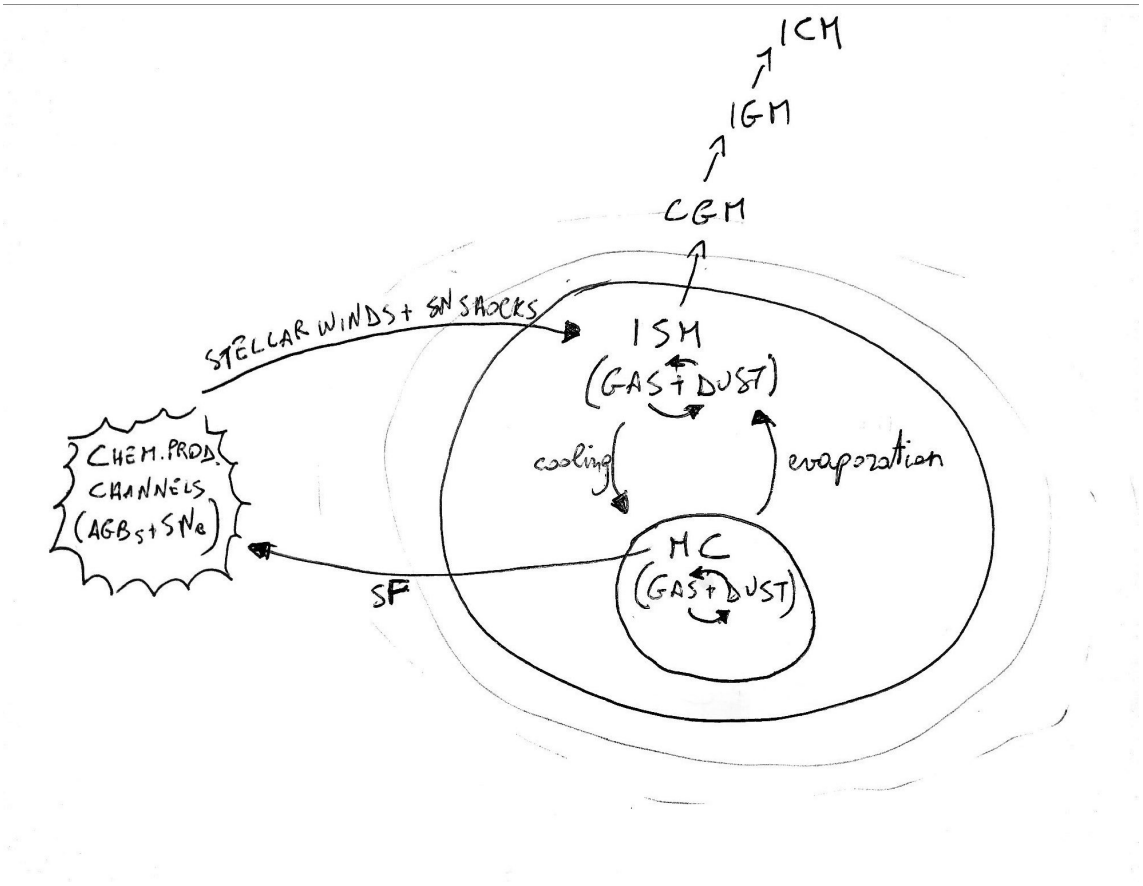

Figure 1.7: ISM cycle diagram.

1.1.2.5 Dust Grain Size Distribution

From extinction curves as we mentioned earlier it is possible to guess the dust grain size distribution. Mathis et al. (1977) famously reproduced the standard extinction curve of the diffuse ISM from 0.1 –1μm. To achieve the result, they assumed a mixture of spherical graphite grains with other substances, predominantly silicates. they derived the power law: $N(a)da \propto a^{-3.5}da$ for grains in the size range of 0.005 to 1μm for graphites, and 0.025 – 2.5μm for the other dust species. Improvements to the model were subsequently found in other works, namely Kim and Martin (1994); Weingartner and Draine (2001); Draine and Li (2007). An in-depth discussion can be found in Section 5.3.2.1.

1.1.3 Dust Cycle

The life of a dust grain evolves as a function of the physical conditions of the medium hosting the grains. Along with matter in the ISM, dust undergoes cycles of production, evolution and destruction as listed in Figure 1.7. From dust production channels, spreading mechanisms disperse dust cospatially within the ISM. Here, depending on the fate of the ISM, dust will either grow in size and mass within molecular clouds, or it will be eroded by photo-dissociation, supernova shocks, and sputtering of highly energetic ions of the hot diffuse WIM/HIM plasma. While in the ISM, interactions with other grains or with gas will alter its size distribution. The process of star formation will naturally destroy any dust trapped in the ISM collapsed to form a star.

Grains are first injected in the ISM via stellar winds of evolved low-mass stars such as AGBs and SN explosions. Evidence that grains originate from stellar outflows comes from the infrared emission in red giants and carbon stars. Oxygen-rich stars also produce dust, and the 10μm feature of their spectra match the expectation that in their atmosphere's condition where $C/O < 1$, dust should mainly consist of silicates (Draine, 2003). Carbon-rich stars with $C/O > 1$ exhibit instead the 11.3μm feature attributed to SiC (Treffers and Cohen, 1974). Dust formed from supernova ejecta is another prime candidate for the production of the bulk of supernova dust. Specific well known supernovae such as SN 2010jl (Gall et al., 2014) and SN 1987A (Alp et al., 2018) will or have produced as much as $0.5M_{\odot}$ in dust mass. However, dust production mechanisms are still unclear (Sarangi et al., 2018) due to the wide range of physical and chemical conditions governing each supernova type. Type Ia SNe however seem to produce a reverse and forward shocks powerful enough to

obliterate any nearby dust (Nozawa et al., 2011).
Once dust is spread to the ISM it has to survive destruction processes, including grain erosion by sputtering, shattering by low-velocity grain-grain collisions, vaporization by high-velocity grain-grain collisions, photolysis by UV starlight, irradiation by cosmic rays and X-rays, and photodesorption of atoms and molecules from grain surfaces (Draine, 2004). Draine and Salpeter (1979) and Jones et al. (1994) found that the destruction lifetime is of the order of 10^8 years. In diffuse hot media such as the ICM, dust has little chance to survive over longer timescales. In the ISM however there is a mismatch between the observed depletion of certain elements and the fraction of those elements which should have survived trapped in dust from production. Draine (2004) makes the following argument: if we assume a certain destruction rate of $\tau \sim 10^8$ yr, even if 100% of all Si atoms were trapped into dust, the rate of Si abundance as determined from the equilibrium state of production and destruction would normalize to a certain value, which Draine computes to be ~ 0.2. Instead, Si observations suggest that as much as 90% of silicon is condensed into dust. The exceeding dust abundance compared to what we expect from production alone hints at the fact that dust growth should be very efficient and significant within the ISM. Most of recent literature is congruent with this result, even at high redshift (e.g., De Cia, 2018). Candidate processes of dust evolution will be further explored in Chapter 4.
Further evidence of ISM processing comes from the observation of lines of sight. The extinction curves vary significantly from one sightline over the other, when one expects instead for dust properties to average out if produced by a large population of fairly well-mixed stars (Chen et al., 2018a).

1.2 Structure Formation

The small anisotropy of the Cosmic Microwave Background (CMB) around a temperature of 2.725 K with fluctuations of order $\langle\rho_\delta\rangle/\langle\rho_U\rangle \sim 10^{-5}$ is evidence of primordial inhomogeneity. These minuscule fluctuations developed into galaxies with overdensities of $\langle\rho_\delta\rangle/\langle\rho_U\rangle \sim 10^6 - 10^7$, voids, and the large scale structure of present-epoch. Models of structure formation embark in the challenging task of describing how those patterns of CMB anisotropy, usually assumed to be Gaussian, evolved into our current Universe. As long as $\langle\rho_\delta\rangle/\langle\rho_U\rangle \ll 1$, or the contrast between the overdensity and the underlying background is smaller than unity, it is possible to describe the evolution of the perturbations linearly with Jean's theory of

gravitational instability. Semi-analytical or numerical models however are needed once the overdensities grow onto the non-linear and eventually into the highly non-linear structures during their collapse of dark matter haloes (for an overview, e.g. Weinberg, 1972; Mo et al., 2010).
For what concerns the assumed Standard ΛCDM (Cosmological constant and cold dark matter) Cosmology, a few studies must be mentioned. Cold Dark Matter gained favors in the community ever since N-body experiments (e.g. Frenk et al., 1985; Efstathiou et al., 1988) supported a CDM scenario with effective slope of the power spectrum $P(k) \propto k^n$ (Press and Schechter, 1974) on galactic mass scales equal to $n_{eff} \sim -1.5$ (e.g. Davis et al., 1985). The scenario that emerges from these studies is a "bottom-up" hierarchy of cosmic structures, i.e. first smaller haloes will form, then they merge into larger structures.

1.2.1 Clusters of Galaxies

Galaxy clusters are the largest gravitationally-bound cosmic structures that have had the time to reach virialization. They reside at the nodes of the cosmic web, and their typical mass inferred from X-ray observations ranges between 10^{13} – $10^{15} M_{\odot}$. They uphold a very important position within cosmic hierarchy. In fact, if clusters are treated with nothing but gravity, they are valid cosmological probes. In fact the bulk properties of dust seem to depend mainly on its initial conditions, the cluster's dark matter as it dominates the mass budget, and the chosen model of gravity. In fact, cosmological models which trace only the dissipationless collapse of dark matter provide surprisingly accurate predictions of cluster properties. One such simple yet accurate model is Kaiser (1986). These studies provided the baseline expectation for how scaling relations in clusters are expected to evolve. In fact, studies of the abundance and spatial distribution of clusters which use DM only and standard cosmology exhibit statistics retaining exceptional memory of its initial conditions. At the same time, at the scales of galaxy clusters, baryonic physics starts to become important. Radiation, heating and dynamical flows occurring in the potential well of galaxy clusters are regulated by the properties of the cluster environment. This places galaxy clusters at a key position in the study of smaller-scale mechanisms such as gas emission or galaxy evolution.
Clusters may contain between 10^2 to 10^3 galaxies, and their size is of the order of up to a couple Mpc. Figure 1.8 shows the massive ($\sim 7 \times 10^{14} M_{\odot}$, (Gavazzi et al., 2009)) Coma Cluster (Abell 1656) in the optical band (left) and X-ray band. The Coma

cluster is located at a distance of 103 Mpc ($z = 0.0231$), and it is visible pointing toward the Coma Berenices constellation, far away from the Galactic plane and therefore largely unobscured by the Galactic gas and dust. The Sunyaev-Zel'dovich effect derived from the Planck image offers a map of the mass distribution of the cluster. The X-ray observation shows that the galaxies of a cluster are immersed in a very bright (10^{43} – 10^{45} erg/s) hot (10^7 – 10^8 K) sparse (10^{-2} – 10^{-4} cm^{-3}) mostly optically-thin plasma (Kellogg et al., 1972) just like the Coma cluster. The gas mirrors the depth of the potential well ($kT \propto GM/R$).

The X-ray emission in clusters is dominated by free-free radiation or thermal Bremsstrahlung (for a review, e.g. Sarazin, 1988). Hydrogen and Helium are here fully ionized. the ICM however presents emission lines from heavy elements, which are also highly ionized. Their metal abundance is about $0.3Z_{\odot}$, but dust abundance is much more uncertain and has an upper limit of 2-3 dex the Galactic abundance at low redshift.

The shape of the X-ray spectrum is dictated by the temperature of the emitting plasma. Given the main feature of the spectrum of the Bremsstrahlung radiation is the exponential cut-off at energies $> kT$. Hard X-rays therefore provide a more reliable determination of the cluster temperature. The thermal structure of the ICM, as it is not isothermal, can help costrain the merging history of the fluster as well as galaxy formation within a certain cluster.

Cluster gas contains the majority (around 90%) of the baryonic matter of the whole Universe. This percentage is high compared to the gas fraction in galaxies ($\sim 13\%$) where most of the baryonic mass is instead locked up in stars (for a review, e.g. Ferrière, 2001; Kravtsov and Borgani, 2012). Interestingly, the ICM gas of clusters correlates with the cluster stellar mass, with a ratio $\log(M_{\star,500}/M_{g,500}) = -0.8 \pm 0.5$, where 500 refers to the mass measured within R_{500}, or the radius at which the overdensity of the structure is at least 500 times larger than the critical mean density of the Universe ($\rho_{cr} = 3H(z)^2/8\pi G$). Larger clusters tend to have a larger gas fraction compared to smaller ones.

Within clusters, galaxies and ICM are nearly in equilibrium within a common gravitational DM-dominated potential well, because ICM temperature is consistent with the galaxy velocities. In terms of element abundance, the ICM plasma is dominated

[21]NASA, ESA, and the Hubble Heritage Team (STScI/AURA); Acknowledgment: D. Carter (Liverpool John Moores University) and the Coma HST ACS Treasury Team.

[2]Planck image: ESA/ LFI & HFI Consortia; ROSAT image: Max-Planck-Institut für extraterrestrische Physik; DSS image: NASA, ESA, and the Digitized Sky Survey 2. Acknowledgment: Davide De Martin (ESA/Hubble)

(a) This Hubble image consists of a section of the cluster that is roughly one-third of the way out from the center of the cluster.

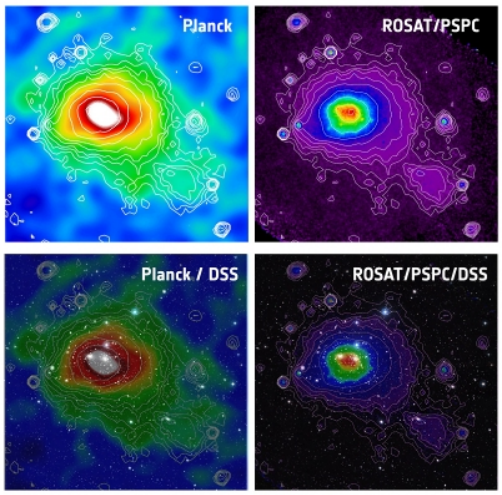

(b) left: Sunyaev-Zel'dovich image of the Coma cluster produced by Planck. Right: the Coma cluster imaged in X-rays by the ROSAT satellite. Colours map the intensity of the measured signals. The X-ray contours are also superimposed on the Planck image as a visual aid. As a comparison, the images are shown superimposed on a wide-field optical image of the Coma cluster from the Digitized Sky Survey in the two lower panels.

Figure 1.8: Images of the Coma Galaxy Cluster, (Abell 1656), taken by the HST (*left*) and by Planck and ROSAT (*right*). [Credits[2,2]]

for the most part by electrons and protons, with a smaller number of Helium nuclei. Heavier elements are only partially ionized and their abundance, decreasing with radius, is a third of the solar metallicity (see Werner et al. 2008 for a review).

Worth mentioning is the impact of active galacic nuclei (AGN) feedback (See Section 2.4.4 for an explanation) in the evolution of galaxy clusters. AGNs are known to reduce star formation in massive clusters. In small clusters or groups, AGNs has the effect of stripping away the hot ICM gas from the structures (e.g. Puchwein et al., 2008; Sijacki et al., 2007). Several theoretical studies indicate that AGN feedback is the driving energy source which regulates the evolution of stellar masses of cluster galaxies. AGNs are also responsible, along with other processes such as magnetic fields, turbulence, injection of cosmic rays, and thermal instabilites, of suppressing the cooling in cluster cores at low redshifts. The precise interplay of these processes

is poorly understood, but it seems that AGN activity, originated from cooling, is a key regulating mechanism that helps slow down cooling rates in a cluster, at least for a few hundred Myr (for a review, e.g. Kravtsov and Borgani, 2012). The metallicity profile of cluster simulations is also improved by AGN-induced large-scale winds at high z (Fabjan et al., 2010; McCarthy et al., 2010).
Figure 1.9 from Martizzi et al. (2012) plots the stellar mass over the halo mass for theoretical models (the solid line) and cosmological simulations (the symbols). The solid back line represents the prediction from the Moster et al. (2010) model capable of reproducing the stellar mass function, with the shaded regions being the scatter around the average relation. From this model it is possible to see how, with increasing halo mass, the star formation is inhibited. The data come from Naab et al. (2009) (open triangle) and Feldmann et al. (2010) (open square). These predictions come from SPH simulations which exclude any AGN feedback model. They overpredict the stellar-to-halo mass relation significantly. The solid triangle and pentagon are simulation results from Martizzi et al. (2012), the pentagon excludes AGN feedback and the triangle includes it. Including a model of AGN feedback hampers star formation to the observed values.

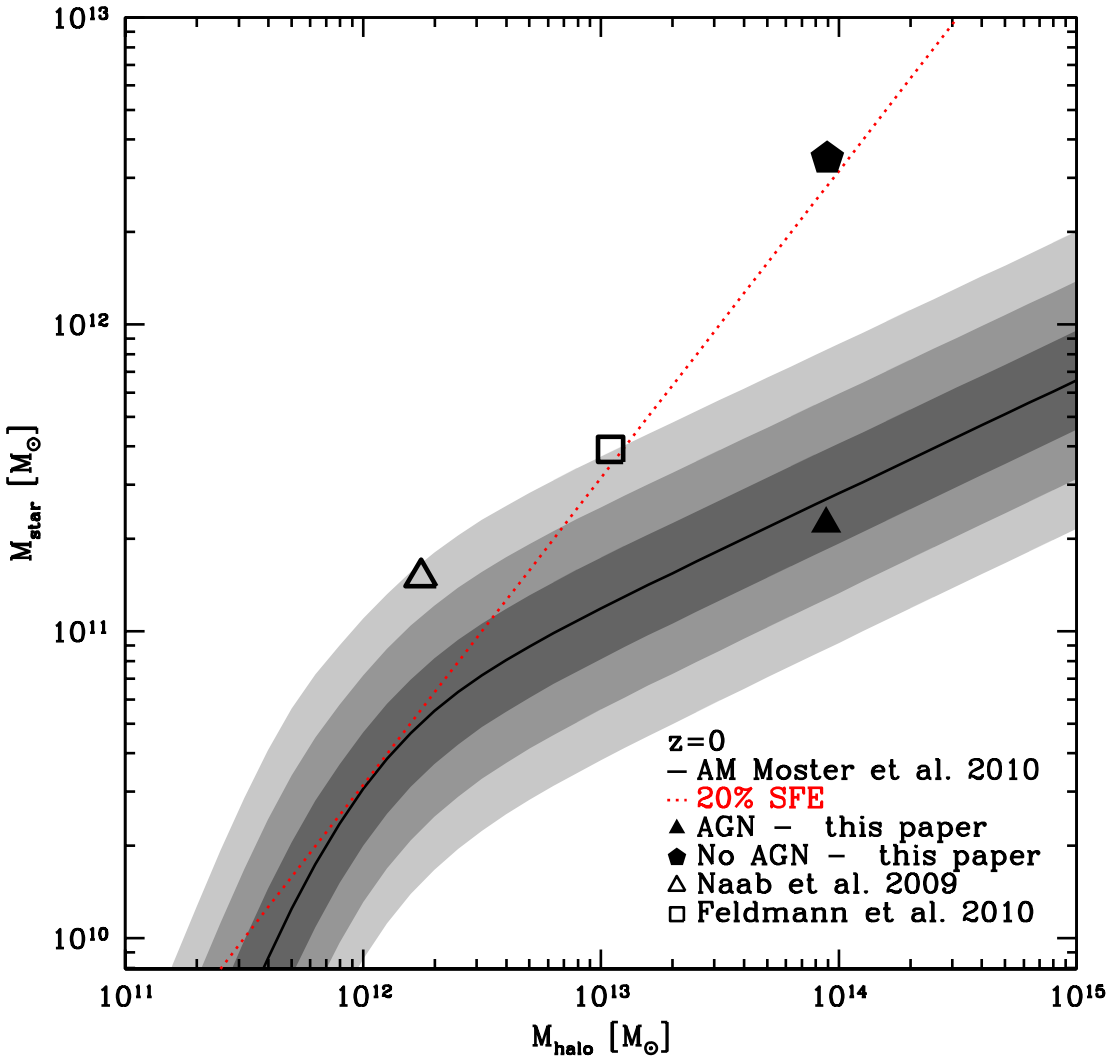

Figure 1.9: Comparison of the relation between stellar mass and total halo mass as predicted by cosmological hydrodynamical simulations of four early-type galaxies (symbols) (from Martizzi et al., 2012). The open triangle and square refer to the simulations presented by Naab et al. (2009) and by Feldmann et al. (2010), both based on the smoothed particle hydrodynamics codes and not including AGN feedback. The filled symbols refer to the simulations by Martizzi et al. (2012) with the brightest cluster galaxies forming at the center of a relatively poor cluster carried out with an AMR code, both including (triangle) and excluding (pentagon) AGN feedback. The red dotted line represents the relation expected for 20% efficiency in the conversion of baryons into stars. The solid black line is the prediction from Moster et al. (2010) of a model in which dark matter halos are populated with stars in such a way as to reproduce the observed stellar mass function. The grey shaded areas represent the 1-, 2- and 3-σ scatter around the average relation. [From Martizzi et al. (2012)]

2

Cosmological Simulations of Galaxy Clusters

Structure formation and evolution of cosmic structures is a complex matter, due to the variety of physical processes and scales involved. The driving phenomena may be simplified to gravitational dynamics, hydrodynamics, and radiative processes. It is not possible to simulate the universe from first principles, not only because of limitations in memory and computing power, but because some of the most essential formulations, such as a full analytical treatment of non-linear gravity, have not been found as of yet. Numerical methods and approximations have instead proven useful in order to predict any observable (e.g., the cluster mass function, luminosity function, gas fraction, star formation history, density profiles, etc.). The leading approaches to cosmic evolution studies are N-body simulations, carried on parallel supercomputers, and semi-analytic modeling (SAMs). SAMs do not solve explicitly the dynamics of individual particles moving on a mesh, rather they implement flow equations on bulk components (e.g. Somerville and Davé, 2015). It should be noted that SAMs have been mainly developed in the context of galaxy formation. They have the advantage of requiring much less computing time compared to N-body simulations. Cosmological simulations proved to be very powerful tools in the past decades. They have been successfully implemented both at smaller galactic scales (a few kpc) and at full cluster scales (1 Gpc and above). There have also been successful attempts at creating hybrid N-body/SAM models of hierarchical galaxy formation (e.g. Hatton et al., 2003). N-body simulations are at the base of many cosmological simulation codes, as very briefly summarised in Section 2.3.2.1. We refer the reader to Benson (2010) for an overview on SAMs, and we proceed to outline what are N-body simulations.

Implementing numerical methods on large N-body simulations is not an easy task. Newtonian gravity alone (See Section 2.1.1) requires approximations for very sim-

ple equations. If simulations were to use full GR, the complexity of the runs would rapidly increase. Fortunately, it has been found (for a review, see Bernardeau et al., 2002) that for scales smaller than the Hubble scale c/H_0, the GR contribution is negligible compared to the Newtonian counterpart, so it is safe to use Newtonian dynamics for scales $\lesssim 1$ Gpc. Cosmological simulations therefore run Newtonian dynamics onto the comoving coordinates, and then attach the scale factor as derived from the cosmology of choice, i.e. FLRW Stanrdard ΛCDM Cosmology. As explained in the Introduction, the bulk properties of the large scale structure is dominated by gravity and its most abundant component which is collisionless, non-relativistic cold dark matter, commonly treated as a fluid. If interested in the evolution of collisional baryonic matter however, gravity is not sufficient. Hydrodynamics must be computed. The most adopted numerical approach to hydrodynamical simulations was called Smoothed Particle Hydrodynamics (Gingold and Monaghan, 1977; Lucy, 1977), and it relies on a numerical solution to the equations of fluid dynamics by replacing the continuous fluid by a finite number of particles (Monaghan, 2005; Rosswog, 2009). A common approach we also adopt is that to compute some initial conditions for the gas at the center of a larger dark matter gravitational potential well. Simulations can be further refined implementing analytical models e.g. of radiative cooling, star formation, chemical evolution, and AGN feedback. These phenomena occur at scales smaller than the resolution achievable by simulations, so they are commonly referred to as "subgrid" models, as they are not resolved.

2.1 N-body simulations (Gravity)

Large scale structure formation will be dictated mainly by gravity. For simplicity, let us consider only gravity on CDM particles. We will describe the particles as having mass m, position $\boldsymbol{x}$ and momentum $\boldsymbol{p}$. Many simulations involving the largest of structures will contain only dark matter "particles". The term "particle" in the simulation is a bit misleading. For dark matter and gas, particles represent a discretization of their fluid. As we will later see with star particles, we do not refer to the individual physical stars, because cosmological simulations are still far from resolving those scales. In general, simulated particles are Monte Carlo realizations of the mass distribution (Dolag et al., 2008). Gravity on these matter particles will be computed on the background of an expanding universe. Any simulation that does not test modified gravity will assume the Standard Model of Cosmology, and therefore will employ the Friedmann-Lemaitre-Robertson-Walker (FLRW) metric as

the geometry of the universe, with $a = 1/(1+z)$. In other geometries, a can be obtained from the Friedmann equation $\dot{a} = H_0\sqrt{1+\Omega_0(a^{-1}-1)+\Omega_\Lambda(a^2-1)}$ (for a review, Peebles, 1980). The cosmological parameters have to be assumed, and in recent times, simulations have adopted the WMAP estimates (Tegmark et al., 2004) or the Planck estimates Planck Collaboration et al. (2014). The Planck collaboration recently updated their final estimates in Planck Collaboration et al. (2018).
If we define the proper mass density of matter as

$$\rho(\boldsymbol{x},t) = \int f(\boldsymbol{x},\boldsymbol{p},t)\,\mathrm{d}^3p \tag{2.1}$$

where $f(\boldsymbol{x},\boldsymbol{p},t)$ is the phase-space distribution function and $\boldsymbol{p} = ma^2\dot{\boldsymbol{x}}$ are the momenta, the evolution of the phase-space distribution function will be described by solving the Vlasov equation (for a review, Mo et al., 2010):

$$\frac{\partial f}{\partial t} = \frac{\boldsymbol{p}}{ma^2}\nabla f - m\nabla\Phi\frac{\partial f}{\partial \boldsymbol{p}} = 0 \tag{2.2}$$

coupled with the Poisson equation:

$$\nabla^2\Phi(\boldsymbol{x},t) = 4\pi G a^2\left[\rho(\boldsymbol{x},t) - \bar{\rho}(t)\right] \tag{2.3}$$

where Φ is the gravitational potential, and $\bar{\rho}(t)$ the mean background density.
As this is a high-dimensional $\mathbb{R}^6$ problem, it is usually solved either by applying the equations of motion to a discrete sampling of f by means of N tracer particles, or by solving the Poisson equation. The rest of the Section will introduce some of the most common solution approaches.

2.1.1 Direct sum (Particle-Particle algorithm)

The most straightforward approach to calculating gravity would be a direct sum of the contributions of each particle to the gravitational potential at coordinate $\boldsymbol{r}$, which is given by:

$$\Phi(\boldsymbol{r}) = -G\sum_j \frac{m_j}{\left(|\boldsymbol{r}-\boldsymbol{r}_j|^2+\epsilon^2\right)^{\frac{1}{2}}} \tag{2.4}$$

Where j represents every particle in the simulation. This equation is a modification of the exact Newtonian potential as it introduces a gravitational softening ϵ. This is a trick introduced to address the numerical artifact that when particles get too close to each other their gravitational force goes to infinity. N-body calculations treat a

smooth collisionless medium (dark matter) as discretized into heavy (10^6 – 10^9 for petascale computations, depending on the scale of the simulated box) particles that treat the medium in bulk. The only way to increase the smoothness of the medium is to increase the number of particles. The softening should be chosen small enough as to not affect the physics of the system. The softening value is usually taken between 0.02 and 0.05 of the mean distance between particles, and the dynamics at scales smaller than 3ϵ is not reliable (Dolag et al., 2008). This method has prohibitive computational costs (N^2 operations per timestep, Binney and Tremaine, 1987, where N is the number of particles). Other techniques achieve acceptable levels of accuracy with cheaper computational costs.

2.1.2 Trees

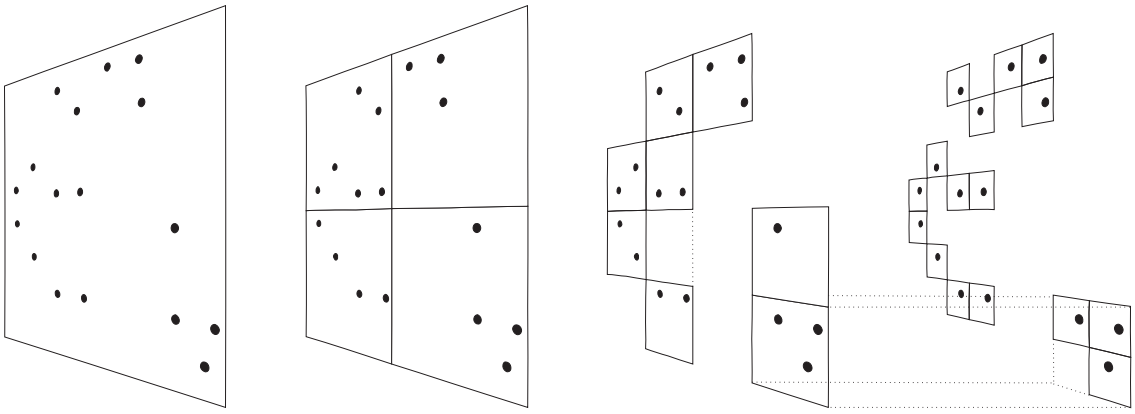

Figure 2.1: Schematic illustration of the Barnes et al. (1986) oct-tree in two dimensions. The particles are first enclosed in a square (root node). This square is then iteratively subdivided into four squares of half the size, until exactly one particle is left in each final square (leaves of the tree). In the resulting tree structure, each square can be the progenitor of up to four siblings. [From Springel et al. (2001)]

A faster method that reduces the number of operations to $\sim N \log N$ is the Tree algorithm (Barnes et al., 1986). This method is approximated. It does not compute the individual forces between each particle in the simulation. The first operation carried out by the method is the construction of hierarchical trees that describe the location of each particle within the simulation box. Afterwards, the cumulative force on every particle is calculated. With the Tree method, the force computations of distant particles are greatly simplified.
The hierarchical tree is constructed with the following procedure: The entire box of the simulation, called root node, is divided recursively to form hierarchical grouping.

Figure 2.1 is a two-dimensional equivalent of how the 3D subdivision is calculated. This root node is divided into 8 octants by the 3 coordinate planes (or into 4 quadrants of the 2D case, as in the figure). These 8 octants (or quadrant in 2D) are considered nodes one level up from the root. For each node the division is repeated recursively. The last divided sub-domains will be the "leaf" nodes. Each leaf node contains either a single particle or no particle at all. Within this scheme, particles are grouped into hierarchies of nodes. The tree will store for each node at every level (from root to leaf) information on the node, such as location of the center of mass, the total mass of the node, and the side length s of each box cube (or square in 2D).

The force calculation will then ensue for every single particle. A parameter θ is taken as threshold parameter and it will dictate the accuracy of the simulation. The algorithm will start at the root node and travel up the tree. Through every level up the tree, the algorithm will identify which node the particle belongs to, it will calculate the distance d from the center of mass of every other node at that level and the position of the particle. The condition for the Tree code is $s/d < \theta$, so if the ratio between the side length of the node and the distance of the particle from the center of mass of the node is less than the parameter θ, the algorithm will compute the force between the particle of interest and the node. The particles in every node are treated as a single body. If the condition is not met, the algorithm will compute the force via the direct method. The process is repeated recursively, so the algorithm will travel "up" the tree, in the progressive inner nodes to which the particle belongs, until every particle is accounted for. A schematic side-by-side comparison of the direct method on the left and the tree method on the right is available in Figure 2.2.

2.1.3 Particle-Mesh

An even faster computation is delivered by particle-mesh (PM) methods (for an overview, see Hockney and Eastwood, 1981). PM entails solving the Poisson equation $\nabla^2\phi = 4\pi G\rho$ for a mesh of mass distributions. The simulated cube of side L is divided into a mesh with spacing $\Delta = L/M$ and $N_g = M^3$ number of grid points. The simulation still contains N_P number of particles. At each of the grid points, the density ρ is estimated via a process called mass assignment. Several techniques can be employed to obtain the mass assignment, from the simplest nearest grid point (NGP), where simply the mass of each particle is assigned to the nearest mesh

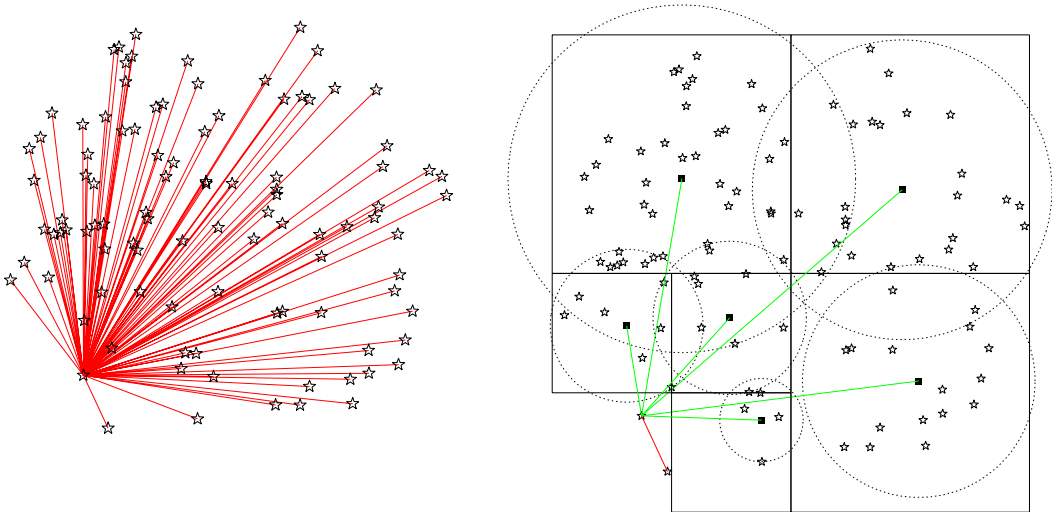

Figure 2.2: Left: Computation of the force for one of 100 particles (asterisks) in two dimensions (for graphical simplicity) using direct summation: every line corresponds to a single particle-particle force calculation. **Right**: approximate calculation of the force for the same particle using the tree code. Cells opened are shown as black squares with their centres z indicated by solid squares and their sizes w by dotted circles. Every green line corresponds to a cell-particle interaction. [From Dehnen and Read (2011)]

point. This technique is not favored as there is no interpolation involved, so the assignment creates discontinuity in the mesh. The cloud-in-cell (CIC) method solves the discontinuity of the forces by interpolating the particle mass over the $2^3 = 8$ nearest mesh points, but the derivatives of the forces are still discontinuous. The triangular-shaped-cloud (TSC) method with its piecewise quadratic interpolation provides a smooth continuous distribution of particle masses over the $3^3 = 27$ nearest points. Once the mass distribution is computed over the mesh, the distribution is transformed into Fourier space where, using the Fast Fourier Transform technique (FFT Cooley and Tukey, 1965) it is easy to solve the Poisson equation in Fourier space and derive the gravitational potential Φ. FFT changes the differential Poisson equation into an algebraic one, with obvious gains in computation times and costs (derivations available e.g. in Moscardini and Dolag, 2011).

PM computations are extremely efficient, with operation costs $\propto N_P + N_g \log(N_g)$, dependent therefore only on the number of particles and grid points. For a mesh that is not too fine, this is the fastest algorithm of the ones presented so far. It used to perform well in simulations of hot (relativistic) dark matter. Unfortunately, fast computations come at the cost of resolution. PM methods cannot follow particle

interactions at scales smaller than the intergrid distance at which the interpolations are computed. It is also a memory-intensive algorithm. Some of the previous methods have complementary pros and cons. It is possible to combine them into hybrid algorithms that contain the best of each.

2.1.4 Hybrid (AP^{3}M, TreePM)

TrePM is a technique that combines tree and PM methods, and it has become quite popular in cosmological simulations (Xu, 1995; Bode et al., 2000; Bagla, 2002). As we've seen, the PM method underperforms at small scales. TreePM codes calculate long ranges with the PM algorithm, whether the small range interactions are evaluated via hierarchical trees. In TreePM, the potential is explicitly expressed as the sum of long-range and short-range potentials in Fourier space. The method is fast yet accurate. TreePM is used in GADGET-2 (Springel, 2005) and it is also the preferred gravitational algorithm of our simulations along with many other groups. The first attempt at hybrid algorithms was the P^{3}M code, which, just like TreePM, implements PM at larger scales, and the particle-particle direct method at small scales. AP^{3}M (Couchman, 1991) used in simulations such as Evrard et al. (2002) is an improved version of the P^{3}M algorithm implemented in adaptive mesh refinement (AMR), where the grid spacing adapts at each timestep and becomes very fine in high particle density regions.

2.2 Initial Conditions and Resolution

Once a certain cosmology is assumed, N-body simulations can produce observables which, tested against observations, may verify or falsify data. The good performance of the simulation is contingent upon reliable initial conditions, or upon a correct initial distribution of the particles within the cosmological box. An initial condition generator must create small density fluctuations with near Gaussian distribution in a field defined by its power spectrum $P(k)$. Power spectrum and Gaussian distribution are calibrated to the constraints of high-precision cosmology, in particular CMB observations.

At the times of the CMB, dark matter, and baryonic matter fluctuations coincided. The initial conditions in our simulations were extracted from a larger low-resolution N-body cosmological simulation. This parent simulation followed 1024^3 dark matter particles within a periodic box of comoving size 1 h^{-1}Gpc. A flat ΛCDM cosmology

is assumed, with matter density parameter $\Omega_m = 0.28$, of which $\Omega_b = 0.04$ is the baryon density and the remaining is DM. The value of the Hubble parameter is taken to be $h = 0.72$, the normalization of the power spectrum $\sigma_8 = 0.8$ and the primordial power spectral index is $n_s = 0.96$. The Lagrangian regions identified from the parent simulation is then re-simulated at higher resolution with the zoomed initial conditions technique (Tormen et al., 1997). The chosen Lagrangian regions are very large, so that within 5 Virial radii, the only particles present are high-resolution. On the initial condition distribution runs our custom version of the TreePM-SPH GADGET-3 code, improved from GADGET-2 (Springel, 2005), a code rich in state-of-the-art subgrid physics as will be explained in section 2.4. The adopted procedure to generate our IC is explained in in Bonafede et al. (2011).

Parameter	Value
Initial N. of Gas Particles	2.32×10^6
Initial N. of high-res DM Particles	8.59×10^5
Gas particle mass	$1.53 \times 10^8 M_\odot h^{-1}$
DM particle mass	$8.47 \times 10^8 M_\odot h^{-1}$
Parent box size	1 Gpc
Gas softening	5.6 h^{-1} kpc (phys coord)
BH softening	3.0 h^{-1} kpc (phys coord)
Star softening	3.0 h^{-1} kpc (phys coord)
Dark Matter softening	16.7 h^{-1} kpc [1]

Table 2.1: The assumed parameters in our simulation.

A summary of some of the adopted parameters in our simulation is reported in Table 2.1. In the high-resolution region, the softening length is $\epsilon = 5.6h^{-1}$ kpc in physical units. Above $z = 2$ however, dark matter softening follows a softening of fixed comoving length set to $16.8h^{-1}$ kpc. The mass of DM particles for the high-resolution region is $8.47 \times 10^8 h^{-1} M_\odot$, and the initial mass of each gas particle is $1.53 \times 10^8 h^{-1} M_\odot$.

[1] The Dark Matter softening is fixed in comoving coordinates for $z > 2$. For lower redshifts it follows the physical coordinates like the gas.

2.3 Hydrodynamics

Astrophysical observations depend strongly on their associated physical processes. Therefore, in order to have a reliable simulation, gravity on dark matter particles is not sufficient, and a reliable representation of baryons is necessary. This matter component is modeled assuming it is an ideal fluid. The following three equations describe its behaviour:

The continuity equation

$$\frac{\mathrm{d}\rho}{\mathrm{d}t} + \rho\nabla\cdot\boldsymbol{v} = \frac{\partial\rho}{\partial t} + \nabla\cdot(\rho\boldsymbol{v}) = 0 \tag{2.5}$$

Euler's equation:

$$\frac{\mathrm{d}\boldsymbol{v}}{\mathrm{d}t} = \frac{\partial\boldsymbol{v}}{\partial t} + (\boldsymbol{v}\cdot\nabla)\boldsymbol{v} = -\frac{1}{\rho}\nabla P - \nabla\Phi \tag{2.6}$$

The Energy equation (first law of thermodynamics):

$$\frac{\mathrm{d}u}{\mathrm{d}t} = \frac{\partial u}{\partial t} + \boldsymbol{v}\cdot\nabla u = -\frac{P}{\rho}\nabla\cdot\boldsymbol{v} \tag{2.7}$$

Where P and u represent the pressure and internal energy per unit mass. For the hydrogen-dominated monoatomic gas at the beginning of the simulation, $P = 2/3\rho u$ is the equation of state that connects these two parameters. At this stage, no radiative process is taken into consideration.

These three equations have to be adapted to an expanding universe. After adding the scale factor, they must be solved in the following form:

$$\frac{\partial\boldsymbol{v}}{\partial t} + \frac{1}{a}(\boldsymbol{v}\cdot\nabla)\,\boldsymbol{v}\frac{\dot{a}}{a}\boldsymbol{v} = -\frac{1}{a\boldsymbol{\rho}}\nabla P - \frac{1}{a}\nabla\boldsymbol{\Phi} \tag{2.8}$$

$$\frac{\partial\boldsymbol{\rho}}{\partial t} + \frac{3\dot{a}}{a}\boldsymbol{\rho} + \frac{1}{a}\nabla\cdot(\boldsymbol{\rho}\boldsymbol{v}) = 0 \tag{2.9}$$

$$\frac{\partial(\boldsymbol{\rho}u)}{\partial t} + \frac{1}{a}\boldsymbol{v}\cdot\nabla(\boldsymbol{\rho}u) = -(\boldsymbol{\rho}u + P)\left(\frac{1}{a}\nabla\cdot\boldsymbol{v} + 3\frac{\dot{a}}{a}\right) \tag{2.10}$$

This system of equations can either be solved with respect to the particles or on the nodes of a grid. Codes which solve for particles are called Lagrangians, codes that solve for grids are Eulerian.

Hydrodynamics entails self-interactions, adding a higher level of complexity com-

pared to non-collisional gravity alone. Evolved density structures induce motions often supersonic, characterized by shocks and discontinuities. Hydrodynamics traces multiple physical quantities (temperature, pressure, etc.) and has to do so on a wide range of scales and orders of magnitude.

2.3.1 Smoothed-Particle Hydrodynamics

Smoothed Particle Hydrodynamics (SPH) is, among Lagrangian methods, the most widely used and also the easiest to couple with gravity. In SPH as we've mentioned earlier in this chapter, the fluid is described by a finite set of mass elements, as opposed to volume elements for Eulerian methods. As the mass resolution is kept fixed, denser regions will have more particles and their average distance will be smaller, therefore SPH is an adaptive code in spatial resolution (Monaghan, 1992). To obtain a continuous fluid, it is necessary to define the kernel smoothing method:

$$\langle A(\boldsymbol{r})\rangle = \int W(|\boldsymbol{r}-\boldsymbol{r}'|, h) A(\boldsymbol{r}')\, \mathrm{d}\boldsymbol{r}'^3 \tag{2.11}$$

Here the continuous fluid is described by the function$A(\boldsymbol{r})$ and the kernel function W has to be normalized, i.e.:

$$\int W(|\boldsymbol{r}-\boldsymbol{r}'|, h)\, \mathrm{d}\boldsymbol{r}^3 = 1 \tag{2.12}$$

h is the SPH smoothing length. It is a variable parameter (Silverman, 1986). When h approaches zero, the kernel collapses into a delta function. The most common kernel is the B_2-spline:

$$W(r,h) = \frac{\sigma}{h^\nu} \begin{cases} 1-6(\frac{r}{h})^2+6(\frac{r}{h})^3 & 0 \le \frac{r}{h} < 0.5 \\ 2(1-\frac{r}{h})^3 & 0.5 \le \frac{r}{h} < 1 \\ 0 & 1 \le \frac{r}{h} \end{cases} \tag{2.13}$$

ν is the dimensionality (3 in 3D, 2 in 2D, etc.). σ is a normalization which varies depending on ν. In the 3D case, $\sigma = 8/\pi$.

A discrete representation of the continuous fluid quantity A may be represented by the discretized SPH mass elements:

$$\langle A_i\rangle = \langle A(\boldsymbol{r}_j)\rangle = \sum_j \frac{m_j}{\rho_j} A_j W(|\boldsymbol{r}_i - \boldsymbol{r}_j|, h) \tag{2.14}$$

Using the identity

$$(\rho\nabla)\cdot A = \nabla\,(\rho\cdot A) - \rho\cdot(\nabla A) \tag{2.15}$$

it is possible from the discretized representation of A to derive the fluid equation and hence describe the motion of the particle.

The SPH method has a series of advantages and disadvantages. It conserves by construction physical quantities such as mass, energy, momentum, and entropy. It performs very efficiently in dense environments, where its resolution increases due to the higher number of particles describing the dense region. However, for this very same high density advantage, SPH underperforms in sparse regions (for a review, e.g. Dolag et al., 2008). SPH also has trouble treating fluid instabilities and discontinuities such as shocks.

2.3.2 Eulerian methods

Eulerian methods, or methods that separate the fluid spatially with a grid, perform well both at high and low density regions, however they are limited in spatial resolution, and they may lead to inaccurate predictions of the thermal energy (Ryu et al., 1993; Bryan et al., 1995). A first attempt at solving the 3 hydrodynamical equations on a mesh was the central difference scheme (e.g. Cen, 1992). In these methods, the relevant hydrodynamical quantities such as density, pressure, and velocity were traced at the center of the mesh, and the derivatives were computed with a central finite difference $[f(x+\frac{1}{2}h) - f(x-\frac{1}{2}h)]/h$. These methods however break down at discontinuities, so artificial viscosities were introduce to treat shocks. Eulerian methods are only first-order accurate as their error is directly proportional to h.

More recently, Eulerian methods have geared toward reconstruction approaches which evolve a grid cell taking into consideration several of the neighboring cells (e.g. Colella and Woodward, 1984; Harten, 1983). Reconstruction approaches do not approximate hydrodynamical variables at specific points like the center of the grid of central finite difference methods, rather they compute the cell average $\hat{u}_n$:

$$\hat{u}_n = \int_{x_n-0.5}^{x_n+0.5} f_{n,u}(x)\,\mathrm{d}x \tag{2.16}$$

Here, $f_{n,u}(x)$ represents the shape of the reconstructed hydrodynamical quantity u, n identifies the cell. A useful practice in the field is that to solve the Riemann problem, i.e. to find the solution to an initial value problem containing a conservation equation, continuous boundaries, and a single discontinuity (e.g. a shock). The

solution has to be found for each coordinate direction independently.

2.3.2.1 Leading Cosmological Simulation Codes

GADGET (GAlaxies with Dark matter and Gas intEracT, Springel et al., 2001; Springel, 2005) and all its variations is among the most popular Lagrangian codes, and the first one to become publicly available in its first two versions. It is also the code of choice of the present work. GADGET is fully parallelized with the MPI message-passing library. Notable are the Millennium II and Millennium XXL runs. In its default mode, gadget uses TreePM to compute gravity, and it includes an SPH prescription (ours follows the scheme by Beck et al., 2016). For what concerns Eulerian codes, ENZO (Bryan et al., 2014) is a popular approach which is written to run in parallel with MPI on supercomputers. Gravity is treated with a PM algorithm combined with a triangular-shaped-cell interpolation. The hydrodynamics is based on Colella and Woodward (1984). Another approach which is gaining traction is AREPO (Springel, 2010). Its gravity is a standard TreePM, but the hydrodynamics is computed on a moving mesh obtained by fully-adaptive Voronoi tessellation, and it is computed on a Galilean-invariant Eulerian code. It has the advantage of good treatment of shocks.

2.4 Sub-grid Physics

As we have seen so far, cosmological simulations often require the discretization either by mass or volume of the content of the Universe. Due to practical limitations in CPU time and memory, the discrete elements of large scale simulations are coarse, and cannot resolve the baryonic processes involved in astrophysical processes. These processes can however still be included in simulations by means of sub-grid modeling. The computations are carried out within individual particles. Prescriptions will read the relevant information from within the gas particle, and they will update the particle quantities (or generate new ones) as necessary. This section will outline the physical processes included in our simulation as subgrid models, with the exception of dust modeling which is reserved to Chapter 5. The included processes are as follows: the gas will dissipate energy and cool. If particles are cool and dense enough, a fraction of their mass may be treated as molecular cloud. At this stage a star particle may spawn. Stars provide feedback to the surrounding simulated particles with either SN shocks, winds, or thermal feedback. From star particles, a

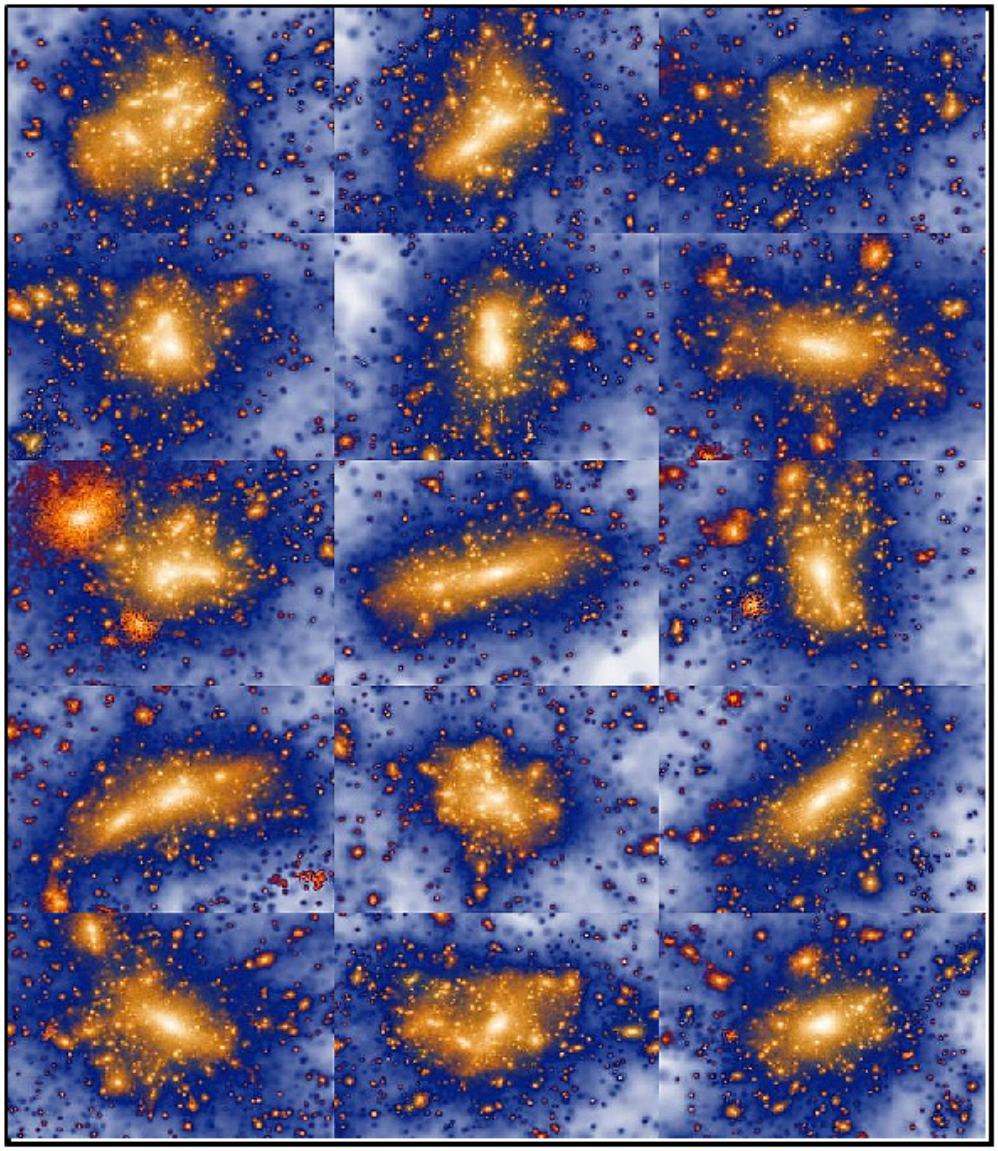

Figure 2.3: Projected dark matter density for the 15 most massive MXXL haloes (according to M_{200} at $z = 0.25$). Each image corresponds to a region of dimensions $6 \times 3.7h^{-1}$ Mpc wide and 20 h^{-1} Mpc deep. Note the large variation in shape and internal structure among these clusters. In particular, the most massive cluster, shown in the top-left corner, has no clear centre but rather displays several distinct density peaks of similar amplitude.[From Angulo et al. (2012) of the Millennium-XXL run]

prescription of chemical evolution produces metals, which are then spread to surrounding gas particles, enriching the medium and affecting gas cooling. An efficient implementation of AGN feedback is also included.

2.4.1 Radiative Cooling

When we presented Equation 2.3, the first law of thermodynamics, we specified that we excluded radiative processes. Here we explain the cooling function, $\Lambda(u, \rho)$ in erg s^{-1} cm^{-3}, to be added to the equation. Cooling in cosmological simulations will usually need to treat media which are hot ($> 10^4$ K) optically thin and in ionization equilibrium. The gas is exposed to CMB radiation and UV/X-ray background radiation from galaxies (we follow Haardt and Madau, 2001). The net cooling function of a plasma will contain collisional line radiation, free-free and two-photon continuum, recombination processes, photoionization heating, collisional ionization, and Compton cooling (for an overview, Sutherland and Dopita, 1993):

$$\Lambda_{net} = \Lambda_{lines} + \Lambda_{cont} \pm \Lambda_{rec} - \Lambda_{photo} + \Lambda_{coll} \pm \Lambda_{Compt} \tag{2.17}$$

As an example, the Compton cooling function will read:

$$\Lambda_{Compt} = 4k(T_e - T_\gamma)\langle e_\gamma \rangle \frac{\Phi \sigma_T n_e}{m_e c} \tag{2.18}$$

Where Φ is the radiation flux, σ_T the Thompson cross section, $\langle e_\gamma \rangle$ the mean photon energy, n_e, m_e, T_e are the electron number density, mass, and temperature, and T_γ is the temperature of the radiation. In Sutherland and Dopita (1993) all the other terms are derived.
In practice, most codes will rely either on tabulations for cooling functions or they will run large grids of photoionization models with packages such as CLOUDY (Ferland et al., 1998, 2017). As implemented by Wiersma et al. (2009) in our code:

$$\Lambda = \Lambda_{\mathrm{H,\ He}} + \sum_{i > \mathrm{He}} \Lambda_i \tag{2.19}$$

Where the combined contributions from hydrogen and helium $\Lambda_{\mathrm{H,\ He}}$ are obtained via 4-dimensional interpolation of CLOUDY tables over $\log n_H$, z, and $n_{\mathrm{He}}/n_{\mathrm{H}}$ of models that contain only H and He. The metals i included in our code are (H, He, C, Ca, O, N, Ne, Mg, S, Si, Fe, Na, Al, Ar and Ni). These are the same traced by chemical evolution. As the cooling functions for solar metallicity are already

computed, it is possible to represent the elemental cooling functions in terms of elemental number density n_i and the free electron number density n_e alone, other than the interpolated grids:

$$\Lambda = \Lambda_{\mathrm{H,\ He}} + \sum_{i>\mathrm{He}} \Lambda_{i,\odot} \frac{n_e/n_H}{(n_e/n_H)\odot} 10^{[i/H]} \tag{2.20}$$

Where $10^{[i/H]} = (n_i/n_H)/(n_i/n_H)_\odot$. The free electron density abundance depends on the number density ratio between Hydrogen and Helium, and can be obtained by interpolating n_{He}/n_H with the Hydrogen number denisty, the particle temperature, and redshift.

If one has an incomplete set of elemental contributions, it is possible to use the less accurate

$$\Lambda = \Lambda_{\mathrm{H,\ He}} + \Lambda_{\mathrm{Z},\ \odot} \frac{n_e/n_H}{(n_e/n_H)_\odot} \tag{2.21}$$

that computes cooling rates in terms of the total metallicity.

In our code, the metallicity field is smoothed in order to compute these cooling rates, because our metallicity field is very noisy due to the fact that no process diffuses metals to neighboring gas particles after a single gas particle is enriched. The smoothing is implemented using the same kernels from the SPH computations (Wiersma et al., 2010).

2.4.2 Star Formation and Feedback

A simple star formation (SF) recipe was introduced by Katz et al. (1996). In the recipe, a gas particle is suited to form stars if its flow is convergent ($\nabla \boldsymbol{v}_i < 0$) and if its density exceeds some threshold value, e.g. $\rho_{th} > 0.1$ atoms cm^{-3}. Furthermore, the particle has to be Jeans unstable:

$$\frac{h_i}{c_i} > \frac{1}{\sqrt{4\pi G \rho_{th}}} \tag{2.22}$$

where h_i is the SPH smoothing length (or the mesh size for Eulerian codes). c_i is the local sound speed. If the density condition is met, usually also the other conditions are. Therefore, density is the decisive SF parameter.

One last constraint is required to avoid that dense particles at high redshift are mistakingly selected into a virialized halo they do not belong to:

$$\frac{\rho_i}{\hat{\rho}} > 55.7 \tag{2.23}$$

Where $\hat{\rho}$ is the average density of the Universe at a specific time. When all the conditions are met, the gas particle will enter a state characterized by 2 phases (referred to as multiphase), one phase is cold and treated with a subgrid function, one is hot. We follow the recipe provided by Springel and Hernquist (2003), in which the cold fraction, representative of molecular clouds and responsible for star formation, is embedded in pressure equilibrium with the hot fraction.

The star formation rate (SFR) follows a Schmidt-type law (Schmidt, 1959):

$$\dot{m}_\star = f m_g / t_{\star,\rho} \tag{2.24}$$

Where f is the cold gas fraction, m_g is the mass of the gas particle, and $t_{\star,\rho}$ is the timescale $t_{\star,\rho} \propto \sqrt{\rho_{th}/\rho}$ (Tornatore et al., 2007). From the Schmidt law follows the mass expected to form in the interval Δt:

$$m_\star = M_{0,\star}\left(1 - e^{f\Delta t/t_{\star,\rho}}\right) \tag{2.25}$$

With $M_{0,\star}$ being the stellar mass at the time the star particle was originated. $M_{0,\star}$ will be a fraction of the progenitor gas particle. How much of the gas particle mass will go into the newly generated star particle depends on the star generations $N_\star$. In our code, $M_{0,\star} = m_g/N_\star$ with $N_\star = 3$.

Whether a gas particle spawns a star particle or not depends on two factors. First, it has to accumulate enough star formation before it is able to create a simulated collisionless star particle. Second, the following probability must be considered:

$$P(t_\star) = N_\star\left(1 - e^{f\Delta t/t_{\star,\rho}}\right) \tag{2.26}$$

If a random number taken between 0 and 1 is larger than $P(t_\star)$, the gas particle will generate a star particle.

The SF episodes are limited in most simulations to 2-3 stellar generations in order to keep stellar and gas masses within at least the same order. If masses varied wildly, numerical artifacts might emerge in the calculation of gravity. Some codes do not split their gas particles, and one SF episode, or a single stellar generation, is sufficient to convert the whole gas particle into a star particle.

Each star particle produced according to this model is described by a simple stellar

population (SSP) characterized by an assumed initial mass function IMF. Under the instantaneous recycling approximation (IRA) all stars with masses $> 8M_{\odot}$ (i.e. Massive stars that explode as Type II supernovae) are taken to explode within a single timestep. Timesteps in our simulations are of the order of 10 Myr. Given that SNIIs explode within time intervals much shorter than this, with IRA we may extrapolate the supernova input energy fed back into the gas by sypernovae explosions, which are of the order of 10^{51} erg per supernova. Part of this feedback is channeled into kinetic energy in our model Springel and Hernquist (2003) and it fuels galactic outflows. It is a robust prescription, because increasing the simulation resolution, the amount of stars formed converges.

2.4.3 Chemical Evolution

The chemical evolution routine was implemented in our simulations by Tornatore et al. (2007). The routine generates metals at each timestep based on the properties of individual star particles, and it will immediately spread said metals to nearby gas particles following the SPH kernels of the spreading function.

The mass of the produced metals will depend on how many stars have died within a certain time interval. The first information we need is that of stellar lifetimes $\tau_{\star}$. For one-zone models, the stellar lifetime depends on the mass of individual stars and their metallicity. Our simulated particles do not contain individual stars, rather a whole simple stellar population characterized by a certain initial mass function (IMF, $\phi(m)$) and a certain metallicity. Our star particles inherit the metallicity Z_0 from the gas particle progenitor, and its value is not altered until the star particle's death.

By taking the inverse of the functions of stellar lifetimes, we can derive for a given lifetime $\tau_{\star}$ and metallicity Z_0 what is the mass of the stars which will die by $\tau_{\star}$. The lifetime $\tau_{\star}$ may be expressed in terms of the time of the simulation. Let us take two consecutive timesteps $t_{i+1} - t_i = \Delta t$. Using the inverse of stellar lifetimes we will find the mass of the star population which will die at t_i and t_{i+1}: M_i and M_{i+1} respectively. If we integrate the star particle's IMF in the interval (M_i, M_{i+1}), we obtain the fraction of the star particle's mass which has died in the time interval Δt. Therefore, the mass of stars which have died in Δt is given by:

$$m_{dead} = M_{0,\star} \int_{M_i}^{M_{i+1}} \mathrm{IMF}(m')\, \mathrm{d}m' \tag{2.27}$$

Part of this ejecta accounts for metals. For the element X, the ejected mass at each

time interval is given by:

$$m_X = M_{0,\star} \int_{M_i}^{M_{i+1}} \mathrm{IMF}(m') \mathrm{Y}_X(m', Z_0)\, \mathrm{d}m' \tag{2.28}$$

Where Y are the yields. Yields are commonly represented in tabulations, which predict for each element (or isotope) what will be the mass ejected by a star based on the star's mass and metallicity. We consider 3 channels which contribute to mass ejection: Asymptotic Giant Branch (AGB) winds, Type II, and Type Ia Supernovae. For Type Ia SNe we adopted the yields provided by Thielemann et al. (2007). For AGB stars, we follow Karakas and Lattanzio (2007). For SNII we take one of the Romano et al. (2010) models which is a slight variant of Woosley and Weaver (1995). The relevant yield is obtained via a linear interpolation between m' and Z_0 for each particle at each timestep for each element. We trace the 15 metals H, He, C, Ca, O, N, Ne, Mg, S, Si, Fe, Na, Al, Ar and Ni.

In our simulations we implement the Chabrier IMF (Chabrier, 2003):

$$\phi(\log m) \propto e^{-(\log m - \log m_C)^2, 2\sigma^2} \qquad \text{for } M \leq 1 M_\odot \tag{2.29}$$

$$\phi(m) \propto m^{-(x \pm 0.3)} \qquad \text{for } M > 1 M_\odot \tag{2.30}$$

Where the IMF slope $x = 1.3$ is practically the Salpeter index $x = 1.35$ for the Salpeter IMF, $\phi(m) \propto m^{-(1+x)}$ (Salpeter, 1955). $m_C = 0.079 M_\odot$ and $\sigma = 0.69$ are good parameter fits to the Chabrier IMF for individual Galactic stars.

For the lifetime $\tau_\star$, we use the timescale presented in Padovani and Matteucci (1993):

$$\tau_\star = 1.2 m^{-1.85} + 0.003 \text{ Gyr} \qquad \text{for } M > 6.6 M_\odot \tag{2.31}$$

$$\tau_\star = 10^{[b - \sqrt{c - d \times (e - \log m)}]/a} - 9 \text{ Gyr} \qquad \text{for } M \leq 6.6 M_\odot \tag{2.32}$$

Where $a = 0.1116$, $b = 1.338$, 1.790, $d = 0.2232$, and $e = 7.764$. The two functions are respectively derived in Matteucci and Greggio (1986) and Renzini and Buzzoni (1986). However, our group is planning on updating this prescription in the near future, because newer, more accurate models for stellar lifetimes depend not only on the star's mass, but also on its metallicity.

2.4.4 AGN feedback

Another important role in galaxy evolution is played by Active Galactic Nuclei (AGN) feedback. AGNs are the manifestation of gas accretion onto SuperMassive Black Holes (SMBHs), and they are among the brightest observable astronomical objects. The infalling gas gathers around the SMBH into an accretion disk (Krolik, 1999), which heats up as the inverse of the distance from the SMBH (Hickox and Alexander, 2018), so that AGNs could be visible on a wide range of wavebands. As the typical AGN gas temperature falls in the range 10^4 - 10^5K, the majority of the emission will occur in the UV/optical bands. Aside from emission by the accretion disk itself, the angular momentum of the accretion disk and SMBH spin axis may cause the emission of highly collimated relativistic jets shooting perpendicularly from either side of the center of the accretion disk (See Figure 2.4). The giant jets cause the formation of hot gas bubbles which may heat the halo gas (Fabian, 2012, for a review). AGNs are also associated with high-velocity winds which may eject the cold galactic ISM to outer regions. The SMBHs will eventually grow to sizes of 10^5 - $10^6 M_\odot$. Almost every medium-to-massive galaxy has a SMBH, especially ellipticals and bulge-dominated spiral galaxies (Kormendy and Ho, 2013, for a review.). On top of being so prevalent, the energy released in SMBH growth is often greater than the gravitational binding energy of the host galaxy (Silk and Rees, 1998) so AGN feedback is bound to play a key role in galaxy formation.

Some AGN feedback properties are well understood. One of these is the tight correlation between the SMBH mass and the velocity dispersion of the host bulge (Ferrarese and Merritt, 2000). Theoretical motivations have been presented to explain such a correlation, ranging from ambient conditions in the host galaxy (Adams et al. 2001), to accretion of collisional dark matter (Ostriker 2000), or star captures by the central accretion disc (Miralda-Escudé and Kollmeier, 2005)). A large class of models (King, 2003, i.e.) propose that once the SMBH reaches a critical size, the outflow winds sweep away ambient gas, thus suffocating further growth. The mechanisms by which AGN interacts with the ISM affect these 3 major categories: thermal feedback, or the heating of gas by AGN radiation (i.e., Compton heating), kinetic feedback, or the generation of winds that causes gas outflows and shocks, and radiative feedback, or the gas ionization and photo-dissociation of molecules.

In cosmological simulations, AGN feedback is being treated with sub-grid models. Springel (2005) was one of the earliest works to include 3D simulations containing AGN feedback, and it used the Bondi approach. More recently, hydrodynamic

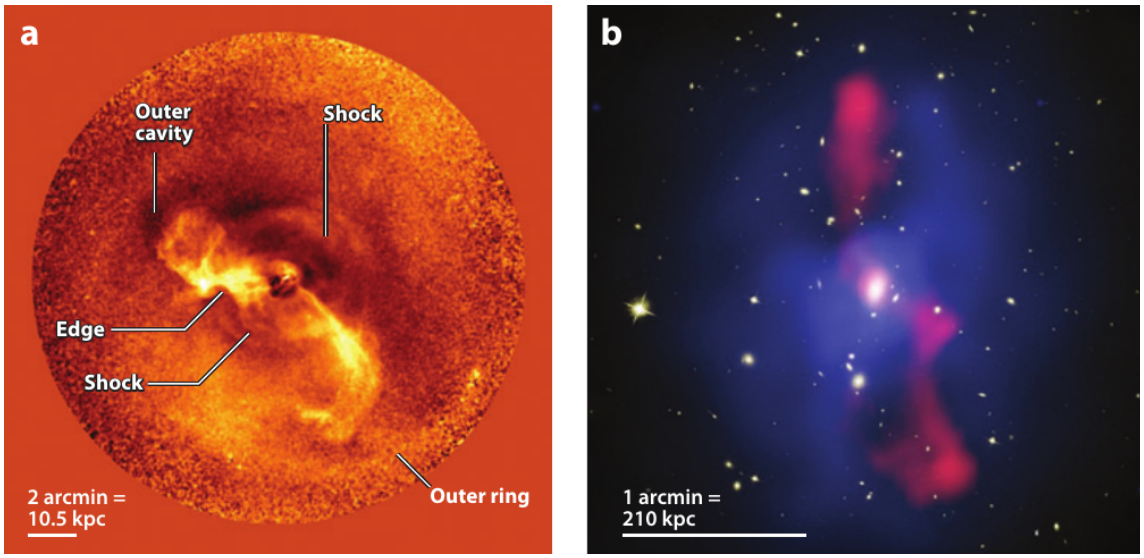

Figure 2.4: From Fabian (2012): (a) The Arms and weak shocks produced by the jets of M87 (Forman et al., 2007). (b) The gigantic interaction of the radio lobes and intracluster gas of MS0735.6 (McNamara et al., 2009). The figure shows the inner 700 kpc of the cluster extending well beyond its cool core.

simulations including radiation pressure on dust (Debuhr et al., 2011) found that these winds may modulate significantly SMBH and galaxy evolution.

2.4.4.1 In the code

AGN feedback implemented in the simulations by the Trieste group has been extensively described in Ragone-Figueroa et al. (2013) where the recipe is laid out, and in Ragone-Figueroa et al. (2018) where some improvements are outlined.

The SMBH is generated in any massive ($M_{\rm halo} > M_{\rm th} = 2.5 \times 10^{11} h^{-1} M_{\odot}$) dark matter halo identified with an on-the-fly FoF algorithm. Here, the gas particle with the smallest gravitational potential energy is turned into a SMBH. Its velocity is preserved, its mass is set to $M_{\rm seed} = 5 \times 10^{6} h^{-1} M_{\odot}$.

BH grows at a rate which is the minimum between what we dub α-*modified* Bondi rate (Bondi, 1952) and the Eddington rate:

$$M_{BH} = \min(\dot{M}_{Bondi,\alpha}, \dot{M}_{Edd})$$

The Bondi rate defined by an α-modified Bondi equation (Bondi, 1952) improved by Gaspari et al. (2013) with the denominator power of 2/3

$$\dot{M}_{Bondi,\alpha} = \alpha \frac{4\pi G^2 M_{BH}^2 \rho}{(c_s^2 + v_{BH}^2)^{2/3}} \tag{2.33}$$

where M_{BH} is the SMBH mass, v_{BH} its velocity relative to the surrounding gas bulk motion, c_s the sound velocity of the gas surrounding the BH, ρ is the gas density, and α is the adimensional fudge factor necessary to produce a reasonable SMBH mass by $z = 0$. Since Ragone-Figueroa et al. (2018), α varies depending on whether the accreting gas is in a cold mode or a hot mode. The former has an α fudge factor set to 100, the latter to 10, following Gaspari et al. (2013).
The Eddington accretion rate is

$$\dot{M}_{Edd} = 4\pi \frac{cGm_p}{\epsilon_r c^2 \sigma_T} M_{BH}$$

where m_p is the proton mass, σ_T the Thompson cross-section, c the speed of light and ϵ_r the radiative efficiency, giving the radiated energy in units of the energy associated with the accreted mass.
We finally reach the assumption of how the coupling between IGM/ICM gas and the energy irradiated by the AGN should occur:

$$\dot{E}_{feed} = \epsilon_f \epsilon_r \dot{M}_{BH} c^2$$

Where ϵ_f is the assumed fraction of irradiated energy that will couple with the gas. AGNs are supposed to be short lived, and an intense first "quasar mode" will be followed by a "radio mode". Our group follows the Sijacki et al. (2007) model. The switch between two modes occurs at the limit $\dot{M}_{BH}/\dot{M}_{Edd} = 10^{-2}$. When this ratio falls below this threshold, ϵ_f is increased by a factor of 4. The reference value for ϵ_r and ϵ_f is 0.2 ($\epsilon_f = 0.8$ for the radio mode) as they reproduce in our simulations the BH mass to stellar mass relation.

3

Dust Observational Properties and Modeling

As we have outlined in the introduction, the strongest constraints on dust come from its interaction with the electromagnetic spectrum. Dust will scatter and polarize the radiation of a bright source from the X-rays to the near-infrared (NIR). It will attenuate the light from vacuum UV to mid-infrared (MIR) by absorbing and scattering such wavelengths ($\sim$ 0.1-20μm), and it will emit a thermal continuum in the IR to mm. Bernstein et al. (2002) estimated that at least 30% of the local Universe starlight is re-emitted in the infrared by dust. And studies such as Clements et al. (1996) show that the percentage can raise to 99% in ultraluminous IR galaxies. Other observational data come from the depletion of elements whose abundance is lower than what is expected from nucleosynthesis, or from the analysis of presolar grains preserved on meteorites.

3.1 Radiative Transfer

The physical and thermodynamic properties of dust can be inferred from observables with the aid of solutions to the radiative transfer equation. The radiation field can be entirely described by the specific intensity I_ν defined as the amount of energy $\mathrm{d}E$ in the frequency beam $\mathrm{d}\nu$ that, originates from the solid angle $\mathrm{d}\Omega$ and crosses the surface $\mathrm{d}A$ in the time $\mathrm{d}t$:

$$I_\nu = \frac{\mathrm{d}E}{\mathrm{d}\Omega\,\mathrm{d}A\,\mathrm{d}\nu\,\mathrm{d}t} \tag{3.1}$$

Its observable is the specific flux F_ν, or the integral of the intensity over the solid angle:

$$F_\nu = \int_{4\pi} I_\nu \cos\theta\,\mathrm{d}\Omega \tag{3.2}$$

The units are erg cm^{-2}s^{-1}Hz^{-1}. It should not be confused with the bolometric flux,

defined as the integrated flux over all frequencies: $F_{bol} = \int_0^{\inf} F_\nu \, \mathrm{d}\nu$.
The interaction of a medium or body with electromagnetic radiation can be divided into absorption, scattering, and emission. In the case of absorption, a fraction of the incident flux is converted into internal energy of the absorbing material. In the case of scattering, a fraction of the incident flux is reflected at a differnet solid angle wbut with the same wavelength. Emission will be proportional to a quantity called emissivity j_ν, and will depend on the physical characteristic and energy state of the emitting material. Conservation of energy implies:

$$\mathrm{d}I_\nu = \frac{\mathrm{d}E^{(em)} - \mathrm{d}E^{abs} - \mathrm{d}E^{scatt}}{\mathrm{d}\nu \, \mathrm{d}\Omega \, \mathrm{d}A \, \mathrm{d}t} \tag{3.3}$$

from which follows the general equation of radiative transfer:

$$\frac{\mathrm{d}I_\nu}{\mathrm{d}l} = j_\nu - k_\nu I_\nu \tag{3.4}$$

Where k_ν is the total opacity, given by the sum of the scattering and absorption opacities. If we define a source function S_ν as the ratio between the emissivity and the total opacity, we can rewrirte the radiative transfer equation in its form: $\mathrm{d}I_\nu / \mathrm{d}l = k_\nu \, (S_\nu - I_\nu)$. Or, by introducing the optical depth $\mathrm{d}\tau_\nu \equiv k_\nu \, \mathrm{d}l$:

$$\frac{\mathrm{d}I_\nu}{\mathrm{d}\tau_\nu} = S_\nu - I_\nu \tag{3.5}$$

From which the formal solution follows:

$$I_\nu(\tau_\nu) = I_\nu(0) e^{-\tau_\nu} + \int_0^{-\tau_\nu} e^{(-\tau_\nu + \tau_\nu^{'})} S_\nu(\tau_\nu^{'}) \, \mathrm{d}\tau_\nu^{'} \tag{3.6}$$

3.2 Dust Extinction

The study of dust extinction in the 50s and 60s offered some first clues on the chemical composition of dust. The reddening of starlight was best fit by graphite as opposed to e.g. ices, which were then a leading candidate (for an overview, see Hoyle and Wickramasinghe, 1962). In the introduction (Section 1.1.2.1) we mentioned the 2175Å bump present in the average extinction curve of the Milky Way. This feature was identified with large uncertainties for the first time by Stecher (1965), after observing 5 pairs of dust-obscured and unobscured stars with similar MK spectral classification. Later for one of these pairs, Stecher (1969) reported the extinction, measured at intervals of 2Å as seen in Figure 3.1. The work confirmed the existence

of the 2175Å feature between this specific pair of stars. Stecher and Donn (1965) and Wickramasinghe (1965) proposed that graphite might be again the culprit to the feature, with the transitions of π-bonds between the sp^2 orbitals of adjacent carbon atoms. Also PAHs possess this kind of bond and they have been put forward as alternative candidates for the feature (e.g. Weingartner and Draine, 2001).

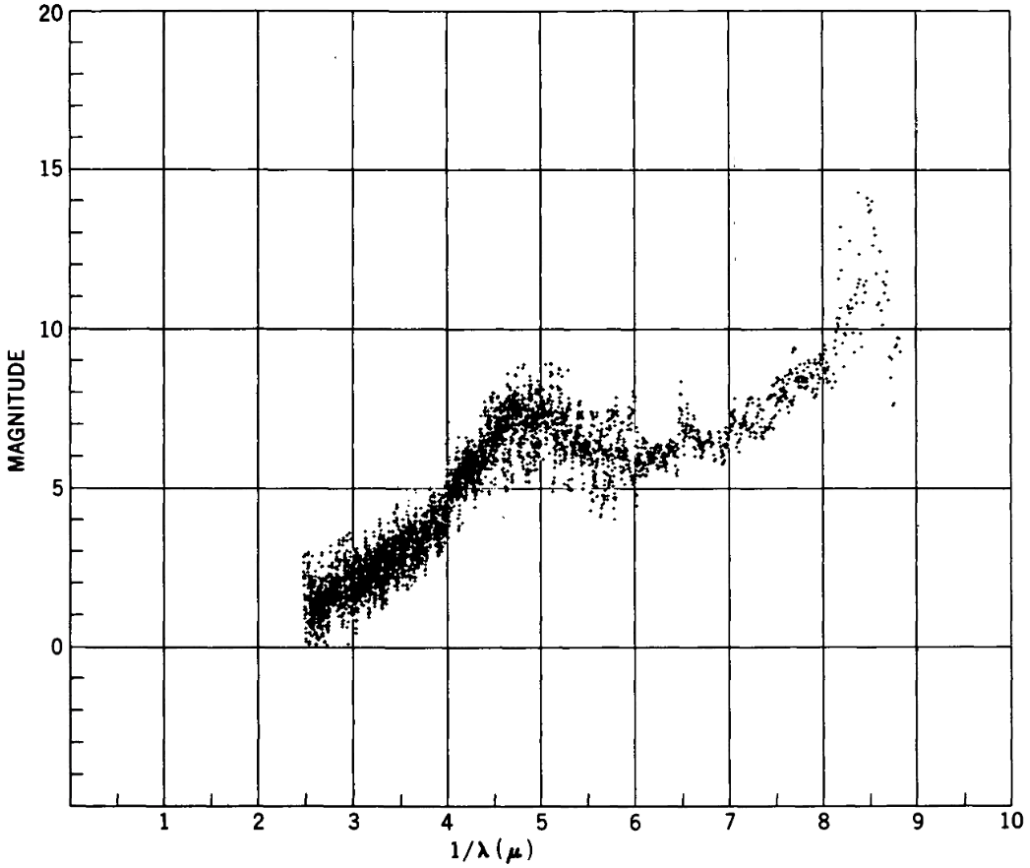

Figure 3.1: Interstellar extinction in magnitudes as a function of inverse wavelength determined from ζ and ϵ Persei. [From Stecher (1969)]

Subsequent studies investigated stars of different spectral classification, the Milky Way's extinction, averaged or along specific lines of sight, and the extinction in other galaxies.

It is important to draw the distinction between extinction and attenuation. Extinction, or the phenomenon by which dust obscures starlight radiation in UV and optical bands, is a combination of absorption and scattering (see e.g. Figure 3.6). Both absorption (from the line of sight) and scattering (from and to the line of sight) are wavelength-dependent processes. As extinction is stronger on bluer wavelengths, it will make an object appear redder than if it were not filtered by dust.

For point sources like nearby stars observed through a single ISM screen, the extinction law can be modeled by taking into account the known properties of the star (i.e. metallicity and spectral classification) and fitting dust properties. However, in complex geometries like within galaxies, the radiation may flow through multiple ISM environments with different dust populations. The observable is the net effect of dust within the complex geometry of a galaxy, where light sources are scattered within media at different depths. In galaxies, light is scattered out of and into the line of sight, damping extinction features. So, while extinction refers exclusively to absorption and scattering, it is a process that can be isolated only in simple environments. Dimming by dust for objects where the geometrical distribution plays a role is called attenuation.

In Figure 3.2 we see for example some attenuation curves obstained using the GRASIL model (Granato et al., 2000) compared to the MW extinction, in the solid line, and the empirical Calzetti attenuation law for starburst galaxies (Calzetti et al., 2000), in the filled circles. The GRASIL model is able to reproduce the Calzetti attenuation law with no fitting, only implementing different geometries and young stellar populations representative of starburst galaxies. The assumed dust properties are identical to the average values observed in the MW.

The UV dust extinction is not usually measured for wavelengths smaller than 912 Å, the Lyman limit, as for this wavebands hydrogen is very efficient at absorbing and emitting radiation, so it becomes the major source of starlight dimming. As a reminder from the introduction, the extinction A_λ is defined as $A_\lambda = 2.5 \log_{10} [F^0_\lambda / F_\lambda]$, where F_λ is the observed flux, and F^0_λ is the intrinsic flux as expected if there were no dust in the line of sight. Extinction is measured in magnitudes. A common measure of the extinction slope is

$$R_V = \frac{A_V}{E(B-V)} \tag{3.7}$$

Where A_B and A_V are the extinctions measured in the B (4405 Å) and V (5470 AA) photometric bands. $E(B-V) = A_B - A_V$ is called reddening or color excess. On average for the Milky Way, $R_V = 3.1$(Fitzpatrick, 1999).

Figure 3.3 from Fitzpatrick (1999) represents some estimates of the average Milky Way extinction profile, with labels of its most important features for three model variations, including Seaton (1979) and Cardelli et al. (1989). It can be broken down in the following way. The extinction in the NIR to red-optical from 900 nm to 5μm can be described with a power law, which can be approximated with $A_\lambda \propto \lambda^{-\beta}$.

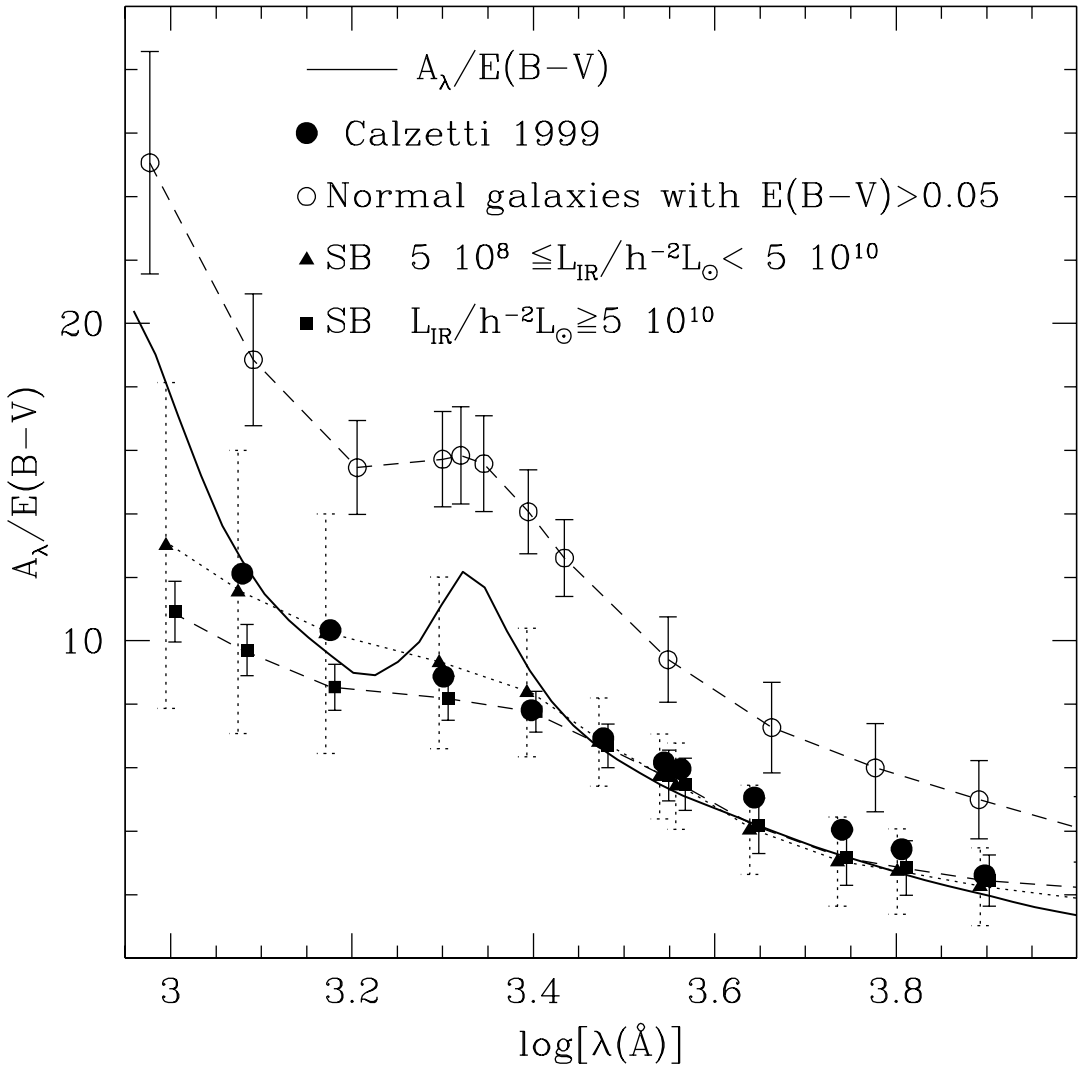

Figure 3.2: Average dust attenuation curves for starlight in different classes of galaxies [normal and starburst (SB)] in the Granato et al. (2000) GRASIL model compared with the average MW extinction law (*solid line*) and with the Calzetti attenuation law (*filled circles* Calzetti et al., 2000), with $R'^{V=4.05}$. The attenuation curves are all normalized to the net reddening of the stellar population, $E(B-V)$. The error bars show the dispersion of the models around the mean attenuation curve. [From Granato et al. (2000)]

The most plausible β values are in a range between 1.61 and 1.8 (e.g. Rieke and Lebofsky, 1985; Whittet et al., 1993). In the optical, the curve rolls over with a slight knee, then there's the 2175Å near-UV bump, and finally the extinction rises more steeply with a far-UV curvature.

Seaton (1979), which extends from the blue-optical to the far-UV, proposes a poly-

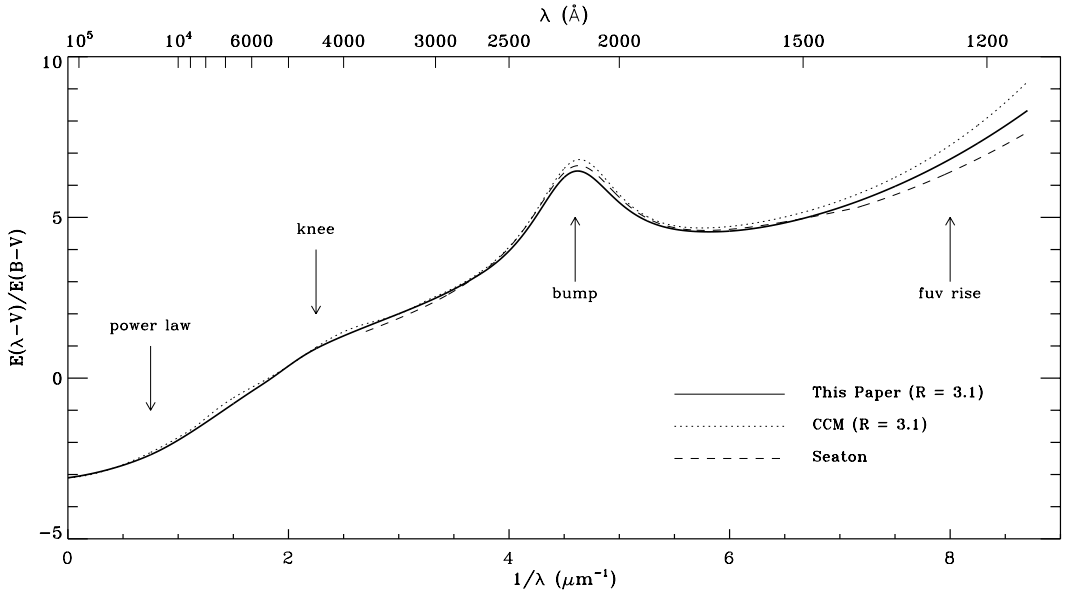

Figure 3.3: Normalized interstellar extinction curves from the far-IR through the UV. The solid and dotted curves are estimates for the MW-average case where $R_V = 3.1$ from the Fitzpatrick (1999) and the Cardelli et al. (1989) papers respectively. The dashed curve shows the average Galactic UV extinction curve from Seaton (1979). [From Fitzpatrick (1999).]

nomial fit given by a linear background term plus a Lorentz function. Cardelli et al. (1989) proposes initially a 7-parameter fit to describe the extinction, one of the parameters being R_V. They then show that all the other parameters (describing the power law for > 3030Å, the shape and prominence of the near-UV band, and the slope and curvature at small wavelengths) can all be estimated using R_V-only. However, the extinction is R_V-independent in the NIR range $0.7\mu\text{m} \lesssim \lambda \lesssim 8\mu\text{m}$ for diffuse clouds. The Fitzpatrick (1999) model can be described by 4 free parameters hich make up for the Cardelli et al. (1989) shortcomings, e.g. the 2175Å bump is not correlated with R. While in the work has been only investigated for the MW, averaged or at different lines of sight, is suited to describe most spiral galaxies. The paper goes on to modify the extinction curve for a range of R_V between 2.2 and 5.8, which corresponds to the observed ranges of extinction slopes as measured by

the *International Ultraviolet Explorer* (IUE) satellite, on which they based their calibrations. Figure 3.4 plots the R-dependence of the Cardelli et al. (1989) model, normalized to $E(B-V)$.

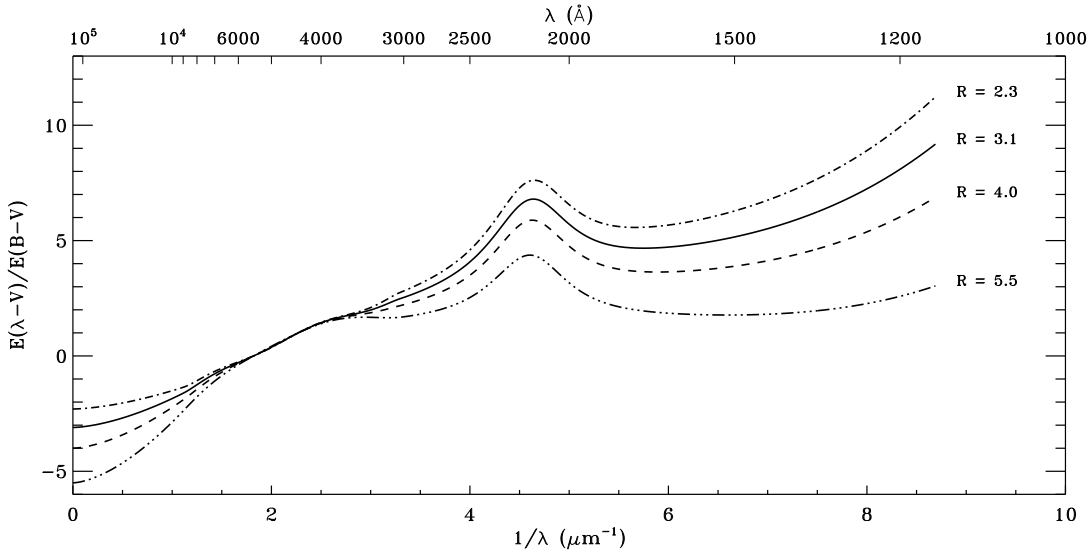

Figure 3.4: Far-IR-through-UV extinction curves for Cardelli et al. (1989). Cardelli et al. (1989) found that extinction curves can be expressed approximately as a one-parameter family that varies linearly with R^{-1}, where $R = A(V)/E(B-V)$ and has a mean value in the diffuse interstellar medium of $R = 3.1$. Other 4 representative R values are shown and labeled. [From Fitzpatrick (1999)]

3.3 Dust Emission

Dust emission is dominated by thermal radiation. In order to radiate thermally, a body must be in thermal equilibrium and therefore posess uniform temperature. When in thermal equilibrium, there is a balance between the energy absorbed by the body and the energy emitted by the body. Kircchoff's Law of thermal radiation (Kirchhoff, 1860) in fact states that the ratio between the emission coefficient ϵ_ν and the absorption coefficient α_ν^{abs} of a body will be proportional to a function of

wavelength and temperature only. This function was later found to be Planck's function $B_\nu(T)$. The emission coefficient, expressed in units of erg g^{-1} s^{-1} Hz^{-1}, is the energy emitted spontaneously by the body per unit frequency per unit time per unit mass. The absorption coefficient, expressed in units of cm^{-1}, represents the loss of intensity in a beam as it travels a distance ds, i.e. $\mathrm{d}I_\nu = -\alpha_\nu I_\nu \,\mathrm{d}s$ (see e.g., Rybicki and Lightman, 1979).

When dealing with fluid media it may be convenient to use the monochromatic[1] spontaneous emission coefficient j_ν which has units of erg cm^{-3} s^{-1} ster^{-1} Hz^{-1} instead of the mass-dependent emission coefficient. The two quantities are related by:

$$j_\nu = \frac{\epsilon_\nu \rho}{4\pi} \tag{3.8}$$

Where ρ is the mass density of the emitting medium. From the emission coefficient it is possible to obtain the emitted energy by integrating $\mathrm{d}E = j_\nu \,\mathrm{d}V \,\mathrm{d}\Omega \,\mathrm{d}t \,\mathrm{d}\nu$. We can express Kircchoff's Law in his common form:

$$j_\nu = \alpha_\nu^{abs} B_\nu(T) \tag{3.9}$$

For microscopic particles with number density n and effective cross section σ_ν, it is customary to relate the coefficient $\alpha_\nu = n\sigma_\nu$. For dust grains specifically it is common to write the effective cross section σ_ν as a function of the geometrical cross section $\sigma = \pi a^2$ (a being the grain radius):

$$\sigma_\nu = Q_{\nu,em}\sigma = (Q_{\nu,abs} + Q_{\nu,scatt})\,\sigma \tag{3.10}$$

Where $Q_{\nu,em}$, $Q_{\nu,abs}$, and $Q_{\nu,scatt}$ are the efficiencies for extinction, absorption, and scattering respectively. In the UV/optical, to first order $Q_{\nu,abs} \sim Q_{\nu,scatt} \sim 1$, in the IR, $Q_{\nu,scatt} \ll Q_{\nu,abs} \propto \lambda^{-\gamma}$ with $1.5 \leq \gamma \leq 2$ (e.g., Draine and Lee, 1984). Similarly, also the emission coefficient is composed of true emission and elastic scattering, i.e. $j_\nu = æ_{\nu,em} + j_{\nu,scatt}$. Both of these terms depend on the radiation field I_ν, scattering emission will depend on the incident radiation angle, and true emission will depend on the grain temperature.

[1] monochromatic refers to the fact that the quantity is wavelength-specific, i.e. the spontaneous emission coefficient j is simply given by $j = j_\nu \,\mathrm{d}\nu$

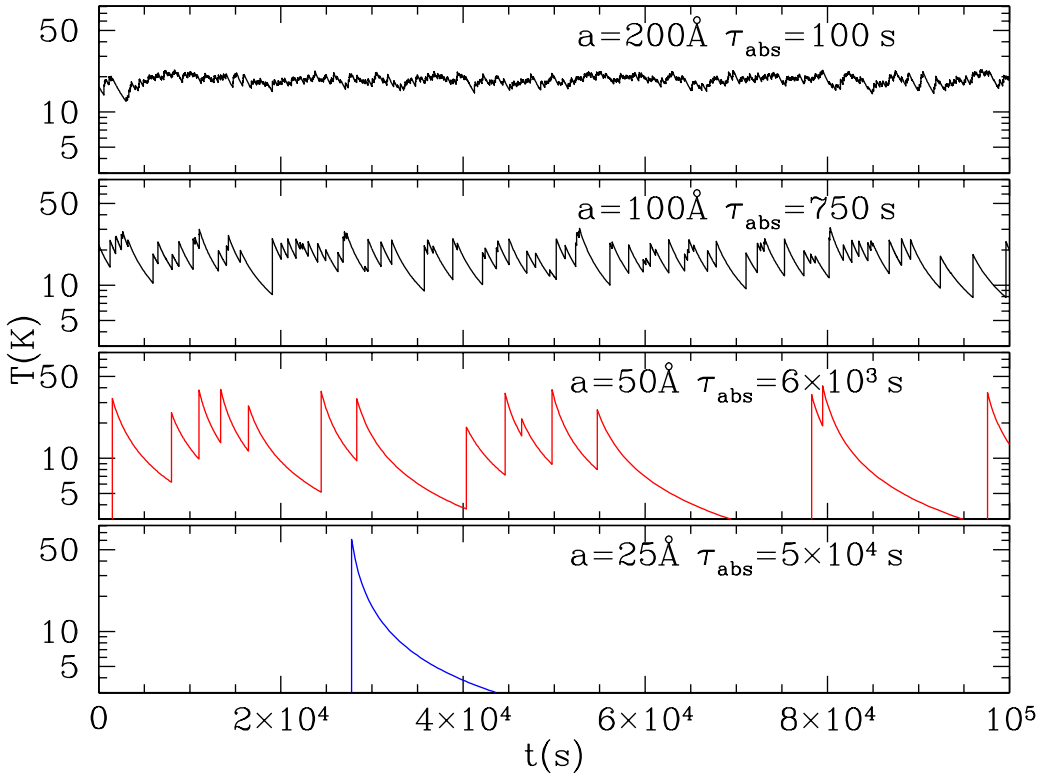

Figure 3.5: A day in the life of an interstellar grain: grain temperature vs. time for 4 grain sizes, for grains heated by the average interstellar radiation field. Grains with $a \gtrsim 0.02\mu$m have a nearly constant temperature, but $a \lesssim 0.01\mu$m grains show conspicuous increases in temperature following each photon absorption, with gradual cooling between photon absorption events. τ_{abs} is the mean time between photon absorptions. [From Draine (2004)]

It is then necessary to understand to what extent a dust grain is in thermal equilibrium with its radiation field. If the grain is relatively large, the grain will be bombarded and absorb more frequently individual photons than smaller sized grains, and it will be kept at its equilibrium temperature with the radiation. If the grain is very small, the time in between photon absorptions will be longer on average. Given their small size, small grains will have time to cool appreciably faster than large grains. Moreover, small grains, having low thermal capacity, will be heated to higher temperatures than larger grains after the absorption of a same photon. The Figure shows that such small grains will fluctuate more than large grains.

This reasoning applies to a population of grains large enough to be characterized by a single average temperature. The temperature of such large grains will be determined

by the energy balance equation:

$$\int_{\nu} Q_{\nu,abs} J_{\nu} \, \mathrm{d}\nu =_{\nu} Q_{\nu,abs} B_{\nu}(T) \, \mathrm{d}\nu \tag{3.11}$$

Here the LHS is the absorption and the RHS the emission. We know that dust absorption is most efficient in the UV/Optical where $Q_{\nu,abs} \sim 1$, and that dust emission is most efficient in the IR where $Q_{\nu,abs} \propto \lambda^{-\gamma}$. Approximating, it follows that the temperature depends on the radiation energy according to the proportionality relation $T \propto U^{1/(4+\gamma)}$. For the typical values of γ between 1.5 and 2, it would take a 60-fold increase in radiation energy to double the grain temperature.

Smaller grains whose temperature decreases appreciably in between photon absorption will require a distribution function to describe their spread in temperature. In calculations, instead of a single Planck function, a population of small grains will be described by the integral $\int_{T_{min}}^{T_{max}} B_{\nu}(T_d) P(T) \, \mathrm{d}T$ where $P(T)$ is a probability function obtained e.g. in Guhathakurta and Draine (1989), to account for the temperature distribution of small grains.

Figure 3.5 from Draine and Li (2001) helps us determine where to draw a rough grain size separation between grains sufficiently large to remain in thermal equilibrium with the radiation, or small to the point that they require a temperature distribution function. The calculations assume carbonaceous grains, but similar behaviors hold for other dust species, e.g. silicates. The temperature distribution function is presented in Draine and Li (2001). The figure plots grain temperature vs time for 4 grain sizes subject to an average interstellar field. Up to 0.01μm, amid fluctuations, the grain temperature is sufficiently stable to approximate it to a constant. Grains of 50Å or below, however, may cool substantially before the next photon heating.

3.3.0.0.1 Luminescence Thermal radiation, while vastly dominant, is not the only form of radiation which dust can emit. In environments such as reflection nebulae where starlight radiation is low and not sufficiently powerful to alter the state of the ISM, scattering cannot account for all the radiation emitted by dust in the wavelength range 6000 – 8000 Å, and Witt and Vijh (2004) identifies red luminescence as the suitable candidate for the excess emission. This luminescence ensues after absorption at shorter wavelengths. Blue luminescence has also been observed by Vijh et al. (2005). The authors suggest that neutral PAHs may be responsible for the blue luminescence and ionized PAHs for the red, but the source

has not been identified conclusively.

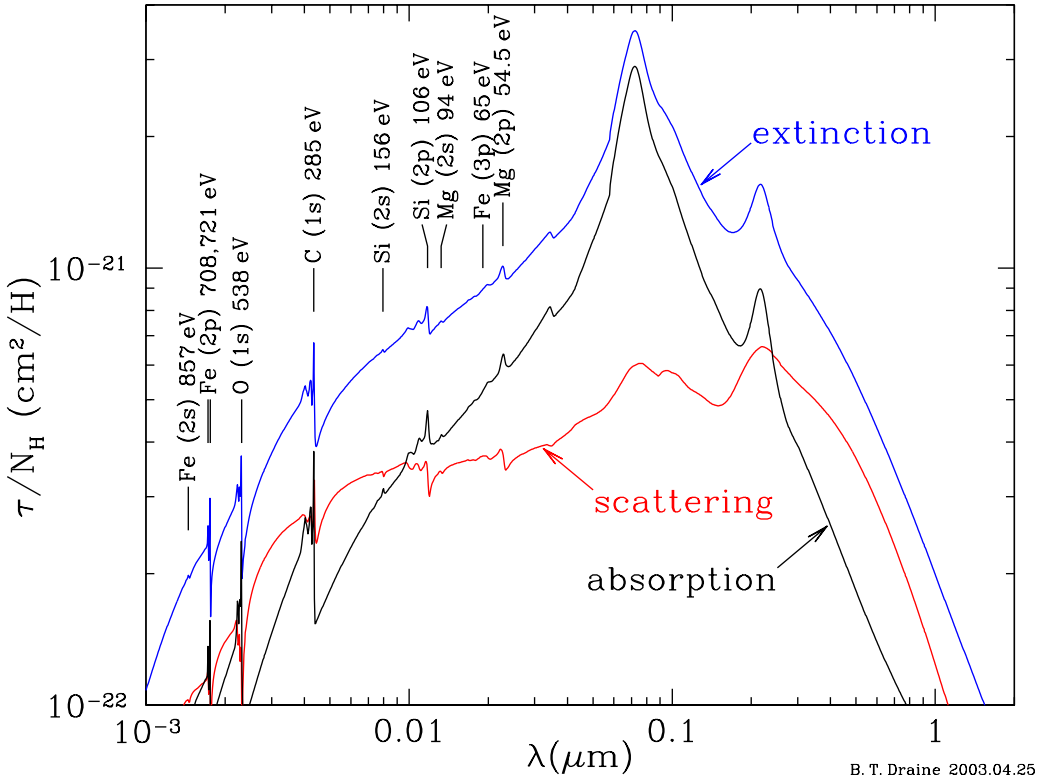

Figure 3.6: Extinction and scattering calculated for Weingartner and Draine (2001) with $R_V = 3.1$ for the Milky Way dust, with abundances reduced by factor 0.93 to match the MW reddening. [From Draine (2003)]

4

On Dust Evolution and its models

In this chapter we will explore the environments in which dust forms, evolves, and gets destroyed. Dust is injected into the ISM either by stellar winds or supernovae. Once it is spread into the ISM, dust evolves in parallel with the gas lifecycle: depending on the physical conditions of the gas phase, it will grow in mass and size, or disintegrate at different rates. Dust will grow rapidly within clumps of molecular clouds, the cradles for newly formed stars. While they reside in molecular clouds, dust grains can agglutinate into larger structures, in a process commonly known as coagulation. Gas-phase species will also aggregate on top of grain surfaces, hence contributing to the dust mass growth. This process is known as accretion. In low density regions characterized by high temperatures or highly energetic photons and ions, dust will not survive long. We will examine collision or erosion processes which either disrupt or destroy the grain. Notable are shattering, or a grain-grain fragmentary collision, SN explosions, and sputtering. Lastly, we will present a dust evolution model which simplifies the grain size distribution to a binary, while still providing reliable results. This is the model which inspired the work we developed during the PhD program, presented in the next chapter.

4.1 Production

Freshly produced gas-phase metals reside mainly around certain star envelopes or in SNe remnants. Dust forms in the proximity of such environments. The original grain seed forms in a self-assembly process, known as nucleation. Nucleation rates will depend on the monomer saturation of a given dust species, as well as its gas density and temperature. Examples of grain nucleation are derived in Krügel (2008), Section 7.5. The grain nucleation calculations must consider both physical clustering and chemical reactions, which form strong valence bonds (e.g., Salpeter, 1974). Being a stochastic process, nucleation usually generates highly disordered seeds. However,

crystalline structures may form for species capable of forming at high temperatures (Nuth, 1996).

Around the early 60s it was verified that the medium in the vicinity of stars is a viable site for grain nucleation (for graphite and silicate grains respectively, Hoyle and Wickramasinghe, 1962; Kamijo, 1963). It was found that stars with surface temperatures below 3600 K may produce dust in the outskirts of their circumstellar envelopes. Therefore, red supergiants, some red giants, and especially Asymptotic Giant Branch stars (AGBs) have been investigated as primary contributors to the dust enrichment (Figure 4.1). AGBs are now known to be one of the major dust contributors, aside from SNe remnants. AGBs are particularly important in the production of carbonaceous dust. While AGBs take longer than SNe to enrich the metallicity of the medium, by present time they are the greatest contributors to the carbon budget (Zijlstra, 2006).

Dust will begin to form at a certain distance from the star's cold surface. In the chromosphere, or the closest circumstellar layer to the star, temperatures may rise for red giants to $\sim 10^4$K as the density drops to 4 dex lower than the star's surface (Gail and Sedlmayr, 1987). From there on out however, temperature decreases monotonically with radius (e.g., Glassgold et al., 1996). Closest to the star, gas-phase molecules will form first. Eventually also dust is formed when the temperature falls below the condensation threshold of a given dust species. If for example a species condensates at 1000K, Bode (p. 73, Bailey and Williams, 1988) found that dust may form at a distance 10 times the star radius. The outer boundary where the stellar atmosphere dilutes into the ISM extends to 10^4-10^5 times the star radius. However, as dust production also depends on the dilution of its monomers into the gas, dust production will be most significant closer to the star, in shells whose temperature is below the condensation threshold, where the number density of the gas is higher. A schematic representation is shown in Figure 4.2.

4.1.1 Production by AGB stars

AGBs are Red Giants in the final stages of their evolution, whose mass falls in the range $0.8 \lesssim m \lesssim 8M_\odot$. They are typically long-period variables with pulsation timescales between tens of days to a couple of years. The shocks generated during this pulsation instability, paired with the radiation field of the stars, induce significant mass losses over the course of the AGB lifetime. In the cooling winds that ensue these episodes, gas-phase molecules will form first, followed by dust (Molster

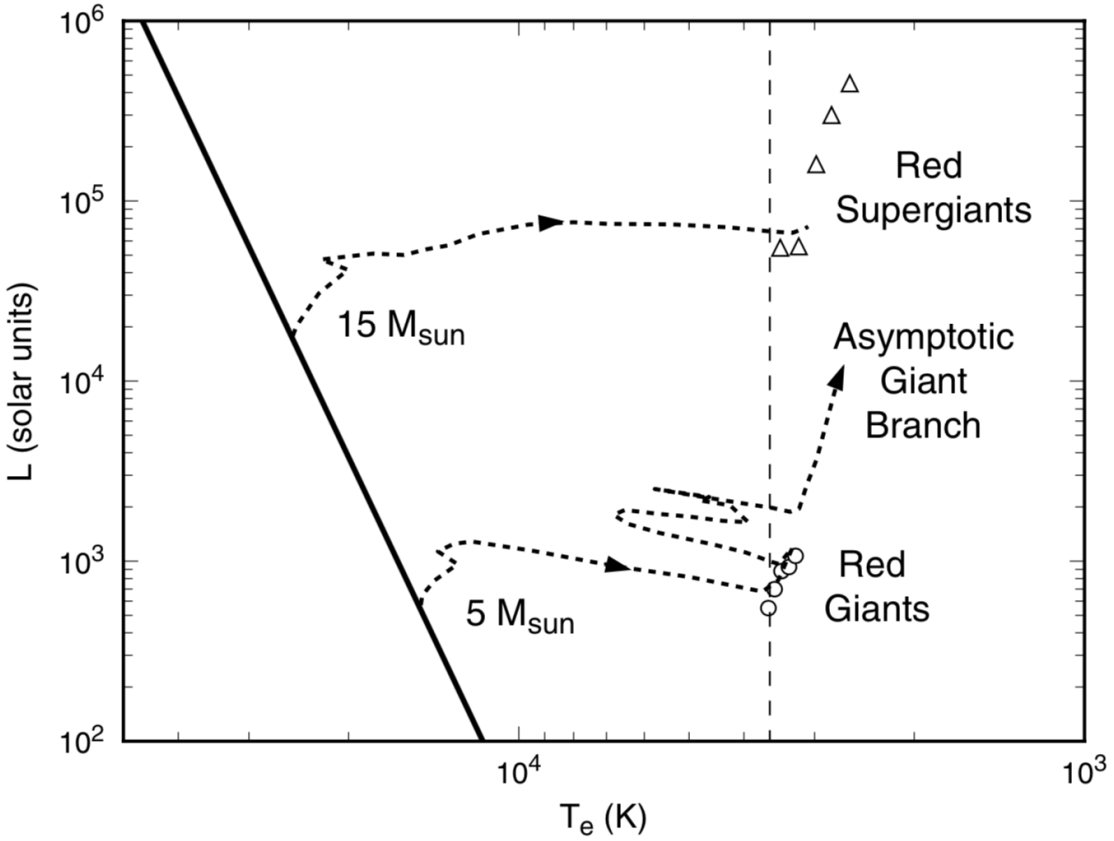

Figure 4.1: From Fig 7.1, Whittet, 2003. Hertzsprung–Russell diagram. The solid diagonal line represents the main sequence. The two evolutionary tracks follow post-main-sequence stars of 5 and 15 $M_\odot$ (from Iben, 1967). Circles indicate the average position of red giants (circles) and supergiants (triangles) in the Milky Way. The vertical dashed line marks the temperature of 3600K. Stars below this temperature may produce dust. Red Giants fluctuate to high temperatures so their radiation destroys most of the newly formed dust. AGBs are the primary dust enrichment channel of the three.

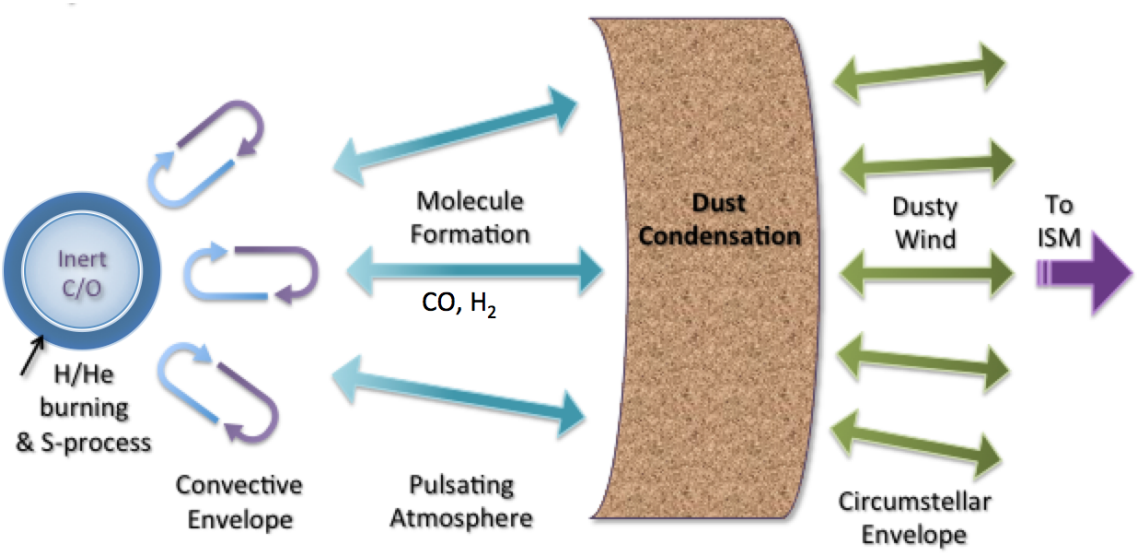

Figure 4.2: AGB structure. ©Martha L. Boyer, NASA's Goddard Space Flight Center (2014) adapted from J. Hron, University of Vienna (2012)

et al., 2010). Aside from yielding most of the carbon in the Universe as previously stated, AGBs may also produce silicates, never simultaneously to carbonaceous dust (e.g. Zhukovska et al., 2008).

An AGB is made up of a degenerate inert carbon-oxygen core, enveloped by a thin Helium shell, and finally a hydrogen convective envelope. Most of the time, known as intershell period, the emitted luminosity of the AGB originates from the H-burning shell. Periodically, the helium shell will ignite, but as the He burning is unstable, it will cause thermal pulses in the interior of the AGB. Over the course of this process, new carbon is produced. The mass loss rates can be as high as $10^{-5} M_{\odot}$ yr^{-1} (Karakas, 2011) during helium burning. Mixing, known as third dredge up (TDU), follows the helium burning and carries the yields, mostly carbon, to the atmosphere. This causes the inversion of the C/O ratio. AGBs will instead produce silicates during the hot bottom burning phase (HBB), activated when the temperature at the bottom of the hydrogen envelope reaches 4×10^7K (García-Hernández et al., 2013). HBB AGBs will mainly produce silicates, and some oxides (Ventura et al., 2012).

4.1.1.1 C/O ratio

Whether an AGB produces carbonaceous or silicate dust depends on which yield is more prevalent between carbon and oxygen. The least abundant element will be saturated in CO molecules, because the CO binding energy is exceptionally high

(11.1 eV). The remaining excess element will be free to combine into dust or enrich the gas metallicity. This is easily summarized in what is known as the Carbon-to-Oxygen (C/O) ratio (e.g. Dwek, 1998).

If there is a Carbon number excess, or $C/O > 1$, carbonaceous dust will form, which takes mainly the form of amorphous carbon, graphite, and Polycyclic Aromatic Hydrocarbons (PAHs). This C/O ratio is prevalent in stars within the mass range $\sim 1.5 - 4M_{\odot}$ (Gail et al., 2009). If Oxygen is in excess, i.e. $C/O < 1$, then silicates (and in minor part, oxides) will dominate the newly produced dust. A C/O ratio < 1 is typical of M-type stars and OH/IR AGBs, stars bright in the NIR with spectroscopy signatures rich in OH radicals.

4.1.1.2 O-rich Stars

The most important monomers that lead to the production of non-carbonated dust (e.g., Gail et al., 2009) are Fe, Mg, SiO, and H_2O. Ices require sub-200 K temperatures. With temperatures of 700 K or below, the majority of the metallic elements will have condensed into dust. Most of the silicate condensation occurs at temperatures between 800 and 1200 K. At temperatues above 1500 K the above monomers are in the gas-phase, but some resilient (called refractory in literature) oxides such as Al_2O_3 and $CaTiO_3$, or tungsten, can condense already (Whittet, 2003). While they contribute little to total dust mass, they may provide the starting seed for nucleation (Onaka et al., 1989). Grains formed around these stars will therefore have a layered structure, formed progressively as the winds cool. Around minor oxide seeds, silicates mainly composed of O, Si, Mg, and Fe will form. A thin layer of ices will coat the grain, but the ice will survive only in protoplanetery systems or molecular clouds. A stable temperature-pressure phase diagram for species formation for oxygen-rich stars is shown in Figure 4.4a. The arrow indicates a typical cooling flow for a red giant or AGB. Silicates form below the bold dot-dashed curve. CO is stable above the thin dotted curve. Temperatures for the formation of ices, iron oxide, and serpentine (a hydrous silicate) are relatively invariant with pressure. Below the + curve for iron oxide, iron can be incorporated into silicates.

Spectra of O-rich AGB stars, planetary nebulae, and other evolved bodies (like luminous blue variables) confirm this composition. In fact, a common feature of all these stars are broadless, structureless bands at 10 to 18 μm (Henning, 2010), which are associated with amorphous silicates. Laboratory spectra of olivine-like compounds, $(MgFe)_2SiO_4$, fit these features well (Dorschner et al., 1995). It is

important to note that, in order to reproduce these features, the dust species must contain iron (Nanni et al., 2016).
Narrow features around 20 and 70 μm could also be caused by olivines and pyroxenes (Jaeger et al., 1998; Molster et al., 2002). Each star however manifests significant variability in the detailed chemical composition, grain size, or morphology. Crystalline silicates have been detected for the first time (Waters et al., 1996) thanks to the spectroscopic breakthroughs of the Infrared Space Observatory (ISO), but they make up only about 10-15% of planetary disks, and survive even less in diffuse environments. Crystalline silicates are generally iron-poor (Molster et al., 2010), but amorphous silicates contain Fe either within its chemical makeup (Dorschner et al., 1995) or in the form of metallic iron, clumped to Mg-rich silicates (Ossenkopf et al., 1992). The increased sensitivity provided by the Spitzer Infrared Telescope allowed for dust spectroscopy around evolved stars to be extended to the Large and Small Magellanic clouds (Kastner et al., 2006; Sloan et al., 2008). In Bressan et al. (2006), the authors took advantage of Spitzer to detect silicate features due to AGB stars in the integrated light of Elliptical galaxies.

Olivines, pyroxenes, crystalline or amorphous silicates Crystalline olivines are rhombic systems whose elemental cell is characterized by $[SiO_4]^{4-}$ interlocked anion tetrahedra linked by divalent cations of either magnesium (Mg_{2+}) or iron (Fe^{2+}). The general formula is $Mg_{2x}Fe_{2-2x}SiO_4$, with x between 1 and 0. The mixture of Mg and Fe can vary. Some treat olivine as a solid solution of Mg_2SiO_4 and Fe_2SiO_4.
Pyroxenes form as chains of $[SiO_3]^{2-}$ anion tetrahedra. The silicon atom is shared between two tetrahedra, while the oxygen triplet bonds with Mg or Fe so that these cations act as links for the tetrahedra chain. The general formula is $Mg_xFe_{1-x}SiO_3$, with x again between 1 and 0. Lattice sheets of silicates can only form in aqueous environments so they are out of the scope of this thesis. For a complete overview, consult Henning (2010).
Amorphous silicates, while sharing the basic structural units with crystalline silicates, form in a 3D disordered network. The incorporation of the Mg or Fe cations or other impurities disrupts some of the oxygen bonds, leading to broader spectral features. Sometimes, Mg^{2+} can replace silicon in the SiO_4 tetrahedron. From calculations of a stationary planetary disk model, Gail (2004) found that most of the crystalline silicates will form under 10AU from the star, and that out to 100AU, silicates will be completely amorphous. 90% will be olivine/pyroxene in a ratio

roughly 3:1, and the rest will be amorphous quartz, or SiO_2 (see Figure 4.3). We can expect this composition to be the one enriching the diffuse ISM with the original dust grains which will undergo growth processes (see Section 4.3.1).

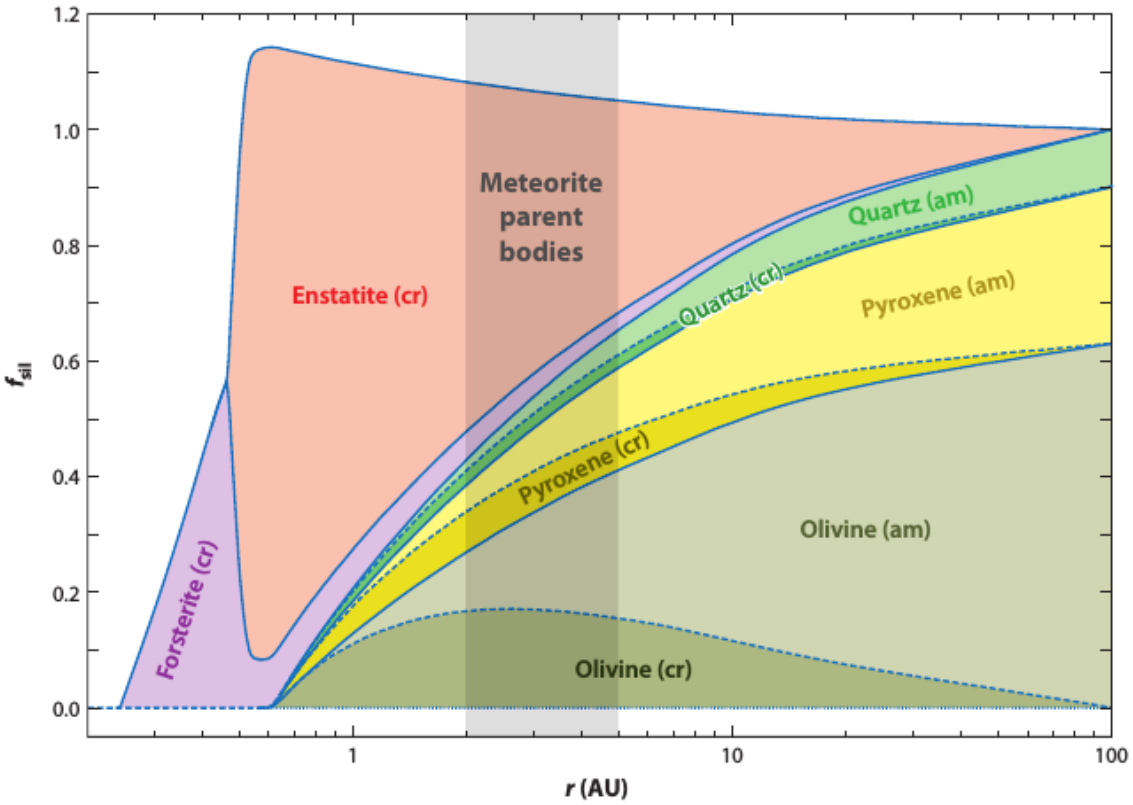

Figure 4.3: From Henning (2010), it represents the abundance profile of the major silicate species for their model of a stationary protoplanetary disk. Amorphous olivine and pyroxine prevail in the outskirts of the system and are likely the species to be injected into the diffuse ISM.

4.1.1.3 C-rich Stars

In Carbon-rich stars (C-stars), most of the oxygen is locked into CO molecules above the pressure-temperature threshold, as marked with the faint dotted curve in Figure 4.4b. The most common monomers produced around red giants and AGBs are C, C_2, C_3, C_2H_2 (acetylene), and CH_4 (e.g., Whittet, 2003). In the figure, the species names are located in the regions where they are most likely to form. C-rich stars are quite common. They derive from red giants of mass smaller than $4M_\odot$, and account for $87\% - 89\%$ of the total dust output from cool evolved stars (Boyer et al., 2012). While Spitzer observations of SMC/LMC stars suggested a dust-to-gas ratio of 0.005

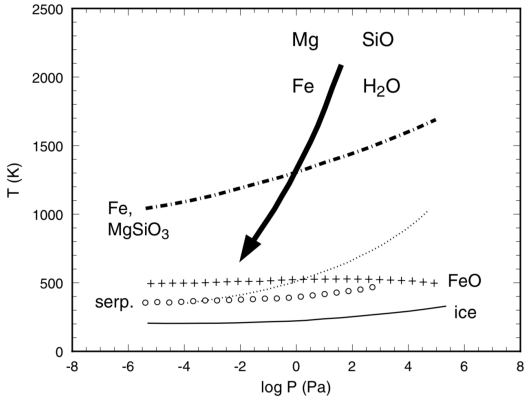

(a) Temperature–pressure phase diagram illustrating stability zones of major solids in an atmosphere of solar composition (adapted from Salpeter, 1974, 1977; Barshay and Lewis, 1976). Above the thin dotted curve, gas-phase CO is stable and essentially all the carbon is locked up in this molecule. The most abundant gas-phase reactants that lead to the production of solids are Mg, SiO, Fe and H2O. The curved arrow indicates the variation in physical conditions that may occur in the outflow of a typical red giant. Magnesium silicates and solid Fe condense below the bold dot–dash curve. At much lower temperatures, Fe is fully oxidized to FeO (below the curve marked +++) and may then become incorporated into silicates. Hydrous silicates such as serpentine are stable below the curve marked ∘ ∘ ∘. Finally, H2O-ice condenses below the continuous curve.

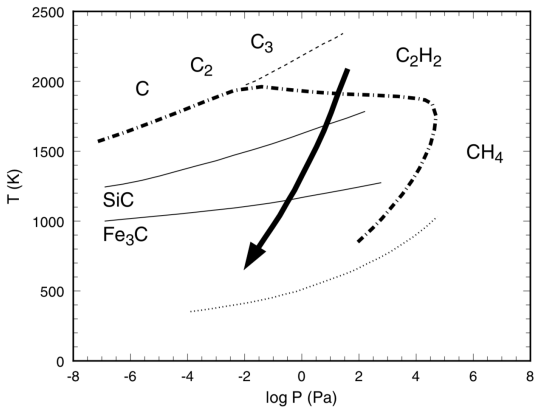

(b) Temperature–pressure phase diagram illustrating stability zones of solids in a C-rich atmosphere (adapted from Salpeter, 1974, 1977; Martin, 1978). Solar abundances are assumed except that the abundance of carbon is enhanced to exceed that of oxygen by 10%. Above the dotted curve, gas-phase CO is stable and essentially all the oxygen is locked up in this molecule. Other gas-phase carriers of carbon (C, C2, C3, C2H2, CH4) are most abundant in the regions labelled. The curved arrow indicates the change in physical conditions associated with a typical outflow from a red giant. Solid carbon is stable in the region enclosed by the bold dot–dash curve. Condensation curves for the carbides SiC and Fe_3C are also shown. The broken line above the centre represents the probable condensation curve for a hydrogen-deficient atmosphere in which C, C_2 and C_3 rather than C_2H_2 are the primary monomers.

Figure 4.4: As it appears in Whittet (2003)

(e.g., Groenewegen et al., 2009), Nanni et al. (2018) found via SED fitting that the range of possible dust outputs are wider, depending on the AGB type. A value of 0.005 represents an upper limit for carbon stars in the VizieR Online Data Catalog of SAGE SMC evolved stars candidates (Srinivasan et al., 2016), with a AGB-type-dependent lower limit up to 5 times smaller. In hydrogen-poor atmospheres, like for

the star R Coronae Borealis, C_2 molecules may assemble into hexagonal ring clusters, nearly devoid of hydrogen. The grains will nonetheless trap metal condensates from the other elements yielded by the stars. SiC and Fe_3C may act as nucleation centers for grain condensation (Frenklach and Feigelson, 1989; Martin, 1978), but oxides and silicates will not form, due to the absence of oxygen trapped in CO. Yet, crystalline silicates are sometimes observed around carbon stars (Waters et al., 1998). They are environmental contaminants of the C-star's previous evolutionary phase as M star (Vollmer et al., 2008).
For stars that are not severely hydrogen-depleted, acetylene is the main species to form, especially around red giants.

Polycyclic Aromatic Hydrocarbons (PAHs) Frenklach and Feigelson (1989) found that the kinetic motion in red giants would lead to the formation of hexagonal carbon rings known as Polycyclic Aromatic Hydrocarbons (PAHs). The 6 carbons are connected by alternating double and single bonds, and hydrogen atoms bond with any remaining valence electron around the rings. In order for these structures to form from acetylene, the hybridization of carbon atoms must change. In fact, carbons in acetylene share a triple sp bond with each other, and a single bond with hydrogen. If an hydrogen atom reacts with acetylene to form a hydrogen molecule, the radical C_2H (with double carbon bonds of sp^2 hybridization) may form (Tielens, 1990). This radical is the unit necessary to form a stable aromatic ring. Rings may grow by annexing more acetylene molecules in the place of hydrogen atoms, eventually forming planar multi-ringed PAH molecules. As the sites of PAH formation will be rich in other metals, non-aromatic units will bond with the growing structure (Duley and Seahra, 1998). Therefore, instead of regular structures, also PAHs are likely to grow into amorphous carbon dust.

4.1.2 Production by Supernovae

Supernovae are some of the most important dust production events, primarily for silicates. However, given the large range of physical conditions affecting chemical processes in various supernovae types, dust production mechanisms are still unclear (Sarangi et al., 2018).
For example, pair-instability SNe are thought to be among the first enrichers of the universe, believed to be common among Pop III and II massive ($> 100 M_\odot$) stars (e.g., Fryer et al., 2001). Using a chemical kinetic model, Cherchneff and Dwek

(2009) predicts a dust mass production of 0.1 $M_\odot$ per pair-instability SNe.

Core-collapse SNe Core-collapse SNe occur when electron degeneracy pressure cannot support the mass of a star core, once it exceeds the Chandrasekhar's mass limit of 1.4 $M_\odot$. Most Core-collapse SNe contain hydrogen in their spectra, they are therefore classified as Supernovae Type II (SNII) (Filippenko, 1997). But also Type Ib/c, while devoid of H, go supernova via the core-collapse mechanism. These supernovae originate from massive stars ($> 25M_\odot$) stripped of their outer shell hydrogen. There are numerous examples of dust production in Type Ib/c, the first of which was observed by Elmhamdi et al. (2004). These SNe manifest dust within 50 to 500 days post explosion, depending on the cooling rate of the remnant (Nozawa et al., 2008; Kankare et al., 2014). Their dust yield is quite high, 1.5 $M_\odot$ in the case of Type Ib SN2006jc, up to 0.7 of which is carbonaceous and at least 0.5 a mixture of silicates and oxides (Nozawa et al., 2008). The must abundant SNII type in the local universe is Type II-P. With progenitor's mass in the range $8 - 25M_\odot$, their massive ejecta travel slowly and are rich in gas metals and dust (Szalai and Vinkó, 2013).
There are specific SNII that have been very well studied by several groups in literature. SN 1987 A in the LMC, for example, is the first case in which newly formed dust was observed in a supernova remnant (Danziger et al., 1989). Kozasa et al. (1989) approached the famous SN with classical nucleation theory so to understand its dust ejecta. From their work, they concluded that at least one third of all the SN yields must have gone into dust. The species they identified were Mg_2SiO_4 (forsterite), Fe_3O_4, and Al_2O_3, with forsterite averaging the grain size of 1 μm and the other two oxide 0.1 μm. Of the $0.23M_\odot$ dust mass formed in SN 1987A, forsterite is the must abundant with a fraction larger than 0.8.

SN Ia Type Ia Supernovae (SNe Ia) are thermonuclear explosions of low mass stars ($< 8M_\odot$) whose spectra contain singly ionized silicon but no hydrogen. Clayton et al. (1997) claims that the isotopic C and Si composition of contaminated silicon carbide extracted from meteorites is characteristic of SNe Ia yields, as well as the relative abundance of N, Mg, and Ca, and of C/Si isotopes. Hence they suggest that dust may form in these type of SNe. According to, Nozawa et al. (2011), while it's true that SNe Ia may yield dust in the range of 3×10^{-4} to $0.2M_\odot$, dust will not survive until ISM injection, due to the powerful reverse and forward shocks of SNe Ia. In their model, gas temperature evolves with time. A combination of drag forces and

erosion due to inertial sputtering (see Section 5.2.4.7) destroys all the dust. Gomez et al. (2012), however, has managed to observe dust around two SNe Ia Milky Way remnants, Tycho, at a 3kpc exploded in 1572, and Kepler, at 6 kpc exploded in 1604. It remains to this day the only observational evidence of dust production by SNe Ia. The SNe yielded respectively a high dust mass production of 8.6 and $\sim 3.1 \times 10^{-3} M_{\odot}$. The authors used *Herschel* PACS and SPIRE photometry. In this thesis we adopted a conservative approach akin to Dwek (1998). We assumed that dust production and condensation efficiency of various dust species follow the same trends of SNII dust formation.

4.1.3 Other sources

Grain production generally co-occurs with gas-phase metal production. Stars that yield new metals may form at least trace amounts of dust. It is therefore necessary to investigate any metal-producing star type as plausible candidate for dust enrichment. This includes red supergiants and Wolf-Rayet stars. However, recent measurements show that neither of the two types contributes significantly to the total dust budget. For example, Boyer et al. (2012) estimated that the dust injection rate of Red supergiants is 10 times lower than AGBs or SNe.
Wolf-Rayet stars (WRs), despite being some of the hottest stars in existence, do produce dust far away from their surface, when their radiation field is sufficiently diluted. One example of stars harboring dust are Carbon-type WRs. They were the first among WRs to be observed (Allen et al., 1972). Their rate of dust injection is expected to contribute even less than red supergiants to the ISM dust enrichment. Breysacher et al. (1999) found, by observing 134 Wolf-Rayet stars in the Small Magellanic Cloud (SMC), that the gas input rate of these massive stars is less than $10^{-3} M_{\odot}$ yr^{-1}. Williams (2011) estimated a lower amorphous carbon grain mass of $1.5 \times 10^{-7} M_{\odot}$ yr^{-1} surrounding the Wolf-Rayet star (HD 36402) in the Large Magellanic Cloud (LMC). In comparison, SNe range well above $10^{-2} M_{\odot}$ yr^{-1} (Matsuura et al., 2011).

4.2 Grain-grain interactions

Dust will be subject to a variety of disruptive processes when it undergoes grain-grain interactions. For example, Borkowski and Dwek (1995) differentiates impinging projectiles causing grain erosion (a case of sputtering) from the partial grinding

(vaporization) of a sizable chunk of grain (cratering), and from the catastrophic fragmentation of the whole grain (shattering) (Figure 4.5a).

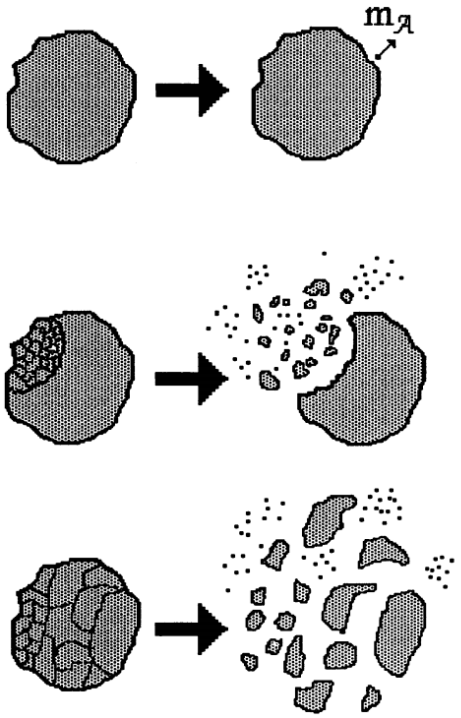

(a) From Borkowski and Dwek (1995): A schematic representation of the grain-grain processes considered in their model. From top to bottom, sputtering, cratering, and and catastrophic fragmentation (shattering). A similar approach with different formulation is considered in Hirashita and Yan (2009).

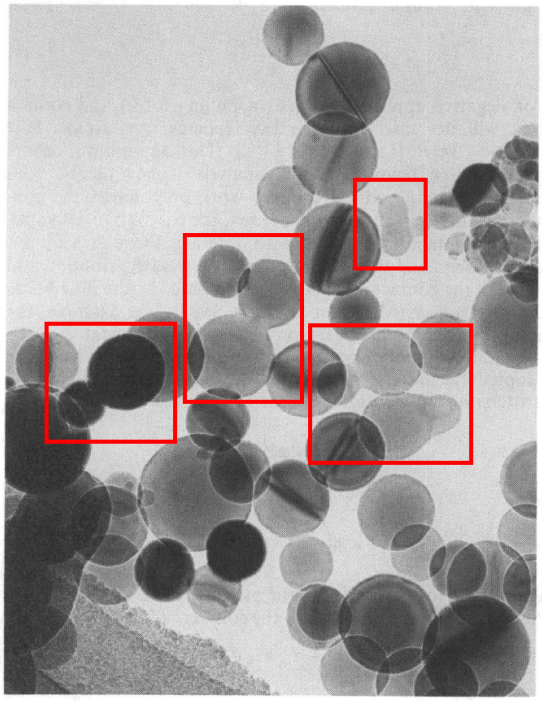

(b) From Iijima (1987): Electromicrograph showing coagulated spherical Si particles, fabricated in a laboratory by a gas evaporation method. A typical grain has a diameter of 0.07μm. There are multiple cases of *coagulation* occurring in this image.

On the other hand, laboratory experiments, e.g. Iijima (1987), found that silicate spheres prepared with a gas evaporation method stick readily to each other in small ($< 0.1\mu$m) filaments like "pearls on a string". They are examples of coagulation, or sticking of low-velocity grains to each other (Figure 4.5b). The process was studied in detail by Hertz in the beginning of the 19th Century. Low impact collisions deform the grains in the region of contact, where van der Waals or chemical forces bind the two grains, which in the presence of ice, grain growth of volatile molecules, and more coagulation, stabilize them into larger grains (Tielens, 1989).
Similar structures are observed in extraterrestrial chondritic (stony, not melted, or otherwise not differentiated from the parent body) porous interplanetary dust particles retrieved in Antarctic ice and snow Noguchi et al. (2015), regarded as

possible candidates for cometary dust (Bradley and Dai, 2004), and whose high deuterium enrichment suggests formation in molecular clouds ($T < 20$K).
Temperature and density conditions we will see are important determining factors in the prevalence of one phenomenon or the other, as the processes are highly sensitive to the impact velocity of grains, and hot diffuse gas is conducive to high velocities (Yan et al., 2004) as opposed to cold dense clouds where there is no significant source of momentum gain.
In this thesis we will follow a modeling of grain-grain processes that distills them into the two dominant ones: shattering and coagulation. We shall assume that grains are spherical.
We present in advance the general collisional timescale for the two processes, as it appears in Aoyama et al. (2017):

$$\tau_{coll} = \frac{1}{\sigma v n_d} \tag{4.1}$$

Where $\sigma \simeq \pi a^2$ is the collisional cross section, v is the typical velocity dispersion, $n_d = \mathcal{D}\mu m_H n_H / \frac{4}{3}\pi a^3 s$ is the number density of gas grains, with s being the material density of dust, $\mu = 1.4$ the mean weight of gas particles per hydrogen atom, and m_H and n_H the hydrogen mass and hydrogen gas density respectively. In τ_{coll}, the gas and hydrogen number density are assumed to coincide. $\mathcal{D}$ is the dust-to-gas ratio, later referred to as DtG. This all leads to:

$$\tau_{coll} = \frac{\frac{4}{3} a s}{v \mathcal{D} \mu m_H n_H} \tag{4.2}$$

When deriving the timescales τ_{sh} for shattering and τ_{co} for coagulation, we will assume characteristic values for the parameters, representative of each process as explained in these next sections. This parameter is simply the coefficient by which we will divide a dust mass to obtain its rate of change due to the given process (See the last section).

4.2.1 Shattering

Inspired by fragmentation theory on asteroids, Biermann and Harwit (1980) proposed that also the grain distribution of dust in the ISM may undergo a similar fragmentation due to high velocity particle-particle collisions. Tielens (1989) found that grain disruption starts at velocities as small as 10 km s^{-1}. We call this process shattering. Shattering affects the continuous spectrum of grain sizes, but it is more

efficient on grains of larger size (Hirashita, 2010). As we have mentioned in section 1.1.2.5, the grain size distribution of the Milky Way and similar spiral galaxies follows roughly the MRN power law $\propto a^{-3.5}$ (Mathis et al., 1977). However, dust factories produce grains biased toward larger grains $\simeq 0.1\mu$m. This is confirmed observationally both within AGB envelopes and SNe remnants, as we have briefly seen in the previous section.

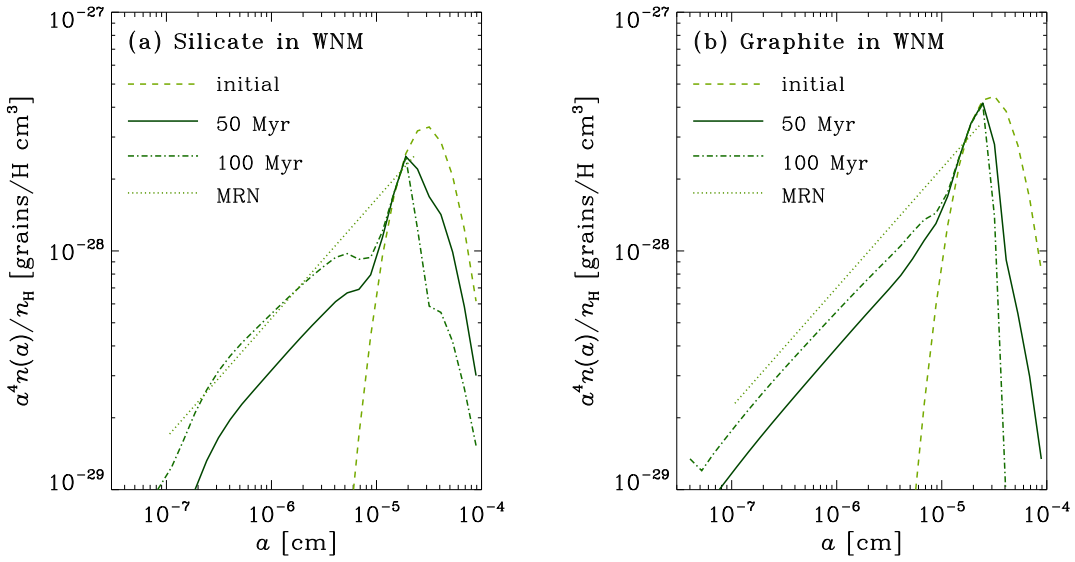

Figure 4.6: From Hirashita (2010). Based on the Hirashita and Yan (2009) dust evolution model, The grain size distribution (*y-axis*). The dashed "initial" line includes only dust production, skewed to larger grain sizes as per observations from Section 4.1. Solid and dashed-dotted line include shattering at 5×10^7 yr and 10^8 yr respectively for silicates (*left*) and graphites (*right*) in the WNM. The inclusion of shattering leads to MW-like curves as represented by (*MRN dotted curve*). The hotter WIM as shown in the paper increases the shattering efficiency up to a factor of 3 for sizes $< 0.1\mu$m. Larger grain sizes are not affected.

The evidence is both observational and theoretical. For AGBs, the evidence of larger sizes first came with Groenewegen (1997) who fitted the SEDs of 44 carbon Mira variables with a dust radiative transfer model. Hofmann et al. (2001) found greater variation of size distribution from a spectrograph of oxygen-rich AGBs, the distribution was close to MRN in their dust-shell modeling. Theoretical studies such as Winters et al. (1997) and Ventura et al. (2012) show that AGB stellar winds should produce dust of size $\gtrsim 0.1\mu$m. Another evidence in favor of larger dust species produced by AGB winds comes from silicon carbide. The isotope composition of this species suggests an AGB origin (Hoppe et al., 1994). From the analysis of primitive

meteorites (Amari et al., 1994), the SiC grain size is also high ($\gtrsim 0.1\mu$m). Grains larger than 0.3μm surprisingly very close to the grain surface, at twice the stellar radius, are also found around 3 extreme red giants, using polarimetric interferometry Norris et al. (2012). For SNe it is reasonable for only large grains to survive, as the reverse shock is most efficient at destroying smaller grains (e.g., Nozawa et al., 2007). Case studies confirming the hypothesis of SNII large grain size bias is found in Section 4.1.2.

Figure 4.6 represents the impact of a shattering model whose formulation is adapted from Jones et al. (1996). Only in warm diffuse media such as the warm neutral medium (WNM) and even better in the warm ionized medium (WIM) shattering is efficient. In these regions there is a compound hydrodynamic and electromagnetic effect. The drag of the warm gas increases the dust grain speed, but also electromagnetic fluctuations exacerbate the effect through resonant interactions (Yan et al., 2004). The WIM physical conditions are such that the timescale, or the parameter that governs the efficiency of a process, is as small as 10 million years (Hirashita et al., 2010). In the WIM, it is possible for PAHs to form, as the grain size distribution is bottom-heavy and exceeds MRN in the lower regimes. The H10 shattering equation treats the grain–grain collision rate and the redistribution of shattered fragments in the grain size distribution. H10 assumes that grains collide with each other under the velocity dispersion induced by dynamical coupling with interstellar turbulence.

4.2.2 Coagulation

Coagulation is the other grain-grain interaction considered in this thesis. Also this process acts essentially on the grain size distribution, and works in the opposite direction to shattering, i.e. it bonds smaller grains into larger ones. These two processes however work in mutually exclusive environments. As we've just seen, shattering is only efficient in warm to highly ionized hot media. Coagulation on the other hand occurs only in molecular clouds.

Chokshi et al. (1993) offers a detailed analysis of coagulation using elastic continuum theory on a variety of dust species: quartz, polystyrene (an aromatic hydrocarbon polymer), graphite, iron and ice. The most important parameter is the critical speed, which will be material-dependent. The dust species will affect the material elasticity as well as the interface energy for bonding. What does not cause significant changes is the sphericity of the grain, as it affects very little the efficiency of coagulation.

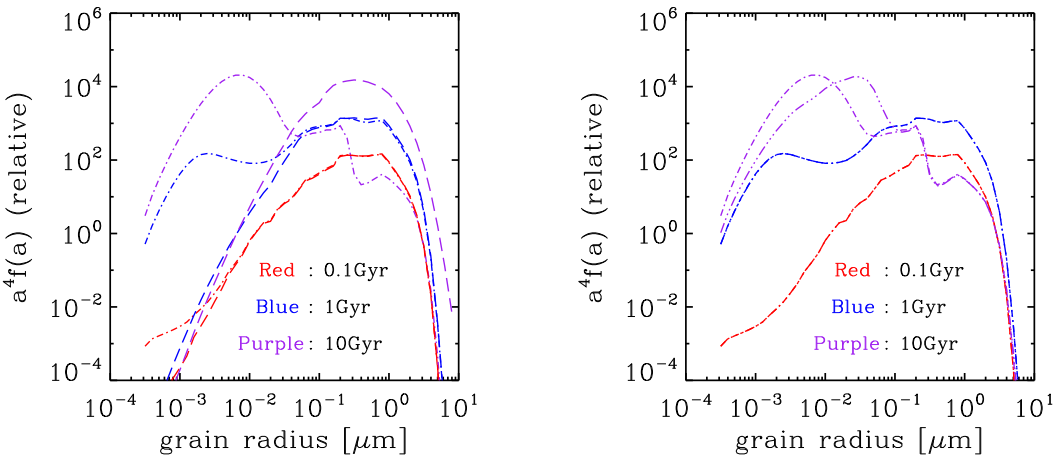

(a) The models turn shattering on (*dash-dotted lines*) and off (*dashed lines*). Coagulation is always off.

(b) The models turn coagulation on (*dashed-triple dotted lines*) and off (*dash-dotted lines*, identical to Fig. 4.7a). Shattering is included in all curves.

Figure 4.7: From Asano et al. (2013). The grain abundance as a function of grain size. The one-zone model treats dust evolution in MW-like galaxies. Both plots include dust production by stellar channels, dust growth in the ISM, and dust destruction by SN shocks. Curves are color-coded according to the age of the galaxy: red is the youngest at 100 Myr old, blue is at 1 Gyr, Purple is the oldest at 10 Gyr.

Sphericity is a handy assumption in deriving the process timescales. Chokshi et al. (1993) has found that the sticking efficiency increases by at least a factor of 3 if not more for graphites and quartz (a crystalline silicate) in the presence of a thin ice mantle on top of the refractory core. This is a common occurrence for molecular gas grains whose average temperatures are 80 K (Table 1, Introduction, Krügel, 2008). Approximations and assumptions on grain size and material density simplify the Chokshi et al. (1993) coagulation timescale to Eq. 4.2 for velocities below the critical. We will assume a fiducial value of 0.1 km s^{-1}. Aoyama et al. (2017) explored a variation of this value, which does not affect the total dust mass production.

In Figure 4.7 we compare the effect of turning coagulation and shattering on and off within the comprehensive one zone spiral galaxy model Asano et al. (2013) which includes shattering, coagulation, accretion, SN destruction, and stellar winds. In 4.7a, the dashed curve is the lognormal dust production distribution for various time intervals from red, 0.1 Gyr, to purple, 10 Gyr. Shattering of the dash-dotted lines takes at least 1 Gyr to pile a bump of smaller grains of the same order to the

larger production bump. The bump peaks at a small size of $\sim 0.001\mu$m. After 10 Gyrs, smaller grains dominate by at least 2 dex over larger grains, and the grain size peak shifts to a larger $\sim 0.01\mu$m. Via the process of shattering, dust clusters and behaves differently in two size regimes. One roughly below 0.03 μm, and one above. Shattering is a disruptive process that, in a grain size distribution, drifts larger grain sizes to smaller ones. Below 0.03μm, shattering hardly has any such effect, therefore it is only efficient in regimes above this limit.
In Fig. 4.7b the model with shattering is reproduced again with dash-dotted line for the 3 galactic evolution times. In dash-triple dotted line we see how the model is affected by coagulation. The abundance of larger sizes ($> 0.2\mu$m) is never affected by coagulation. In the model in fact larger grains are coupled with larger-scale turbulence, causing them to gain high velocity dispersions above the critical velocity, hence halting coagulation. We also do not observe significant changes due to the coagulation contribution to smaller grains, as their abundance is low. At 10 Gyr, shattering has had the time to produce sufficient small grains to render coagulation effective, so coagulation shifts the peak of the small grain bump toward a larger size, still below 0.1μm. Here, the regime of coagulation efficiency is complementary to shattering. In fact, it is primarily grains at the $\sim 0.01\mu$m peak to drift to larger sizes and has negligible effects on larger grains.

4.3 Gas-grain Interactions

Atoms colliding on the surface of a grain may attach (adsorb) and may migrate on said surface, interacting with other atoms and desorbing. Gas-grain interactions are also another major source of mass growth, via the process of accretion, or the attachment of gas-phase molecules onto a grain surface. The process may be physical or chemical. The physical attachment requires binding energies < 0.1 eV and are driven by weak van der Waals forces (Whittet, 2003). The many lattice defects and impurities enhance the chemical reactivity of dust species (Duley and Williams, 1984). However, this approach to accretion modeling is not practical. We will next investigate an efficient way to model accretion while producing reliable results.

4.3.1 Accretion

Accretion is an important gas-grain growth mechanism that may increase by several factors the total dust mass, and it is often a necessary mechanism to describe high

redshift galaxies (Dwek, 1998; Zhukovska et al., 2008; Draine, 2009). It is the most efficient in dense regions, like molecular clouds. It consists in the deposition of gas-phase metals onto grain surfaces, hence enlarging thier size.

One of the best proofs for the existence of accretion consists in the flattening of the extinction curve in molecular clouds (Mathis, 1990; Cardelli et al., 1989), justifiable by a larger grain size in combination with significant depletion of gas-phase elements (Voshchinnikov and Henning, 2010). Also this depletion is consistently observed in molecular clouds (Savage and Sembach, 1996). In order for accretion to occur, naturally the ISM has to be fairly enriched with refractory metals (Draine, 2009). Volatile elements like nitrogen and oxygen may evaporate as quickly as they accrete, whether refractory elements (with a high condensation temperature) will survive beyond the cold molecular phase.

Whittet (2003) derives the timescale for accretion stating all the relevant assumptions, namely the kinetic temperature, density of the gas (Spitzer, 1978), the sphericity of the grain, etc.. The mean speed of a particle in a Maxwellian distribution of velocities is

$$\bar{v} = \left(\frac{8kT_g}{\pi m}\right)^{\frac{1}{2}} \tag{4.3}$$

where T_g is the gas temperature. As the principal adsorption concerns atomic hydrogen and the typical temperature of a molecular cloud is 80K (Table 1.1), equation (4.3) gives $\bar{v}_H \approx 1.4$ km s^{-1}.

Chokshi et al. (1993) finds that the shape of a microscopic dust grain does not affect significantly the grain-grain interaction, therefore it is safe to simply calculations by considering grains of spherical radii. The collisions per second of hydrogen atoms onto a grain of size a is given by $\pi a^2 n_H \bar{v}_H$, where n_H is the gas number density. The colliding atom may be accreted or returned into the medium, with accretion probability, the sticking coefficient, $0 \leq \xi \leq 1$. Therefore the accretion timescale, or its mean free time, will be given by the reciprocal of the number of atoms accreted per second:

$$t_{ad} = \frac{1}{\xi \pi a^2 n_H \bar{v}_H} \tag{4.4}$$

There is some debate on which value the sticking coefficient will take. The value depends on the chemical species on the surface of the dust, on environmental conditions and dust properties such as temperature. Some laboratory data suggest ξ

values not larger than 0.1 (Nagahara and Ozawa, 1996) this value is adopted by i.e. Nanni et al. (2016). Other works find that if the grain is amorphous, the sticking coefficient will $\xi \approx 1$ (Tielens and Allamandola, 1987).
Combining Equation 4.3 with the accretion rate equation we get:

$$\frac{\mathrm{d}m_d}{\mathrm{d}t} = \xi \pi a^2 n (8kT_g m/\pi)^{1/2} \tag{4.5}$$

Where this time n is the number density of a dust population of identical masses m. From here we can obtain the grain rate of growth:

$$\frac{\mathrm{d}a}{\mathrm{d}t} = \frac{1}{4\pi a^2 s} \frac{\mathrm{d}m_d}{\mathrm{d}t} \tag{4.6}$$

Where s is the density of the newly formed mantle. If the growth rate and s are constant with time, integrating Equation 4.6 gives $a = a_0 + \Delta a(t)$ where a_0 iss the seed radius. The thickness of the mantle will then be $\Delta a(t) = 0.4 \xi n s^{-1} (kT_g m)^{\frac{1}{2}} t$, which is independent of the grain radius. With time, all grains will grow mantles of equal thickness. Therefore, the dust mass growth will occur more efficiently on dust of smaller size. We will use this observation in the next chapter.

4.3.2 Destruction

As seen in the previous section, several studies confirm that grain-grain collisions are not a significant source of dust destruction, rather they mainly alter the grain size distribution. The major source of destruction is sputtering, or the collision of energetic particles with dust grains, slowly eroding the grain.
There are two forms of sputtering that concern dust, one non-thermal and the thermal. If the charged particles velocity follows a Maxwell-Boltzmann distribution, they are thermal. Otherwise they're non-thermal. Usually, warm/ionized diffuse gas (density ≤ 0.25 cm^{-3}, temperature $\geq 10^4$ K) is associated with thermal sputtering, whether SNae shocks are the major source of non-thermal sputtering. Thermal and non-thermal sputtering have characteristic velocities associated with each type, with thermal sputtering typically consisting of velocities above 150 km s^{-1} and non-thermal sputtering ranging $50 < v_{Non-Th} < 150$ km s^{-1} (Tielens et al., 1994). Sputtering will destroy dust, small grains more efficiently than larger, but will not contribute significantly to the production of smaller grains (with grain radius smaller than ~ 0.01 microns) from larger grains (Nozawa et al., 2006).
Physical sputtering generally refers to the process by which highly energetic ions

bombard a surface, in our case the grain's, to the point that the grain is eroded away. Electrons are not capable of transferring energy efficiently during collisions (Scalo, 1977) so they do not contribute to sputtering. Physical sputtering may be thermal or non-thermal. Thermal sputtering is driven kinetically by a hot gas, non-thermal sputtering occurs when dust and gas move rapidly with respect to each other (for a review, Dwek and Arendt, 1992). Sputtering may also be chemical, and consists in the gradual desorption of dust material from the grain surface in low velocity collisions with particular molecules (i.e. H_2). This is not a process we have considered in our present work.

4.3.2.1 Thermal sputtering

Hot ($> 10^5$ K) gas is a harsh environment for dust. Dust grains are subject to collisions with highly energetic photons, as well as Helium ions. From the computations first of Draine and Salpeter (1979) and then of Tielens et al. (1994), Tsai and Mathews (1995) adopted the analytic form of sputtering for both graphite and silicate grains:

$$\frac{\mathrm{d}a}{\mathrm{d}t} = -\tilde{h}\left(\frac{\rho}{m_p}\right)\left[\left(\frac{T_0}{T}\right)^{\omega} + 1\right]^{-1} \tag{4.7}$$

This rate equation computes how fast a grain size a diminishes with time as a function of gas density ρ and temperature T. The $\tilde{h} = 3.2 \times 10^{-18}$ cm^4 s^{-1} parameter depends on the grain density for grains and silicates. The equation is a well fit to these two main dust species when $\omega = 2.5$ and $T_0 = 2 \times 10^6$ K.
From Eq. (4.7) Tsai and Mathews (1995) extrapolated the sputtering timescale as:

$$\tau_{sp} = a\left|\frac{\mathrm{d}a}{\mathrm{d}t}\right|^{-1} \tag{4.8}$$

and therefore

$$\tau_{sp} = \tau_{sp,0}\left(\frac{a}{n_{gas}}\right)\left[\left(\frac{T_{sp,0}}{T}\right)^{\omega} + 1\right] \tag{4.9}$$

4.4 The Two-size approximation

To summarize the picture that emerges from the Asano et al. (2013) model, dust is originally produced by SNII and AGBs. The grain size distribution for production

Process	Small grains	Large grains	Total
Stellar ejecta	Δ	$\nearrow$	$\nearrow$
Accretion	$\nearrow$	Δ	$\nearrow$
Shock destruction	$\searrow$	$\searrow$	$\searrow$
Coagulation	$\searrow$	$\nearrow$	$\longrightarrow$
Shattering	$\nearrow$	$\searrow$	$\longrightarrow$

Table 4.1: From Hirashita (2015), a summary table of the processes involved in their model.

is high in the microns. When the system reaches a certain metallicity referred to as critical metallicity, shattering efficiently produces grains of smaller size. Small grains, having more total surface per unit mass, are efficient at accretion, which dominates mass growth beyond the critical metallicity. Coagulation shifts back the grains toward larger sizes.

The recurrent pattern in these processes is that each affects differently the two size regimes. There is no fixed limit that divides the two size populations, as it is dependent on parameter choices. However, the separation falls somewhere between 0.01 and 0.1 μm. With cosmological simulations in mind, Hirashita (2015) proposed an approximation (Table 4.1) to the Asano et al. (2013) model. He questioned whether a binary discretization of grain sizes could reproduce statistical properties of galaxies.

Figure 4.8 displays a Monte Carlo simulation obtained by varying the timescales of dust processes. The method was previously applied by Mattsson et al. (2014) to predict the dust-to-gas ratio on a different model. Accretion and coagulation range between 10^6 and 10^8 yrs, shattering between 10^7 and 10^9 yrs. On the log of each parameter is assumed a uniform distribution between the given ranges. The logarithm of the metallicity is taken to be uniform as well. On top of the mentioned processes, the Hirashita (2015) model also varies SN destruction, stellar ejecta condensation, and star formation, all of them with uniform logarithmic distribution. On these arrays, they computed 10^5 random parameter combinations, and ran the Hirashita (2015) model to compute the dust-to-gas ratio vs metallicity tracks for the top plot, and the ratio between small grain mass and large grain mass ($\mathcal{D}_S/\mathcal{D}_L$, where $\mathcal{D}_S = M_S/M_g$ is the small grain mass to total gas ratio, and similarly $\mathcal{D}_L = M_L/M_g$ for large grains) vs metallicity Z for the lower plot. The color maps represent the

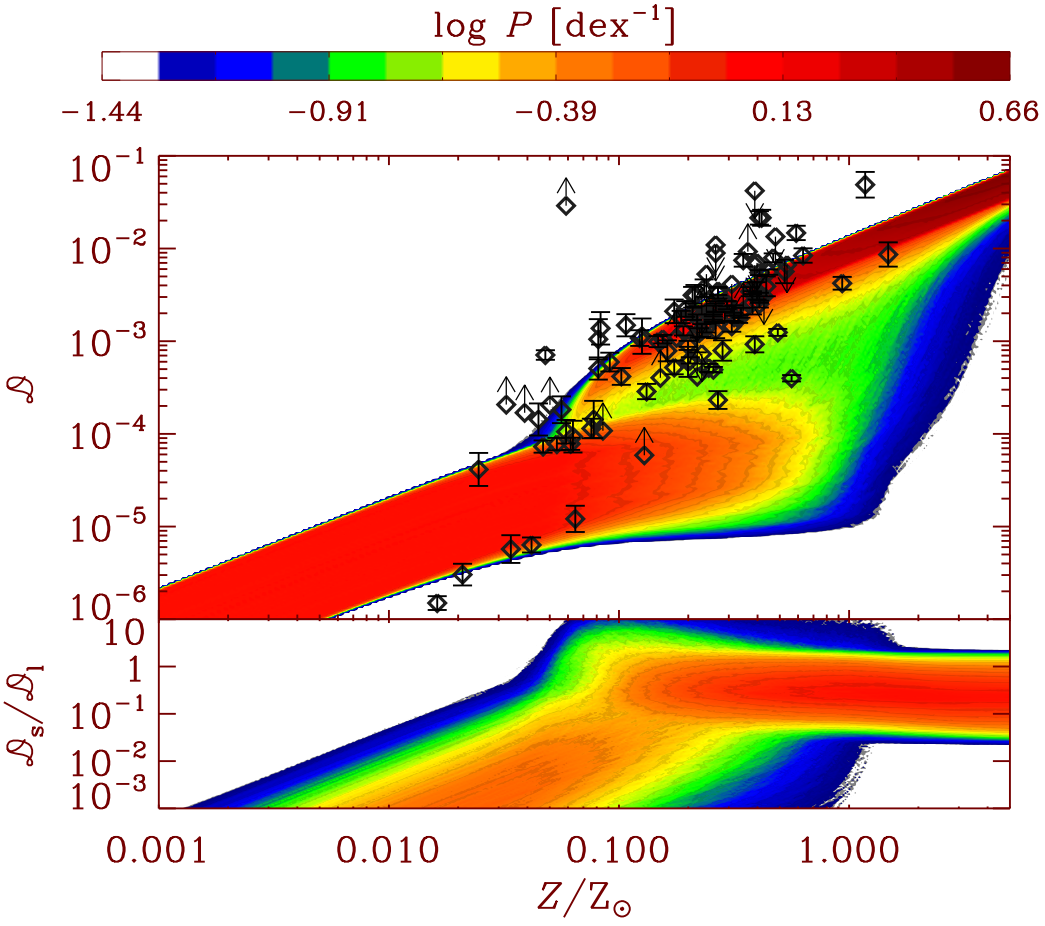

Figure 4.8: From Hirashita (2015). Probability distribution on the $\mathcal{D} - Z$ and $\mathcal{D}_S/\mathcal{D}_L \breve{} Z$ planes for the Monte Carlo simulation with randomly selected values of the parameters. The probability P at each metallicity is shown with the colour maps. The scale is shown in the colour bar above the figures. For reference, we also plot observational data for nearby galaxies taken from Rémy-Ruyer et al. (2014) (diamonds with error bars). The arrows show the upper or lower limits depending on the direction.

probability of having evolutionary tracks on a given region of the phase space.
At low metallicity, the top plot is nearly constant. In this regime, only the stellar ejecta condensation affects the $\mathcal{D} - Z$ relation. The condensation, being uniform, leads to the uniform probability in the range of possibilities. At metallicities higher than $0.1Z_{\odot}$ accretion supersedes as dominant dust growth mechanism. Therefore, the lower band up to $Z/Z_{\odot} = 1$ is caused by stellar event production, and the upper red band starting from $0.1Z/Z_{\odot}$ is caused by accretion. On top of them in black is the data of nearby galaxies from Rémy-Ruyer et al. (2014).

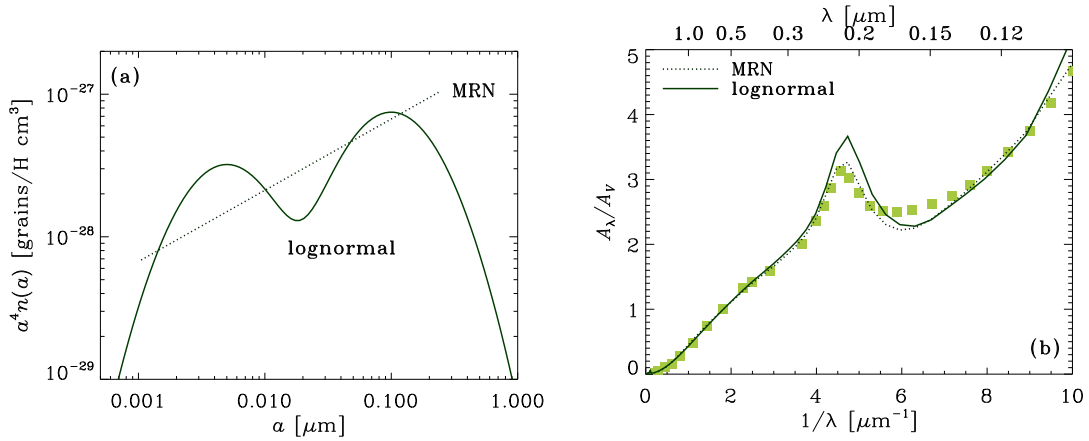

Figure 4.9: From Hirashita (2015): (a) Comparison between the two grain size distribution models (MRN and lognormal models) with the same small-to-large grain abundance ratio. The grain size distributions are presented after multiplying by a^4 to show the mass distribution in each logarithmic bin of the grain radius a. (b) Extinction curves calculated with the lognormal and MRN models (solid and dotted lines, respectively). The extinction is normalized to the value for the V band (0.55μm). The filled squares are the observed mean extinction curve of the Milky Way taken from Pei (1992).

In Figure 4.9, Hirashita (2015) tests the two-size approximation on the Milky Way extinction and against MRN (Mathis et al., 1977). They extrapolated from the two grain sizes the continuous lognormal distribution using the following function, adopted to ensure a lognormal mass distribution $\propto a^3 n_i(a)$:

$$n_i(a) = \frac{C_i}{a^4} \exp\left\{\left\{ - \frac{[\ln(a/a_{0,1})]^2}{2\sigma^2} \right\}\right\} \tag{4.10}$$

Where $n_i(a)da$ is the number of grains per hydrogen nucleus (between a and $a+da$). i identifies small ($i = S$) or large ($i = L$) grains. $a_{0,i}$ the grain radius (0.005μm for small and 0.1μm for large) and $\sigma = 0.75$ the standard deviation of the lognormal distribution. C_i is the normalization constant dictated by solving:

$$\mu m_H \mathcal{D}_i = \int_0^\infty \frac{4}{3}\pi a^3 s n_i(a) da \tag{4.11}$$

Which, as we've seen for Eq. 4.2 are $\mu = 1.4$, the gas mass per hydrogen nucleus. m_H is the hydrogen atom mass, s is the material density of a dust grain. a mixing of silicate to carbonaceous dust is assumed (0.54:0.46) as well as the small-to-large grain abundance ratio of 0.30:0.70 from the MRN model, known to reproduce well the MW distribution. MRN ($\propto a^{-3.5}$) is plotted in the radius range of $0.001 - 0.25\mu$m.

In the grain distribution plot, the lognormal and MRN models are congruent except for the lognormal small grain excess deriving from small graphite grains. This excess also causes a deviation of less than 20% in the extinction curve bump around a wavelength of $\sim 0.22\mu$m.

These checks show that the two-size approximation is a viable alternative to a continuous grain size distribution, as it still produces meaningful dust abundances and properties such as extinction and grain size distribution.

From the general collisional timescale (Eq. 4.2) we are now ready to obtain the timescales for shattering and coagulation. As applied to the two-size approximation, the dust-to-gas ratio will include only large grains for shattering and small grains for coagulation. Shattering will depend on the gas number density of the warm diffuse gas, whether coagulation, as we've seen, will be a function of the collisional velocity. The normalization of the velocity is taken from the Yan et al. (2004) study on magnetodynamic turbulence. From the same paper, the velocity of large grains for shattering is taken to be 10 km s^{-1}. The 1 cm^{-3} normalization is an upper limit on the number density a gas may have in the WNM. The material density s from the collisional timescale is taken to be 3 g cm^{-3} for a typical dust grain of unspecified composition.

4.4.0.0.1 Theoretical reference values In Figure 4.10 I plot a popular prescription for the number density of the grain size distribution from Weingartner and Draine (2001), the fourth line of table 2 in their paper. This grain size distribution provides an excellent fit for Milky-Way like extinction curve. I also assume $R_V = 3.1$. The green/cyan curve refers to silicate dust, the red/blue line is carbon dust. The magenta vertical line separates the large and small grain sizes in the Hirashita (2015) model. The mass ratios as shown in the legend, I compute the integral of the two curves above and below the Hirashita threshold, and I then combine them in different ratios of interest. In the next chapter, when I will present

small and large grain evolution within our cosmological simulation, I will refer back to these reference value to check how, without any calibration, our numbers hold against these spiral galaxy like expected values.

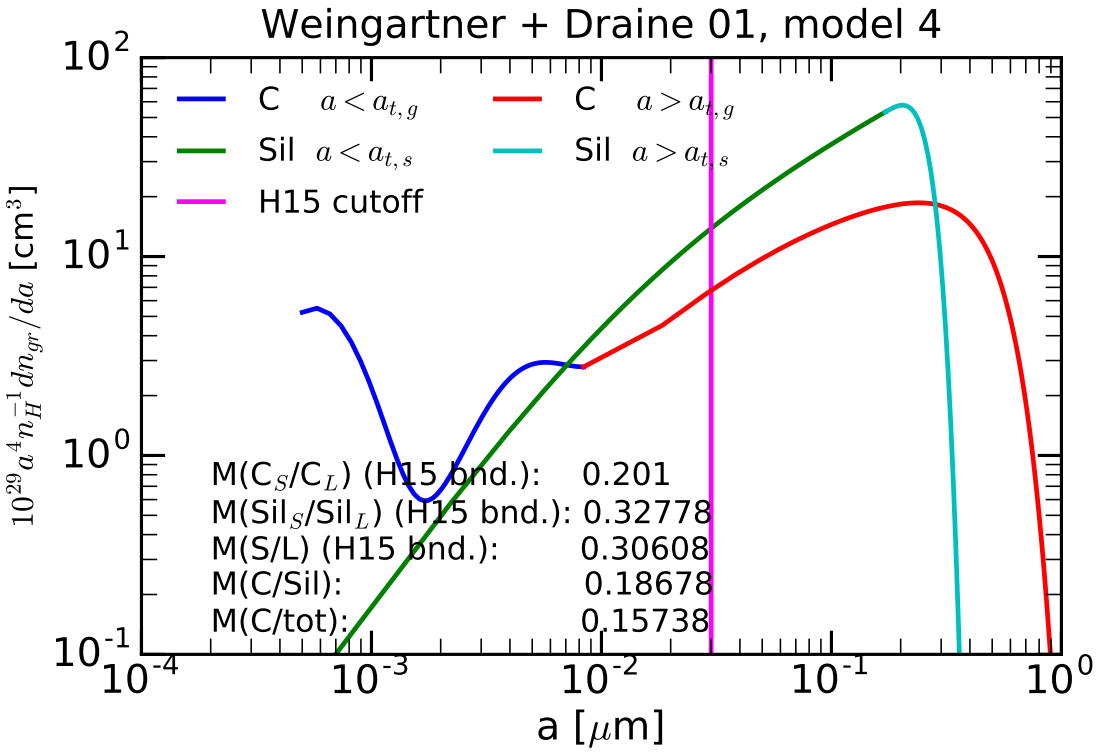

Figure 4.10: Grain size distributions for model 4 of Weingartner and Draine (2001), split by dust species (graphite/carbonaceous dust - C, or Silicates - Sil), model paramters to join the piecewise functions for graphite $a_{t,g} = 0.0837\mu$m and silicates $a_{t,s} = 0.171\mu$m, and the Hirashita (2015) threshold of separation (magenta line) between small grains and large grains of 0.03μm. Labels show various significant ratios such as small grain vs large grain mass ratios for C and Sil, total small grains vs large grain mass ratio, total C over total Sil, and Carbon over total, as labelled. These are the theoretical reference values against which we will compare the results from our simulation.

5

Dust evolution in Galaxy Cluster Simulations

In this chapter we will explore a state-of-the-art treatment of the processes affecting the production and ISM evolution of carbonaceous and silicate dust grains within SPH simulations. We trace the dust grain size distribution by means of a two-size approximation. We test our method on zoom-in simulations of four massive ($M_{200} \geq 3 \times 10^{14} M_{\odot}$) galaxy clusters.

We predict that during the early stages of cluster assembly at $z \gtrsim 3$, where our simulations peak in star formation activity, the proto-cluster regions are rich in dusty gas. The processes occurring in the cold ISM enhance the dust content by a factor 2 to 3 compared to the case where we include only production and destruction. Throughout their evolution, dust properties turn out to vary significantly from those observationally derived in the *average* Milky Way, values which are commonly adopted in calculations of dust reprocessing. We show that these differences may have a strong impact on the predicted spectral energy distributions. At low redshift in star forming regions, our model reproduces reasonably well the trend of dust abundances over metallicity observed in local galaxies. However, we under-produce by a factor of 2 to 3 the total dust content of clusters estimated observationally at low redshift ($z \lesssim 0.5$) using IRAS, Planck and Herschel satellite data. This discrepancy does not subsist if we assume a lower sputtering efficiency, which erodes dust grains in the hot Intracluster Medium (ICM). [1]

[1] This Chapter is based on results appearing in the paper Gjergo et al. (2018). In this chapter will converge all the concepts introduced or explored in the previous chapters.

5.1 Introduction

A significant fraction of metals present in the interstellar medium (ISM) is *depleted* from the gas phase and locked into small solid particles, the *cosmic dust*. The size of these particles is distributed over a broad range, from a few tens of Å up to a few μm. In the Milky Way, about 50% of the metal mass, or about 1% of the ISM mass, is in dust. Theoretical works (e.g. Dwek, 1998) predict the first percentage to be roughly constant, and as a consequence the second is approximately proportional to the ambient gas metallicity Z_{gas}. This estimate is confirmed by observations of metal-rich galaxies, but it is subject to a broad scatter. On the other hand, low metallicity dwarf galaxies, having a low dust-to-gas (DtG) mass ratio, deviate substatially (e.g. Galametz et al., 2011; Rémy-Ruyer et al., 2014). As for the detailed chemical composition of dust, as a first approximation it is accepted that dust consists of two major chemical classes: one carbon-based, and another named “astronomical silicates", composed of essentially four elements, O, Si, Mg and Fe. This is supported by depletion and dust-reprocessing studies (e.g. Draine, 2003; Jenkins, 2009, and references therein).

Despite this deceivingly reassuring summary of cosmic dust properties, it is clear that the situation is much more complex (e.g. Jones, 2013, and references therein). All the above mentioned properties of dust represent only the average at late cosmic times. However, observations show significant deviations, both from galaxy to galaxy in the local Universe, and within different environments of the Milky Way itself. Moreover, observations suggest substantial differences at early cosmic times. From a theoretical perspective, this is all but surprising. Indeed, dust grains constitute a living component of the ISM. Once dust grain seeds are produced, mostly in stellar outflows, they are subject to several evolutionary processes in the ambient gas, whose effectiveness depends on the physical and chemical gas conditions, as well as on the properties of the grains themselves. These processes, which we will describe in Section 5.2.4, alter the abundance, chemical composition and size distribution of dust grains.

Most galaxy properties cannot be described accurately without accounting for dust. For instance, the chemical species that dust depletes are key ISM coolants. Moreover, dust surfaces catalyze the formation of molecular species such as H_2 (e.g. Barlow and Silk, 1976). H_2 is the primary constituent of molecular clouds (MCs), the star formation sites. Among all dust effects, the best studied is the dust reprocessing of radiation emitted by astrophysical objects. Therefore, dust is of paramount

importance in interpreting observations. Dust absorbs efficiently stellar (or AGN) UV and optical light. The absorbed energy is thermally re-emitted in the IR, mostly at $\lambda >$ a few μm, with a peak at about 100 μm. In the local Universe, dust contributes only to less than 1% of the ISM mass. Despite being so scarce, it reprocesses about 30% of all the photons emitted by stars and AGNs (Soifer and Neugebauer, 1991). The reprocessed fraction increases as a function of the specific star formation activity of galaxies (Sanders and Mirabel, 1996). This is because in star forming objects, the primary radiative power originates from young stars, which are close or still embedded in their parent MCs (Silva et al., 1998; Granato et al., 2000; Charlot and Fall, 2000). Thus, IR turns out to be a very good observational tracer for star formation (eg Kennicutt and Evans, 2012). It is worth noticing that the absorption and scattering cross sections of grains depend not only on their composition but also, and strongly, on their radius a[2]. Therefore, reliable galactic SED models must take dust size distribution into account (Silva et al., 1998).

In this work, we implement within the GADGET-3 SPH code a state-of-the-art treatment of the processes affecting the production, evolution and destruction of carbonaceous and silicate dust grains. We model the size distribution of dust grains by means of the two-size approximation developed by Hirashita (2015). His work demonstrates that it is possible to reproduce the broad results of a full grain-size treatment just considering only two well-chosen representative sizes. The computation of this solution is not very demanding and therefore it is well-suited for cosmological simulations. Moreover, the method can be generalized in the future to increase the number of grain sizes.

While the GADGET-3 code is suitable for simulations of galaxy formation, we apply it here to zoom-in simulations of two massive ($\sim 10^{15} M_{\odot}$) and two smaller ($\sim 5 \times 10^{14} M_{\odot}$) galaxy clusters. We are mainly interested in the high redshift stages, where the star formation activity is at its maximum, and the proto-cluster regions are rich of cold dusty gas. The first aim of our dust evolution model is to couple it in the near future with post-processing radiative transfer computations. We plan to replace the uncertain assumptions on the dust content, chemical composition, and size distribution, with estimates derived from the computation of these properties in the simulated ISM. The presence of dust production and evolution will allow, at a second stage, to account for the role of dust as a catalyst for the formation of molecules, as well as the impact of gas heating and cooling due to dust (Montier and Giard, 2004).

[2]Usually dust grains are simply approximated by spheres.

A few groups have successfully included some aspects of the evolution of dust content of the ISM within hydrodynamical simulations (e.g. Bekki, 2013; McKinnon et al., 2016, 2017; Aoyama et al., 2017; Hou et al., 2017).Another possibility is to investigate the problem by means of post-processing computations (e.g. Zhukovska et al., 2016) or within semi-analytic models Popping et al. (2017). However the present work provides a more comprehensive description of dust as we predict both the size distribution and the chemical composition of dust grains *at the same time*, self consistently with a full treatment of the chemical evolution of the ISM. Moreover, while the focus of the aforementioned papers was on galactic disks, our work represents the first attempt to trace the evolution of dust component in simulations of galaxy clusters.

We follow Dwek (1998) in using a notation for metallicity that specifies when we refer to metals in the gas form Z_{gas}, metals in the solid form, i.e. dust Z_{dust}, or the sum of the two Z_{tot}. This is not a standard convention as in other works dealing with the evolution of the dust in the ISM, the symbol Z has been employed to refer to the *total* metal fraction (metallicity) of the ISM (e.g. Calura et al., 2008; Hirashita, 2015), including both metals in gas and metals locked up in solid state grains.

This chapter is organized as follows: in Section 5.2 we describe the model. We give a brief overview of our cosmological simulation set and we present our implementation of the dust evolution model. In Section 5.3 we describe and analyze the outcome of said dust model for a variety of global and internal properties. We also offer a preliminary data comparison.

5.2 Model

After implementing a treatment of dust evolution, in this work we re-run and analyze four zoom-in simulations for the formation of massive galaxy clusters, taken from a sample already presented in a number of papers by our group. We recall briefly in this section the main aspects of these simulations, while we refer the reader in particular to Ragone-Figueroa et al. (2013) and Ragone-Figueroa et al. (2018) for further numerical and technical details. The modifications introduced to take into account the evolution of dust in the ISM are fully described in Section 5.2.4.

5.2.1 The parent sample of simulated clusters

The full set of initial conditions describe 29 zoomed-in Lagrangian regions, selected from a parent DM-only and low resolution simulation of a 1 h^{-1} Gpc box. The regions are built to safely contain the 24 dark matter halos with $M_{200} > 8 \times 10^{14}$ and 5 smaller ones with $M_{200} = [1-4] \times 10^{14}$ [3]. We adopt the following cosmological parameters: $\Omega_{\rm m} = 0.24$, $\Omega_{\rm b} = 0.04$, $n_{\rm s} = 0.96$, $\sigma_8 = 0.8$ and $H_0 = 72\, kms^{-1}\, Mpc^{-1}$. These regions are re-simulated with a custom version of the GADGET-3 code (Springel, 2005) to achieve better resolution and to include the baryonic physics. The mass resolution for the DM and gas particles is $m_{\rm DM} = 8.47 \times 10^8$ and $m_{\rm gas} = 1.53 \times 10^8$, respectively. Note that the latter value is the *initial* mass of gas particles. However, as described in Section 5.2.1.1, during the simulation these particles can decrease their mass by spawning up to 4 stellar particles, to simulate star formation. On the other hand, they can also gain mass due to gas ejecta produced by neighborhood stellar particles. Thus the mass of each gas particle evolve with time. At $z = 0$, the 5% and 95% percentiles of their mass distribution turns out to be 0.6 and 1.06 the initial value respectively.
For the gravitational force, a Plummer-equivalent softening length of $\epsilon = 5.6\, h^{-1}\,$kpc is used for DM and gas particles, whereas $\epsilon = 3\, h^{-1}\,$kpc for black hole and star particles. The DM softening length is kept fixed in comoving coordinates for $z > 2$ and in physical coordinates at lower redshift. To treat hydrodynamical forces, we adopt the SPH formulation by Beck et al. (2016), that includes artificial thermal diffusion and a higher-order interpolation kernel, which improves the standard SPH performance in its capability of treating discontinuities and following the development of gas-dynamical instabilities.

5.2.1.1 Unresolved physics

Our simulations include a treatment of all the unresolved baryonic processes usually taken into account in galaxy formation simulations. For details on the adopted implementation of cooling, star formation (SF), and associated feedback, we refer the reader to Planelles et al. (2014). In brief, the model of SF is an updated version of the implementation by Springel and Hernquist (2003), in which gas particles with a density above $0.1\,{\rm cm}^{-3}$ and a temperature below $T_{MPh} = 5 \times 10^5\,$K are classified as multiphase. Multiphase particles consist of a cold and a hot-phase, in pressure equi-

[3] M_{200} (M_{500}) is the mass enclosed by a sphere whose mean density is 200 (500) times the critical density at the considered redshift.

librium. The cold phase is the star formation reservoir. At each timestep, multiphase particles can stochastically spawn non-collisional star particles, each representing a simple stellar population, with expectation value consistent with the star formation rate. The latter is computed on the basis of the physical state of the particle. Each star-forming gas particle can generate up to N_g (=4 in our simulations) star particles. The N_g-th event, when it occurs, consists in the complete conversion into a star particle. We implement kinetic feedback following the prescription by Springel and Hernquist (2003), in which a multiphase star-forming particle has a probability to be loaded into galactic outflows (we assume $v_w = 350\text{km s}^{-1}$ for the outflow velocity). This probability is set to generate on average an outflow rate proportional to the star formation rate, with a proportionality factor of 2.

A full account of the AGN feedback model can be found in Appendix A of Ragone-Figueroa et al. (2013), with some modifications described in (Ragone-Figueroa et al., 2018). We refer the reader to those papers for the numerical details. In short the BHs are represented by collision-less particles, seeded at the center of a DM halos when they become more massive than $M_{th} = 2.5 \times 10^{11} h^{-1}$ M$_\odot$ and do not already contain a SMBH. The initial BH mass at seeding is $M_{seed} = 5 \cdot 10^6 h^{-1}$ M$_\odot$. We reposition at each time-step the SMBHs particle at the position of the nearby particle, of whatever type, having the minimum value of the gravitational potential within the gravitational softening. The SMBH grows with an accretion rate given by the minimum between the α-modified Bondi accretion rate and the Eddington limit. The formula for the α-modified Bondi accretion rate:

$$\dot{M}_{Bondi,\alpha} = \alpha \frac{4\pi G^2 M_{BH}^2 \rho}{\left(c_s^2 + v_{BH}^2\right)^{2/3}} \tag{5.1}$$

is applied separately to the hot and cold gas components. The threshold between the two components is set at $T = 5 \times 10^5$ K, and the adopted values of the fudge factor α are 100 and 10 respectively. This distinction between cold and hot accretion modes has been inspired by the result of high resolution AMR simulations of the gas flowing to SMBHs (Gaspari et al., 2013). BHs particles merge when they fall within the gravitational softening. The accretion of gas onto the SMBH produces an energy determined by the radiative efficiency parameter ϵ_r. Another parameter ϵ_f defines the fraction of this energy that is thermally coupled to the surrounding gas. We calibrated these parameters to reproduce the observed scaling relations of SMBH mass in spheroids. Here we set $\epsilon_r = 0.07$ and $\epsilon_f = 0.1$, Finally, we assume a transition from a *quasar mode* to a *radio mode* AGN feedback when the accretion

rate becomes smaller than a given limit, $\dot{M}_{BH}/\dot{M}_{Edd} = 10^{-2}$. In this case, we increase the feedback efficiency ϵ_f to 0.7.

5.2.2 The model for chemical enrichment

Stellar evolution and metal enrichment follow Tornatore et al. (2007). The production of heavy elements considers separately contributions from Asymptotic Giant Branch (AGB) stellar winds, Type Ia Supernovae (SNIa) and Type II Supernovae (SNII), which is required also when implementing the production of dust from the different stellar channels (Section 5.2.4.1). Whereas all three types of stars contribute to the chemical enrichment, only SNIa and SNII provide thermal feedback. In addition, as described in Springel and Hernquist (2003), kinetic feedback from SNII is implemented as galactic outflows with a wind velocity of 350 km s^{-1}. The initial mass distribution for the star population is described by the initial mass function of Chabrier (2003). We assume the mass-dependent lifetimes of Padovani and Matteucci (1993) to account for the different time-scales of stars of different masses. To estimate the production of metals due to the evolution of stellar particles, we consider different sets of stellar yields, as detailed in Biffi et al. (2017). We trace the production and evolution of 15 chemical elements: H, He, C, Ca, O, N, Ne, Mg, S, Si, Fe, Na, Al, Ar and Ni. Consistently, metallicity-dependent radiative cooling of gas is calculated by taking into account the contribution of these 15 chemical species. The code do not include any special treatment of metal diffusion, although it accounts for the spreading of metals (both in gaseous and dust form, see below) from star particles to the surrounding gas particles by using the same kernel of the SPH interpolation. This is mainly done in order to avoid a noisy estimation of metal-dependent cooling rates. Therefore heavy elements and dust can be spatially distributed after that only via dynamical processes involving the metal-rich gas.

5.2.3 The test subsample for this work

To test our implementation of dust evolution we select 4 of the 29 zoomed-in regions. Two of them, dubbed D2 and D3, belong to the small mass sample of 5 regions discussed above, while the other 2, D1 and D6, are in the large mass sample. Their respective M_{200} at $z = 0$ are 5.4, 6.8, 11.8, and $17.5 \times 10^{14} M_{\odot}$. Most of the following analysis refers to the main cluster of region D2.

5.2.4 Dust formation and evolution

We implemented within our version of GADGET-3 a treatment of dust evolution similar to that introduced by Hirashita (2015) and Aoyama et al. (2017), with some modifications. We anticipate them here for the sake of clarity, before detailing our approach in the rest of this section: (i) We take advantage of a detailed treatment of chemical evolution (Section 5.2.2), which tracks individually several heavy elements instead of just the global metallicity. Therefore we can follow separately the fate of the two distinct dust chemical phases which are believed to populate the ISM, namely carbonaceous and silicate grains; (ii) rather than considering just the instantaneous ISM dust pollution due to SNII explosions, we are able to properly compute also the delayed effect of SNIa explosions and of AGB stars winds; (iii) we take into account also the dust erosion caused by thermal sputtering, which becomes dominant in the hot intra-cluster medium (ICM).

As for the chemical composition of dust, we adopt the standard view, supported by depletion and radiative studies (e.g. Draine, 2003; Jenkins, 2009, and references therein), that dust composition is dominated by C, O, Si, Mg and Fe. These elements are believed to be organized in two major chemical classes, one composed mostly by carbon and another one composed by "astronomical silicates", comprising the four latter elements. More specifically, we accept that the former one is reasonably well approximated for our purposes by pure C grains, and the latter one by Olivine $MgFeSiO_4$ grains (Draine, 2003). We explicitly note that the majority of radiative transfer computations in astrophysical dusty media are done adopting optical properties of dust grains calculated according to these assumptions. However it is also worth pointing out that our treatment can be immediately adapted to different dust composition models, as long as the relevant elements are included in the chemical evolution treatment described in Section 5.2.2.

As in Aoyama et al. (2017), we account for the grain size using the two-size approximation proposed by Hirashita (2015), which has been derived from the full treatment of grain size distribution put forward by Asano et al. (2013). In the two size approach, just two discrete size populations are considered to represent the whole continuum range of grain radii a. We refer to the two populations as large and small grains. This is justified by the fact that the various processes affecting dust population in the ISM act differently in these two representative populations. The boundary between them is set by Hirashita (2015) at $a \simeq 0.03\,\mu$m. We thus track four types of dust grains: large and small carbonaceous grains, and large and

small silicates grains.

It is worth pointing out that specifying the grain size distribution, albeit minimal, has a two-fold effect. It allows a more realistic treatment of the evolution of dust population, and it is also useful for post-processing computations involving radiative transfer that we plan to include in the next future. Indeed, the optical properties of grains strongly depends on their size. The two-size approximation allows for such a grain size treatment without affecting too heavily computation times and memory requirements. In the present application the overhead of computing time arising from the inclusion of dust evolution is limited to less than 20 per cent.

This two size approximation has been already adopted in previous simulations works (Hou et al., 2016, 2017; Chen et al., 2018b) which also tracked separately carbon and silicate dust. Note however that their simulations used a simplified treatment of chemical evolution, the Instantaneous Recycling Approximation (IRA). As a consequence, they included only SNII for the primary production of dust grains from stars, neglecting both AGB and SNIa. According to our results, based on a full treatment of chemical evolution, the SNII channel turns out to be insufficient to properly predict the relative abundance of silicate and carbon grains, and thus the radiative effect of dust (see 5.3.2.3).

Previous studies have identified the main processes that should be taken into account to understand the dust content of galaxies. The life cycle of grains begins with *dust production* in the ejecta of stars, including the relatively quiescent winds of AGB stars, but also SNII and SNIa explosion. It can be assumed that dust production affects directly only large grains. Indeed, SNae shocks are more efficient at the destruction of small grains than of large grains, therefore over chemical evolution timescales only the latter will survive (Nozawa et al., 2007; Bianchi and Schneider, 2007)). As for AGB winds, their infrared SEDs suggest that the typical grain size is skewed toward large grains (Groenewegen, 1997; Gauger et al., 1999). These findings are supported by expectations of models including dust formation in AGB winds (e.g. Winters et al., 1997).

Once injected into the ISM, the grain population is subject to several evolutionary processes. Metals from the surrounding gas can deposit on the grain surface, causing the grains to gain mass, in a process named *accretion* (Dwek, 1998; Hirashita, 1999). An important role of this process has been invoked to explain the remarkable amount of dust in high-z quasars and starbursts (e.g. Michałowski et al., 2010; Rowlands et al., 2014; Nozawa et al., 2015, and references therein), which cannot be accounted by stellar production only. Being a surface process, it acts more efficiently on small

grains, which have larger total surface per unit mass. However, accretion is not efficient enough to increase significantly a small grain's radius. Its effect is just to increase the amount of small grains, while the evolution of small grains into large grains by accretion is safely negligible. Grain-grain collision can either result in grain *coagulation* or *shattering*. The former process dominates in dense ISM, and can be regarded as a destruction mechanism for small grains and a formation mechanism for large ones. The latter mechanism wins in the diffuse ISM, leading to the formation of small grains and destruction of large ones.

Sputtering, also a surface process, consists of grain erosion due to collisions with energetic ions. The eroded atoms are given back to the gas phase. It occurs both when grains are swept by SNae shocks, and when they are subject to the harsh ion collisions in the hot ICM. On top of SNae dust destruction, we include thermal sputtering in the ICM, which is important only when grains are surrounded by hot gas $T \gtrsim 10^6$ K . Hirashita (2015) and Aoyama et al. (2017) did not consider ICM thermal sputtering, because they were interested only in galactic ISM. We refer to this process simply as *sputtering*, whether we call the former one *SNae destruction*.

Needless to say, when gas is turned into stars, its dust content is proportionally subtracted from the ISM. This event is often referred to as *astration*. A visual summary of how the various processes act on the components of a galaxy is provided in Figure 5.1.

We implement this sequence of processes at the sub-grid level. A variable fraction of every metal produced by star particles is given to neighbor gas particles in the form of solid state dust rather than gas. Accordingly, we modified the gas particle structure to trace two extra vectors along with the gas metals: one for large and one for small grains. The three vectors have a length equal to the number of chemical species we trace, which are 15 in this chapter. Thus a certain fraction of the mass of each SPH "gas" particle, never exceeding a few %, is actually used to represent metals which are locked up in solid grains. We still refer to them simply as SPH gas particles.

For a SPH gas particle of total mass M_{gas}, the time derivatives of the dust mass content in the two size populations of small grains $M_{d,S}$ and large grains $M_{d,L}$ can be expressed as follows:

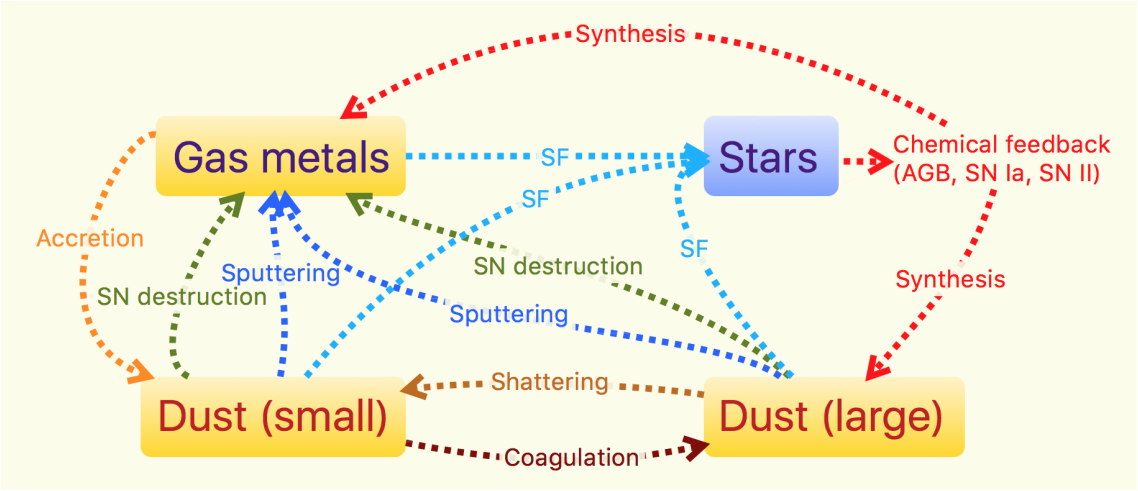

Figure 5.1: Diagram of mass flows due to dust processes. Boxed in yellow are gas metals, large and small dust, which belong to the gas particle structure. Boxed in blue is the star particle, responsible for the production of metals in the subgrid chemical evolution through AGB winds, SN Ia, and SN II. Star particles spread metals to the surrounding gas particles by enriching gas metals and large dust alike. When a gas particle is ready to form a star particle, all 3 of the gas particle metal channels are depleted in proportion, in favor of the star particle. SN destruction and sputtering subtract metals from both dust channels and enrich the gas metals.

$$\begin{aligned}\frac{dM_{d,L}}{dt} &= \frac{dM_{p*}}{dt} - \frac{M_{d,L}}{\tau_{sh}} + \frac{M_{d,S}}{\tau_{co}} - \frac{M_{d,L}}{\tau_{SN,L}} - \frac{M_{d,L}}{\tau_{sp,L}} - \frac{M_{d,L}}{M_{gas}}\psi \\ \frac{dM_{d,S}}{dt} &= \frac{M_{d,S}}{\tau_{acc}} + \frac{M_{d,L}}{\tau_{sh}} - \frac{M_{d,S}}{\tau_{co}} - \frac{M_{d,S}}{\tau_{SN,S}} - \frac{M_{d,S}}{\tau_{sp,S}} - \frac{M_{d,S}}{M_{gas}}\psi\end{aligned} \tag{5.2}$$

where $\frac{dM_{p*}}{dt}$ is the dust enrichment arising from production by stars, and local timescales for the various dust processes occurring in the ISM are introduced: τ_{sh} for shattering, τ_{co} for coagulation, $\tau_{SN,L}$ and $\tau_{SN,S}$ for SN shock destruction, τ_{sp} for sputtering and τ_{acc} for accretion. The last term of each equation represents the dust mass loss due to star formation (astration), specifically ψ is the star formation rate. These equations are applied separately for each element entering into the dust grains. This implies that if a gas particle has gas-phase metals for accretion of silicates but not gas phase C (a quite unlikely possibility, in particular at our relatively coarse resolution), only the mass of small silicates is affected by accretion, but not that of C grains. In the next subsections we give details on how each of these terms is computed in our simulations.

5.2.4.1 Dust production by stars

We adapt to each simulation star particle the formalism for dust production by stars introduced by Dwek (1998), in the context of *monolithic* galaxy formation models. However, we introduce an important modification related to our specific assumption for the chemical composition of silicate grains.

Dust is produced by the same stellar enrichment channels which are responsible of metals production, namely AGB winds, SNIa, and SNII. We assume that a certain fraction of the elements concurring to dust formation is originally given to the ISM locked to solid dust particles rather than in gaseous form. These elements are C, Si, O, Mg, and Fe. This is because, as motivated at the beginning of Section 5.2.4, we consider carbon and silicate dust, and we approximate silicates with olivine $MgFeSiO_4$. In this exploratory work we maintain for simplicity the assumption that, for each stellar channel the fraction dust elements that condense to dust does not depend on stellar mass nor on metallicity. This approach, introduced in one-zone models by Dwek (1998), has been adopted by many later computations (e.g. Calura et al., 2008; Hirashita, 2015; Aoyama et al., 2017). However we point out that there are several works that studied how dust condensation efficiencies actually depend on stellar mass, metallicity and ambient gas density (see e.g. Nozawa et al., 2007; Schneider et al., 2014, and references therein). In the future it will be relatively straightforward to incorporate the results of such computations into our formalism.

5.2.4.2 AGB stars

As for AGB winds, following Dwek (1998) we assume that the formation of carbon or silicate dust is mutually exclusive, and depends on the C/O number ratio in the ejecta. When C/O>1, all the oxygen is tied up in CO molecules and only carbon dust is formed. If instead C/O<1, all the carbon is consumed to form CO molecules, while the excess oxygen will combine with Si, Mg and Fe to produce mainly silicate grains. This view is broadly supported by many observations (e.g. Kastner et al., 1993), and implies the assumption that AGB ejecta are mixed at microscopic level, so that the maximum possible amount of CO is formed.

Let $M_{ej,C}^{AGB}$ and $M_{ej,O}^{AGB}$ be the C and O masses ejected by a star particle through the AGB enrichment channel during a given time-step. Carbon (silicate) grains form when $M_{ej,C}^{AGB}$ is greater (smaller) than $0.75 M_{ej,O}^{AGB}$, where 0.75 is the ratio between O and C atomic weights. Due to the C mass lost to CO, the mass of carbon dust

produced during the time-step is given by

$$M^{AGB}_{dust,C} = \max\left[\delta_{AGB,C}\left(M^{AGB}_{ej,C} - 0.75\, M^{AGB}_{ej,O}\right),\, 0\right] \tag{5.3}$$

where $\delta_{AGB,C}$ is a *condensation efficiency* of carbon grains in AGB winds, which we set equal to 1, as in Dwek (1998) (see also Calura et al., 2008).

If $M^{AGB}_{ej,C} < 0.75 M^{AGB}_{ej,O}$, silicate grains are instead produced. Dwek (1998) estimated the masses of the elements going into silicate dust under the simple assumption that for each atom of them, a single O atom will go into dust as well (see his equation 23). While we have implemented in our code also his formulation, we prefer a more specific assumption on the chemical composition of silicates produced by stars, which leads us to different formulae. As expected we have verified with our code that Dwek (1998) approach leads to the production of 'silicate grains' featuring very variable mass ratios between the various elements, and typically very different from those implicitly assumed by most radiative transfer computations. This is particularly true for the SNIa channel, since these stellar events produce mostly iron, much in excess to the quantity that can be bound directly with O in the SNae ejecta. When we use the formalism by Dwek (1998), dust grains reach a mass fraction for Fe which is double that of olivine. Mg is under-abundant by a factor of 3. Our method on the other hand, described below, preserves the olivine-like mass fractions in the four metal components at all redshifts.

Generalizing the notation introduced above, we indicate as $M^{AGB}_{ej,X}$ the masses ejected by a star particle, through the AGB enrichment channel and during a given time-step, in form of the X element which enters into the olivine compound. X stands then for Mg, Fe, Si and O. We indicate $N^{AGB}_{mol,sil}$ as the number of "molecules" of $MgFeSiO_4$ that can be formed over the time-step. This is set to the least abundant element, taking into account how many atoms of each element N^{X}_{ato} enter into the compound (1 for Mg, Fe, Si, and 4 for O). Then

$$N^{AGB}_{mol,sil} = \delta_{AGB,sil} \min_{X\in\{Mg,Fe,Si,O\}} \left(\frac{M^{AGB}_{ej,X}}{\mu_X\, N^{X}_{ato}}\right) \tag{5.4}$$

where μ_X is the atomic weight of the X element, and we have introduced an efficiency factor of condensation for silicate grains $\delta_{AGB,sil}$, set to 1 in our reference model.

Therefore, the mass of the X element locked into silicate grains is given by

$$M_{dust,X}^{AGB} = \begin{cases} N_{mol,sil}^{AGB}\,\mu_X\,N_{ato}^{X} & \text{for } \frac{M_{ej,C}^{AGB}}{M_{ej,O}^{AGB}} < 0.75 \\ 0 & \text{otherwise} \end{cases} \tag{5.5}$$

It is straightforward to adapt the above treatment to chemical compounds different from olivine.

5.2.4.3 SNae II and Ia

Unlike AGB winds, it is reasonable to assume that the explosive outflows produced by SNae are mixed only at a macroscopic level (e.g. Dwek, 1998, and references therein), which implies that these channels can produce both carbon and silicate dust at the same time. Hence:

$$M_{dust,C}^{SNx} = \delta_{SNx} M_{ej,C}^{SNx} \tag{5.6}$$

$$M_{dust,X}^{SNx} = N_{mol,sil}^{SNx}\,\mu_X\,N_{ato}^{X} \tag{5.7}$$

$$N_{mol,sil}^{SNx} = \delta_{SNx,sil} \min_{X\in\{Mg,Fe,Si,O\}} \left(\frac{M_{ej,X}^{SNx}}{\mu_X\,N_{ato}^{X}} \right) \tag{5.8}$$

where SNx stands either for $SNII$ or $SNIa$, and $M_{ej,X}^{SNx}$ is the mass of the generic element X ejected by a star particle through the SNx enrichment channel during a given time-step. In the case of SNae we decrease the dust condensation efficiency to $\delta_{SNII,C} = \delta_{SNIa,C} = 0.5$ and $\delta_{SNII,sil} = \delta_{SNIa,sil} = 0.8$. These values are the same as those adopted in Dwek (1998) and are meant to account for the grains destroyed by the SN shock or incomplete condensation of available elements.

5.2.4.4 Shattering

In the diffuse gas, large grains tend to have high velocities (typically $v = 10$ km s^{-1}, Yan et al. 2004) due to decoupling from small-scale turbulent motions (Hirashita and Yan, 2009). Therefore in such environments, large grains are most prone to shattering due to collision, forming small grains. In our framework, shattering is the process which originates small grains, without directly affecting the total dust mass. The growth of small grain mass occurs by accretion (Section 5.2.4.5). The shattering timescale is derived following the prescription in Appendix B of Aoyama et al. (2017). The gas environment diffuse enough to promote efficient shattering is

identified by the condition $n_{gas} < 1$ cm^{-3} (see Hirashita and Yan, 2009), in which case:

$$\tau_{sh} = \tau_{sh,0} \left(\frac{0.01}{D_L}\right) \left(\frac{1\,\mathrm{cm}^{-3}}{n_{gas}}\right) \text{ if } n_{gas} < 1 \text{ cm}^{-3} \tag{5.9}$$

where $D_L = M_{dust,L}/M_{gas}$ is the dust to gas ratio for large grains. The value of the proportionality constant suggested by Aoyama et al. (2017) is $\tau_{sh,0} = 5.41 \times 10^7$yr, obtained assuming the typical grain velocity dispersion quoted above $v = 10$ km s^{-1}, a grain size of 0.1μm, and a material density of grains 3 g cm^{-3}.

5.2.4.5 Accretion and Coagulation in dense molecular gas

Accretion of gas metals onto dust grains as well as coagulation of grains are processes whose timescale is inversely proportional to the gas density, and become significant only in the densest regions of molecular clouds, at $n_H \gtrsim 10^2 - 10^3$ cm^{-3} (see Hirashita and Voshchinnikov, 2014, equations 7 and 8). These high densities are unresolved in cosmological simulations, therefore we have to resort to a sub-resolution prescription to estimate the fraction of gas f_{dense} that is locally in this condition. Aoyama et al. (2017) simply assumed a fixed fraction. Although for their simulated galaxy the results are weakly sensitive to the adopted value, this solution could be in general unsatisfactory. In fact, f_{dense} should depend on the local condition of the gas and on the numerical resolution reached in a simulation. We thus introduce a more flexible approach. According to the results of high resolution ($\lesssim 10$ pc) simulations (e.g. Wada and Norman, 2007; Tasker and Tan, 2009) the probability distribution functions of ISM density is well described by a log-normal function, characterized by a dispersion σ, found to lie in the range 2 to 3, and a number density normalization parameter n_0.

$$f_{pd}(n)\, dn = \frac{1}{\sqrt{2\pi}\sigma} \exp\left[-\frac{\ln(n/n_0)^2}{2\sigma^2}\right] d\ln n \tag{5.10}$$

Therefore the mass fraction $f(> n_{th})$ of ISM gas above a given density threshold n_{th} is (Wada and Norman, 2007, equation 19)

$$f(> n_{th}) = \frac{1}{2}\left[1 - \mathrm{erf}\left(\left[\ln\left(\frac{n_{th}}{n_0}\right) - \sigma^2\right]\left(\sqrt{2}\sigma\right)^{-1}\right)\right] \tag{5.11}$$

We use this equation in order to estimate $f_{dense} \equiv f(> n_{th})$ for each SPH gas particle, we adopt $\sigma = 2.5$ and $n_{th} = 10^3$ cm^{-3} in our fiducial model. In order to set the local value of the density normalization n_0, we take into account that for the distribution given by equation 5.10, the mass averaged density is $\langle n \rangle_M = n_0 \exp(2\sigma^2)$ and we identify $\langle n \rangle_M$ with a suitable number density associated to the SPH particle. Since conditions suitable for accretion and coagulation can only be achieved in star forming multiphase particles (see Section 5.2.1), we set $\langle n \rangle_M$ equal to the density of the cold phase n_{cold}. In the multiphase models of SF by Springel and Hernquist (2003) n_{cold} is computed from the condition of pressure equilibrium between the two phases, and assuming $T_{cold} = 1000$ K, while the temperature of the ionized hot phase T_{hot} is the SPH gas temperature. In our simulations, both the median and the standard deviation of n_{cold} distribution increases with redshift, and range (in cm^{-3}) from about ~ 1 to ~ 20 and from a few tens to a few hundreds respectively.

As already remarked, in the two size approximations, only small grains increase their mass when gas metals deposit on their surface. Following Aoyama et al. (2017), we use the following expression to estimate the corresponding timescale:

$$\tau_{acc} = \tau_{acc,0} \left(\frac{Z_\odot}{Z_{gas}} \right) f_{dense}^{-1} f_{cld}^{-1} \tag{5.12}$$

where f_{cld} is the fraction of cold gas in multiphase particles (MP). Indeed this equation does not apply to single-phase particles, nor to the hot phase of multiphase particles, since their density is far too low for the process to occur. Aoyama et al. (2017) set $\tau_{acc,0} = 1.2 \times 10^6$yr.

In MP particles, small grains can also coagulate to form large grains. The timescale is given by (see Aoyama et al., 2017)

$$\tau_{co} = \tau_{co,0} \left(\frac{0.01}{D_S} \right) \left(\frac{0.1\,\mathrm{km\ s^{-1}}}{v_{co}} \right) f_{dense}^{-1} f_{cld}^{-1} \tag{5.13}$$

where $D_S = M_{dust,S}/M_{gas}$ is the dust to gas ratio for small grains and v_{co} is the velocity dispersion of small grains, for which a value of 0.1 km s^{-1} is adopted based on calculations from Yan et al. (2004). Just like with τ_{acc}, the equation has been modified to consider only the cold phase of multiphase particles. Aoyama et al. (2017) used $\tau_{co,0} = 2.71 \times 10^5$ yr, a value derived assuming a typical size of small grains of 0.005 μm, a material density of 3 g cm^{-3} and $n_{gas} = 10^3\,\mathrm{cm}^{-3}$.

run name	I.C.	$M^{200}_{z=0}$ [$10^{14} M_\odot$]	production	$\tau_{sh,0}$ [Myr]	$\tau_{co,0}$ [Myr]	$\tau_{acc,0}$ [Myr]	$\tau_{sp,0}$ [Myr]
`fid`	D2	5.41	new	54.1	0.271	1.20	5.5
`f-crsp`	‘’	‘’	‘’	off	off	off	5.5
`f-nosp`	‘’	‘’	‘’	54.1	0.271	1.20	off
`f-sp.2`	‘’	‘’	‘’	‘’	‘’	‘’	27.5
`f-snII`	‘’	‘’	SNII-only	‘’	‘’	‘’	5.5
`f-dw`	‘’	‘’	Dwek	‘’	‘’	‘’	‘’
`f-D3`	D3	6.80	new	‘’	‘’	1.20	‘’
`f-D6`	D6	15.5	‘’	‘’	‘’	‘’	‘’
`f-D1`	D1	17.5	‘’	‘’	‘’	‘’	‘’

Table 5.1: List of the test runs discussed in this chapter with their respective parameters. Column 1 represents the run name used in the text. Column 2 is the chosen initial condition region. Column 3 is the $z = 0$ M_{200} of the main cluster of the region. Column 4 is the dust production method from stars: with "new" we refer to the prescription presented in this chapter, assuring that dust grains at production respect a given proportion of O, Mg, Fe and Si, namely that of olivine $MgFeSiO_4$ in this work, "dwek" is the prescription proposed by Dwek (1998) (see 5.2.4.1 for details). Finally with "SNII-only" we refer to runs in which stellar dust production is active only for the snII channel, as done by Aoyama et al. (2017). This is to test the relative importance of the other two channels SNIa and AGB used in our full implementation. Columns 5 to 9 are the normalization timescales defined in the text for each ISM evolution process (5.2.4).

5.2.4.6 SNae destruction

Dust grains are efficiently destroyed by thermal and non-thermal sputtering in SNae shocks (for a review see McKee, 1989). To avoid confusion, hereafter we refer to destruction by SNae events as SNae destruction, and we reserve the term sputtering to what we describe in Section 5.2.4.7. To treat this process we follow Aoyama et al. (2017). Let N_{SN} be the number of supernovae exploding over a given integration timestep Δt. For simplicity, we do not distinguish by now between the effects of SNII and SNIa. However the code can be trivially adapted to take into account different values of the relevant parameters for the two classes, since the respective $N_{SN,II}$ and $N_{SN,Ia}$ are already computed separately. The timescale for the process in the timestep can be written as

$$\tau_{SN} = \frac{\Delta t}{1 - (1 - \eta)^{N_{SN}}} \tag{5.14}$$

where

$$\eta = \epsilon_{SN} \min\left(\frac{m_{SW}}{m_g}, 1\right) \tag{5.15}$$

In this expression m_g is the gas mass of the SPH particle, m_{SW} is the gas mass swept by a single SN event[4], and ϵ_{SN} is the efficiency of grain destruction in the shock, that we set to the same reference value 0.1 used by Aoyama et al. (2017). The shocked gas mass has been estimated in McKee (1989) as:

$$m_{SW} = 6800 M_\odot \left(\frac{E_{SN}}{10^{51}\mathrm{erg}}\right)\left(\frac{v_s}{100\ \mathrm{km\ s^{-1}}}\right)^{-2} \tag{5.16}$$

where E_{SN} is the energy from a single SN explosion and v_s the shock velocity. We adopt the fiducial value of $E_{SN} = 10^{51}$ erg. McKee et al. (1987) give the for v_s the following expression

$$v_s = 200\ \mathrm{km\ s^{-1}} \left(n_0/1\mathrm{cm}^{-3}\right)^{1/7} \left(E_{SN}/10^{51}\mathrm{erg}\right)^{1/14} \tag{5.17}$$

However, since the number density of ambient gas for single SN blasts is not resolved, we simply set $v_s = 200$ km s^{-1}. As a result, $\eta = 170\, M_\odot/M_g$ in our simulations.

5.2.4.7 Thermal Sputtering

Dust grains can be efficiently eroded by collisions with energetic ions. This process becomes important whenever the ambient gas is hot enough, $T_g \gtrsim 10^6$ K, in which case it is dubbed *thermal sputtering*. To describe it, we employ the analytical formula given by Tsai and Mathews (1995). This is an accurate enough approximations of detailed calculations for both carbonaceous and silicate grains, at least for gas temperature smaller than a few times 10^7 K. Above this temperature the process efficiency tends to stall (Tielens et al., 1994). Taking this into account and combining equations (14) and (15) of Tsai and Mathews (1995) we get:

$$\tau_{sp} = \tau_{sp,0} \left(\frac{a}{0.1\,\mu\mathrm{m}}\right)\left(\frac{0.01\,\mathrm{cm}^{-3}}{n_g}\right)\left[\left(\frac{T_{sp,0}}{\max(T_g, 3\times 10^7\mathrm{K})}\right)^{\omega} + 1\right] \tag{5.18}$$

with $T_{sp,0} = 2\times10^6 K$, $\omega = 2.5$ and $\tau_{sp,0} = 5.5\times10^6$yrs. In this equation $n_g = \rho/\mu m_p$ is the number density including both ions and electrons. To derive the normalization constant $\tau_{sp,0}$, we adopted the mean molecular weight $\mu = 0.59$ of a mixture of 75% H and 25% He, both fully ionized. Moreover, we have taken into account that for

[4]In our relative low resolution simulation $m_s << m_g$.

spherical grains the mass variations timescale is related to that for radius variations by $m/\dot{m} = a/3\dot{a}$. We adopt $a = 0.05\,\mu$m and a ten times smaller value for the typical radii of large and small grains, respectively. The former is the average radius for a power law size distribution with index -3.5, ranging from 0.03 μm (the adopted boundary between small and large grains) to 0.25 μm (e.g. Silva et al., 1998).

5.2.5 Fiducial run and its variations

In 5.1 we list a selection of interesting runs discussed in the chapter. Most of the analysis refers to the "fiducial" run `fid`, for which we essentially adopted the same parameters values as Aoyama et al. (2017). These authors simulated an isolated spiral galaxy, and found results broadly consistent with spatially resolved observations of nearby dusty galaxies. It is however worth pointing out that we are working at resolutions lower by about three orders of magnitude in gas particle mass. Moreover, our model has two significant differences with respect to their work: we treat separately the production and evolution of the two distinct chemical species of carbon and silicate grains, and we include a treatment of thermal sputtering in the hot ICM. The latter process is crucial for galaxy cluster environments. Nevertheless, we believe that the parameter values defined by Aoyama et al. (2017) are a good starting point for our work. We will not explore the full dependence of dust properties on the parameters. Such work is postponed to future papers. As for sputtering, we adopt the fiducial run parameter value derived from the classic work by Tielens et al. (1994).

In order to separate the other dust evolutionary processes from dust production and sputtering, we performed runs `f-crsp`, where only the latter processes are turned on, and `f-nosp` in which all processes but sputtering and SN destruction are active. To compare our dust production method, conserving the element fraction of olivine, to that by Dwek (1998) we run `f-dw` in which his method is instead employed. We also performed a run `f-snII` where only SNII contributes to dust production, but not SNIa nor AGBs. With this run we test, and to some extent disprove, the claim by Aoyama et al. (2017) that dust production by SNII is sufficient to predict the dust properties. In `f-sp.2` we increase the sputtering timescale by a factor 5, for illustrative reasons discussed in Section 5.3.3. These different runs were performed on the small mass region D2 of our set of initial conditions. The fiducial model was also applied to the other three regions D3, D1 and D6 (See Section 5.2.3). Unless otherwise specified, the analysis that follows applies to the fiducial run `fid`.

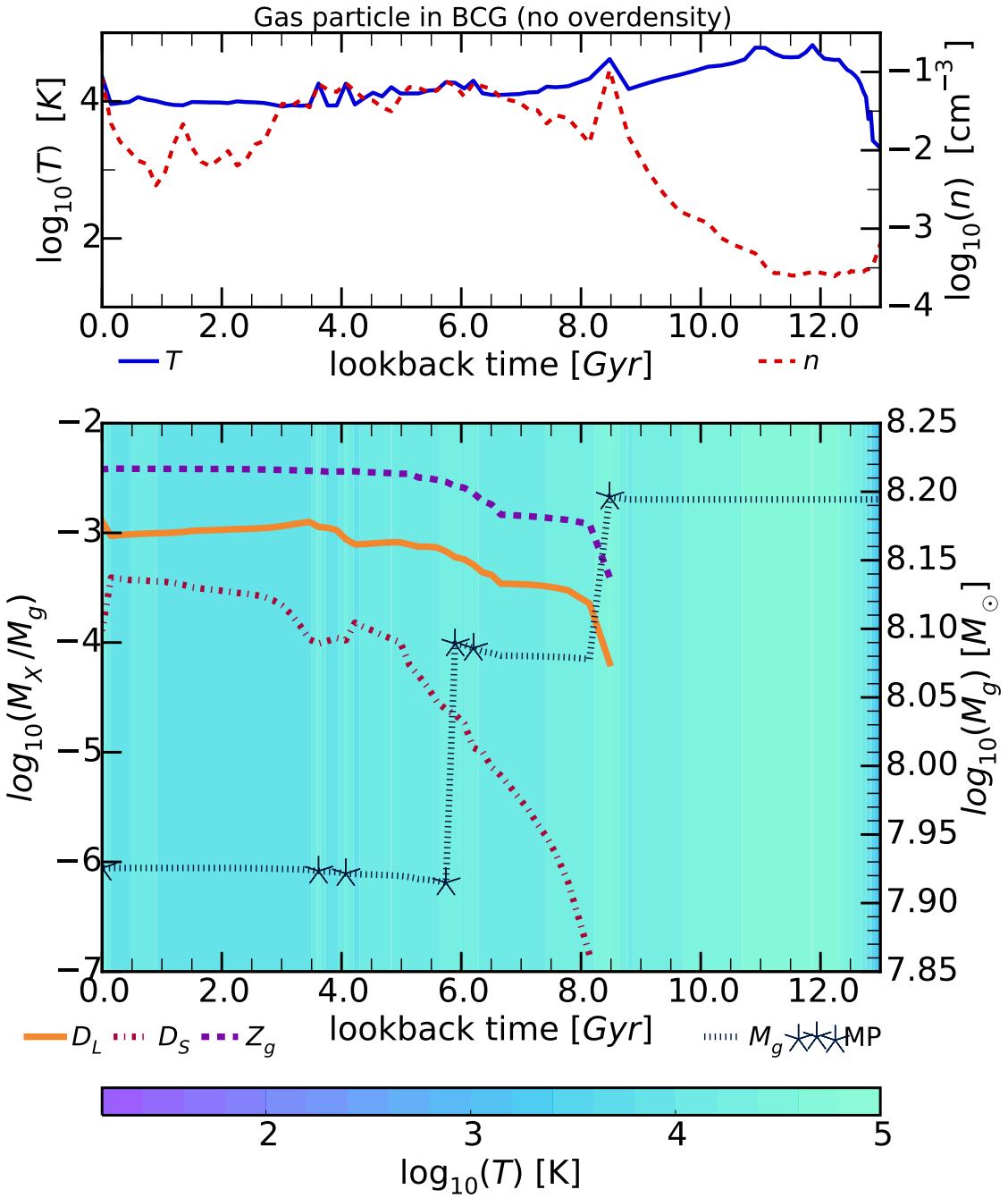

Figure 5.2: For a gas particle in the fiducial run residing in a small, quiet, peripheral galaxy by $z = 0$: Top and bottom plots represent the time evolution (*x-axis* t_{lb} time in Gyrs, with 0 being today) of various gas properties: (**top plot**) temperature (*left y-axis, blue solid line*) and number density (*right y-axis, red dashed line*). (**bottom plot**) Gas metallicity (*left y-axis, dashed purple line*), as well as the Dust-to-Gas (DtG) for large dust grains (*left y-axis, solid orange line*) and small dust grains (*left y-axis, dot-dashed red line*), total mass (*right y-axis, dotted dark blue line*) of the gas particle. The stars mark the snapshots in which the gas particle was captured in multiphase state (MP).

5.3 Results

In this section we study the behavior of the dust model within the simulation. First we follow the evolution of a couple token SPH gas particles representative of two interesting environments. A single gas particle could be thought of as the ISM of a one zone-model, such as those put forward by Dwek (1998) and Hirashita (2015). Then we investigate the evolution of global properties of dust in the main cluster region. We conclude with a preliminary comparison to observations.

5.3.1 Inside individual gas particles

In Figure 5.2 we follow the dust, gas metal, total mass, temperature, and density of a simulated gas particle which by $z = 0$ is located within an isolated galaxy at the periphery of a cluster in our fiducial run. This particle features a relatively quiet evolution. It spawns two star particles, around a lookback time (t_{lb}) of 8.5 Gyr and 6 Gyr, as a consequence of its star forming state. The particle's mass drops to about 75% and 50% of its original value during each episode (see Section 5.2.1; dotted dark blue line of the bottom panel). It begins to be enriched in gas metals and large grains by the neighboring stellar particles at a t_{lb} of 8.5 Gyr, around the time of star formation. Soon after that, shattering begins to produce a population of small grains. Its growth rate is steady for the first 4 Gyrs, thanks to a fairly constant gas density (red dashed line in the top panel). The gas temperature does not deviate significantly from 10^4 K throughout its history, whether the gas density starts low at 3×10^{-3} cm^{-3} and then fluctuates by 1 dex below 10^{-1} cm^{-3}. The second star particle formation episode at 6 Gyrs does not affect the DtG and metallicity, as these quantities decrease proportionally to the mass loss.

While the particle is multiphase, accretion sticks gas metals onto small grains and small grain coagulation in turn convert small grains to large ones. The seven multiphase snapshots are highlighted by a star symbol on the mass line of the bottom panel. The last three ones, two around 4 Gyr in t_{lb} and the third very recent, occurs while the small grain abundance is within 1 dex to that of large grains. In this case, coagulation prevails over accretion, and therefore a depletion of small grains is visible, whilst a tiny bump in the large grains mass ratio can be recognized. Note that it is possible that the particle underwent other multiphase periods between two subsequent snapshots. Similar periods are not highlighted by star symbols in the plot.

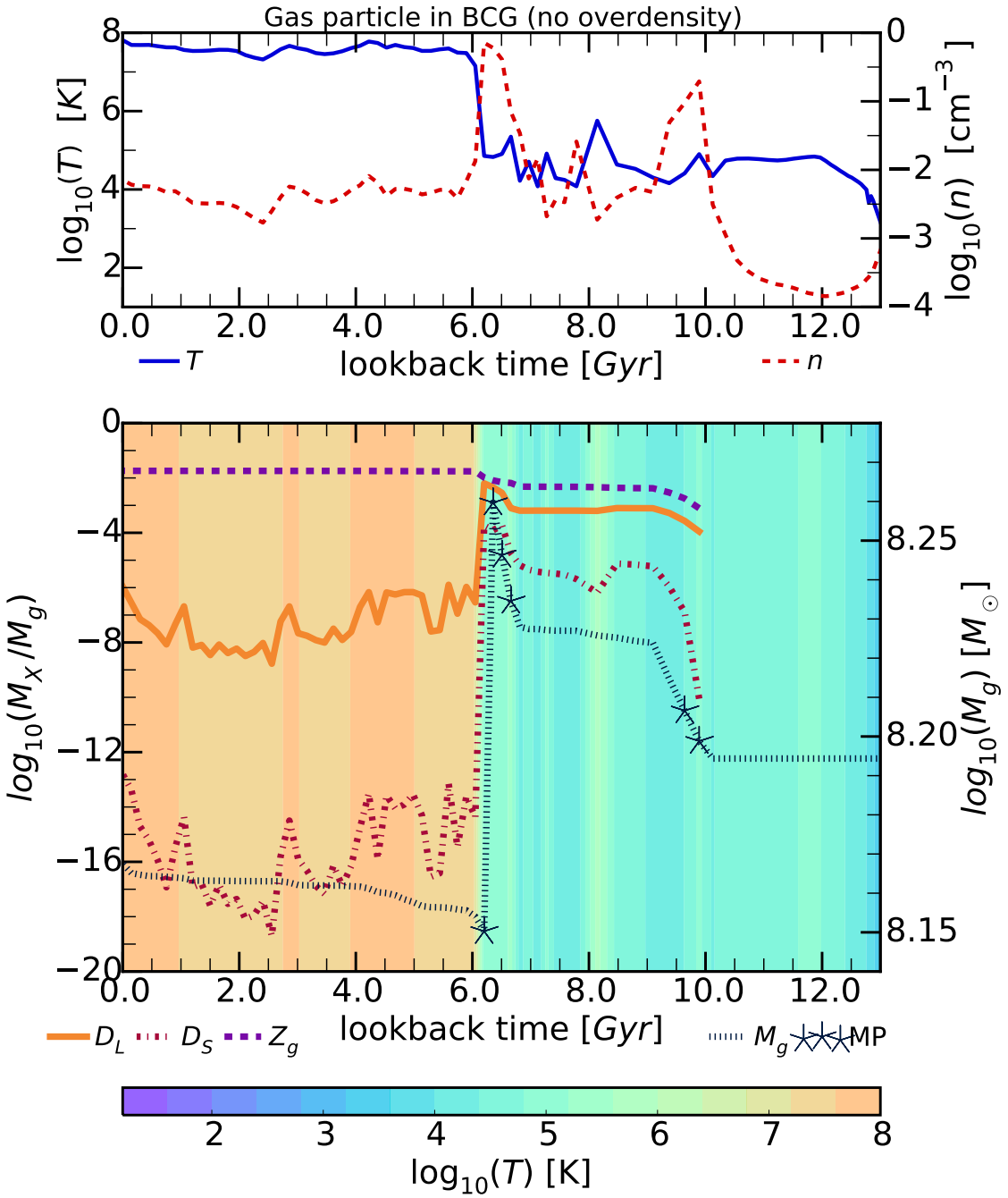

Figure 5.3: Same as Figure 5.2 but for a gas particle residing in the BCG by $z = 0$. The colorbar gradient for temperature is fixed for both of the lower plots in the two figures.

Figure 5.3 represents the evolution of another particle which instead ends up in the brightest cluster galaxy (BCG) by $z = 0$. This gas particle is first enriched with gas metals and large grains as soon as it becomes multiphase and enters a

cold overdensity of star forming gas. This period lasts a few hundred million years around 10 Gyrs in t_{lb}. The particle density spikes, and with it shattering increases and produces small grains. At 8 Gyr the particle temperature increases above 10^5 K for a while, increasing the efficiency of sputtering enough to cause a small dip of DtG, visible (almost) only for small grains. This is because the sputtering timescale for small grains is 10 times smaller than that for large grains. At a t_{lb} of about 6.5 Gyrs the particle enters another cold overdensity. At this time the large grains abundance approaches values, similar to the expected ISM values in galaxies (Li and Draine, 2001), close to the gas metal abundance via coagulation, and also small grains manage to rise via accretion. Shortly after, at 6 Gyrs in t_{lb}, this gas particle spawns a star particle. Soon after it enters in a hot state $T \gtrsim 10^7$ K, where it remains until the present time. In the hot state, sputtering becomes a strong source of dust destruction. Notice again the steeper decay of small grains caused by the size dependence of sputtering. The fluctuations in dust abundances after 8 Gyrs are due to slight enrichments from the surrounding star particles. While these contributions are negligible in the relatively high gas metals mass fraction, they are evident in that of large grains, and even more so in that of small grains.

5.3.2 Evolution of the global properties of dust

5.3.2.1 Dust distribution in the cluster region

In this section we analyze the global evolution of dust distribution around the central cluster. Figure 5.4 follows from top to bottom the redshifts $z = 4, 3, 2, 1, 0$, and from left to right the column densities of total gas mass, gas-phase metals, large dust and small dust grains. At each redshift we project a physical cube of size 1 Mpc around the main cluster's progenitor. Regions in which the column density is lower than $10^{-8}\sigma_{peak}$ where σ_{peak} is the peak column density, are omitted.
The maps shows that gas-phase metals approximately mirror the total gas distribution at all redshifts. Large grains follow loosely a similar pattern until $z \sim 2$. At lower z, this correlation breaks down since many particles reach $T \gtrsim T_{sp,0} = 2 \times 10^6$ K, above which sputtering erodes grains effectively, particularly small ones. Moreover, small grains are less abundant than large ones at all times and do not grow as rapidly, except in cold ($T < T_{MPh} = 5 \times 10^5$ K) star forming gas over-densities, where shattering and accretion work efficiently.
Figure 5.5 refers to the same 1 Mpc physical cube around the main progenitor. It represents from left to right the star particle column density, the star formation

rate (SFR) column density, the mass weighted mean temperature and mean number density of gas particles. These maps help in interpreting the former ones. For instance, it can be appreciated that the structures wherein dust survives and evolves undisturbed by sputtering are characterized by low temperature. They feature SFR between 0.01 and 0.1 $M_{\odot} yr^{-1}\mathrm{kpc}^{-2}$. As the cluster gains mass its average temperature rises, and sputtering begins to destroy efficiently dust in the ICM.

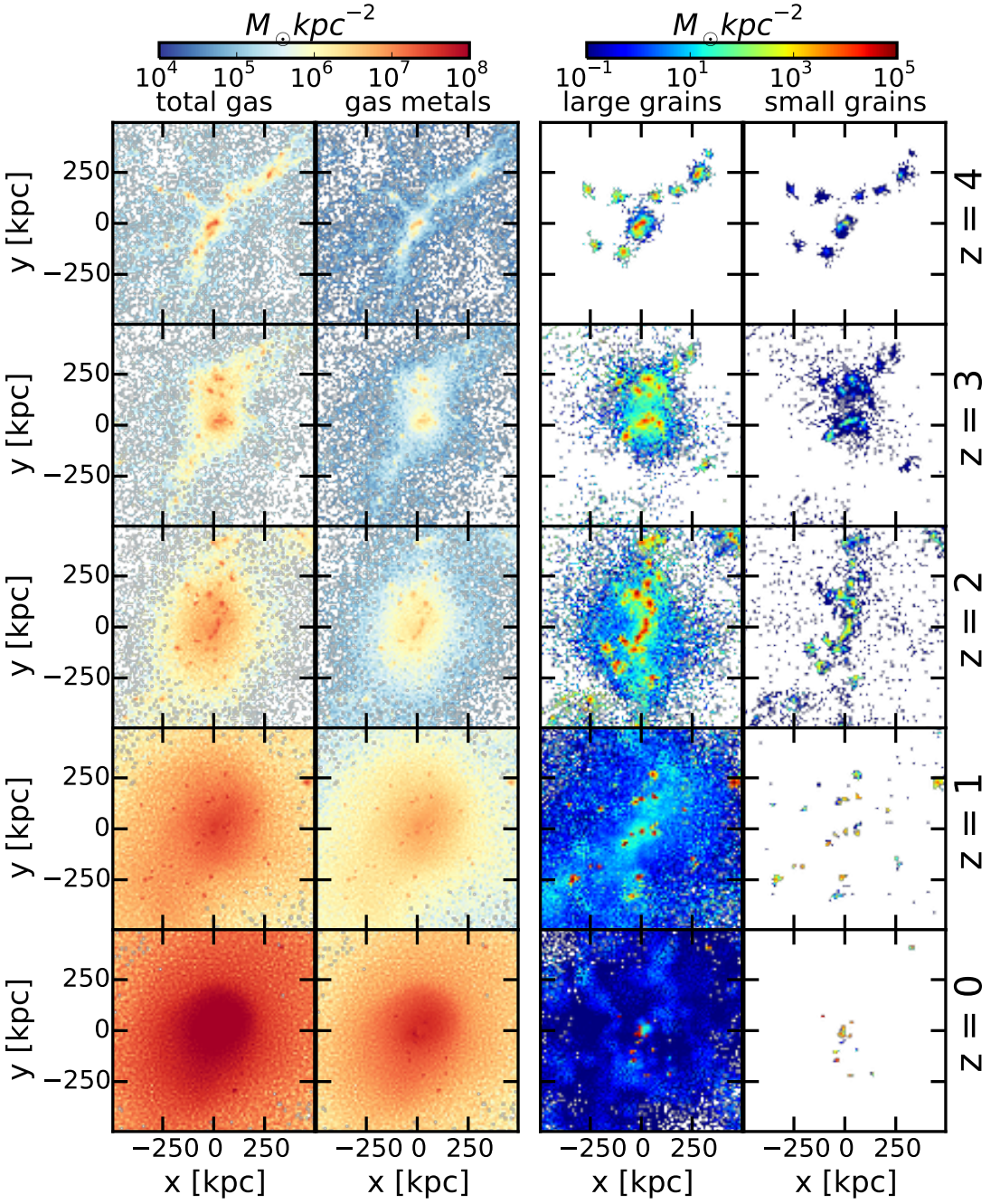

Figure 5.4: For the `fid` run, column density maps for total gas mass, gas-phase metals, large dust grains, and small dust grains, in a box of 1 Mpc in physical size over 5 redshifts (from top to bottom, z = 4, 3, 2, 1, and 0). The two colorbars are fixed at all redshifts from total gas and gas metals and for large and small grains respectively. Dust abundances trace gas mass distributions until about $z = 2$. After $z = 2$ sputtering destroys dust. Small grains evolve to the point of reaching large grains abundances only in cold overdensities, but they are destroyed more efficiently than large grains in hot gas particles.

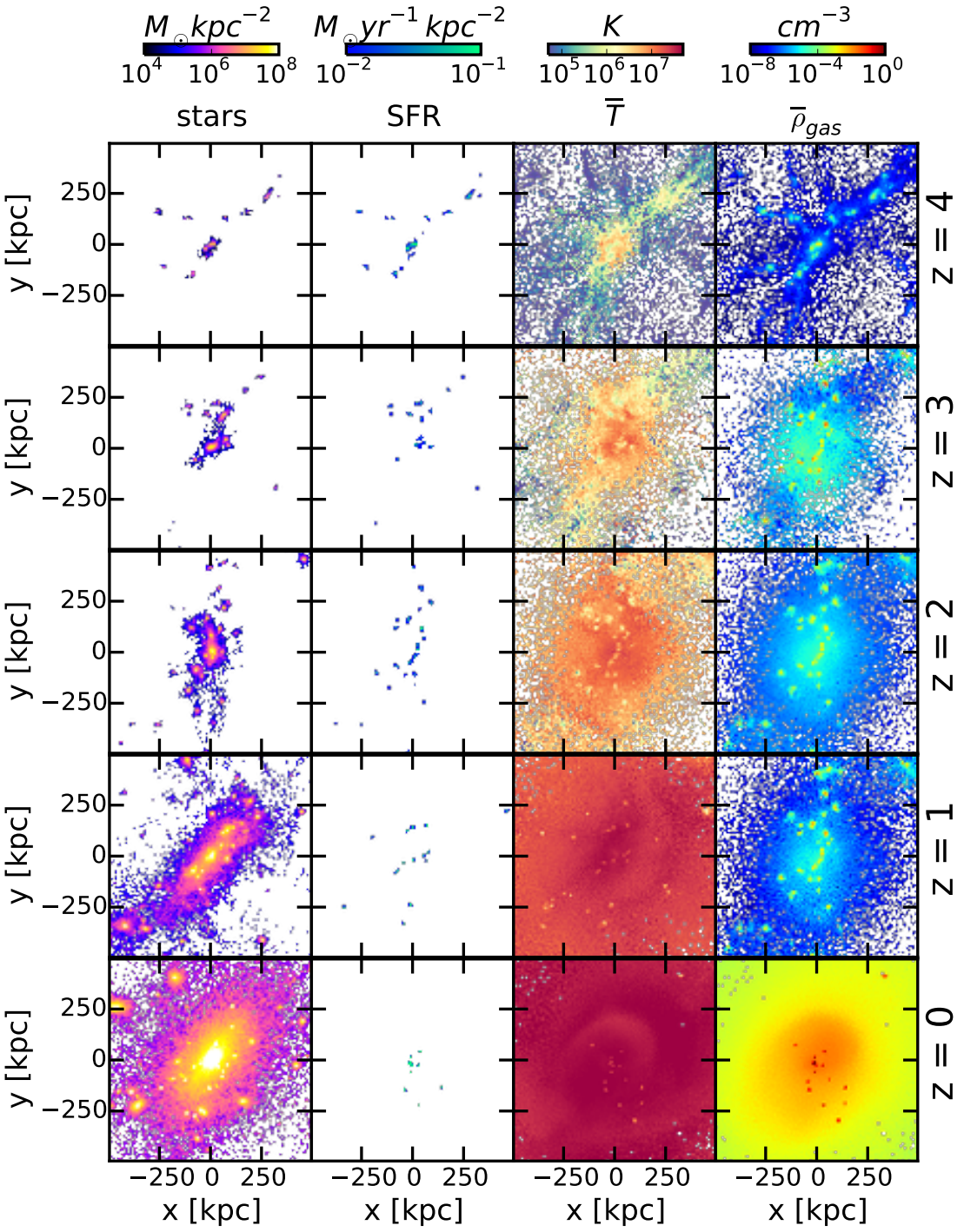

Figure 5.5: Similarly to 5.4 for the `fid` run, columns represent from left to right: maps of stellar mass and SFR column densities, and of mean mass-weighted temperature and mean number density in a box of 1 Mpc in physical size over 5 redshifts (z = 4, 3, 2, 1, and 0). Both means are weighted with the gas particle masses. Star formation occurs in cold overdensities mostly occupied by multiphase gas particles.

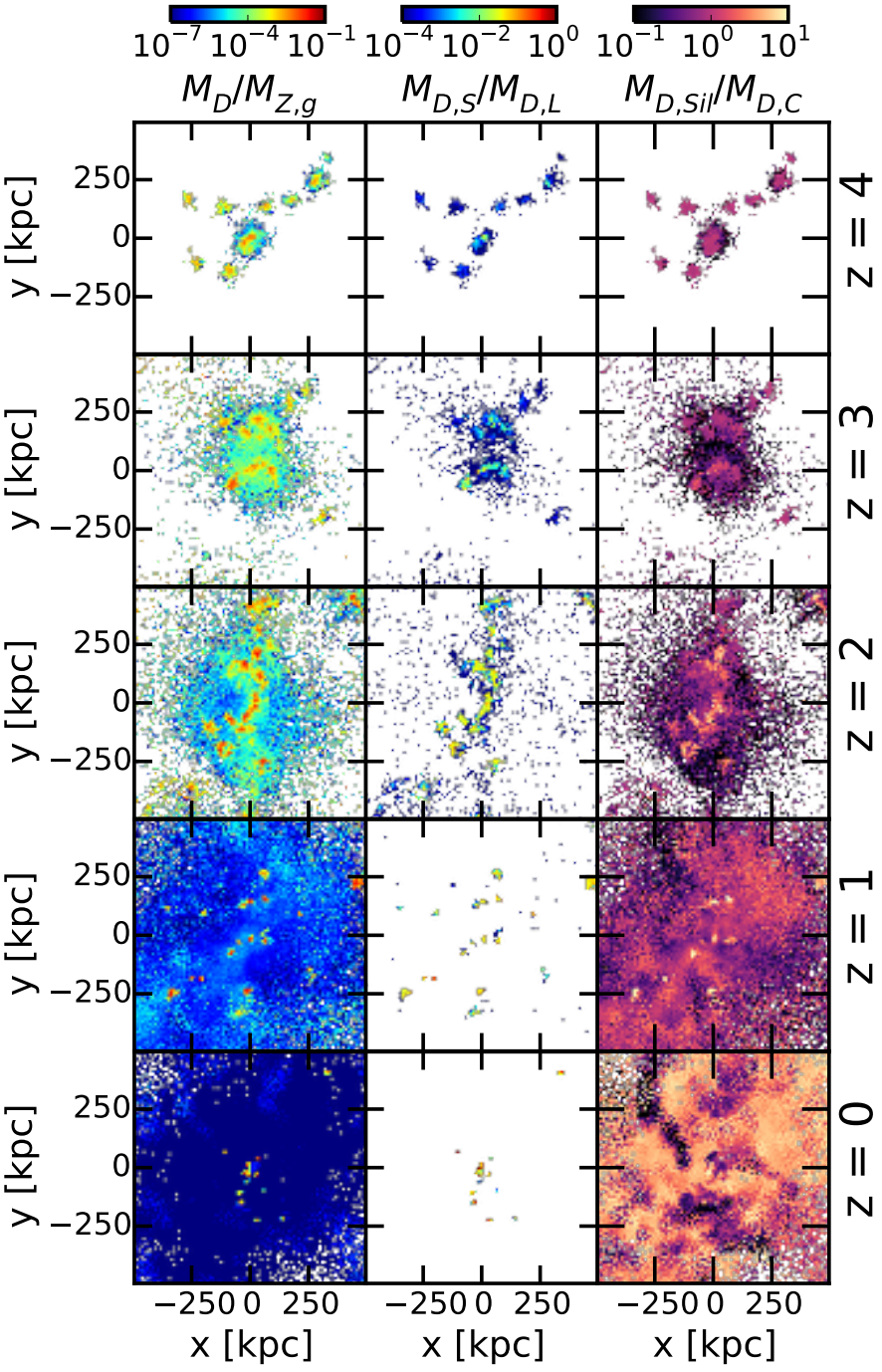

Figure 5.6: Similarly to Figure 5.4, columns represent maps of the dust-to-gas-metal ratio (left), small-to-large grain ratio (center) and silicates vs carbonaceous dust (right) in a box of 1 Mpc in physical size over 5 redshifts (z = 4, 3, 2, 1, and 0).

Figure 5.6 maps the average dust-to-gas-metal ratio (left), small-to-large grain ratio (center) and silicates vs carbonaceous dust (right). At $z > 3$, when the SF activity in the proto-cluster region is at its maximum and dust reprocessing is expected to be important, dust properties are predicted to differ significantly from those derived for the MW dust. The latter are almost always adopted in computations to account for dust reprocessing (e.g. Domínguez-Tenreiro et al., 2014, and references therein). For instance, compared to the dust models proposed for the MW by Weingartner and Draine (2001), in the central 100 kpc at z=4 the mass ratio of small/large carbon grains is more than 2 dex smaller, while the silicate/carbon mass ratio is about twice smaller.

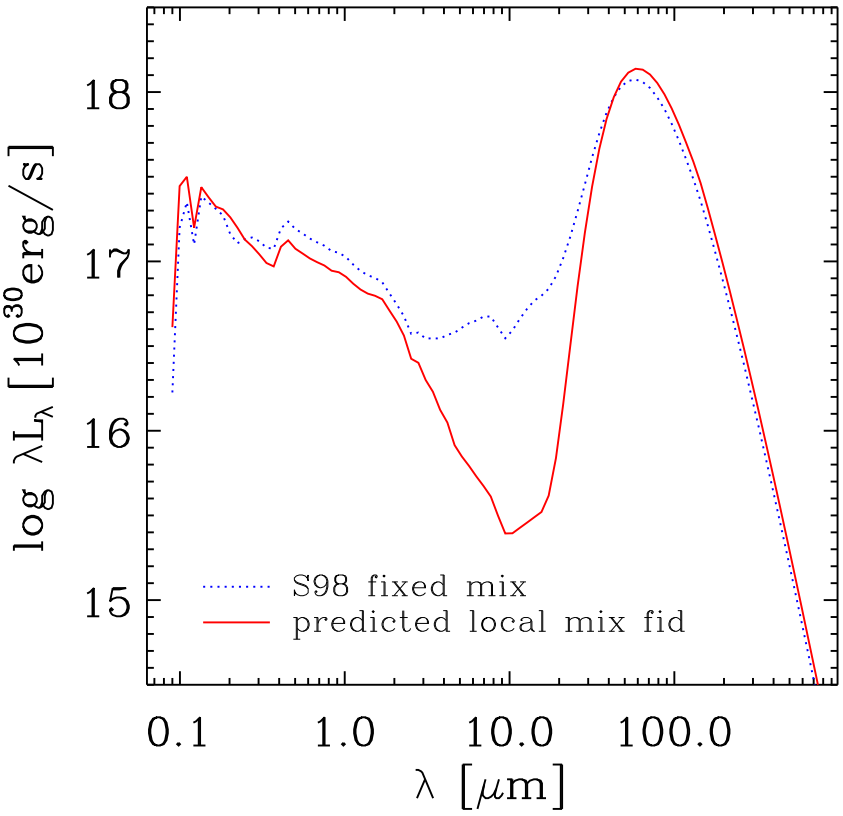

Figure 5.7: Spectral energy distributions predicted by SKIRT (Camps and Baes, 2015) for the 100 kpc central box of the region D2 at z=4. The dotted blue line has been computed adopting for the whole volume a "standard" dust mixture reproducing the properties of dust in the diffuse ISM of the MW. The solid red line instead takes into account the point to point variations predicted by the simulation for the relative abundances of small and large grains, as well as those for silicate and graphite grains. See Section 5.3.2.1 for more details.

For the most commonly adopted model 4 by Weingartner and Draine (2001), the mass ratio of small to large C grains is 0.34, while the mass ratio of Silicate to Carbon grains is 2.5. The model proposed by Silva et al. (1998) for the MW dust, usually adopted in GRASIL code features values not significantly different. We illustrate the possible consequences of these differences on the predicted SEDs in Figure 5.7. Here we show two SEDs computed with the public radiative transport code SKIRT[5] (Camps and Baes, 2015). In one case we have simply used a dust mixture similar to that adopted so far in most GRASIL (Silva et al., 1998) and all GRASIL3D (Domínguez-Tenreiro et al., 2014) applications. These codes are often employed to compute dust reprocessing in semi-analytic models and galaxy formation simulations respectively. They both allow for custom variations of the mixture, albeit this feature is seldom used due to lack of information. A spatial dependence on these properties is not implemented in the present versions. Here, the only information on dust derived from the simulation is the total dust content of each SPH particle. In another computation we have instead exploited the full information concerning the relative partition in the four categories of dust grains (graphite and silicate, small and large), by locally adjusting the adopted mixture at the position of each SPH particle, in order to reflect this partition. We fed SKIRT with a superposition of four spatial distribution of dust densities, each one to represent one of the four grain types followed by our model. The size distributions for each of them, provided by suitable input parameters of SKIRT, were the same as that proposed by Silva et al. (1998), but having 0.03 μm as the limiting size to distinguish between small and large grains respectively. Moreover, the normalization of each of the four distributions has been computed at each point according to the local density of the corresponding grain type, as predicted by the simulation. As it can be seen, the differences are important, particularly in the optical to mid-IR regime. We plan to explore in detail the observational consequences of these differences in the near future.

The ratio silicate-to-carbon dust takes some time to reach values close to those adopted in "standard" dust mixtures. Actually the ratio arising from dust production by stars is significantly lower in the model, and its increase occurs via dust evolution in the ISM. The behavior can be appreciated from the maps shown in Fig.5.8. From left to right, the three columns compare maps of the ratio for the fiducial run (`fid`), the run including only dust production from stars and sputtering (`f-crsp`), and the run in which the silicate dust is produced by stars adopting the prescription by

[5]http://www.skirt.ugent.be

Dwek (1998) (`f-dw`, see Section 5.2.4.1) respectively.

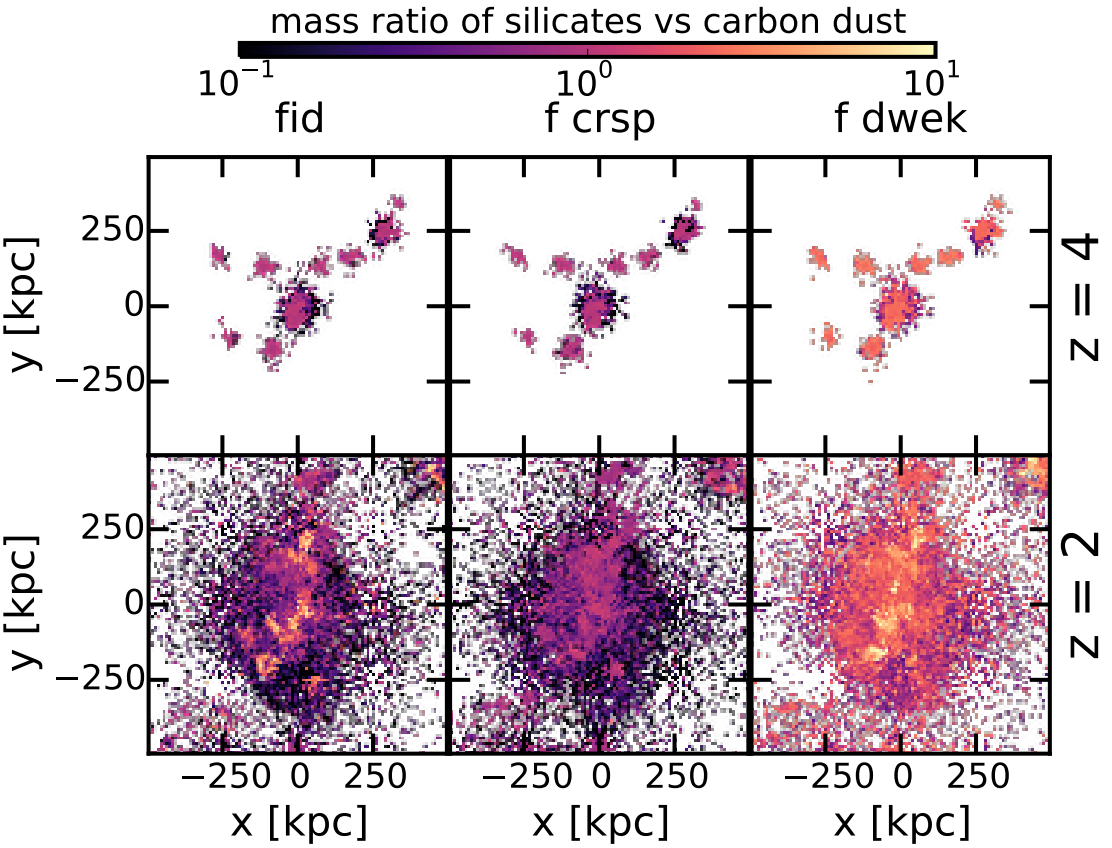

Figure 5.8: Similarly to Figure 5.6 right column, The three columns compare maps of the ratio for the fiducial run (`fid`), the run including only dust production from stars and sputtering(`f-crsp`), and the run in which the silicate dust is produced by stars adopting the prescription by Dwek (1998)

At early time z=4, the first two runs are virtually indistinguishable. It is also worth noticing that the last one is characterized by substantially higher Sil-to-C ratios, already closer to, or even higher than, the standard one. Indeed the prescription put forward by Dwek (1998) is substantially more liberal in using the ejecta to produce silicate dust. At lower redshift z=2, when evolution in the ISM has been important (if included in the computation), the fiducial run has increased the ratio in most of the region. This is not the case for the production and sputtering only run (`f-crsp`, lacking all the processes causing dust evolution in the cold ISM). Also the `f-dw` run does not show a sizable increment with respect to z=4, but in that case it was already high. This is because it leaves by construction less silicate elements in the gas phase at stellar production, meaning that gas accretion onto grains has less to add. The time evolution of the silicate-to-carbon ratio, integrated over r_{200}

is also shown in a later figure.

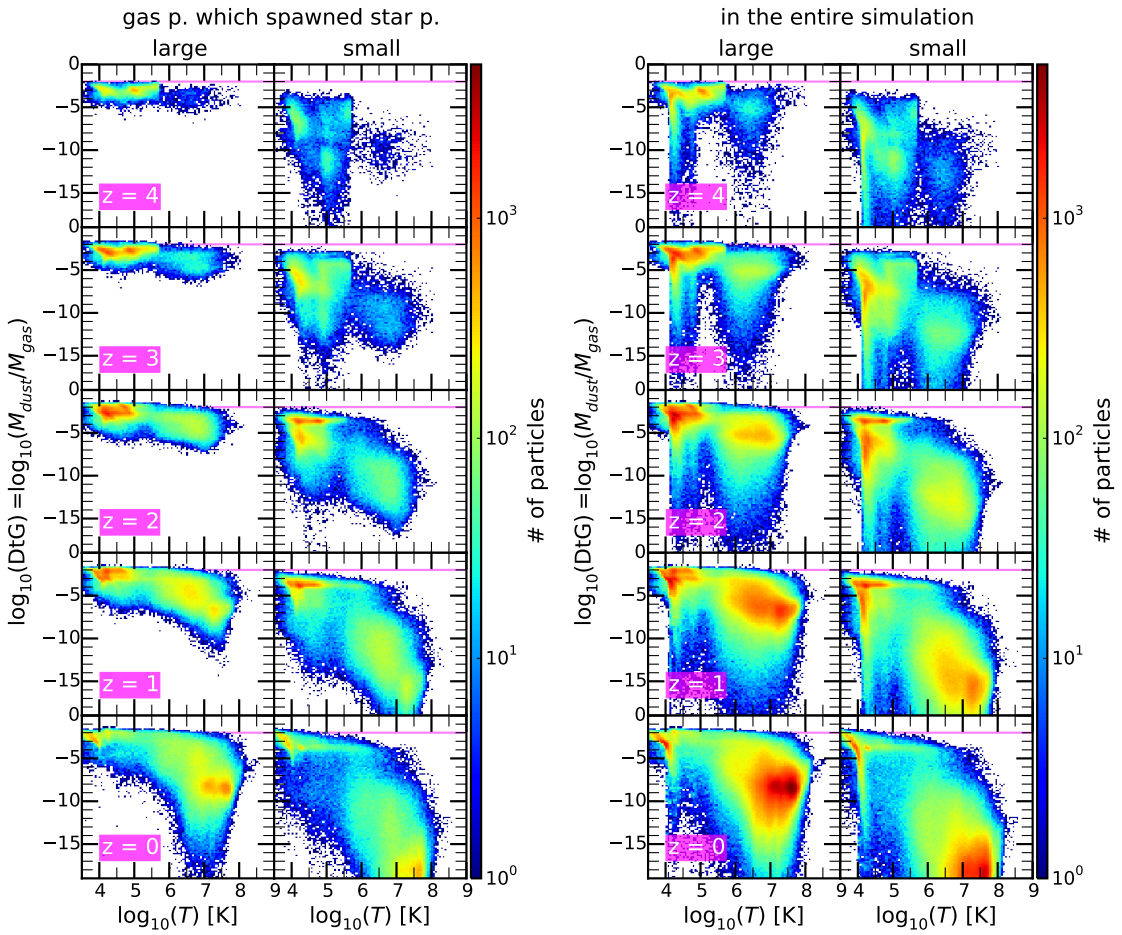

Figure 5.9: 2D Histograms of the total DtG vs temperature for gas particles which have spawned star particles in their past (left) and in the entire simulation (right) for the fiducial run and over 5 redshifts (z = 4, 3, 2, 1, and 0). The magenta line represents DtG $=10^{-2}$, close to the commonly accepted ISM dust abundance in the MW.

5.3.2.2 Temperature dependence of dust contents

Additional insights on how and when the various processes affect the dust content of the SPH gas particles can be obtained from inspection of Figure 5.9. Here we plot 2D histograms for DtG (y-axis) vs temperature (x-axis) over the usual 5 redshifts. DtGs are separately shown for large and small grains. The figure on the right refers to the entire simulation. That on the left includes instead only particles that have spawned at least one stellar particle before. This is meant to select preferentially

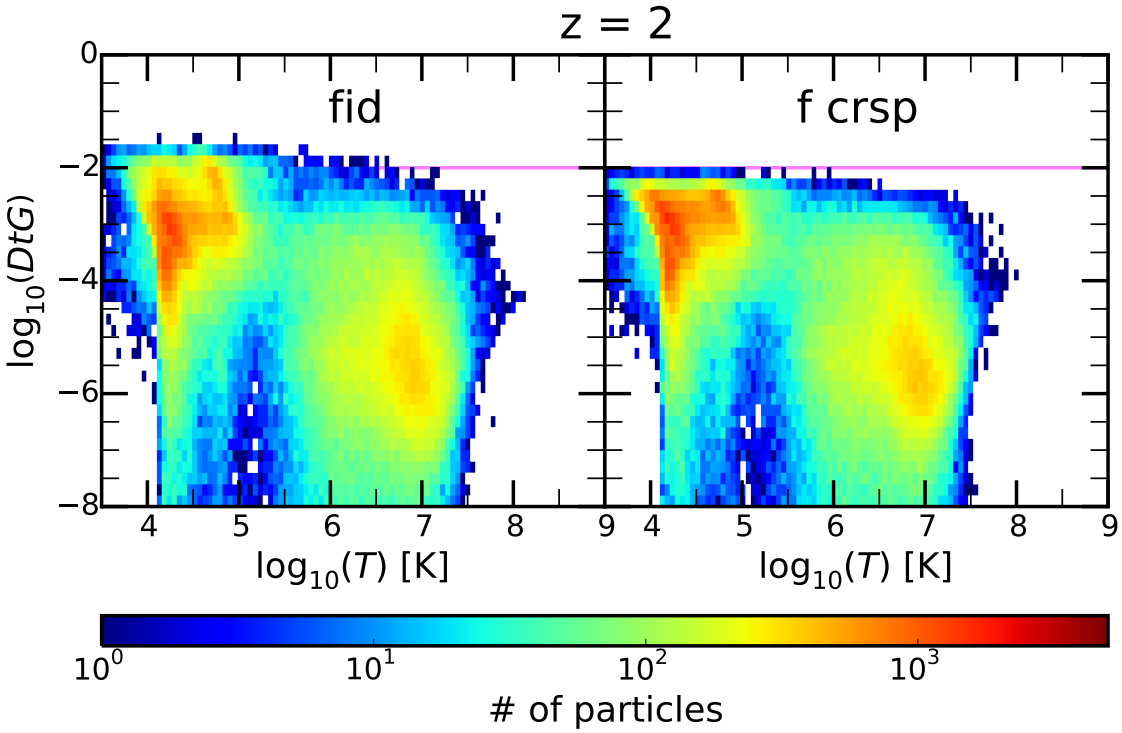

Figure 5.10: 2D histogram of DtG vs temperature within the `fid` and `f-crsp` at $z = 2$ including all gas particles.

gas particles which have spent a significant fraction of their life in a star forming environment.

At $z \geq 3$ large grains show a peak in the two dimensional distributions at $T \lesssim 10^4$ and DtG $\sim 10^{-4}$. This last value is about two orders of magnitude below the standard Galactic DtG of $\simeq 0.01$, marked by horizontal magenta lines in the panels. Indeed, at these early epochs the evolutionary processes in the ISM have not had sufficient time to affect much the dust content of most SPH particles. We have verified this by comparing with the run `f-crsp`. The major effect of ISM evolution before $z \simeq 3$ is the production of a certain amount of small grains by sputtering. ISM evolution effects manifest appreciably at $z = 2$. A population of gas particles featuring DtG close to 10^{-2} for large grains and 10^{-3} for small ones shows up at $T \lesssim 10^5$. The particles belonging to this population have undergone multiphase periods, during which accretion onto small grains and their coagulation to form large ones have raised the DtG up to values similar to the Galactic one. Indeed these local peaks appears very similar in the right and in the left figures. As pointed out, the latter is meant to select gas particles characterized by multiphase star forming periods in their past. Moreover, in run `f-crsp`, gas particles featuring DtG

$\geq 10^{-2}$ are not produced, as it can be seen in Figure 5.10. In this case the peak of the DtG distribution remains 1 to 2 orders of magnitude lower even at $z \leq 2$, only becoming more and more populated.

At still lower redshift the high temperatures reached by most SPH gas particles promote efficient thermal sputtering. As a result, a well defined maximum in the 2D histograms of the entire simulation plots develops at $T \gtrsim 10^7$ and at very low DtG$\lesssim 10^{-5}$ for large grains. The peak for small grains occurs at an even smaller DtG, since they are more strongly disrupted by sputtering.

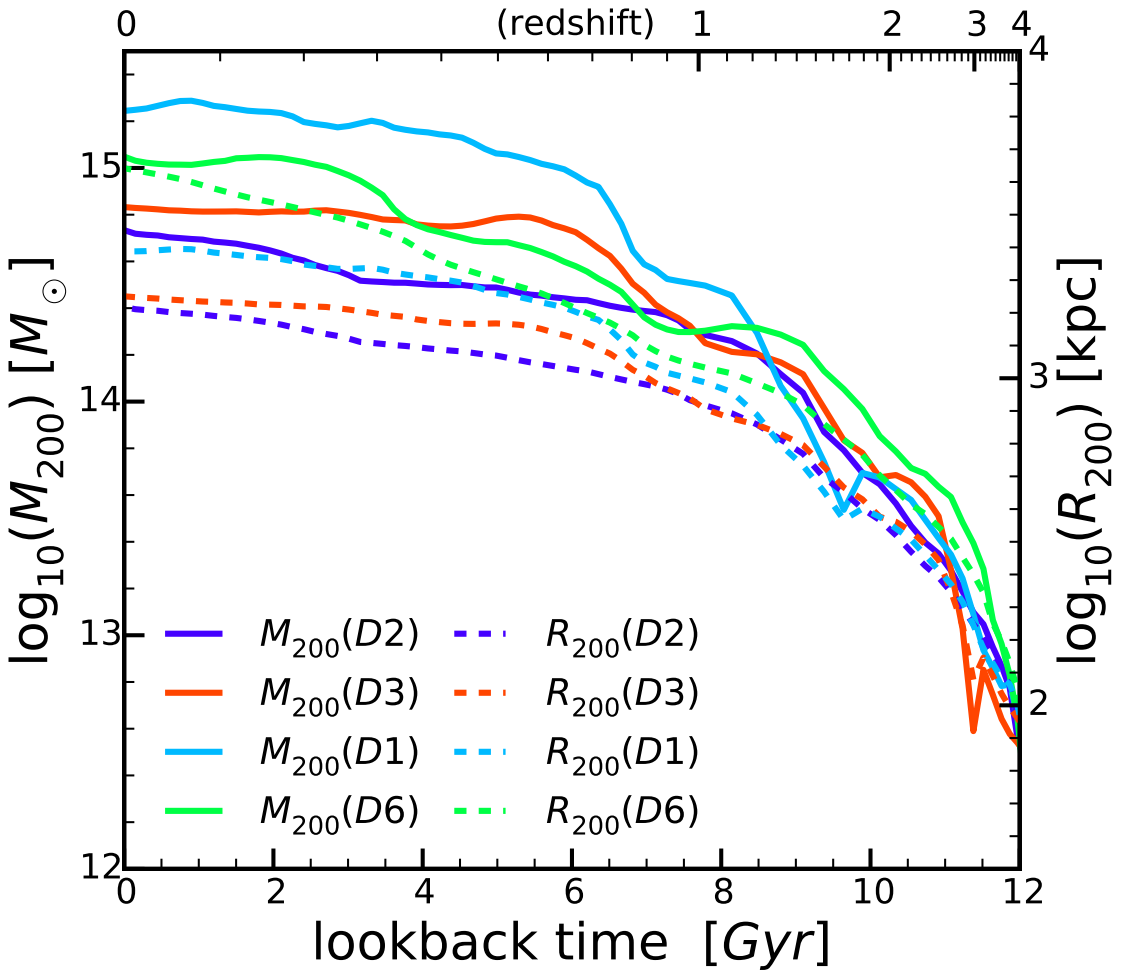

Figure 5.11: M200 and R200 of the fiducial run for the D2, D3, D1, and D6 regions.

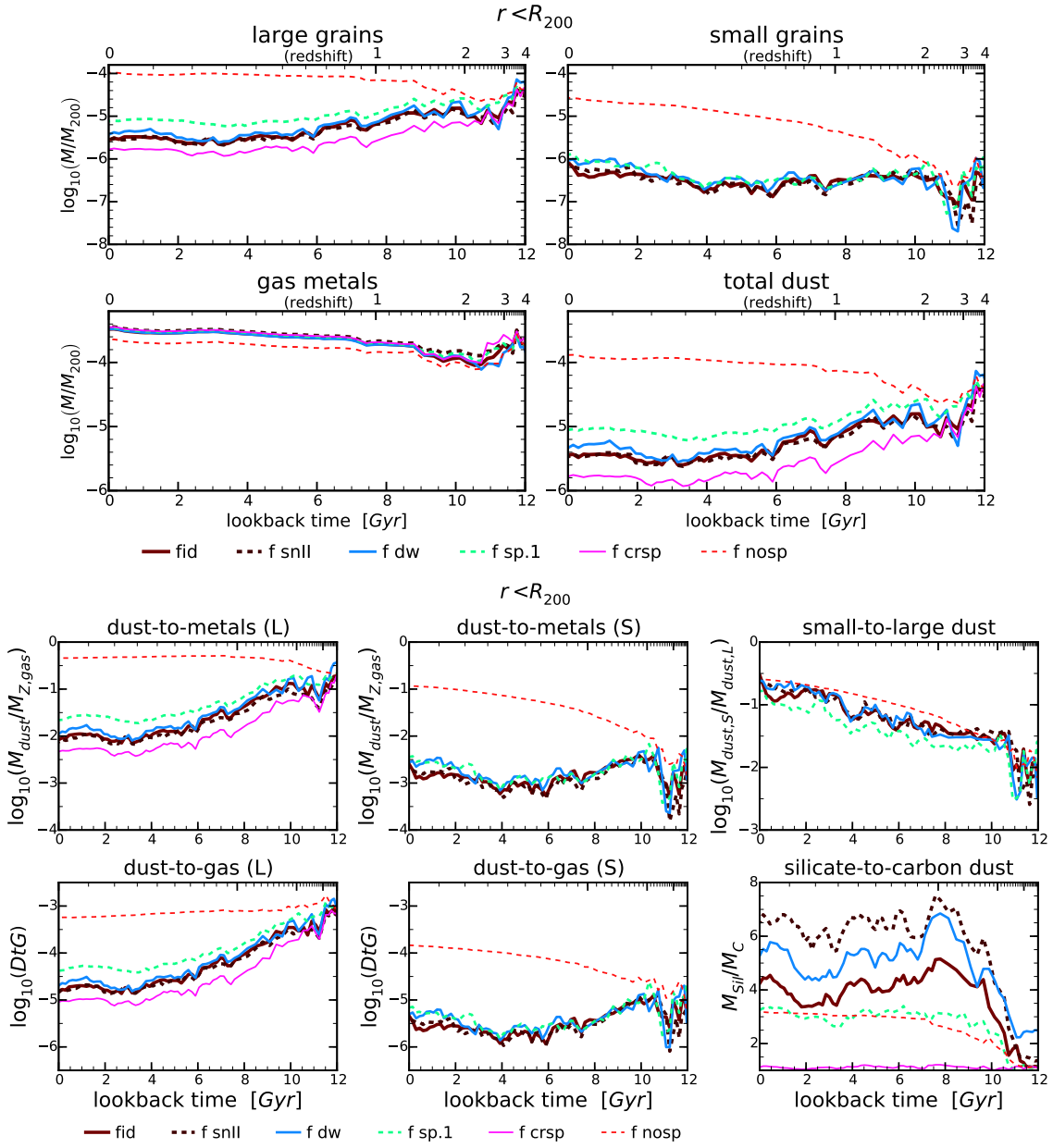

Figure 5.12: Time evolution within R_{200} of the main progenitor for a selection of runs. (*top 4 plots*) masses of large grains, small grains, gas metals, total dust mass and (*bottom 6 plots*) large-dust-to-gas-metal, small-dust-to-gas-metal, small-to-large ratios, DtG for large and small grains, and lastly the mass ratio between carbonaceous dust and silicates. Small grains are affected more strongly than large grains by the timescales of the evolution processes.

5.3.2.3 Evolution history of run variations

Figure 5.12 illustrates the evolutionary history of various masses computed within R_{200}, in the main progenitor of the $z = 0$ cluster. We include results for a selection of run variations on the D2 region. The 4 top plots show the gas metal and dust masses normalized to the evolving M_{200}, while the 6 plots in the bottom show various interesting ratios. In order to facilitate the interpretation, the evolution of M_{200} and R_{200} can be seen in Figure 5.11.

From the total dust panel we can appreciate that, excluding the run without sputtering `f-nosp`, the dust production is faster than or comparable to the increase of the cluster mass only in the t_{lb} lapse between 11 and 9 Gyr and at $t_{lb} \lesssim 4$ Gyr. In the former interval, this is achieved thanks to the combined effect of shattering, accretion and coagulation occurring in the the gas, which enhance the dust content by a factor $\sim 2 - 3$ after $t_{lb} \sim 10$ Gyr, as can be understood by comparing the runs `fid` with `f-crsp`. In the latter run, the three above mentioned processes are switched off, and the ratio M_{dust}/M_{200} is monotonically decreasing down to low z. The late $t_{lb} \lesssim 4$ Gyr flattening of the evolution is instead related to slow down of the M_{200} increase and to the fact that sputtering has already destroyed most of the dust in the hot ICM.

By adopting the (Dwek, 1998) recipe to compute the production rate of silicate grains from stars (run `f-dw`), more liberal than our fiducial method imposing the chemical composition of olivine, we get about 50% more dust at early time $t_{lb} \gtrsim 9$ Gyr, and a higher ratio M_{sil}/M_C over the whole evolution.

It is interesting to note that by considering only the SNII channel for the production of dust (run `f-snII`), the total dust content is somewhat under-predicted with respect to the fiducial run by up to $\sim 50\%$. But what is more important is that the ratio M_{sil}/M_C is significantly over-predicted. Thus this approximation, sometimes adopted in other works (e.g. Hou et al., 2016; Aoyama et al., 2017; Hou et al., 2017; Chen et al., 2018b) seems to be insufficient at least for certain purposes, such as computing the radiative effects of dust.

As we already pointed out, in the fiducial run the mass fraction of small grains at high redshift, when SF is most active in the simulated region is much lower than that of standard mixtures (~ 0.2). These mixtures are calibrated on the average properties of MW dust. This result is quite robust, in the sense that occurs in all the run variations we considered. On the other hand, the ratio M_{sil}/M_C is not very different from the standard value ~ 2 at early time, while it ends up significantly

higher in most runs. The only exception are those runs with no or simply reduced sputtering (runs `f-nosp`) and `f-sp.2`), in which the ratio increases less. The latter run could be also more consistent than the fiducial one with recent estimates of dust content in clusters at low redshift (see Section 5.3.3). On average, the total dust surviving in `f-sp.2` is a factor of 3 greater than in `fid`. This dust excess is almost entirely due to the increased survival of large grains in the hot ICM, while small grains do not deviate significantly in the two cases. This could seem at first sight unexpected, since sputtering affects more promptly small grains than large ones (Eq. 5.18). What happens is that increasing its timescale by a factor of 5 impacts on the survival of large grains, but the process remains still sufficiently effective to obliterate almost entirely small ones in the hot ICM. Consequently, in the hot environment we predict that the small-to-large grain ratio is affected considerably. In both `fid` and `f-sp.2`, the small grain content shown in Figure 5.12 comes from regions characterized by gas temperature $\lesssim 10^6$ K.

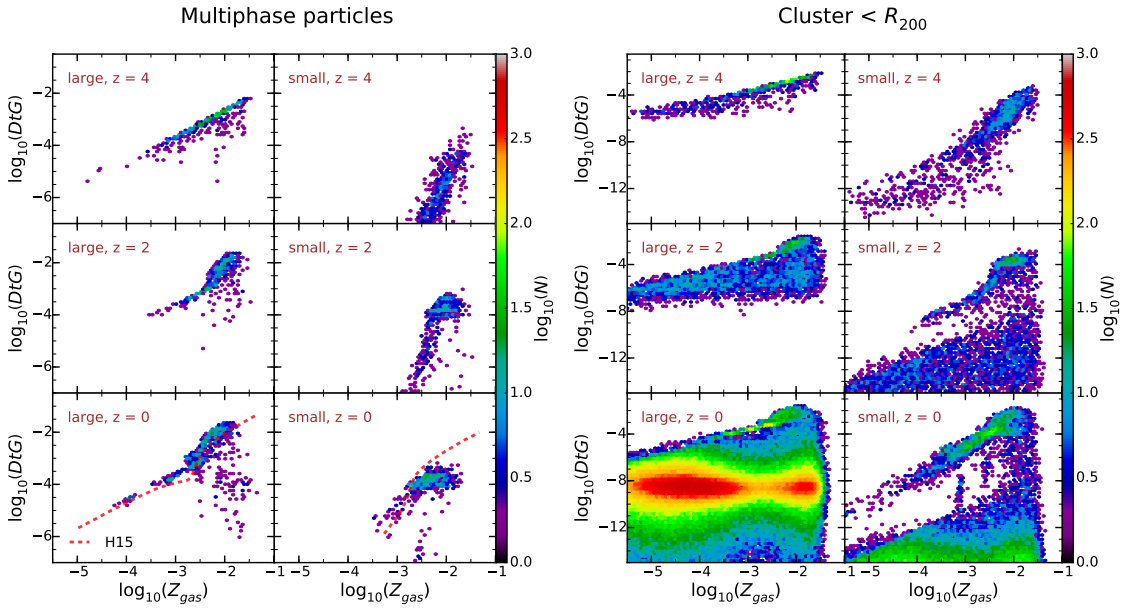

Figure 5.13: 2D histogram of the DtG vs gas metallicity for multiphase star forming gas particles (left) and for all gas particles (right) in the standard run `fid` within R_{200}. The red dashed lines represent the relationship predicted by the one-zone model by Hirashita (2015).

5.3.2.4 DtG and metallicity

Figure 5.13 presents 2D histograms of the DtG vs gas metallicity Z_{gas} at $z = 4$, 2, and 0 for gas particles which are either multiphase in the entire simulated region

(left) or within R_{200} of the main cluster (right). In both cases we used the `fid` run.

Looking at the multiphase star forming particles, we notice that at an early time of $z = 4$, the gas particles cluster along a linear relationship between DtG of large grains and Z. Large grains dominate the dust content so this also represents the total behaviour. In this initial phase, the often adopted approximation of a constant ratio between dust and gas metal content is qualitatively good enough over the entire metallicity range of star forming particles. Note that the normalization of this linear relationship between DtG and Z is lower by a factor ~ 3 than that generally adopted (i.e. DtG $\simeq 0.01$ for $Z \simeq Z_{\odot}$). The linearity arises because initially the dominating mechanism responsible for the presence of dust in the system is production by stars, for which the basic assumption is that a certain fraction of produced metals goes to the solid state rather than gaseous form. As time goes on, the ISM evolution processes boost the dust content for a given metallicity. Accretion of gas metals onto small grains provides sufficient mass to enhance the coagulation of small grains onto large ones. Hence, coagulation dominates over shattering in dense regions. This occurs only above a critical $\log Z \simeq -2,5$ for the fiducial parameters, producing a more than linear increase of DtG with Z. However, at still 2-3 times higher Z, the DtG slope slows down again toward a linear relationship, now featuring a normalization close to that given by standard MW values.

As noticed by Aoyama et al. (2017, see their figure 7), the overall result of this evolution is that at late time $z \leq 2$ multiphase particles tend to concentrate in a region whose shape resembles the line along which the one-zone model by Hirashita (2015) *evolves in time*, shown in the figure with a black line. However when evaluating this result one should keep in mind the very different nature of one-zone computations and simulations. In the latter the gas and star density fields are sampled with a certain resolution. In the one-zone model, both quantities reported in the 2D histograms of Figure 5.13 are a function of time. In other words, the system moves with time along the line. On the contrary, in the simulation at any given time the gas particles have a broad distribution in the plane, albeit with well defined concentrations.

The right panels of Figure 5.13 shows that when the 2D distributions are computed for the main cluster of the region and including also non multiphase particles, a population of particles characterized by very low values of DtG shows up. This population becomes more and more dominant over time, because it is produced by sputtering which efficiently destroy dust grains in the hot ICM at $T \gtrsim 10^6$ K.

5.3.3 Observational consistency

5.3.3.1 Dust abundance vs metallicity

In Figure 5.14 we show the 2D distribution of DtG vs (gas) Oxygen abundances of star forming multiphase particles at $z = 0$, for the four regions on which we run our fiducial model. This information is similar to that already reported in Figure 5.13, but now for all the regions considered in the present work, and in a form more directly comparable with observations. We include in the figure data on nearby galaxy samples from Kennicutt et al. (2011) and Madden et al. (2012). It is apparent the broad similarity between the distribution of simulated and the data points. Note however that the former refers to individual particles residing in star forming regions rather than entire unresolved galaxies, which could explain the larger dispersion. In any case, it is reassuring that the model reproduces reasonably well the observed trend of dust abundance with metallicity.

5.3.3.2 Dust content at low redshift

In this section we briefly compare with the still limited reliable detections of global dust content in galaxy clusters. Gutiérrez and López-Corredoira (2017) analyzed 327 clusters of galaxies in the redshift range 0.06-0.70, using maps and catalogs from the Herschel MerMES project. They reported average integrated fluxes of 118.2, 82.3 and 38.0 mJy within 5 arcmin of the cluster centers at 250 μm, 350 μm and 500 μm respectively. Adopting their same assumptions on the dust optical properties and temperature (essentially the same as the "average" MW dust), these fluxes translate to a total dust mass of 1.7×10^9 $M_\odot$. Given that their average cluster mass is 1.1×10^{14} $M_\odot$ within the same radius, the fraction of dust mass turns out to be about 1.5×10^{-5}. For the main clusters in our four regions we predict an average fraction in the same redshift range of 0.25×10^{-5}. Thus we are under-predicting the dust content by a factor ~ 6. On one hand this discrepancy could be due at least in part to the quite strong and uncertain assumptions entering into the masses estimated from observations, such as the dust optical properties and (constant) temperature. In particular, they adopted a long wavelength emissivity that scales as $\lambda^{-\beta}$, with $\beta = 2$, which is the standard result of first principle computations of dust opacities by Draine and Lee (1984). There are several indications that dust emission is better represented at long λ by a shallower index $\beta \sim 1.5$, when it is described by single T blackbody (e.g. Planck Collaboration (XXII) et al., 2015).

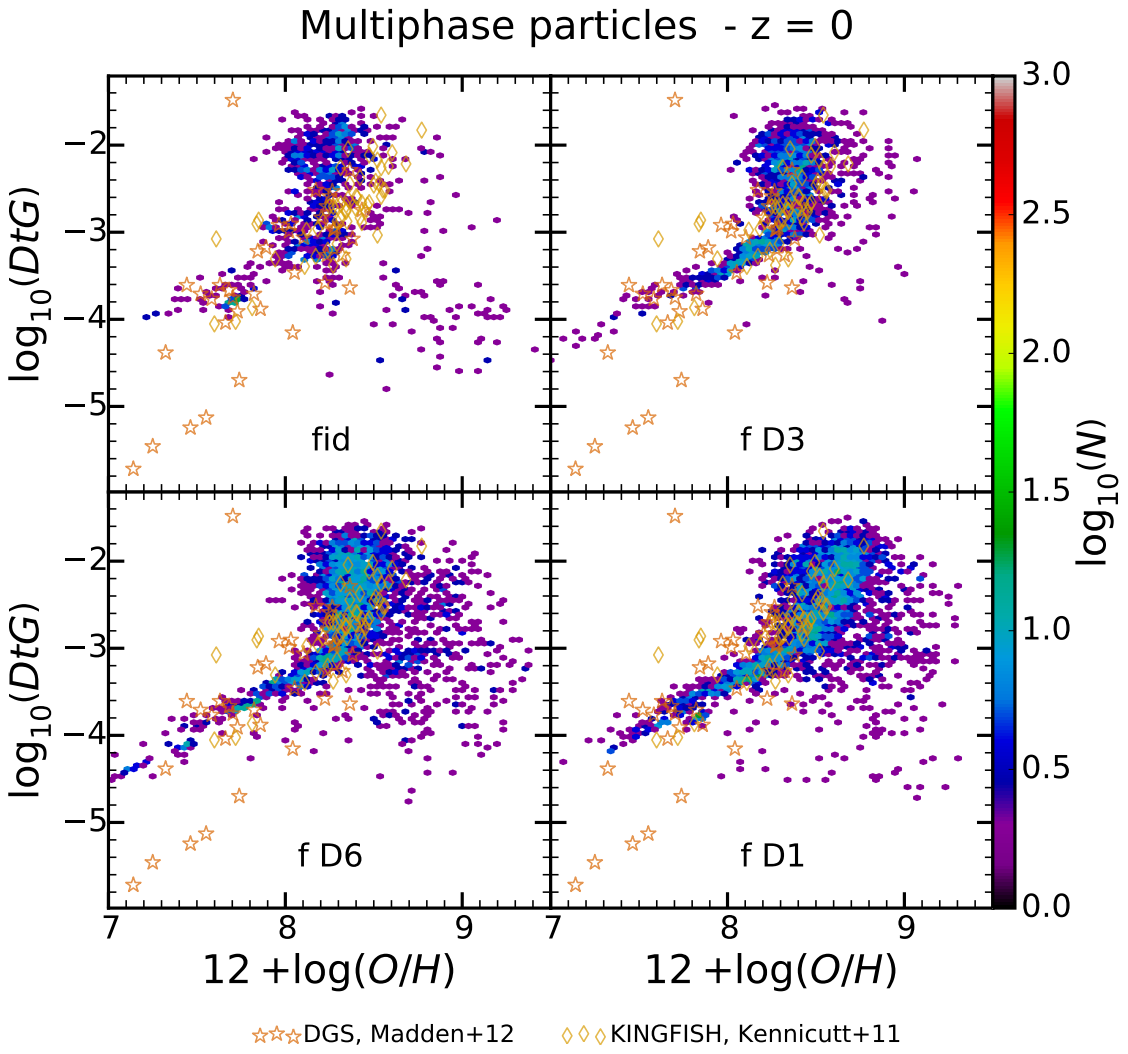

Figure 5.14: 2D histogram of the DtG vs Oxygen abundance at $z = 0$ compared with galactic data from Kennicutt et al. (2011) (red diamonds) and Madden et al. (2012) (black stars).

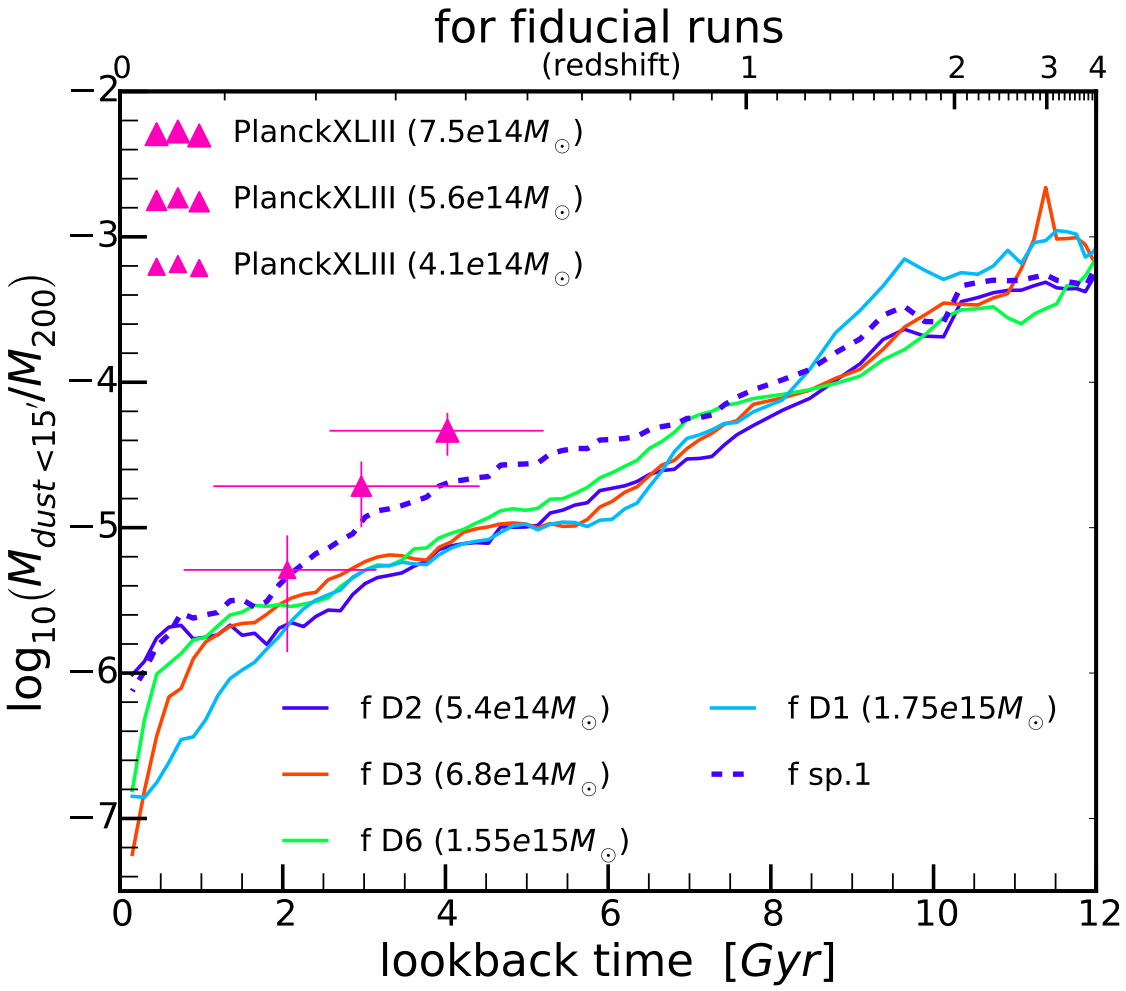

Figure 5.15: For the the 4 different zoom-in cluster simulations considered in this work (`fid (D2), f-D3, f-D1, f-D6`) we show the evolution of the ratio between the dust mass within a 15 arcmin aperture and M_{200}. For the region D2, we show also the run with reduced sputtering, `f-sp.2`. These are compared with the same quantity as estimated in Planck Collaboration (XLIII) et al. (2016), for the whole sample (central point) and for the subsamples at $z < 0.25$ and $z > 0.25$. The error-bars represent dispersions.

From a physical point of view, this could be actually the result of a spread in dust temperature. In any case, adopting a smaller β in interpreting observed fluxes would lead to smaller dust masses in better agreement with our result. On the other hand the dust content at low redshift in our model clusters is strongly dictated by the sputtering efficiency. For instance, assuming a timescale longer than that favored by existing literature (e.g. Tsai and Mathews, 1995, and references therein) by a factor 5 (Eq. 5.18), the final dust content increases by a factor ~ 3 (See Fig. 5.12).
Planck Collaboration (XLIII) et al. (2016) performed a stacking analysis of several hundreds of clusters, wherein IRAS and Planck data are combined to provide a well sampled FIR-submm average SED of clusters. Then they fit this SED with modified black body models to derive dust masses and temperature simultaneously. For the whole sample, whose mean redshift is 0.26 and mean total mass is $M_{200} = 5.6 \times 10^{14}$ $M_\odot$, the estimated dust mass is 1.1×10^{10} $M_\odot$, adopting their preferred emissivity index $\beta = 1.5$. Strictly speaking their dust mass refers to the radius of 15 arcmin within which the fluxes have been integrated.
In Figure 5.15, the time evolution of the ratio $M_{dust}(r < 15')/M_{200}$ is shown individually for the 4 clusters simulated with the fiducial set of parameters. This is compared with the same ratio as derived from these Planck data. The comparison is shown not only with the full sample, but also for the two subsample at $z \leq 0.25$ and $z > 0.25$, comprising 307 and 254 clusters respectively. This figure confirms that our fiducial models under-predict the dust content of the clusters, albeit by a smaller factor ~ 3. As such, the model with increased sputtering timescale turns out to be in reasonable agreement with the data.

6

Conclusion, summary, and future prospects

6.1 In brief

In this work we have introduced a state of the art treatment of dust production and evolution in our version of the simulation code GADGET-3. We take advantage of the detailed description of chemical evolution already included in our version of GADGET-3 to trace separately the two dust species that are believed to populate the ISM, namely carbonaceous and silicate grains. We also trace at a basic level the continuum size distribution of grains by means of the two-grain-size approximation introduced and tested by Hirashita (2015). In our code, large (nominally 0.1μm) dust grains are originated by simulated star particles from three stellar channels, AGB winds, core collapse SNae, and SNIa. Along with metals, these grains are spread to the surrounding SPH gas particles. Within gas particles, we model other ISM evolution processes that affect dust properties. In brief, large grains are shattered onto small (nominally 0.01μm) grains if the gas density is low enough. On the other hand in dense star forming SPH gas particles, metals accrete onto small grains and small grains coagulate onto large grains. We also take into account dust destruction by SN shocks and by sputtering in the hot ($T \gtrsim 10^6$ K) ICM. We evaluate timescales for the above mentioned ISM processes as a function of the physical conditions of the SPH particles, and within each we evolve the dust and gas metal contents. As remarked above, the dust contents are divided into 4 types, namely large carbon, small carbon, large silicates, and small silicates.

As a first test, we apply the method to cosmological zoom-in simulations of four massive ($M_{200} \geq 3 \times 10^{14} M_\odot$) galaxy clusters. During the early stages of assembly of the cluster at $z \gtrsim 3$, where the star formation activity is at its maximum in our simulations, the proto-cluster regions are rich of dusty gas (Figure 5.4). Compared

to runs in which only dust production in stellar ejecta is active, runs including processes occurring in the cold ISM enhance the dust content by a factor $2-3$. However, the dust properties in this stage turn out to be significantly different than those observationally derived for the *average* Milky Way dust, and commonly adopted in calculations of dust reprocessing (Figure 5.8). We stress that this results is not unexpected. We show that these differences may have a strong impact on the predicted spectral energy distributions (Figure 5.7). At low redshift our model reproduces reasonably well the trend of dust abundances over metallicity as observed in local galaxies (Figure 5.145.14). However we under-produce by a factor of 2 to 3 the total dust content of clusters estimated observationally at low-z $\lesssim 0.5$ using IRAS, Planck and Herschel satellites data. This discrepancy can be solved by decreasing the efficiency of sputtering which erodes dust grains in the hot ICM (Figure 5.15).

The most immediate purpose of our effort is to have enough information on the simulated ISM/ICM to compute observational properties of simulated objects by means of radiative transfer post processing. This is in line with what we already achieved in Granato et al. (2015), but with less assumptions required on dust properties. However this work can be also regarded as a first step in the direction of a more sophisticated prescriptions for the sub-resolution physics. For instance, it will be possible to estimate the contribution of dust to the formation of molecular gas. This estimate is a primary ingredient in more advanced implementations of star formation in simulations (e.g. MUPPI, Murante et al., 2015).

6.2 Summary

Dust affects both galaxy evolution and observations. A combination of simulations and radiative transfer computations can produce mock data, to be compared with observations. Until now, however, dust properties have only been included by means of post-processing assumptions, leaving room for uncertainties, which are particularly significant at wavelengths shorter than 100 microns. To reduce these uncertainties, we implemented a state-of-the-art treatment of the production and evolution of dust grains within our simulation code, GADGET-3[1] , which we run to

[1]The group of numerical cosmology and extra-galactic astrophysics at the Astronomical Observatory of Trieste produces state-of-the art cosmological simulations, with a zoom-in technique of selected Lagrangian regions on a custom version of GADGET-3. The simulation implemented already Tree-PM dynamics, Smoothed-Particle Hydrodynamics, radiative cooling, star formation, stellar and AGN feedback, chemical evolution.

produce zoom-in simulations of massive (3×10^{14} to $10^{15} M_{\odot}$) galaxy clusters. This model traces the creation, evolution, and destruction of dust through a series of comprehensive processes. The model accounts for dust grain size, a crucial parameter for grain reprocessing calculations, via a two-grain-size approximation (Hirashita, 2015). The approximation produces correct metallicities and dust abundances both in the local Universe and in Ly-α emitters at high redshift ($z \sim 5$).
The processes work as follows: A diagram summarizing our method can be found in Figure 5.1. Hirashita's approximation was conceived as a one-zone interstellar medium (ISM) analytical model, so we had to treat it with care to ensure we could extend it to the Intracluster Medium (ICM) for simulations. The biggest change to the method was the addition of sputtering, a destruction process caused by the collision of dust with highly-energetic particles in the hot, highly-ionized diffuse medium in the outskirts of galaxies and clusters.
Another significant modification is a novel dust production mechanism. In our simulation we assume the existence of only two dust species, graphite and a silicate species called olivine ($(MgFe)SiO_4$). Most other dust production models assume a fixed dust condensation efficiency for every element (or metal, in astrophysics). We first establish what proportion each condensed metal must have with respect to the other metals, and then we store these metals into dust, subtracting them from the gas metals.

6.3 Introduction

A significant fraction of metals present in the interstellar medium (ISM) is *depleted* from the gas phase and locked into small solid particles, the *cosmic dust*. The size of these particles is distributed over a broad range, from a few tens of Å up to a few μm. In the Milky Way, about 50% of the metal mass, or about 1% of the ISM mass, is in dust. Theoretical works (e.g. Dwek, 1998) predict the first percentage to be roughly constant, and as a consequence the second is approximately proportional to the ambient gas metallicity Z_{gas}. This estimate is confirmed by observations of metal-rich galaxies, but it is subject to a broad scatter. On the other hand, low metallicity dwarf galaxies, having a low dust-to-gas (DtG) mass ratio, deviate substatially (e.g. Galametz et al., 2011; Rémy-Ruyer et al., 2014). As for the detailed chemical composition of dust, as a first approximation it is accepted that dust consists of two major chemical classes: one carbon-based, and another named “astronomical silicates", composed of essentially four elements, O, Si, Mg

and Fe. This is supported by depletion and dust-reprocessing studies (e.g. Draine, 2003; Jenkins, 2009, and references therein).
Despite this deceivingly reassuring summary of cosmic dust properties, it is clear that the situation is much more complex (e.g. Jones, 2013, and references therein). All the above mentioned properties of dust represent only the average at late cosmic times. However, observations show significant deviations, both from galaxy to galaxy in the local Universe, and within different environments of the Milky Way itself. Moreover, observations suggest substantial differences at early cosmic times. From a theoretical perspective, this is all but surprising. Indeed, dust grains constitute a living component of the ISM. Once dust grain seeds are produced, mostly in stellar outflows, they are subject to several evolutionary processes in the ambient gas, whose effectiveness depends on the physical and chemical gas conditions, as well as on the properties of the grains themselves. These processes, which we have described in Section 5.2.4, alter the abundance, chemical composition and size distribution of dust grains.
Most galaxy properties cannot be described accurately without accounting for dust. For instance, the chemical species that dust depletes are key ISM coolants. Moreover, dust surfaces catalyze the formation of molecular species such as H_2 (e.g. Barlow and Silk, 1976). H_2 is the primary constituent of molecular clouds (MCs), the star formation sites. Among all dust effects, the best studied is the dust reprocessing of radiation emitted by astrophysical objects. Therefore, dust is of paramount importance in interpreting observations. Dust absorbs efficiently stellar (or AGN) UV and optical light. The absorbed energy is thermally re-emitted in the IR, mostly at $\lambda >$ a few μm, with a peak at about 100 μm. In the local Universe, dust contributes only to less than 1% of the ISM mass. Despite being so scarce, it reprocesses about 30% of all the photons emitted by stars and AGNs (Soifer and Neugebauer, 1991). The reprocessed fraction increases as a function of the specific star formation activity of galaxies (Sanders and Mirabel, 1996). This is because in star forming objects, the primary radiative power originates from young stars, which are close or still embedded in their parent MCs (Silva et al., 1998; Granato et al., 2000; Charlot and Fall, 2000). Thus, IR turns out to be a very good observational tracer for star formation (eg Kennicutt and Evans, 2012). It is worth noticing that the absorption and scattering cross sections of grains depend not only on their composition but also, and strongly, on their radius a[2]. Therefore, reliable galactic SED models must take dust size distribution into account (Silva et al., 1998).

[2]Usually dust grains are simply approximated by spheres.

In this work, we implement within the GADGET-3 SPH code a state-of-the-art treatment of the processes affecting the production, evolution and destruction of carbonaceous and silicate dust grains. We model the size distribution of dust grains by means of the two-size approximation developed by Hirashita (2015). His work demonstrates that it is possible to reproduce the broad results of a full grain-size treatment just considering only two well-chosen representative sizes. The computation of this solution is not very demanding and therefore it is well-suited for cosmological simulations. Moreover, the method can be generalized in the future to increase the number of grain sizes.

While the GADGET-3 code is suitable for simulations of galaxy formation, we apply it here to zoom-in simulations of two massive ($\sim 10^{15} M_{\odot}$) and two smaller ($\sim 5 \times 10^{14} M_{\odot}$) galaxy clusters. We are mainly interested in the high redshift stages, where the star formation activity is at its maximum, and the proto-cluster regions are rich of cold dusty gas. The first aim of our dust evolution model is to couple it in the near future with post-processing radiative transfer computations. We plan to replace the uncertain assumptions on the dust content, chemical composition, and size distribution, with estimates derived from the computation of these properties in the simulated ISM. The presence of dust production and evolution will allow, at a second stage, to account for the role of dust as a catalyst for the formation of molecules, as well as the impact of gas heating and cooling due to dust (Montier and Giard, 2004).

A few groups have successfully included some aspects of the evolution of dust content of the ISM within hydrodynamical simulations (e.g. Bekki, 2013; McKinnon et al., 2016, 2017; Aoyama et al., 2017; Hou et al., 2017).Another possibility is to investigate the problem by means of post-processing computations (e.g. Zhukovska et al., 2016) or within semi-analytic models Popping et al. (2017). However the present work provides a more comprehensive description of dust as we predict both the size distribution and the chemical composition of dust grains *at the same time*, self consistently with a full treatment of the chemical evolution of the ISM. Moreover, while the focus of the aforementioned papers was on galactic disks, our work represents the first attempt to trace the evolution of dust component in simulations of galaxy clusters.

We follow Dwek (1998) in using a notation for metallicity that specifies when we refer to metals in the gas form Z_{gas}, metals in the solid form, i.e. dust Z_{dust}, or the sum of the two Z_{tot}. This is not a standard convention as in other works dealing with the evolution of the dust in the ISM, the symbol Z has been employed to refer to

the *total* metal fraction (metallicity) of the ISM (e.g. Calura et al., 2008; Hirashita, 2015), including both metals in gas and metals locked up in solid state grains.

6.4 Method

We implement a state-of-the-art treatment of the processes affecting the production and Interstellar Medium (ISM) evolution of carbonaceous and silicate dust grains within SPH simulations. We trace the dust grain size distribution by means of a two-size approximation. We test our method on zoom-in simulations of four massive ($M_{200} \geq 3 \times 10^{14} M_{\odot}$) galaxy clusters. We predict that during the early stages of assembly of the cluster at $z \gtrsim 3$, where the star formation activity is at its maximum in our simulations, the proto-cluster regions are rich in dusty gas. Compared to the case in which only dust production in stellar ejecta is active, if we include processes occurring in the cold ISM,the dust content is enhanced by a factor $2 - 3$. However, the dust properties in this stage turn out to be significantly different from those observationally derived for the *average* Milky Way dust, and commonly adopted in calculations of dust reprocessing. We show that these differences may have a strong impact on the predicted spectral energy distributions. At low redshift in star forming regions our model reproduces reasonably well the trend of dust abundances over metallicity as observed in local galaxies. However we under-produce by a factor of 2 to 3 the total dust content of clusters estimated observationally at low redshift, $z \lesssim 0.5$ using IRAS, Planck and Herschel satellites data. This discrepancy does not subsist by assuming a lower sputtering efficiency, which erodes dust grains in the hot Intracluster Medium (ICM).

6.5 Results

In Figure 5.14 we show the 2D distribution of DtG vs (gas) Oxygen abundances of star forming multiphase particles at $z = 0$, for the four regions on which we run our fiducial model. We include in the figure data on nearby galaxy samples from Kennicutt et al. (2011) and Madden et al. (2012). It is apparent the broad similarity between the distribution of simulated and the data points. Note however that the former refers to individual particles residing in star forming regions rather than entire unresolved galaxies, which could explain the larger dispersion. In any case, it is reassuring that the model reproduces reasonably well the observed trend

of dust abundance with metallicity.
In Figure 5.15, the time evolution of the ratio $M_{dust}(r < 15')/M_{200}$ is shown individually for the 4 clusters simulated with the fiducial set of parameters. This is compared with the same ratio as derived from these Planck data. The comparison is shown not only with the full sample, but also for the two subsample at $z \leq 0.25$ and $z > 0.25$, comprising 307 and 254 clusters respectively. This figure confirms that our fiducial models under-predict the dust content of the clusters, albeit by a smaller factor ~ 3. As such, the model with increased sputtering timescale turns out to be in reasonable agreement with the data.

6.6 Conclusion

During my PhD we introduced a state of the art treatment of dust production and evolution in our version of the simulation code GADGET-3. We take advantage of the code's detailed description of chemical evolution to trace the two dust species that are believed to populate the ISM, namely carbonaceous and silicate grains. We also trace the grain size distribution by means of the two-size approximation introduced and tested by Hirashita (2015).
In our code, large (nominally 0.1μm) dust grains are originated by simulated stellar particles from three stellar channels, AGB winds, core collapse SNae, and SNIa. These grains are spread along with metals to the surrounding SPH gas particles, where we allow for various ISM evolution processes affecting dust properties to occur. Large grains are then shattered onto small (nominally 0.01μm) grains if the gas density is sufficiently low. In dense star forming SPH gas particles, metals accrete onto small grains and small grains coagulate onto large grains. We also take into account dust destruction by SN shocks and by sputtering in the hot ($T \gtrsim 10^6$ K) ICM. We evaluate timescales for the above mentioned ISM processes as a function of the physical conditions of the SPH particles, and within each we evolve the dust and gas metal contents.
As a first test, we applied the method to cosmological zoom-in simulations of four massive ($M_{200} \geq 3 \times 10^{14} M_{\odot}$) galaxy clusters. During the early stages of assembly of the cluster at $z \gtrsim 3$, where the star formation activity is at its maximum in our simulations, the proto-cluster regions are rich of dusty gas. Compared to runs in which only dust production in stellar ejecta is active, runs including processes occurring in the cold ISM enhance the dust content by a factor of 2 to 3.
At low redshift our model reproduces reasonably well the trend of dust abundances

over metallicity as observed in local galaxies (Figure 5.14). However we underproduce by a factor of 2 to 3 the total dust content of clusters estimated observationally at low-z $\lesssim 0.5$ using IRAS, Planck and Herschel satellites data. This discrepancy can be solved by decreasing the efficiency of sputtering which erodes dust grains in the hot ICM (Figure 5.15).

6.7 Future Prospects

The efforts of this Doctoral project meant to gather detailed information on the ISM/ICM composition and evolution. By taking advantage of these results, we can improve past methods of mock data production developed at the Observatory, such as the ones presented in Granato et al. (2015). In the paper, they used post processing routines with radiative transfer on galaxy cluster simulations. Their tool required assumptions on dust composition, abundance, and grain size. Now it will be possible to read this information directly from the simulations.
The group also plans on porting and adapting our dust evolution model to the MUlti Phase Particle Integrator model (e.g.MUPPI, Murante et al., 2015). MUPPI can produce realistic galaxy populations inside cosmological volumes of low to medium resolution with a sophisticated star formation method based on multi-phase gas particles.
The cold fraction of molecular gas for multi-phase particles is currently computed using the phenomenological hydrostatic pressure relation Blitz and Rosolowsky (2006). In the near future, this method will be improved with the Maio et al. (2007) molecular network. We will extend it so that the network will account for the catalysis of H_2 molecules on grain surfaces. Dust production will also be improved by the candidate's latest research interests, geared on a dust composition in line with the breakdown observed in local molecular clouds.

Bibliography

D. A. Allen, J. P. Swings, and P. M. Harvey. Infrared photometry of northern Wolf-Rayet stars. *A&A*, 20:333–336, 1972.

D. Alp, J. Larsson, C. Fransson, R. Indebetouw, A. Jerkstrand, A. Ahola, D. Burrows, P. Challis, P. Cigan, A. Cikota, R. P. Kirshner, J. T. van Loon, S. Mattila, C.-Y. Ng, S. Park, J. Spyromilio, S. Woosley, M. Baes, P. Bouchet, R. Chevalier, K. A. Frank, B. M. Gaensler, H. Gomez, H.-T. Janka, B. Leibundgut, P. Lundqvist, J. Marcaide, M. Matsuura, J. Sollerman, G. Sonneborn, L. Staveley-Smith, G. Zanardo, M. Gabler, F. Taddia, and J. C. Wheeler. The 30 Year Search for the Compact Object in SN 1987A. *ApJ*, 864:174, September 2018. doi: 10.3847/1538-4357/aad739.

S. Amari, R. S. Lewis, and E. Anders. Interstellar grains in meteorites. I - Isolation of SiC, graphite, and diamond; size distributions of SiC and graphite. II - SiC and its noble gases. *Geochim. Cosmochim. Acta*, 58:459, January 1994. doi: 10.1016/0016-7037(94)90477-4.

R. E. Angulo, V. Springel, S. D. M. White, A. Jenkins, C. M. Baugh, and C. S. Frenk. Scaling relations for galaxy clusters in the Millennium-XXL simulation. *MNRAS*, 426:2046–2062, November 2012. doi: 10.1111/j.1365-2966.2012.21830.x.

S. Aoyama, K.-C. Hou, I. Shimizu, H. Hirashita, K. Todoroki, J.-H. Choi, and K. Nagamine. Galaxy simulation with dust formation and destruction. *MNRAS*, 466:105–121, April 2017. doi: 10.1093/mnras/stw3061.

R. G. Arendt, N. Odegard, J. L. Weiland, T. J. Sodroski, M. G. Hauser, E. Dwek, T. Kelsall, S. H. Moseley, R. F. Silverberg, D. Leisawitz, K. Mitchell, W. T. Reach, and E. L. Wright. The COBE Diffuse Infrared Background Experiment Search for the Cosmic Infrared Background. III. Separation of Galactic Emission from the Infrared Sky Brightness. *ApJ*, 508:74–105, November 1998. doi: 10.1086/306381.

N. Arimoto. Stellar Population Synthesis Models for Elliptical Galaxies. In C. Leitherer, U. Fritze-von-Alvensleben, and J. Huchra, editors, *From Stars to Galaxies: the Impact of Stellar Physics on Galaxy Evolution*, volume 98 of *Astronomical Society of the Pacific Conference Series*, page 287, 1996.

R. S. Asano, T. T. Takeuchi, H. Hirashita, and T. Nozawa. What determines the grain size distribution in galaxies? *MNRAS*, 432:637–652, June 2013. doi: 10.1093/mnras/stt506.

M. Asplund, N. Grevesse, A. J. Sauval, and P. Scott. The Chemical Composition of the Sun. *ARA&A*, 47:481–522, September 2009. doi: 10.1146/annurev.astro.46.060407.145222.

J. S. Bagla. TreePM: A Code for Cosmological N-Body Simulations. *Journal of Astrophysics and Astronomy*, 23:185–196, December 2002. doi: 10.1007/BF02702282.

M. E. Bailey and D. A. Williams, editors. *Dust in the universe; Proceedings of the Conference, Victoria University of Manchester, England, Dec. 14-18, 1987*, 1988.

M. J. Barlow and J. Silk. H2 recombination on interstellar grains. *ApJ*, 207:131–140, July 1976. doi: 10.1086/154477.

J. Barnes, J. Goodman, and P. Hut. Dynamical instabilities in spherical stellar systems. *ApJ*, 300:112–131, January 1986. doi: 10.1086/163786.

S. S. Barshay and J. S. Lewis. Chemistry of primitive solar material. *ARA&A*, 14:81–94, 1976. doi: 10.1146/annurev.aa.14.090176.000501.

A. M. Beck, G. Murante, A. Arth, R.-S. Remus, A. F. Teklu, J. M. F. Donnert, S. Planelles, M. C. Beck, P. Förster, M. Imgrund, K. Dolag, and S. Borgani. An improved SPH scheme for cosmological simulations. *MNRAS*, 455:2110–2130, January 2016. doi: 10.1093/mnras/stv2443.

D. A. Beintema, M. E. van den Ancker, F. J. Molster, L. B. F. M. Waters, A. G. G. M. Tielens, C. Waelkens, T. de Jong, T. de Graauw, K. Justtanont, I. Yamamura, A. Heras, F. Lahuis, and A. Salama. The rich spectrum of circumstellar PAHs. *A&A*, 315:L369–L372, November 1996.

K. Bekki. Coevolution of dust, gas and stars in galaxies - I. Spatial distributions and scaling-relations of dust and molecular hydrogen. *MNRAS*, 432:2298–2323, July 2013. doi: 10.1093/mnras/stt589.

A. J. Benson. Galaxy formation theory. *Phys. Rep.*, 495:33–86, October 2010. doi: 10.1016/j.physrep.2010.06.001.

F. Bernardeau, S. Colombi, E. Gaztañaga, and R. Scoccimarro. Large-scale structure of the Universe and cosmological perturbation theory. *Phys. Rep.*, 367:1–248, September 2002. doi: 10.1016/S0370-1573(02)00135-7.

R. A. Bernstein, W. L. Freedman, and B. F. Madore. The First Detections of the Extragalactic Background Light at 3000, 5500, and 8000 Å. I. Results. *ApJ*, 571: 56–84, May 2002. doi: 10.1086/339422.

L. Bianchi. The Galaxy Evolution Explorer (GALEX). Its legacy of UV surveys, and science highlights. *Ap&SS*, 354:103–112, November 2014. doi: 10.1007/s10509-014-1935-6.

S. Bianchi and R. Schneider. Dust formation and survival in supernova ejecta. *MNRAS*, 378:973–982, July 2007. doi: 10.1111/j.1365-2966.2007.11829.x.

P. Biermann and M. Harwit. On the origin of the grain-size spectrum of interstellar dust. *ApJ*, 241:L105–L107, October 1980. doi: 10.1086/183370.

V. Biffi, S. Planelles, S. Borgani, D. Fabjan, E. Rasia, G. Murante, L. Tornatore, K. Dolag, G. L. Granato, M. Gaspari, and A. M. Beck. The history of chemical enrichment in the intracluster medium from cosmological simulations. *MNRAS*, 468:531–548, June 2017. doi: 10.1093/mnras/stx444.

J. Binney and S. Tremaine. *Galactic dynamics*. 1987.

L. Blitz and E. Rosolowsky. The Role of Pressure in GMC Formation II: The H_2-Pressure Relation. *ApJ*, 650:933–944, October 2006. doi: 10.1086/505417.

L. Blitz, Y. Fukui, A. Kawamura, A. Leroy, N. Mizuno, and E. Rosolowsky. Giant Molecular Clouds in Local Group Galaxies. *Protostars and Planets V*, pages 81–96, 2007.

M. Bocchio and A. Jones. Dust Lifetime Re-evaluation in the Light of a New Dust Model. In *Proceedings of The Life Cycle of Dust in the Universe: Observations, Theory, and Laboratory Experiments (LCDU2013). 18-22 November, 2013. Taipei, Taiwan. Editors: Anja Andersen (University of Copenhagen, Denmark), Maarten Baes (Universiteit Gent, Belgium), Haley Gomez (Cardiff University, UK), Ciska Kemper (Academia Sinica, Taiwan), Darach Watson (University of Copenhagen, Denmark). Online at <A href="http://pos.sissa.it/cgi-*

bin/reader/conf.cgi?confid=207">http://pos.sissa.it/cgi-bin/reader/conf.cgi?confid=207</A>, id.28, page 28, 2013.

P. Bode, J. P. Ostriker, and G. Xu. The Tree Particle-Mesh N-Body Gravity Solver. *ApJS*, 128:561–569, June 2000. doi: 10.1086/313398.

A. Bonafede, K. Dolag, F. Stasyszyn, G. Murante, and S. Borgani. A non-ideal magnetohydrodynamic GADGET: simulating massive galaxy clusters. *MNRAS*, 418:2234–2250, December 2011. doi: 10.1111/j.1365-2966.2011.19523.x.

H. Bondi. On spherically symmetrical accretion. *MNRAS*, 112:195, 1952. doi: 10.1093/mnras/112.2.195.

K. J. Borkowski and E. Dwek. The Fragmentation and Vaporization of Dust in Grain-Grain Collisions. *ApJ*, 454:254, November 1995. doi: 10.1086/176480.

F. Boulanger and M. Perault. Diffuse infrared emission from the galaxy. I - Solar neighborhood. *ApJ*, 330:964–985, July 1988. doi: 10.1086/166526.

M. L. Boyer, S. Srinivasan, D. Riebel, I. McDonald, J. T. van Loon, G. C. Clayton, K. D. Gordon, M. Meixner, B. A. Sargent, and G. C. Sloan. The Dust Budget of the Small Magellanic Cloud: Are Asymptotic Giant Branch Stars the Primary Dust Source at Low Metallicity? *ApJ*, 748:40, March 2012. doi: 10.1088/0004-637X/748/1/40.

J. P. Bradley and Z. R. Dai. Mechanism of Formation of Glass with Embedded Metal and Sulfides. *ApJ*, 617:650–655, December 2004. doi: 10.1086/425292.

A. Bressan, P. Panuzzo, L. Buson, M. Clemens, G. L. Granato, R. Rampazzo, L. Silva, J. R. Valdes, O. Vega, and L. Danese. Spitzer IRS spectra of Virgo Early-Type Galaxies: Detection of Stellar Silicate Emission. *ApJ*, 639:L55–L58, March 2006. doi: 10.1086/502970.

J. Breysacher, M. Azzopardi, and G. Testor. The fourth catalogue of Population I Wolf-Rayet stars in the Large Magellanic Cloud. *A&A Supp.*, 137:117–145, May 1999. doi: 10.1051/aas:1999240.

G. L. Bryan, M. L. Norman, J. M. Stone, R. Cen, and J. P. Ostriker. A piecewise parabolic method for cosmological hydrodynamics. *Computer Physics Communications*, 89:149–168, August 1995. doi: 10.1016/0010-4655(94)00191-4.

G. L. Bryan, M. L. Norman, B. W. O'Shea, T. Abel, J. H. Wise, M. J. Turk, D. R.

Reynolds, D. C. Collins, P. Wang, S. W. Skillman, B. Smith, R. P. Harkness, J. Bordner, J.-h. Kim, M. Kuhlen, H. Xu, N. Goldbaum, C. Hummels, A. G. Kritsuk, E. Tasker, S. Skory, C. M. Simpson, O. Hahn, J. S. Oishi, G. C. So, F. Zhao, R. Cen, Y. Li, and Enzo Collaboration. ENZO: An Adaptive Mesh Refinement Code for Astrophysics. *ApJS*, 211:19, April 2014. doi: 10.1088/0067-0049/211/2/19.

F. Calura, A. Pipino, and F. Matteucci. The cycle of interstellar dust in galaxies of different morphological types. *A&A*, 479:669–685, March 2008. doi: 10.1051/0004-6361:20078090.

D. Calzetti, L. Armus, R. C. Bohlin, A. L. Kinney, J. Koornneef, and T. Storchi-Bergmann. The Dust Content and Opacity of Actively Star-forming Galaxies. *ApJ*, 533:682–695, April 2000. doi: 10.1086/308692.

P. Camps and M. Baes. SKIRT: An advanced dust radiative transfer code with a user-friendly architecture. *Astronomy and Computing*, 9:20–33, March 2015. doi: 10.1016/j.ascom.2014.10.004.

J. A. Cardelli, G. C. Clayton, and J. S. Mathis. The relationship between infrared, optical, and ultraviolet extinction. *ApJ*, 345:245–256, October 1989. doi: 10.1086/167900.

J. A. Cardelli, J. S. Mathis, D. C. Ebbets, and B. D. Savage. Abundance of interstellar carbon toward Zeta Ophiuchi. *ApJ*, 402:L17–L20, January 1993. doi: 10.1086/186689.

J. A. Cardelli, U. J. Sofia, B. D. Savage, F. P. Keenan, and P. L. Dufton. Interstellar detection of the intersystem line Si II lambda 2335 toward zeta Ophiuchi. *ApJ*, 420:L29–L32, January 1994. doi: 10.1086/187155.

R. Cen. A hydrodynamic approach to cosmology - Methodology. *ApJS*, 78:341–364, February 1992. doi: 10.1086/191630.

D. Cesarsky, J. Lequeux, A. Abergel, M. Perault, E. Palazzi, S. Madden, and D. Tran. Infrared spectrophotometry of NGC 7023 with ISOCAM. *A&A*, 315: L305–L308, November 1996.

G. Chabrier. Galactic Stellar and Substellar Initial Mass Function. *Publ. Astr. Soc. Pac.*, 115:763–795, July 2003. doi: 10.1086/376392.

S. Charlot and S. M. Fall. A Simple Model for the Absorption of Starlight by Dust in Galaxies. *ApJ*, 539:718–731, August 2000. doi: 10.1086/309250.

B.-Q. Chen, Y. Huang, X.-W. Liu, H.-B. Yuan, C. Wang, D.-W. Fan, M.-S. Xiang, H.-W. Zhang, and Z.-J. Tian. Three-dimensional interstellar dust reddening maps of the Galactic plane. *ArXiv e-prints*, July 2018a.

L.-H. Chen, H. Hirashita, K.-C. Hou, S. Aoyama, I. Shimizu, and K. Nagamine. Populating H_2 and CO in galaxy simulation with dust evolution. *MNRAS*, 474: 1545–1563, February 2018b. doi: 10.1093/mnras/stx2863.

I. Cherchneff and E. Dwek. The Chemistry of Population III Supernova Ejecta. I. Formation of Molecules in the Early Universe. *ApJ*, 703:642–661, September 2009. doi: 10.1088/0004-637X/703/1/642.

A. Chokshi, A. G. G. M. Tielens, and D. Hollenbach. Dust coagulation. *ApJ*, 407: 806–819, April 1993. doi: 10.1086/172562.

D. D. Clayton, D. Arnett, J. Kane, and B. S. Meyer. Type X Silicon Carbide Presolar Grains: Type Ia Supernova Condensates? *ApJ*, 486:824–834, September 1997. doi: 10.1086/304545.

D. L. Clements, W. J. Sutherland, W. Saunders, G. P. Efstathiou, R. G. McMahon, S. Maddox, A. Lawrence, and M. Rowan-Robinson. A new large sample of ultraluminous IRAS galaxies. *MNRAS*, 279:459–476, March 1996. doi: 10.1093/mnras/279.2.459.

P. Colella and P. R. Woodward. The Piecewise Parabolic Method (PPM) for Gas-Dynamical Simulations. *Journal of Computational Physics*, 54:174–201, September 1984. doi: 10.1016/0021-9991(84)90143-8.

James W. Cooley and John W. Tukey. An algorithm for the machine calculation of complex Fourier series. *Mathematics of Computation*, 19:297–301, 1965. ISSN 0025–5718. URL: `http://cr.yp.to/bib/entries.html#1965/cooley`.

F. Costagliola, K. Sakamoto, S. Muller, S. Martín, S. Aalto, N. Harada, P. van der Werf, S. Viti, S. Garcia-Burillo, and M. Spaans. Exploring the molecular chemistry and excitation in obscured luminous infrared galaxies. An ALMA mm-wave spectral scan of NGC 4418. *A&A*, 582:A91, October 2015. doi: 10.1051/0004-6361/201526256.

E. Costantini, M. J. Freyberg, and P. Predehl. Absorption and scattering

by interstellar dust: an XMM-Newton observation of <ASTROBJ>Cyg X-2</ASTROBJ>. *A&A*, 444:187–200, December 2005. doi: 10.1051/0004-6361:20042562.

H. M. P. Couchman. Mesh-refined P3M - A fast adaptive N-body algorithm. *ApJ*, 368:L23–L26, February 1991. doi: 10.1086/185939.

D. A. Dale, A. Gil de Paz, K. D. Gordon, H. M. Hanson, L. Armus, G. J. Bendo, L. Bianchi, M. Block, S. Boissier, A. Boselli, B. A. Buckalew, V. Buat, D. Burgarella, D. Calzetti, J. M. Cannon, C. W. Engelbracht, G. Helou, D. J. Hollenbach, T. H. Jarrett, R. C. Kennicutt, C. Leitherer, A. Li, B. F. Madore, D. C. Martin, M. J. Meyer, E. J. Murphy, M. W. Regan, H. Roussel, J. D. T. Smith, M. L. Sosey, D. A. Thilker, and F. Walter. An Ultraviolet-to-Radio Broadband Spectral Atlas of Nearby Galaxies. *ApJ*, 655:863–884, February 2007. doi: 10.1086/510362.

I. J. Danziger, C. Gouiffes, P. Bouchet, and L. B. Lucy. Supernova 1987A in the Large Magellanic Cloud. , 4746, March 1989.

J. I. Davies, M. Baes, S. Bianchi, A. Jones, S. Madden, M. Xilouris, M. Bocchio, V. Casasola, L. Cassara, C. Clark, I. De Looze, R. Evans, J. Fritz, M. Galametz, F. Galliano, S. Lianou, A. V. Mosenkov, M. Smith, S. Verstocken, S. Viaene, M. Vika, G. Wagle, and N. Ysard. DustPedia: A Definitive Study of Cosmic Dust in the Local Universe. *Publ. Astr. Soc. Pac.*, 129(4):044102, April 2017. doi: 10.1088/1538-3873/129/974/044102.

M. Davis, G. Efstathiou, C. S. Frenk, and S. D. M. White. The evolution of large-scale structure in a universe dominated by cold dark matter. *ApJ*, 292:371–394, May 1985. doi: 10.1086/163168.

A. De Cia. Metals and dust in the neutral ISM: the Galaxy, Magellanic Clouds, and damped Lyman-α absorbers. *A&A*, 613:L2, May 2018. doi: 10.1051/0004-6361/201833034.

J. Debuhr, E. Quataert, and C.-P. Ma. The growth of massive black holes in galaxy merger simulations with feedback by radiation pressure. *MNRAS*, 412:1341–1360, April 2011. doi: 10.1111/j.1365-2966.2010.17992.x.

W. Dehnen and J. I. Read. N-body simulations of gravitational dynamics. *European Physical Journal Plus*, 126:55, May 2011. doi: 10.1140/epjp/i2011-11055-3.

K. Dolag, S. Borgani, S. Schindler, A. Diaferio, and A. M. Bykov. Simulation

Techniques for Cosmological Simulations. *SSR*, 134:229–268, February 2008. doi: 10.1007/s11214-008-9316-5.

R. Domínguez-Tenreiro, A. Obreja, G. L. Granato, A. Schurer, P. Alpresa, L. Silva, C. B. Brook, and A. Serna. GRASIL-3D: an implementation of dust effects in the SEDs of simulated galaxies. *MNRAS*, 439:3868–3889, April 2014. doi: 10.1093/mnras/stu240.

J. Dorschner, B. Begemann, T. Henning, C. Jaeger, and H. Mutschke. Steps toward interstellar silicate mineralogy. II. Study of Mg-Fe-silicate glasses of variable composition. *A&A*, 300:503, August 1995.

B. T. Draine. Interstellar Dust Grains. *ARA&A*, 41:241–289, 2003. doi: 10.1146/annurev.astro.41.011802.094840.

B. T. Draine. Interstellar Dust. *Origin and Evolution of the Elements*, page 317, 2004.

B. T. Draine. Interstellar Dust Models and Evolutionary Implications. In T. Henning, E. Grün, and J. Steinacker, editors, *Cosmic Dust - Near and Far*, volume 414 of *Astronomical Society of the Pacific Conference Series*, page 453, December 2009.

B. T. Draine. *Physics of the Interstellar and Intergalactic Medium*. Princeton University Press, 2011.

B. T. Draine and H. M. Lee. Optical properties of interstellar graphite and silicate grains. *ApJ*, 285:89–108, October 1984. doi: 10.1086/162480.

B. T. Draine and A. Li. Infrared Emission from Interstellar Dust. I. Stochastic Heating of Small Grains. *ApJ*, 551:807–824, April 2001. doi: 10.1086/320227.

B. T. Draine and A. Li. Infrared Emission from Interstellar Dust. IV. The Silicate-Graphite-PAH Model in the Post-Spitzer Era. *ApJ*, 657:810–837, March 2007. doi: 10.1086/511055.

B. T. Draine and E. E. Salpeter. Destruction mechanisms for interstellar dust. *ApJ*, 231:438–455, July 1979. doi: 10.1086/157206.

W. W. Duley and S. Seahra. Graphite, Polycyclic Aromatic Hydrocarbons, and the 2175 Å Extinction Feature. *ApJ*, 507:874–888, November 1998. doi: 10.1086/306344.

W. W. Duley and D. A. Williams. Interstellar polyynes from the disruption of carbon grains. *MNRAS*, 211:97–103, November 1984. doi: 10.1093/mnras/211.1.97.

E. Dwek. The Evolution of the Elemental Abundances in the Gas and Dust Phases of the Galaxy. *ApJ*, 501:643, July 1998. doi: 10.1086/305829.

E. Dwek. Iron: A Key Element for Understanding the Origin and Evolution of Interstellar Dust. *ApJ*, 825:136, July 2016. doi: 10.3847/0004-637X/825/2/136.

E. Dwek and R. G. Arendt. Dust-gas interactions and the infrared emission from hot astrophysical plasmas. *ARA&A*, 30:11–50, 1992. doi: 10.1146/annurev.aa.30.090192.000303.

G. Efstathiou, C. S. Frenk, S. D. M. White, and M. Davis. Gravitational clustering from scale-free initial conditions. *MNRAS*, 235:715–748, December 1988. doi: 10.1093/mnras/235.3.715.

Á. Elíasdóttir, J. P. U. Fynbo, J. Hjorth, C. Ledoux, D. J. Watson, A. C. Andersen, D. Malesani, P. M. Vreeswijk, J. X. Prochaska, J. Sollerman, and A. O. Jaunsen. Dust Extinction in High-z Galaxies with Gamma-Ray Burst Afterglow Spectroscopy: The 2175 Å Feature at z = 2.45. *ApJ*, 697:1725–1740, June 2009. doi: 10.1088/0004-637X/697/2/1725.

A. Elmhamdi, I. J. Danziger, E. Cappellaro, M. Della Valle, C. Gouiffes, M. M. Phillips, and M. Turatto. SN Ib 1990I: Clumping and dust in the ejecta? *A&A*, 426:963–977, November 2004. doi: 10.1051/0004-6361:20041318.

A. E. Evrard, T. J. MacFarland, H. M. P. Couchman, J. M. Colberg, N. Yoshida, S. D. M. White, A. Jenkins, C. S. Frenk, F. R. Pearce, J. A. Peacock, and P. A. Thomas. Galaxy Clusters in Hubble Volume Simulations: Cosmological Constraints from Sky Survey Populations. *ApJ*, 573:7–36, July 2002. doi: 10.1086/340551.

A. C. Fabian. Observational Evidence of Active Galactic Nuclei Feedback. *ARA&A*, 50:455–489, September 2012. doi: 10.1146/annurev-astro-081811-125521.

D. Fabjan, S. Borgani, L. Tornatore, A. Saro, G. Murante, and K. Dolag. Simulating the effect of active galactic nuclei feedback on the metal enrichment of galaxy clusters. *MNRAS*, 401:1670–1690, January 2010. doi: 10.1111/j.1365-2966.2009.15794.x.

R. Feldmann, C. M. Carollo, L. Mayer, A. Renzini, G. Lake, T. Quinn, G. S. Stinson,

and G. Yepes. The Evolution of Central Group Galaxies in Hydrodynamical Simulations. *ApJ*, 709:218–240, January 2010. doi: 10.1088/0004-637X/709/1/218.

G. J. Ferland, K. T. Korista, D. A. Verner, J. W. Ferguson, J. B. Kingdon, and E. M. Verner. CLOUDY 90: Numerical Simulation of Plasmas and Their Spectra. *Publ. Astr. Soc. Pac.*, 110:761–778, July 1998. doi: 10.1086/316190.

G. J. Ferland, M. Chatzikos, F. Guzmán, M. L. Lykins, P. A. M. van Hoof, R. J. R. Williams, N. P. Abel, N. R. Badnell, F. P. Keenan, R. L. Porter, and P. C. Stancil. The 2017 Release Cloudy. , 53:385–438, October 2017.

L. Ferrarese and D. Merritt. A Fundamental Relation between Supermassive Black Holes and Their Host Galaxies. *ApJ*, 539:L9–L12, August 2000. doi: 10.1086/312838.

K. M. Ferrière. The interstellar environment of our galaxy. *Reviews of Modern Physics*, 73:1031–1066, October 2001. doi: 10.1103/RevModPhys.73.1031.

G. B. Field. Interstellar Clouds. *Comments on Astrophysics and Space Physics*, 1:107, May 1969.

G. B. Field. The physics of the interstellar matter. *Highlights of Astronomy*, 3:37–49, 1974.

A. V. Filippenko. Optical Spectra of Supernovae. *ARA&A*, 35:309–355, 1997. doi: 10.1146/annurev.astro.35.1.309.

D. P. Finkbeiner, M. Davis, and D. J. Schlegel. Extrapolation of Galactic Dust Emission at 100 Microns to Cosmic Microwave Background Radiation Frequencies Using FIRAS. *ApJ*, 524:867–886, October 1999. doi: 10.1086/307852.

A. Finoguenov, A. Burkert, and H. Böhringer. Role of Clusters of Galaxies in the Evolution of the Metal Budget in the Universe. *ApJ*, 594:136–143, September 2003. doi: 10.1086/376778.

E. L. Fitzpatrick. Correcting for the Effects of Interstellar Extinction. *Publ. Astr. Soc. Pac.*, 111:63–75, January 1999. doi: 10.1086/316293.

W. Forman, C. Jones, E. Churazov, M. Markevitch, P. Nulsen, A. Vikhlinin, M. Begelman, H. Böhringer, J. Eilek, S. Heinz, R. Kraft, F. Owen, and M. Pahre.

Filaments, Bubbles, and Weak Shocks in the Gaseous Atmosphere of M87. *ApJ*, 665:1057–1066, August 2007. doi: 10.1086/519480.

C. S. Frenk, S. D. M. White, G. Efstathiou, and M. Davis. Cold dark matter, the structure of galactic haloes and the origin of the Hubble sequence. *Nature*, 317: 595–597, October 1985. doi: 10.1038/317595a0.

M. Frenklach and E. D. Feigelson. Formation of polycyclic aromatic hydrocarbons in circumstellar envelopes. *ApJ*, 341:372–384, June 1989. doi: 10.1086/167501.

C. L. Fryer, S. E. Woosley, and A. Heger. Pair-Instability Supernovae, Gravity Waves, and Gamma-Ray Transients. *ApJ*, 550:372–382, March 2001. doi: 10.1086/319719.

M. Fukugita and P. J. E. Peebles. Massive Coronae of Galaxies. *ApJ*, 639:590–599, March 2006. doi: 10.1086/499556.

H.-P. Gail. Radial mixing in protoplanetary accretion disks. IV. Metamorphosis of the silicate dust complex. *A&A*, 413:571–591, January 2004. doi: 10.1051/0004-6361:20031554.

H. P. Gail and E. Sedlmayr. Dust formation in stellar winds. III - Self-consistent models for dust-driven winds around C-stars. *A&A*, 171:197–204, January 1987.

H.-P. Gail, S. V. Zhukovska, P. Hoppe, and M. Trieloff. Stardust from Asymptotic Giant Branch Stars. *ApJ*, 698:1136–1154, June 2009. doi: 10.1088/0004-637X/698/2/1136.

M. Galametz, S. C. Madden, F. Galliano, S. Hony, G. J. Bendo, and M. Sauvage. Probing the dust properties of galaxies up to submillimetre wavelengths. II. Dust-to-gas mass ratio trends with metallicity and the submm excess in dwarf galaxies. *A&A*, 532:A56, August 2011. doi: 10.1051/0004-6361/201014904.

C. Gall, J. Hjorth, D. Watson, E. Dwek, J. R. Maund, O. Fox, G. Leloudas, D. Malesani, and A. C. Day-Jones. Rapid formation of large dust grains in the luminous supernova 2010jl. *Nature*, 511:326–329, July 2014. doi: 10.1038/nature13558.

D. A. García-Hernández, O. Zamora, A. Yagüe, S. Uttenthaler, A. I. Karakas, M. Lugaro, P. Ventura, and D. L. Lambert. Hot bottom burning and s-process nucleosynthesis in massive AGB stars at the beginning of the thermally-pulsing phase. *A&A*, 555:L3, July 2013. doi: 10.1051/0004-6361/201321818.

R. T. Garrod, A. Belloche, H. S. P. Müller, and K. M. Menten. Exploring molecular complexity with ALMA (EMoCA): Simulations of branched carbon-chain chemistry in Sgr B2(N). *A&A*, 601:A48, May 2017. doi: 10.1051/0004-6361/201630254.

M. Gaspari, M. Ruszkowski, and S. P. Oh. Chaotic cold accretion on to black holes. *MNRAS*, 432:3401–3422, July 2013. doi: 10.1093/mnras/stt692.

A. Gauger, Y. Y. Balega, P. Irrgang, R. Osterbart, and G. Weigelt. High-resolution speckle masking interferometry and radiative transfer modeling of the oxygen-rich AGB star AFGL 2290. *A&A*, 346:505–519, June 1999.

R. Gavazzi, C. Adami, F. Durret, J.-C. Cuillandre, O. Ilbert, A. Mazure, R. Pelló, and M. P. Ulmer. A weak lensing study of the coma cluster. *Astronomy & Astrophysics*, 498(2):L33–L36, apr 2009. doi: 10.1051/0004-6361/200911841. URL `https://doi.org/10.1051/0004-6361/200911841`.

R. A. Gingold and J. J. Monaghan. Smoothed particle hydrodynamics - Theory and application to non-spherical stars. *MNRAS*, 181:375–389, November 1977. doi: 10.1093/mnras/181.3.375.

E. Gjergo, G. L. Granato, G. Murante, C. Ragone-Figueroa, L. Tornatore, and S. Borgani. Dust evolution in galaxy cluster simulations. *MNRAS*, 479:2588–2606, September 2018. doi: 10.1093/mnras/sty1564.

A. E. Glassgold, J. Igea, and J. Najita. X-ray ionization of protostellar disks. In E. F. van Dishoeck, editor, *Molecules in Astrophysics: Probes & Processes*, volume 178 of *IAU Symposium*, page 155, 1996.

O. Gnat and G. J. Ferland. Ion-by-ion Cooling Efficiencies. *ApJS*, 199:20, March 2012. doi: 10.1088/0067-0049/199/1/20.

H. L. Gomez, C. J. R. Clark, T. Nozawa, O. Krause, E. L. Gomez, M. Matsuura, M. J. Barlow, M.-A. Besel, L. Dunne, W. K. Gear, P. Hargrave, T. Henning, R. J. Ivison, B. Sibthorpe, B. M. Swinyard, and R. Wesson. Dust in historical Galactic Type Ia supernova remnants with Herschel. *MNRAS*, 420:3557–3573, March 2012. doi: 10.1111/j.1365-2966.2011.20272.x.

G. L. Granato, C. G. Lacey, L. Silva, A. Bressan, C. M. Baugh, S. Cole, and C. S. Frenk. The Infrared Side of Galaxy Formation. I. The Local Universe in the Semianalytical Framework. *ApJ*, 542:710–730, October 2000. doi: 10.1086/317032.

G. L. Granato, C. Ragone-Figueroa, R. Domínguez-Tenreiro, A. Obreja, S. Borgani, G. De Lucia, and G. Murante. The early phases of galaxy clusters formation in IR: coupling hydrodynamical simulations with GRASIL-3D. *MNRAS*, 450:1320–1332, June 2015. doi: 10.1093/mnras/stv676.

M. A. T. Groenewegen. IRC +10 216 revisited. I. The circumstellar dust shell. *A&A*, 317:503–520, January 1997.

M. A. T. Groenewegen, G. C. Sloan, I. Soszyński, and E. A. Petersen. Luminosities and mass-loss rates of SMC and LMC AGB stars and red supergiants. *A&A*, 506: 1277–1296, November 2009. doi: 10.1051/0004-6361/200912678.

P. Guhathakurta and B. T. Draine. Temperature fluctuations in interstellar grains. I - Computational method and sublimation of small grains. *ApJ*, 345:230–244, October 1989. doi: 10.1086/167899.

C. M. Gutiérrez and M. López-Corredoira. Dust in Clusters: Separating the Contribution of Galaxies and Intracluster Media. *ApJ*, 835:111, January 2017. doi: 10.3847/1538-4357/835/1/111.

F. Haardt and P. Madau. Modelling the UV/X-ray cosmic background with CUBA. In D. M. Neumann and J. T. V. Tran, editors, *Clusters of Galaxies and the High Redshift Universe Observed in X-rays*, page 64, 2001.

A. Harten. High Resolution Schemes for Hyperbolic Conservation Laws. *Journal of Computational Physics*, 49:357–393, March 1983. doi: 10.1016/0021-9991(83)90136-5.

S. Hatton, J. E. G. Devriendt, S. Ninin, F. R. Bouchet, B. Guiderdoni, and D. Vibert. GALICS- I. A hybrid N-body/semi-analytic model of hierarchical galaxy formation. *MNRAS*, 343:75–106, July 2003. doi: 10.1046/j.1365-8711.2003.05589.x.

M. G. Hauser and E. Dwek. The Cosmic Infrared Background: Measurements and Implications. *ARA&A*, 39:249–307, 2001. doi: 10.1146/annurev.astro.39.1.249.

C. Heiles and T. H. Troland. The Millennium Arecibo 21 Centimeter Absorption-Line Survey. II. Properties of the Warm and Cold Neutral Media. *ApJ*, 586: 1067–1093, April 2003. doi: 10.1086/367828.

T. Henning. Cosmic Silicates. *ARA&A*, 48:21–46, September 2010. doi: 10.1146/annurev-astro-081309-130815.

R. C. Hickox and D. M. Alexander. Obscured Active Galactic Nuclei. *ARA&A*, 56: 625–671, September 2018. doi: 10.1146/annurev-astro-081817-051803.

H. Hirashita. Global Law for the Dust-to-Gas Ratio of Spiral Galaxies. *ApJ*, 510: L99–L102, January 1999. doi: 10.1086/311806.

H. Hirashita. Shattering by turbulence as a production source of very small grains. *MNRAS*, 407:L49–L53, September 2010. doi: 10.1111/j.1745-3933.2010.00902.x.

H. Hirashita. Two-size approximation: a simple way of treating the evolution of grain size distribution in galaxies. *MNRAS*, 447:2937–2950, March 2015. doi: 10.1093/mnras/stu2617.

H. Hirashita and N. V. Voshchinnikov. Effects of grain growth mechanisms on the extinction curve and the metal depletion in the interstellar medium. *MNRAS*, 437:1636–1645, January 2014. doi: 10.1093/mnras/stt1997.

H. Hirashita and H. Yan. Shattering and coagulation of dust grains in interstellar turbulence. *MNRAS*, 394:1061–1074, April 2009. doi: 10.1111/j.1365-2966.2009.14405.x.

H. Hirashita, T. Nozawa, H. Yan, and T. Kozasa. Effects of grain shattering by turbulence on extinction curves in starburst galaxies. *MNRAS*, 404:1437–1448, May 2010. doi: 10.1111/j.1365-2966.2010.16354.x.

R. W. Hockney and J. W. Eastwood. *Computer Simulation Using Particles*. 1981.

K.-H. Hofmann, Y. Balega, T. Blöcker, and G. Weigelt. A multi-wavelength study of the oxygen-rich AGB star <ASTROBJ>CIT 3</ASTROBJ>: Bispectrum speckle interferometry and dust-shell modelling. *A&A*, 379:529–539, November 2001. doi: 10.1051/0004-6361:20011318.

P. Hoppe, S. Amari, E. Zinner, T. Ireland, and R. S. Lewis. Carbon, nitrogen, magnesium, silicon, and titanium isotopic compositions of single interstellar silicon carbide grains from the Murchison carbonaceous chondrite. *ApJ*, 430:870–890, August 1994. doi: 10.1086/174458.

K.-C. Hou, H. Hirashita, and M. J. Michałowski. Dust evolution processes constrained by extinction curves in nearby galaxies. *Pub. Astron. Soc. Japan*, 68:94, December 2016. doi: 10.1093/pasj/psw085.

K.-C. Hou, H. Hirashita, K. Nagamine, S. Aoyama, and I. Shimizu. Evolution of

dust extinction curves in galaxy simulation. *MNRAS*, 469:870–885, July 2017. doi: 10.1093/mnras/stx877.

F. Hoyle and N. C. Wickramasinghe. On graphite particles as interstellar grains. *MNRAS*, 124:417, 1962. doi: 10.1093/mnras/124.5.417.

J. D. Hunter. Matplotlib: A 2d graphics environment. *Computing In Science & Engineering*, 9(3):90–95, 2007. doi: 10.1109/MCSE.2007.55.

S. Iijima. Fine Particles of Silicon. I. Crystal Growth of Spherical Particles of Si. *Japanese Journal of Applied Physics*, 26:357, March 1987. doi: 10.1143/JJAP.26.357.

C. D. Impey, C. G. Wynn-Williams, and E. E. Becklin. Infrared studies of elliptical galaxies. I - an optically selected sample. *ApJ*, 309:572–592, October 1986. doi: 10.1086/164626.

C. Jaeger, F. J. Molster, J. Dorschner, T. Henning, H. Mutschke, and L. B. F. M. Waters. Steps toward interstellar silicate mineralogy. IV. The crystalline revolution. *A&A*, 339:904–916, November 1998.

E. B. Jenkins. A Unified Representation of Gas-Phase Element Depletions in the Interstellar Medium. *ApJ*, 700:1299–1348, August 2009. doi: 10.1088/0004-637X/700/2/1299.

A. Jones. The physical and compositional properties of dust: what do we really know? In *Proceedings of Science*, 2013.

A. P. Jones. A framework for resolving the origin, nature and evolution of the diffuse interstellar band carriers? *P&SS*, 100:26–31, October 2014. doi: 10.1016/j.pss.2013.11.011.

A. P. Jones, A. G. G. M. Tielens, D. J. Hollenbach, and C. F. McKee. Grain destruction in shocks in the interstellar medium. *ApJ*, 433:797–810, October 1994. doi: 10.1086/174689.

A. P. Jones, A. G. G. M. Tielens, and D. J. Hollenbach. Grain Shattering in Shocks: The Interstellar Grain Size Distribution. *ApJ*, 469:740, October 1996. doi: 10.1086/177823.

Eric Jones, Travis Oliphant, Pearu Peterson, et al. SciPy: Open source scientific tools for Python, 2001.

N. Kaiser. Evolution and clustering of rich clusters. *MNRAS*, 222:323–345, September 1986. doi: 10.1093/mnras/222.2.323.

F. Kamijo. A Theoretical Study on the Long Period Variable Star, III. Formation of Solid or Liquid Particles in the Circumstellar Envelope. *Pub. Astron. Soc. Japan*, 15:440, 1963.

E. Kankare, M. Fraser, S. Ryder, C. Romero-Cañizales, S. Mattila, R. Kotak, P. Laursen, L. A. G. Monard, M. Salvo, and P. Väisänen. SN 2005at - A neglected type Ic supernova at 10 Mpc. *A&A*, 572:A75, December 2014. doi: 10.1051/0004-6361/201424563.

A. Karakas and J. C. Lattanzio. Stellar Models and Yields of Asymptotic Giant Branch Stars. *Public. of the Astron. Socia. of Australia*, 24:103–117, October 2007. doi: 10.1071/AS07021.

A. I. Karakas. Current Status of Stellar Evolutionary Models for AGB Stars. In F. Kerschbaum, T. Lebzelter, and R. F. Wing, editors, *Why Galaxies Care about AGB Stars II: Shining Examples and Common Inhabitants*, volume 445 of *Astronomical Society of the Pacific Conference Series*, page 3, September 2011.

J. H. Kastner, T. Forveille, B. Zuckerman, and A. Omont. Probing the AGB Tip - Luminous Carbon Stars in the Galactic Plane. *A&A*, 275:163, August 1993.

J. H. Kastner, C. L. Buchanan, B. Sargent, and W. J. Forrest. Spitzer Spectroscopy of Dusty Disks around B[e] Hypergiants in the Large Magellanic Cloud. *ApJ*, 638: L29–L32, February 2006. doi: 10.1086/500804.

N. Katz, D. H. Weinberg, and L. Hernquist. Cosmological Simulations with TreeSPH. *ApJS*, 105:19, July 1996. doi: 10.1086/192305.

E. Kellogg, H. Gursky, H. Tananbaum, R. Giacconi, and K. Pounds. The Extended X-Ray Source at M87. *ApJ*, 174:L65, June 1972. doi: 10.1086/180950.

F. Kemper, W. J. Vriend, and A. G. G. M. Tielens. The Absence of Crystalline Silicates in the Diffuse Interstellar Medium. *ApJ*, 609:826–837, July 2004. doi: 10.1086/421339.

R. C. Kennicutt and N. J. Evans. Star Formation in the Milky Way and Nearby Galaxies. *ARA&A*, 50:531–608, September 2012. doi: 10.1146/annurev-astro-081811-125610.

R. C. Kennicutt, D. Calzetti, G. Aniano, P. Appleton, L. Armus, P. Beirão, A. D. Bolatto, B. Brandl, A. Crocker, K. Croxall, D. A. Dale, J. Donovan Meyer, B. T. Draine, C. W. Engelbracht, M. Galametz, K. D. Gordon, B. Groves, C.-N. Hao, G. Helou, J. Hinz, L. K. Hunt, B. Johnson, J. Koda, O. Krause, A. K. Leroy, Y. Li, S. Meidt, E. Montiel, E. J. Murphy, N. Rahman, H.-W. Rix, H. Roussel, K. Sandstrom, M. Sauvage, E. Schinnerer, R. Skibba, J. D. T. Smith, S. Srinivasan, L. Vigroux, F. Walter, C. D. Wilson, M. Wolfire, and S. Zibetti. KINGFISH Key Insights on Nearby Galaxies: A Far-Infrared Survey with Herschel: Survey Description and Image Atlas. *Publ. Astr. Soc. Pac.*, 123:1347, December 2011. doi: 10.1086/663818.

R. C. Kennicutt, Jr. The Global Schmidt Law in Star-forming Galaxies. *ApJ*, 498: 541–552, May 1998. doi: 10.1086/305588.

R. C. Kennicutt, Jr., D. Calzetti, F. Walter, G. Helou, D. J. Hollenbach, L. Armus, G. Bendo, D. A. Dale, B. T. Draine, C. W. Engelbracht, K. D. Gordon, M. K. M. Prescott, M. W. Regan, M. D. Thornley, C. Bot, E. Brinks, E. de Blok, D. de Mello, M. Meyer, J. Moustakas, E. J. Murphy, K. Sheth, and J. D. T. Smith. Star Formation in NGC 5194 (M51a). II. The Spatially Resolved Star Formation Law. *ApJ*, 671:333–348, December 2007. doi: 10.1086/522300.

S.-H. Kim and P. G. Martin. The size distribution of interstellar dust particles as determined from polarization: Infinite cylinders. *ApJ*, 431:783–796, August 1994. doi: 10.1086/174529.

A. King. Black Holes, Galaxy Formation, and the M_{BH}-σ Relation. *ApJ*, 596: L27–L29, October 2003. doi: 10.1086/379143.

G. Kirchhoff. Ueber das Verhältniss zwischen dem Emissionsvermögen und dem Absorptionsvermögen der Körper für Wärme und Licht. *Annalen der Physik*, 185:275–301, 1860. doi: 10.1002/andp.18601850205.

R. S. Klessen and S. C. O. Glover. Physical Processes in the Interstellar Medium. *Star Formation in Galaxy Evolution: Connecting Numerical Models to Reality, Saas-Fee Advanced Course, Volume 43. ISBN 978-3-662-47889-9. Springer-Verlag Berlin Heidelberg, 2016, p. 85*, 43:85, 2016. doi: 10.1007/978-3-662-47890-5_2.

J. Kormendy and L. C. Ho. Coevolution (Or Not) of Supermassive Black Holes and Host Galaxies. *ARA&A*, 51:511–653, August 2013. doi: 10.1146/annurev-astro-082708-101811.

T. Kozasa, H. Hasegawa, and K. Nomoto. Formation of dust grains in the ejecta of SN 1987A. *ApJ*, 344:325–331, September 1989. doi: 10.1086/167801.

A. V. Kravtsov and S. Borgani. Formation of Galaxy Clusters. *ARA&A*, 50:353–409, September 2012. doi: 10.1146/annurev-astro-081811-125502.

J. H. Krolik. Magnetized Accretion inside the Marginally Stable Orbit around a Black Hole. *ApJ*, 515:L73–L76, April 1999. doi: 10.1086/311979.

E. Krügel. *An introduction to the physics of interstellar dust*. 2008.

A. Li and B. T. Draine. Infrared Emission from Interstellar Dust. II. The Diffuse Interstellar Medium. *ApJ*, 554:778–802, June 2001. doi: 10.1086/323147.

J. E. Lindberg, J. K. Jørgensen, C. Brinch, T. Haugbølle, E. A. Bergin, D. Harsono, M. V. Persson, R. Visser, and S. Yamamoto. ALMA observations of the kinematics and chemistry of disc formation. *A&A*, 566:A74, June 2014. doi: 10.1051/0004-6361/201322651.

K. Lodders. Solar System Abundances and Condensation Temperatures of the Elements. *ApJ*, 591:1220–1247, July 2003. doi: 10.1086/375492.

L. B. Lucy. A numerical approach to the testing of the fission hypothesis. *AJ*, 82: 1013–1024, December 1977. doi: 10.1086/112164.

S. C. Madden, A. Rémy, F. Galliano, M. Galametz, G. Bendo, D. Cormier, V. Lebouteiller, and S. Hony. Low Metallicity ISM: excess submillimetre emission and CO-free H_2 gas. In R. J. Tuffs and C. C. Popescu, editors, *The Spectral Energy Distribution of Galaxies - SED 2011*, volume 284 of *IAU Symposium*, pages 141–148, August 2012. doi: 10.1017/S1743921312008939.

U. Maio, K. Dolag, B. Ciardi, and L. Tornatore. Metal and molecule cooling in simulations of structure formation. *MNRAS*, 379:963–973, August 2007. doi: 10.1111/j.1365-2966.2007.12016.x.

P. G. Martin. *Cosmic dust. Its impact on astronomy*. 1978.

D. Martizzi, R. Teyssier, and B. Moore. The Effect of AGN Feedback on the Brightest Cluster Elliptical Galaxies. In R. Capuzzo-Dolcetta, M. Limongi, and A. Tornambè, editors, *Advances in Computational Astrophysics: Methods, Tools, and Outcome*, volume 453 of *Astronomical Society of the Pacific Conference Series*, page 365, July 2012.

J. S. Mathis. Interstellar dust and extinction. *ARA&A*, 28:37–70, 1990. doi: 10.1146/annurev.aa.28.090190.000345.

J. S. Mathis, W. Rumpl, and K. H. Nordsieck. The size distribution of interstellar grains. *ApJ*, 217:425–433, October 1977. doi: 10.1086/155591.

M. Matsuura, E. Dwek, M. Meixner, M. Otsuka, B. Babler, M. J. Barlow, J. Roman-Duval, C. Engelbracht, K. Sandstrom, M. Lakićević, J. T. van Loon, G. Sonneborn, G. C. Clayton, K. S. Long, P. Lundqvist, T. Nozawa, K. D. Gordon, S. Hony, P. Panuzzo, K. Okumura, K. A. Misselt, E. Montiel, and M. Sauvage. Herschel Detects a Massive Dust Reservoir in Supernova 1987A. *Science*, 333: 1258, September 2011. doi: 10.1126/science.1205983.

F. Matteucci, editor. *The chemical evolution of the Galaxy*, volume 253 of *Astrophysics and Space Science Library*, 2001. doi: 10.1007/978-94-010-0967-6.

F. Matteucci and L. Greggio. Relative roles of type I and II supernovae in the chemical enrichment of the interstellar gas. *A&A*, 154:279–287, January 1986.

L. Mattsson, A. De Cia, A. C. Andersen, and T. Zafar. On the (in)variance of the dust-to-metals ratio in galaxies. *MNRAS*, 440:1562–1570, May 2014. doi: 10.1093/mnras/stu370.

P. Mazzei, G. de Zotti, and C. Xu. Models for the evolution of the spectral energy distribution of elliptical galaxies from ultraviolet to far-infrared wavelengths. *ApJ*, 422:81–91, February 1994. doi: 10.1086/173705.

I. G. McCarthy, J. Schaye, T. J. Ponman, R. G. Bower, C. M. Booth, C. Dalla Vecchia, R. A. Crain, V. Springel, T. Theuns, and R. P. C. Wiersma. The case for AGN feedback in galaxy groups. *MNRAS*, 406:822–839, August 2010. doi: 10.1111/j.1365-2966.2010.16750.x.

C. McKee. Dust Destruction in the Interstellar Medium. In L. J. Allamandola and A. G. G. M. Tielens, editors, *Interstellar Dust*, volume 135 of *IAU Symposium*, page 431, 1989.

C. F. McKee and J. P. Ostriker. A theory of the interstellar medium - Three components regulated by supernova explosions in an inhomogeneous substrate. *ApJ*, 218:148–169, November 1977. doi: 10.1086/155667.

C. F. McKee, D. J. Hollenbach, G. C. Seab, and A. G. G. M. Tielens. The structure

of the time-dependent interstellar shocks and grain destruction in the interstellar medium. *ApJ*, 318:674–701, July 1987. doi: 10.1086/165403.

R. McKinnon, P. Torrey, and M. Vogelsberger. Dust formation in Milky Way-like galaxies. *MNRAS*, 457:3775–3800, April 2016. doi: 10.1093/mnras/stw253.

R. McKinnon, P. Torrey, M. Vogelsberger, C. C. Hayward, and F. Marinacci. Simulating the dust content of galaxies: successes and failures. *MNRAS*, 468:1505–1521, June 2017. doi: 10.1093/mnras/stx467.

B. R. McNamara, F. Kazemzadeh, D. A. Rafferty, L. Bîrzan, P. E. J. Nulsen, C. C. Kirkpatrick, and M. W. Wise. An Energetic AGN Outburst Powered by a Rapidly Spinning Supermassive Black Hole or an Accreting Ultramassive Black Hole. *ApJ*, 698:594–605, June 2009. doi: 10.1088/0004-637X/698/1/594.

M. J. Michałowski, E. J. Murphy, J. Hjorth, D. Watson, C. Gall, and J. S. Dunlop. Dust grain growth in the interstellar medium of 5 z 6.5 quasars. *A&A*, 522:A15, November 2010. doi: 10.1051/0004-6361/201014902.

E. J. Mierkiewicz, R. J. Reynolds, F. L. Roesler, J. M. Harlander, and K. P. Jaehnig. Detection of Diffuse Interstellar [O II] Emission from the Milky Way Using Spatial Heterodyne Spectroscopy. *ApJ*, 650:L63–L66, October 2006. doi: 10.1086/508745.

J. Miralda-Escudé and J. A. Kollmeier. Star Captures by Quasar Accretion Disks: A Possible Explanation of the M-σ Relation. *ApJ*, 619:30–40, January 2005. doi: 10.1086/426467.

H. Mo, F. C. van den Bosch, and S. White. *Galaxy Formation and Evolution*. May 2010.

F. J. Molster, L. B. F. M. Waters, A. G. G. M. Tielens, C. Koike, and H. Chihara. Crystalline silicate dust around evolved stars. III. A correlations study of crystalline silicate features. *A&A*, 382:241–255, January 2002. doi: 10.1051/0004-6361:20011552.

F. J. Molster, L. B. F. M. Waters, and F. Kemper. The Mineralogy of Interstellar and Circumstellar Dust in Galaxies. In T. Henning, editor, *Lecture Notes in Physics, Berlin Springer Verlag*, volume 815 of *Lecture Notes in Physics, Berlin Springer Verlag*, pages 143–201, 2010. doi: 10.1007/978-3-642-13259-9_3.

J. J. Monaghan. Smoothed particle hydrodynamics. *ARA&A*, 30:543–574, 1992. doi: 10.1146/annurev.aa.30.090192.002551.

J. J. Monaghan. Smoothed particle hydrodynamics. *Reports on Progress in Physics*, 68:1703–1759, August 2005. doi: 10.1088/0034-4885/68/8/R01.

L. A. Montier and M. Giard. The importance of dust in cooling and heating the InterGalactic Medium. *A&A*, 417:401–409, April 2004. doi: 10.1051/0004-6361:20034365.

D. C. Morton. Atomic Data for Resonance Absorption Lines. III. Wavelengths Longward of the Lyman Limit for the Elements Hydrogen to Gallium. *ApJS*, 149:205–238, November 2003. doi: 10.1086/377639.

L. Moscardini and K. Dolag. Cosmology with Numerical Simulations. In S. Matarrese, M. Colpi, V. Gorini, and U. Moschella, editors, *Astrophysics and Space Science Library*, volume 370 of *Astrophysics and Space Science Library*, page 217, 2011. doi: 10.1007/978-90-481-8685-3_4.

B. P. Moster, R. S. Somerville, C. Maulbetsch, F. C. van den Bosch, A. V. Macciò, T. Naab, and L. Oser. Constraints on the Relationship between Stellar Mass and Halo Mass at Low and High Redshift. *ApJ*, 710:903–923, February 2010. doi: 10.1088/0004-637X/710/2/903.

H. Murakami, M. Komiyama, K. Matsushita, R. Nagino, T. Sato, K. Sato, M. Kawaharada, K. Nakazawa, T. Ohashi, and Y. Takei. Suzaku and XMM-Newton Observations of the Fornax Cluster: Temperature and Metallicity Distribution. *Pub. Astron. Soc. Japan*, 63:S963–S977, November 2011. doi: 10.1093/pasj/63.sp3.S963.

G. Murante, P. Monaco, S. Borgani, L. Tornatore, K. Dolag, and D. Goz. Simulating realistic disc galaxies with a novel sub-resolution ISM model. *MNRAS*, 447:178–201, February 2015. doi: 10.1093/mnras/stu2400.

T. Naab, P. H. Johansson, and J. P. Ostriker. Minor Mergers and the Size Evolution of Elliptical Galaxies. *ApJ*, 699:L178–L182, July 2009. doi: 10.1088/0004-637X/699/2/L178.

H. Nagahara and K. Ozawa. Evaporation Kinetics of Silicate Melt. *Meteoritics and Planetary Science Supplement*, 31, January 1996.

A. Nanni, P. Marigo, M. A. T. Groenewegen, B. Aringer, L. Girardi, G. Pastorelli, A. Bressan, and S. Bladh. Constraining dust properties in circumstellar envelopes of C-stars in the Small Magellanic Cloud: optical constants and grain size of carbon dust. *MNRAS*, 462:1215–1237, October 2016. doi: 10.1093/mnras/stw1681.

A. Nanni, P. Marigo, L. Girardi, S. Rubele, A. Bressan, M. A. T. Groenewegen, G. Pastorelli, and B. Aringer. Estimating the dust production rate of carbon stars in the Small Magellanic Cloud. *MNRAS*, 473:5492–5513, February 2018. doi: 10.1093/mnras/stx2641.

Takaaki Noguchi, Noriaki Ohashi, Shinichi Tsujimoto, Takuya Mitsunari, John P. Bradley, Tomoki Nakamura, Shoichi Toh, Thomas Stephan, Naoyoshi Iwata, and Naoya Imae. Cometary dust in antarctic ice and snow: Past and present chondritic porous micrometeorites preserved on the earth's surface. *Earth and Planetary Science Letters*, 410:1 – 11, 2015. ISSN 0012-821X. doi: https://doi.org/10.1016/j.epsl.2014.11.012. URL `http://www.sciencedirect.com/science/article/pii/S0012821X14007031`.

B. R. M. Norris, P. G. Tuthill, M. J. Ireland, S. Lacour, A. A. Zijlstra, F. Lykou, T. M. Evans, P. Stewart, and T. R. Bedding. A close halo of large transparent grains around extreme red giant stars. *Nature*, 484:220–222, April 2012. doi: 10.1038/nature10935.

T. Nozawa, T. Kozasa, and A. Habe. Dust Destruction in the High-Velocity Shocks Driven by Supernovae in the Early Universe. *ApJ*, 648:435–451, September 2006. doi: 10.1086/505639.

T. Nozawa, T. Kozasa, A. Habe, E. Dwek, H. Umeda, N. Tominaga, K. Maeda, and K. Nomoto. Evolution of Dust in Primordial Supernova Remnants: Can Dust Grains Formed in the Ejecta Survive and Be Injected into the Early Interstellar Medium? *ApJ*, 666:955–966, September 2007. doi: 10.1086/520621.

T. Nozawa, T. Kozasa, N. Tominaga, I. Sakon, M. Tanaka, T. Suzuki, K. Nomoto, K. Maeda, H. Umeda, M. Limongi, and T. Onaka. Early Formation of Dust in the Ejecta of Type Ib SN 2006jc and Temperature and Mass of the Dust. *ApJ*, 684:1343–1350, September 2008. doi: 10.1086/589961.

T. Nozawa, K. Maeda, T. Kozasa, M. Tanaka, K. Nomoto, and H. Umeda. Formation of Dust in the Ejecta of Type Ia Supernovae. *ApJ*, 736:45, July 2011. doi: 10.1088/0004-637X/736/1/45.

T. Nozawa, R. S. Asano, H. Hirashita, and T. T. Takeuchi. Evolution of grain size distribution in high-redshift dusty quasars: integrating large amounts of dust and unusual extinction curves. *MNRAS*, 447:L16–L20, February 2015. doi: 10.1093/mnrasl/slu175.

J. A. Nuth, III. Grain formation and metamorphism. In *NATO Advanced Study Institute on the Cosmic Dust Connection, 3rd Course of the International School of Space Chemistry, p. 205 - 221*, pages 205–221, 1996.

T. Onaka, T. de Jong, and F. J. Willems. A study of M Mira variables based on IRAS LRS observations. I - Dust formation in the circumstellar shell. *A&A*, 218: 169–179, July 1989.

T. Onaka, I. Yamamura, T. Tanabe, T. L. Roellig, and L. Yuen. Detection of the Mid-Infrared Unidentified Bands in the Diffuse Galactic Emission by IRTS. *Pub. Astron. Soc. Japan*, 48:L59–L63, October 1996. doi: 10.1093/pasj/48.5.L59.

V. Ossenkopf, T. Henning, and J. S. Mathis. Constraints on cosmic silicates. *A&A*, 261:567–578, August 1992.

J. W. Overbeck. Small-Angle Scattering of Celestial X-Rays by Interstellar Grains. *ApJ*, 141:864, April 1965. doi: 10.1086/148180.

P. Padovani and F. Matteucci. Stellar Mass Loss in Elliptical Galaxies and the Fueling of Active Galactic Nuclei. *ApJ*, 416:26, October 1993. doi: 10.1086/173212.

P. J. E. Peebles. *The large-scale structure of the universe*. 1980.

Y. C. Pei. Interstellar dust from the Milky Way to the Magellanic Clouds. *ApJ*, 395:130–139, August 1992. doi: 10.1086/171637.

Fernando Pérez and Brian E. Granger. Ipython: A system for interactive scientific computing. *Computing in Science & Engineering*, 9(3):21–29, 2007. doi: 10.1109/MCSE.2007.53. URL `https://aip.scitation.org/doi/abs/10.1109/MCSE.2007.53`.

D. A. Perley, A. N. Morgan, A. Updike, F. Yuan, C. W. Akerlof, A. A. Miller, J. S. Bloom, S. B. Cenko, W. Li, A. V. Filippenko, J. X. Prochaska, D. A. Kann, N. R. Tanvir, A. J. Levan, N. R. Butler, P. Christian, D. H. Hartmann, P. Milne, E. S. Rykoff, W. Rujopakarn, J. C. Wheeler, and G. G. Williams. Monster in the Dark: The Ultraluminous GRB 080607 and Its Dusty Environment. *AJ*, 141:36, February 2011. doi: 10.1088/0004-6256/141/2/36.

G. L. Pilbratt, J. R. Riedinger, T. Passvogel, G. Crone, D. Doyle, U. Gageur, A. M. Heras, C. Jewell, L. Metcalfe, S. Ott, and M. Schmidt. Herschel Space

Observatory. An ESA facility for far-infrared and submillimetre astronomy. *A&A*, 518:L1, July 2010. doi: 10.1051/0004-6361/201014759.

J. L. Pineda, W. D. Langer, T. Velusamy, and P. F. Goldsmith. A Herschel [C ii] Galactic plane survey. I. The global distribution of ISM gas components. *A&A*, 554:A103, June 2013. doi: 10.1051/0004-6361/201321188.

Planck Collaboration, P. A. R. Ade, N. Aghanim, C. Armitage-Caplan, M. Arnaud, M. Ashdown, F. Atrio-Barandela, J. Aumont, C. Baccigalupi, A. J. Banday, and et al. Planck 2013 results. XVI. Cosmological parameters. *A&A*, 571:A16, November 2014. doi: 10.1051/0004-6361/201321591.

Planck Collaboration, N. Aghanim, Y. Akrami, M. Ashdown, J. Aumont, C. Baccigalupi, M. Ballardini, A. J. Banday, R. B. Barreiro, N. Bartolo, S. Basak, R. Battye, K. Benabed, J.-P. Bernard, M. Bersanelli, P. Bielewicz, J. J. Bock, J. R. Bond, J. Borrill, F. R. Bouchet, F. Boulanger, M. Bucher, C. Burigana, R. C. Butler, E. Calabrese, J.-F. Cardoso, J. Carron, A. Challinor, H. C. Chiang, J. Chluba, L. P. L. Colombo, C. Combet, D. Contreras, B. P. Crill, F. Cuttaia, P. de Bernardis, G. de Zotti, J. Delabrouille, J.-M. Delouis, E. Di Valentino, J. M. Diego, O. Doré, M. Douspis, A. Ducout, X. Dupac, S. Dusini, G. Efstathiou, F. Elsner, T. A. Enßlin, H. K. Eriksen, Y. Fantaye, M. Farhang, J. Fergusson, R. Fernandez-Cobos, F. Finelli, F. Forastieri, M. Frailis, E. Franceschi, A. Frolov, S. Galeotta, S. Galli, K. Ganga, R. T. Génova-Santos, M. Gerbino, T. Ghosh, J. González-Nuevo, K. M. Górski, S. Gratton, A. Gruppuso, J. E. Gudmundsson, J. Hamann, W. Handley, D. Herranz, E. Hivon, Z. Huang, A. H. Jaffe, W. C. Jones, A. Karakci, E. Keihänen, R. Keskitalo, K. Kiiveri, J. Kim, T. S. Kisner, L. Knox, N. Krachmalnicoff, M. Kunz, H. Kurki-Suonio, G. Lagache, J.-M. Lamarre, A. Lasenby, M. Lattanzi, C. R. Lawrence, M. Le Jeune, P. Lemos, J. Lesgourgues, F. Levrier, A. Lewis, M. Liguori, P. B. Lilje, M. Lilley, V. Lindholm, M. López-Caniego, P. M. Lubin, Y.-Z. Ma, J. F. Macías-Pérez, G. Maggio, D. Maino, N. Mandolesi, A. Mangilli, A. Marcos-Caballero, M. Maris, P. G. Martin, M. Martinelli, E. Martínez-González, S. Matarrese, N. Mauri, J. D. McEwen, P. R. Meinhold, A. Melchiorri, A. Mennella, M. Migliaccio, M. Millea, S. Mitra, M.-A. Miville-Deschênes, D. Molinari, L. Montier, G. Morgante, A. Moss, P. Natoli, H. U. Nørgaard-Nielsen, L. Pagano, D. Paoletti, B. Partridge, G. Patanchon, H. V. Peiris, F. Perrotta, V. Pettorino, F. Piacentini, L. Polastri, G. Polenta, J.-L. Puget, J. P. Rachen, M. Reinecke, M. Remazeilles, A. Renzi, G. Rocha, C. Rosset, G. Roudier, J. A. Rubiño-Martín, B. Ruiz-Granados, L. Salvati, M. Sandri,

M. Savelainen, D. Scott, E. P. S. Shellard, C. Sirignano, G. Sirri, L. D. Spencer, R. Sunyaev, A.-S. Suur-Uski, J. A. Tauber, D. Tavagnacco, M. Tenti, L. Toffolatti, M. Tomasi, T. Trombetti, L. Valenziano, J. Valiviita, B. Van Tent, L. Vibert, P. Vielva, F. Villa, N. Vittorio, B. D. Wandelt, I. K. Wehus, M. White, S. D. M. White, A. Zacchei, and A. Zonca. Planck 2018 results. VI. Cosmological parameters. *ArXiv e-prints*, July 2018.

Planck Collaboration (XLIII), R. Adam, P. A. R. Ade, N. Aghanim, M. Ashdown, J. Aumont, C. Baccigalupi, A. J. Banday, R. B. Barreiro, N. Bartolo, E. Battaner, K. Benabed, A. Benoit-Lévy, M. Bersanelli, P. Bielewicz, I. Bikmaev, A. Bonaldi, J. R. Bond, J. Borrill, F. R. Bouchet, R. Burenin, C. Burigana, E. Calabrese, J.-F. Cardoso, A. Catalano, H. C. Chiang, P. R. Christensen, E. Churazov, L. P. L. Colombo, C. Combet, B. Comis, F. Couchot, B. P. Crill, A. Curto, F. Cuttaia, L. Danese, R. J. Davis, and de Bernardis. Planck intermediate results. XLIII. Spectral energy distribution of dust in clusters of galaxies. *A&A*, 596:A104, December 2016. doi: 10.1051/0004-6361/201628522.

Planck Collaboration (XXII), R. Adam, P. A. R. Ade, N. Aghanim, M. Ashdown, J. Aumont, C. Baccigalupi, A. J. Banday, R. B. Barreiro, N. Bartolo, E. Battaner, K. Benabed, A. Benoit-Lévy, M. Bersanelli, P. Bielewicz, I. Bikmaev, A. Bonaldi, J. R. Bond, J. Borrill, F. R. Bouchet, R. Burenin, C. Burigana, E. Calabrese, J.-F. Cardoso, A. Catalano, H. C. Chiang, P. R. Christensen, E. Churazov, L. P. L. Colombo, C. Combet, B. Comis, F. Couchot, B. P. Crill, A. Curto, F. Cuttaia, L. Danese, R. J. Davis, P. de Bernardis, A. de Rosa, and de Zotti. . *A&A*, 576: A107, December 2015.

S. Planelles, S. Borgani, D. Fabjan, M. Killedar, G. Murante, G. L. Granato, C. Ragone-Figueroa, and K. Dolag. On the role of AGN feedback on the thermal and chemodynamical properties of the hot intracluster medium. *MNRAS*, 438: 195–216, February 2014. doi: 10.1093/mnras/stt2141.

G. Popping, R. S. Somerville, and M. Galametz. The dust content of galaxies from z = 0 to z = 9. *MNRAS*, 471:3152–3185, November 2017. doi: 10.1093/mnras/stx1545.

P. Predehl and J. H. M. M. Schmitt. X-raying the interstellar medium: ROSAT observations of dust scattering halos. *A&A*, 293:889–905, January 1995.

W. H. Press and P. Schechter. Formation of Galaxies and Clusters of Galaxies by

Self-Similar Gravitational Condensation. *ApJ*, 187:425–438, February 1974. doi: 10.1086/152650.

E. Puchwein, D. Sijacki, and V. Springel. Simulations of AGN Feedback in Galaxy Clusters and Groups: Impact on Gas Fractions and the L_X-T Scaling Relation. *ApJ*, 687:L53, November 2008. doi: 10.1086/593352.

C. Ragone-Figueroa, G. L. Granato, G. Murante, S. Borgani, and W. Cui. Brightest cluster galaxies in cosmological simulations: achievements and limitations of active galactic nuclei feedback models. *MNRAS*, 436:1750–1764, December 2013. doi: 10.1093/mnras/stt1693.

C. Ragone-Figueroa, G. L. Granato, M. E. Ferraro, G. Murante, V. Biffi, S. Borgani, S. Planelles, and E. Rasia. BCG Mass Evolution in Cosmological Hydro-Simulations. *ArXiv e-prints*, March 2018.

A. Rémy-Ruyer, S. C. Madden, F. Galliano, M. Galametz, T. T. Takeuchi, R. S. Asano, S. Zhukovska, V. Lebouteiller, D. Cormier, A. Jones, M. Bocchio, M. Baes, G. J. Bendo, M. Boquien, A. Boselli, I. DeLooze, V. Doublier-Pritchard, T. Hughes, O. Ł. Karczewski, and L. Spinoglio. Gas-to-dust mass ratios in local galaxies over a 2 dex metallicity range. *A&A*, 563:A31, March 2014. doi: 10.1051/0004-6361/201322803.

A. Renzini and A. Buzzoni. Global properties of stellar populations and the spectral evolution of galaxies. In C. Chiosi and A. Renzini, editors, *Spectral Evolution of Galaxies*, volume 122 of *Astrophysics and Space Science Library*, pages 195–231, 1986. doi: 10.1007/978-94-009-4598-2_19.

R. J. Reynolds, F. Scherb, and F. L. Roesler. Observations of Diffuse Galactic HA and [n II] Emission. *ApJ*, 185:869–876, November 1973. doi: 10.1086/152461.

G. H. Rieke and M. J. Lebofsky. The interstellar extinction law from 1 to 13 microns. *ApJ*, 288:618–621, January 1985. doi: 10.1086/162827.

D. P. Rolf. Evidence for the detection of X-ray scattering from interstellar dust grains. *Nature*, 302:46–48, March 1983. doi: 10.1038/302046a0.

D. Romano, A. I. Karakas, M. Tosi, and F. Matteucci. Quantifying the uncertainties of chemical evolution studies. II. Stellar yields. *A&A*, 522:A32, November 2010. doi: 10.1051/0004-6361/201014483.

P. Rosati, S. Borgani, and C. Norman. The Evolution of X-ray Clusters of Galaxies. *ARA&A*, 40:539–577, 2002. doi: 10.1146/annurev.astro.40.120401.150547.

S. Rosswog. Astrophysical smooth particle hydrodynamics. , 53:78–104, April 2009. doi: 10.1016/j.newar.2009.08.007.

K. Rowlands, H. L. Gomez, L. Dunne, A. Aragón-Salamanca, S. Dye, S. Maddox, E. da Cunha, and P. van der Werf. The dust budget crisis in high-redshift submillimetre galaxies. *MNRAS*, 441:1040–1058, June 2014. doi: 10.1093/mnras/stu605.

G. B. Rybicki and A. P. Lightman. *Radiative processes in astrophysics*. 1979.

D. Ryu, J. P. Ostriker, H. Kang, and R. Cen. A cosmological hydrodynamic code based on the total variation diminishing scheme. *ApJ*, 414:1–19, September 1993. doi: 10.1086/173051.

E. E. Salpeter. The Luminosity Function and Stellar Evolution. *ApJ*, 121:161, January 1955. doi: 10.1086/145971.

E. E. Salpeter. Formation and flow of dust grains in cool stellar atmospheres. *ApJ*, 193:585–592, November 1974. doi: 10.1086/153196.

E. E. Salpeter. Formation and destruction of dust grains. *ARA&A*, 15:267–293, 1977. doi: 10.1146/annurev.aa.15.090177.001411.

D. B. Sanders and I. F. Mirabel. Luminous Infrared Galaxies. *ARA&A*, 34:749, 1996. doi: 10.1146/annurev.astro.34.1.749.

S. A. Sandford. The collection and analysis of extraterrestrial dust particles. *Fundamental Cosmic Physics*, 12:1–73, 1987.

A. Sarangi, M. Matsuura, and E. R. Micelotta. Dust in Supernovae and Supernova Remnants I: Formation Scenarios. *SSR*, 214:63, April 2018. doi: 10.1007/s11214-018-0492-7.

C. L. Sarazin. *X-ray emission from clusters of galaxies*. 1988.

B. D. Savage and K. R. Sembach. Interstellar Gas-Phase Abundances and Physical Conditions toward Two Distant High-Latitude Halo Stars. *ApJ*, 470:893, October 1996. doi: 10.1086/177919.

B. D. Savage, J. A. Cardelli, and U. J. Sofia. Ultraviolet observations of the gas

phase abundances in the diffuse clouds toward Zeta Ophiuchi at 3.5 kilometers per second resolution. *ApJ*, 401:706–723, December 1992. doi: 10.1086/172098.

J. M. Scalo. Heating of dense interstellar clouds by magnetic ion slip - A constraint on cloud field strengths. *ApJ*, 213:705–711, May 1977. doi: 10.1086/155200.

P. Schady, S. Savaglio, T. Krühler, J. Greiner, and A. Rau. The missing gas problem in GRB host galaxies: evidence for a highly ionised component. *A&A*, 525:A113, January 2011. doi: 10.1051/0004-6361/201015608.

M. Schmidt. Derivation of the initial luminosity function and the past rate of star formation. In J. L. Greenstein, editor, *The Hertzsprung-Russell Diagram*, volume 10 of *IAU Symposium*, page 99, 1959.

R. Schneider, R. Valiante, P. Ventura, F. dell'Agli, M. Di Criscienzo, H. Hirashita, and F. Kemper. Dust production rate of asymptotic giant branch stars in the Magellanic Clouds. *MNRAS*, 442:1440–1450, August 2014. doi: 10.1093/mnras/stu861.

A. Schurer, F. Calura, L. Silva, A. Pipino, G. L. Granato, F. Matteucci, and R. Maiolino. The importance of following the evolution of the dust in galaxies on their SEDs. In L. K. Hunt, S. C. Madden, and R. Schneider, editors, *Low-Metallicity Star Formation: From the First Stars to Dwarf Galaxies*, volume 255 of *IAU Symposium*, pages 147–151, December 2008. doi: 10.1017/S1743921308024721.

N. Scoville, K. Sheth, H. Aussel, P. Vanden Bout, P. Capak, A. Bongiorno, C. M. Casey, L. Murchikova, J. Koda, J. Álvarez-Márquez, N. Lee, C. Laigle, H. J. McCracken, O. Ilbert, A. Pope, D. Sanders, J. Chu, S. Toft, R. J. Ivison, and S. Manohar. ISM Masses and the Star formation Law at Z = 1 to 6: ALMA Observations of Dust Continuum in 145 Galaxies in the COSMOS Survey Field. *ApJ*, 820:83, April 2016. doi: 10.3847/0004-637X/820/2/83.

M. J. Seaton. Interstellar extinction in the UV. *MNRAS*, 187:73P–76P, June 1979. doi: 10.1093/mnras/187.1.73P.

D. Sijacki, V. Springel, T. Di Matteo, and L. Hernquist. A unified model for AGN feedback in cosmological simulations of structure formation. *MNRAS*, 380:877–900, September 2007. doi: 10.1111/j.1365-2966.2007.12153.x.

J. Silk and M. J. Rees. Quasars and galaxy formation. *A&A*, 331:L1–L4, March 1998.

L. Silva, G. L. Granato, A. Bressan, and L. Danese. Modeling the Effects of Dust on Galactic Spectral Energy Distributions from the Ultraviolet to the Millimeter Band. *ApJ*, 509:103–117, December 1998. doi: 10.1086/306476.

B. W. Silverman. *Density estimation for statistics and data analysis*. 1986.

G. C. Sloan, K. E. Kraemer, P. R. Wood, A. A. Zijlstra, J. Bernard-Salas, D. Devost, and J. R. Houck. The Magellanic Zoo: Mid-Infrared Spitzer Spectroscopy of Evolved Stars and Circumstellar Dust in the Magellanic Clouds. *ApJ*, 686:1056–1081, October 2008. doi: 10.1086/591437.

U. J. Sofia, V. S. Parvathi, B. R. S. Babu, and J. Murthy. Determining Interstellar Carbon Abundances from Strong-line Transitions. *AJ*, 141:22, January 2011. doi: 10.1088/0004-6256/141/1/22.

B. T. Soifer and G. Neugebauer. The properties of infrared galaxies in the local universe. *AJ*, 101:354–361, February 1991. doi: 10.1086/115691.

R. S. Somerville and R. Davé. Physical Models of Galaxy Formation in a Cosmological Framework. *ARA&A*, 53:51–113, August 2015. doi: 10.1146/annurev-astro-082812-140951.

J. S. Spilker, D. P. Marrone, M. Aravena, M. Béthermin, M. S. Bothwell, J. E. Carlstrom, S. C. Chapman, T. M. Crawford, C. de Breuck, C. D. Fassnacht, A. H. Gonzalez, T. R. Greve, Y. Hezaveh, K. Litke, J. Ma, M. Malkan, K. M. Rotermund, M. Strandet, J. D. Vieira, A. Weiss, and N. Welikala. ALMA Imaging and Gravitational Lens Models of South Pole Telescope-Selected Dusty, Star-Forming Galaxies at High Redshifts. *ApJ*, 826:112, August 2016. doi: 10.3847/0004-637X/826/2/112.

L. Spitzer, Jr. Review of Publications: Physical Processes in the Interstellar Medium. , 72:349, December 1978.

V. Springel. The cosmological simulation code GADGET-2. *MNRAS*, 364:1105–1134, December 2005. doi: 10.1111/j.1365-2966.2005.09655.x.

V. Springel. E pur si muove: Galilean-invariant cosmological hydrodynamical simulations on a moving mesh. *MNRAS*, 401:791–851, January 2010. doi: 10.1111/j.1365-2966.2009.15715.x.

V. Springel and L. Hernquist. Cosmological smoothed particle hydrodynamics simulations: a hybrid multiphase model for star formation. *MNRAS*, 339:289–311, February 2003. doi: 10.1046/j.1365-8711.2003.06206.x.

V. Springel, N. Yoshida, and S. D. M. White. GADGET: a code for collisionless and gasdynamical cosmological simulations. *New Astronomy*, 6:79–117, April 2001. doi: 10.1016/S1384-1076(01)00042-2.

S. Srinivasan, M. L. Boyer, F. Kemper, M. Meixner, B. A. Sargent, and D. Riebel. VizieR Online Data Catalog: SAGE SMC evolved stars candidates (Srinivasan+, 2016). *VizieR Online Data Catalog*, 745, November 2016.

T. P. Stecher. Interstellar Ectinction in the Ultraviolet. *ApJ*, 142:1683, November 1965. doi: 10.1086/148462.

T. P. Stecher. Interstellar Extinction in the Ultraviolet. II. *ApJ*, 157:L125, August 1969. doi: 10.1086/180400.

T. P. Stecher and B. Donn. On Graphite and Interstellar Extinction. *ApJ*, 142:1681, November 1965. doi: 10.1086/148461.

R. S. Sutherland and M. A. Dopita. Cooling functions for low-density astrophysical plasmas. *ApJS*, 88:253–327, September 1993. doi: 10.1086/191823.

T. Szalai and J. Vinkó. Twelve type II-P supernovae seen with the eyes of Spitzer. *A&A*, 549:A79, January 2013. doi: 10.1051/0004-6361/201220015.

M. Tanaka, T. Matsumoto, H. Murakami, M. Kawada, M. Noda, and S. Matsuura. IRTS Observation of the Unidentified 3.3-Micron Band in the Diffuse Galactic Emission. *Pub. Astron. Soc. Japan*, 48:L53–L57, October 1996. doi: 10.1093/pasj/48.5.L53.

E. J. Tasker and J. C. Tan. Star Formation in Disk Galaxies. I. Formation and Evolution of Giant Molecular Clouds via Gravitational Instability and Cloud Collisions. *ApJ*, 700:358–375, July 2009. doi: 10.1088/0004-637X/700/1/358.

M. Tegmark, M. A. Strauss, M. R. Blanton, K. Abazajian, S. Dodelson, H. Sandvik, X. Wang, D. H. Weinberg, I. Zehavi, N. A. Bahcall, F. Hoyle, D. Schlegel, R. Scoccimarro, M. S. Vogeley, A. Berlind, T. Budavari, A. Connolly, D. J. Eisenstein, D. Finkbeiner, J. A. Frieman, J. E. Gunn, L. Hui, B. Jain, D. Johnston, S. Kent, H. Lin, R. Nakajima, R. C. Nichol, J. P. Ostriker, A. Pope, R. Scranton, U. Seljak, R. K. Sheth, A. Stebbins, A. S. Szalay, I. Szapudi, Y. Xu, J. An-

nis, J. Brinkmann, S. Burles, F. J. Castander, I. Csabai, J. Loveday, M. Doi, M. Fukugita, B. Gillespie, G. Hennessy, D. W. Hogg, Ž. Ivezić, G. R. Knapp, D. Q. Lamb, B. C. Lee, R. H. Lupton, T. A. McKay, P. Kunszt, J. A. Munn, L. O'Connell, J. Peoples, J. R. Pier, M. Richmond, C. Rockosi, D. P. Schneider, C. Stoughton, D. L. Tucker, D. E. vanden Berk, B. Yanny, and D. G. York. Cosmological parameters from SDSS and WMAP. *Phys. Rev. D*, 69(10):103501, May 2004. doi: 10.1103/PhysRevD.69.103501.

F.-K. Thielemann, C. Fröhlich, R. Hirschi, M. Liebendörfer, I. Dillmann, D. Mocelj, T. Rauscher, G. Martinez-Pinedo, K. Langanke, K. Farouqi, K.-L. Kratz, B. Pfeiffer, I. Panov, D. K. Nadyozhin, S. Blinnikov, E. Bravo, W. R. Hix, P. Höflich, and N. T. Zinner. Production of intermediate-mass and heavy nuclei. *Progress in Particle and Nuclear Physics*, 59:74–93, July 2007. doi: 10.1016/j.ppnp.2006.12.019.

A. Tielens. Dust in Dense Clouds. In L. J. Allamandola and A. G. G. M. Tielens, editors, *Interstellar Dust*, volume 135 of *IAU Symposium*, page 239, 1989.

A. G. G. M. Tielens. Carbon stardust: From soot to diamonds. In J. C. Tarter, S. Chang, and D. J. Defrees, editors, *NASA Conference Publication*, volume 3061 of *NASA Conference Publication*, April 1990.

A. G. G. M. Tielens and L. J. Allamandola. Evolution of interstellar dust. In G. E. Morfill and M. Scholer, editors, *NATO ASIC Proc. 210: Physical Processes in Interstellar Clouds*, pages 333–376, 1987.

A. G. G. M. Tielens, C. F. McKee, C. G. Seab, and D. J. Hollenbach. The physics of grain-grain collisions and gas-grain sputtering in interstellar shocks. *ApJ*, 431: 321–340, August 1994. doi: 10.1086/174488.

P. Todini and A. Ferrara. Dust formation in primordial Type II supernovae. *MNRAS*, 325:726–736, August 2001. doi: 10.1046/j.1365-8711.2001.04486.x.

G. Tormen, F. R. Bouchet, and S. D. M. White. The structure and dynamical evolution of dark matter haloes. *MNRAS*, 286:865–884, April 1997. doi: 10.1093/mnras/286.4.865.

L. Tornatore, S. Borgani, K. Dolag, and F. Matteucci. Chemical enrichment of galaxy clusters from hydrodynamical simulations. *MNRAS*, 382:1050–1072, December 2007. doi: 10.1111/j.1365-2966.2007.12070.x.

R. Treffers and M. Cohen. High-resolution spectra of cool stars in the 10- and 20-micron regions. *ApJ*, 188:545–552, March 1974. doi: 10.1086/152746.

J. C. Tsai and W. G. Mathews. Interstellar Grains in Elliptical Galaxies: Grain Evolution. *ApJ*, 448:84, July 1995. doi: 10.1086/175943.

J. Tumlinson, M. S. Peeples, and J. K. Werk. The Circumgalactic Medium. *ARA&A*, 55:389–432, August 2017. doi: 10.1146/annurev-astro-091916-055240.

Y. Ueda, K. Mitsuda, H. Murakami, and K. Matsushita. Study of the Galactic Interstellar Medium from High-Resolution X-Ray Spectroscopy: X-Ray Absorption Fine Structure and Abundances of O, Mg, Si, S, and Fe. *ApJ*, 620:274–286, February 2005. doi: 10.1086/426933.

S. Van Der Walt, S. C. Colbert, and G. Varoquaux. The NumPy array: a structure for efficient numerical computation. *ArXiv e-prints*, February 2011.

P. Ventura, M. D. Criscienzo, R. Schneider, R. Carini, R. Valiante, F. D'Antona, S. Gallerani, R. Maiolino, and A. Tornambé. Dust formation around AGB and SAGB stars: a trend with metallicity? *MNRAS*, 424:2345–2357, August 2012. doi: 10.1111/j.1365-2966.2012.21403.x.

M. Viel, E. Branchini, R. Cen, J. P. Ostriker, S. Matarrese, P. Mazzotta, and B. Tully. Tracing the warm-hot intergalactic medium in the local Universe. *MNRAS*, 360:1110–1122, July 2005. doi: 10.1111/j.1365-2966.2005.09097.x.

U. P. Vijh, A. N. Witt, and K. D. Gordon. Blue Luminescence and the Presence of Small Polycyclic Aromatic Hydrocarbons in the Interstellar Medium. *ApJ*, 633: 262–271, November 2005. doi: 10.1086/447763.

C. Vollmer, P. Hoppe, and F. E. Brenker. Si Isotopic Compositions of Presolar Silicate Grains from Red Giant Stars and Supernovae. *ApJ*, 684:611–617, September 2008. doi: 10.1086/589913.

N. V. Voshchinnikov and T. Henning. From interstellar abundances to grain composition: the major dust constituents Mg, Si, and Fe. *A&A*, 517:A45, July 2010. doi: 10.1051/0004-6361/200912817.

K. Wada and C. A. Norman. Density Structure of the Interstellar Medium and the Star Formation Rate in Galactic Disks. *ApJ*, 660:276–287, May 2007. doi: 10.1086/513002.

L. B. F. M. Waters, F. J. Molster, T. de Jong, D. A. Beintema, C. Waelkens, A. C. A. Boogert, D. R. Boxhoorn, T. de Graauw, S. Drapatz, H. Feuchtgruber, R. Genzel, F. P. Helmich, A. M. Heras, R. Huygen, H. Izumiura, K. Justtanont, D. J. M. Kester, D. Kunze, F. Lahuis, H. J. G. L. M. Lamers, K. J. Leech, C. Loup, D. Lutz, P. W. Morris, S. D. Price, P. R. Roelfsema, A. Salama, S. G. Schaeidt, A. G. G. M. Tielens, N. R. Trams, E. A. Valentijn, B. Vandenbussche, M. E. van den Ancker, E. F. van Dishoeck, H. Van Winckel, P. R. Wesselius, and E. T. Young. Mineralogy of oxygen-rich dust shells. *A&A*, 315:L361–L364, November 1996.

L. B. F. M. Waters, D. A. Beintema, A. A. Zijlstra, A. de Koter, F. J. Molster, J. Bouwman, T. de Jong, S. R. Pottasch, and T. de Graauw. Crystalline silicates in planetary nebulae with [WC] central stars. *A&A*, 331:L61–L64, March 1998.

S. Weinberg. *Gravitation and Cosmology: Principles and Applications of the General Theory of Relativity*. July 1972.

J. C. Weingartner and B. T. Draine. Dust Grain-Size Distributions and Extinction in the Milky Way, Large Magellanic Cloud, and Small Magellanic Cloud. *ApJ*, 548:296–309, February 2001. doi: 10.1086/318651.

D. C. B. Whittet, editor. *Dust in the galactic environment*, 2003.

D. C. B. Whittet, P. G. Martin, E. L. Fitzpatrick, and D. Massa. Interstellar extinction in the infrared - The molecular cloud toward HD 62542. *ApJ*, 408: 573–578, May 1993. doi: 10.1086/172615.

N. C. Wickramasinghe. On the growth and destruction of ice mantles on interstellar graphite grains. *MNRAS*, 131:177, 1965. doi: 10.1093/mnras/131.1.177.

N. C. Wickramasinghe and A. N. Wickramasinghe. Evidence for iron whiskers in SN1987A. *Ap&SS*, 200:145–150, February 1993. doi: 10.1007/BF00658117.

R. P. C. Wiersma, J. Schaye, and B. D. Smith. The effect of photoionization on the cooling rates of enriched, astrophysical plasmas. *MNRAS*, 393:99–107, February 2009. doi: 10.1111/j.1365-2966.2008.14191.x.

R. P. C. Wiersma, J. Schaye, C. Dalla Vecchia, C. M. Booth, T. Theuns, and A. Aguirre. The enrichment history of cosmic metals. *MNRAS*, 409:132–144, November 2010. doi: 10.1111/j.1365-2966.2010.17299.x.

P. M. Williams. Heated dust around the LMC Wolf-Rayet system HD 36402 (BAT99-

38). *Bulletin de la Societe Royale des Sciences de Liege*, 80:195–198, January 2011.

J. M. Winters, A. J. Fleischer, T. Le Bertre, and E. Sedlmayr. Circumstellar dust shells around long-period variables. V. A consistent time-dependent model for the extreme carbon star AFGL 3068. *A&A*, 326:305–317, October 1997.

A. N. Witt and U. P. Vijh. Extended Red Emission: Photoluminescence by Interstellar Nanoparticles. In A. N. Witt, G. C. Clayton, and B. T. Draine, editors, *Astrophysics of Dust*, volume 309 of *Astronomical Society of the Pacific Conference Series*, page 115, May 2004.

S. E. Woosley and T. A. Weaver. The Evolution and Explosion of Massive Stars. II. Explosive Hydrodynamics and Nucleosynthesis. *ApJS*, 101:181, November 1995. doi: 10.1086/192237.

E. L. Wright, P. R. M. Eisenhardt, A. K. Mainzer, M. E. Ressler, R. M. Cutri, T. Jarrett, J. D. Kirkpatrick, D. Padgett, R. S. McMillan, M. Skrutskie, S. A. Stanford, M. Cohen, R. G. Walker, J. C. Mather, D. Leisawitz, T. N. Gautier, III, I. McLean, D. Benford, C. J. Lonsdale, A. Blain, B. Mendez, W. R. Irace, V. Duval, F. Liu, D. Royer, I. Heinrichsen, J. Howard, M. Shannon, M. Kendall, A. L. Walsh, M. Larsen, J. G. Cardon, S. Schick, M. Schwalm, M. Abid, B. Fabinsky, L. Naes, and C.-W. Tsai. The Wide-field Infrared Survey Explorer (WISE): Mission Description and Initial On-orbit Performance. *AJ*, 140:1868–1881, December 2010. doi: 10.1088/0004-6256/140/6/1868.

G. Xu. A New Parallel N-Body Gravity Solver: TPM. *ApJS*, 98:355, May 1995. doi: 10.1086/192166.

H. Yan, A. Lazarian, and B. T. Draine. Dust Dynamics in Compressible Magnetohydrodynamic Turbulence. *ApJ*, 616:895–911, December 2004. doi: 10.1086/425111.

Y. Yao, S. N. Zhang, X. Zhang, and Y. Feng. A New Method to Resolve X-Ray Halos around Point Sources with Chandra Data and Its Application to Cygnus X-1. *ApJ*, 594:L43–L46, September 2003. doi: 10.1086/378510.

E. T. Young, E. E. Becklin, P. M. Marcum, T. L. Roellig, J. M. De Buizer, T. L. Herter, R. Güsten, E. W. Dunham, P. Temi, B.-G. Andersson, D. Backman, M. Burgdorf, L. J. Caroff, S. C. Casey, J. A. Davidson, E. F. Erickson, R. D. Gehrz, D. A. Harper, P. M. Harvey, L. A. Helton, S. D. Horner, C. D. Howard, R. Klein, A. Krabbe, I. S. McLean, A. W. Meyer, J. W. Miles, M. R. Morris,

W. T. Reach, J. Rho, M. J. Richter, H.-P. Roeser, G. Sandell, R. Sankrit, M. L. Savage, E. C. Smith, R. Y. Shuping, W. D. Vacca, J. E. Vaillancourt, J. Wolf, and H. Zinnecker. Early Science with SOFIA, the Stratospheric Observatory For Infrared Astronomy. *ApJ*, 749:L17, April 2012. doi: 10.1088/2041-8205/749/2/L17.

G. Zanardo, L. Staveley-Smith, R. Indebetouw, R. A. Chevalier, M. Matsuura, B. M. Gaensler, M. J. Barlow, C. Fransson, R. N. Manchester, M. Baes, J. R. Kamenetzky, M. Lakićević, P. Lundqvist, J. M. Marcaide, I. Martí-Vidal, M. Meixner, C.-Y. Ng, S. Park, G. Sonneborn, J. Spyromilio, and J. T. van Loon. Spectral and Morphological Analysis of the Remnant of Supernova 1987A with ALMA and ATCA. *ApJ*, 796:82, December 2014. doi: 10.1088/0004-637X/796/2/82.

S. T. Zeegers, E. Costantini, C. P. de Vries, A. G. G. M. Tielens, H. Chihara, F. de Groot, H. Mutschke, L. B. F. M. Waters, and S. Zeidler. Absorption and scattering by interstellar dust in the silicon K-edge of GX 5-1. *A&A*, 599:A117, March 2017. doi: 10.1051/0004-6361/201628507.

S. Zhukovska, H.-P. Gail, and M. Trieloff. Evolution of interstellar dust and stardust in the solar neighbourhood. *A&A*, 479:453–480, February 2008. doi: 10.1051/0004-6361:20077789.

S. Zhukovska, C. Dobbs, E. B. Jenkins, and R. S. Klessen. Modeling Dust Evolution in Galaxies with a Multiphase, Inhomogeneous ISM. *ApJ*, 831:147, November 2016. doi: 10.3847/0004-637X/831/2/147.

S. Zhukovska, T. Henning, and C. Dobbs. Iron and Silicate Dust Growth in the Galactic Interstellar Medium: Clues from Element Depletions. *ApJ*, 857:94, April 2018. doi: 10.3847/1538-4357/aab438.

A. A. Zijlstra. Mass loss on the Asymptotic Giant Branch. In M. J. Barlow and R. H. Méndez, editors, *Planetary Nebulae in our Galaxy and Beyond*, volume 234 of *IAU Symposium*, pages 55–62, 2006. doi: 10.1017/S1743921306002754.